Design of a MEMS micro-resistojet

22 June, 2011

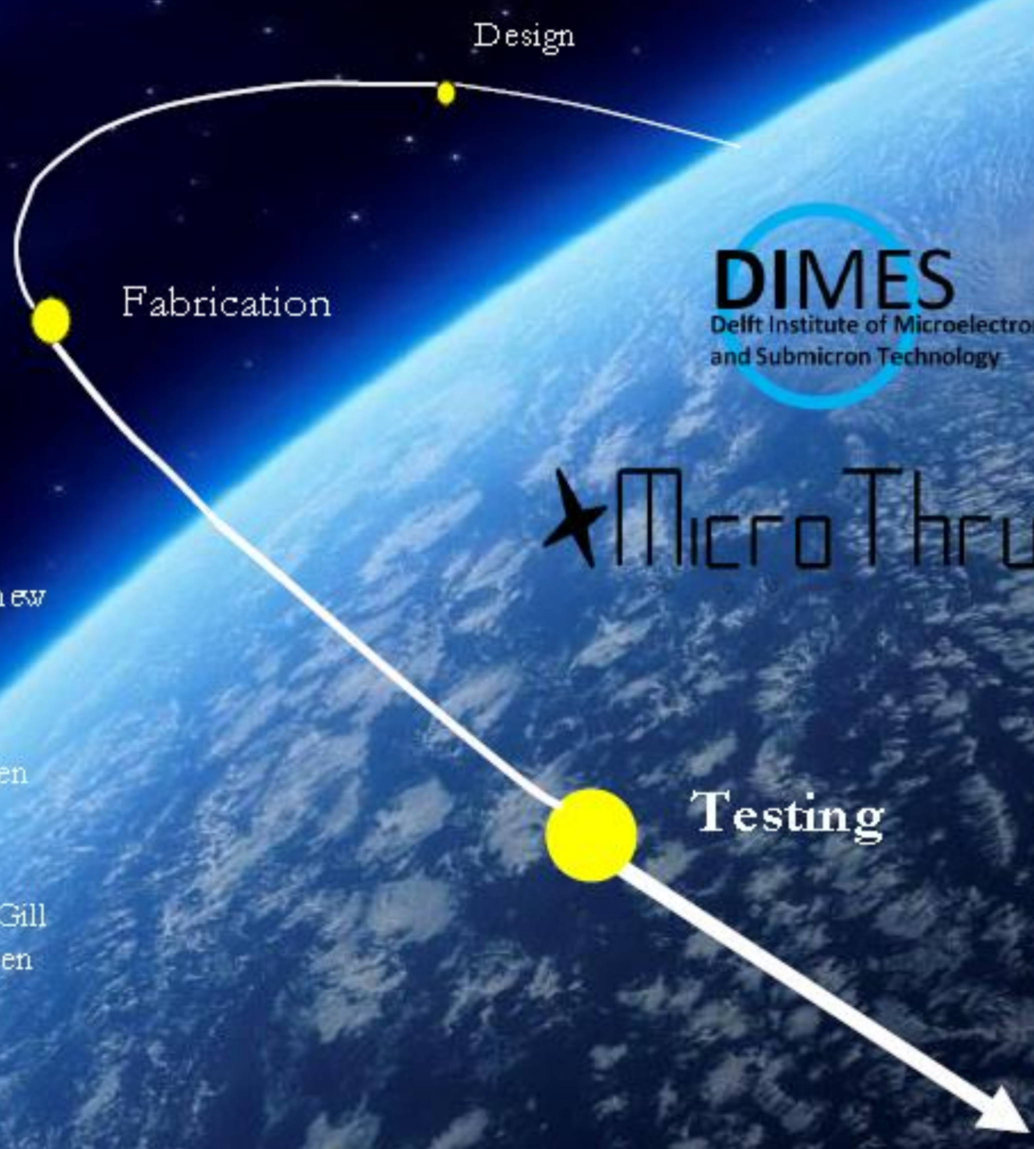

DIMES
Delft Institute of Microelectronics and Submicron Technology

MicroThrust

Candidate:
Tittu Varghese Mathew
1529927

Daily supervisor:
Ir. B.T.C. Zandbergen

Committee:
Prof. dr. ir. E.K.A. Gill
Ir. B.T.C. Zandbergen
Marko Mihailovic

TU Delft Delft University of Technology

Faculty of Aerospace engineering

Challenge the future

Acknowledgements

"Many of the great achievements of the world were accomplished by tired and discouraged men who kept on working" – Author Unknown

So goes one of the greatest quotes on work ethics. It's been more than a year since I started of with my research on the first prototype of a MEMS micro-resistojet from the Netherlands. Though this cannot be counted as a great achievement yet, I am convinced that the output from my work can be counted as a first small step in developing the competency of TUDelft in MEMS micro-propulsion technology and thereby help to define a framework to achieve the next higher goal of developing an integrated product. Over the past year, I have benefited from the help, encouragements, and criticism offered by many people.

First and foremost, I would like to give my sincere gratitude to my advisor, ir Barry Zandbergen, for giving me this opportunity to work on this exciting project. His deep scientific insight and serious attitude towards research has helped to nurture my potential of reasoning, to come to conclusions and to think things through. His quality of seeking the details in whatever job undertaken has helped to fine-tune my small engineering mind. At times I had spent time worrying about events that were out of my control, which later made me feel lost, helpless and powerless in taking an action. But his constant encouragement to bring out a little more persistence and effort from me has helped to turn what seemed a hopeless failure to a promising result.

I would also like to thank Geert Brouwer for his help with the purchase of sensors and test hardware. His expertise in hardware selection and the constructive criticism during the test setup preparation has helped to highlight the mistakes in my approach to test planning.

I also thank all my friends and colleagues in SSE group for their companionship and support. Especially, I would like to thank Alessandro Migliaccio for letting me to learn from him during his time inside the cleanroom and for sharing his knowledge and passion for rocket science in particular and space in general with me.

I have sincere gratitude to Prof. P. M. Sarro and Prof. J. F. Creemer for their foresight in seeing a window of opportunity in collaborating with the space engineering department and their unrelenting help and support with the correction of abstract and technical papers. I owe a great sense of appreciation for the time I have spent working with Marko Mihailovic, whose design of MEMS micro-evaporator was modified to suite our requirements. At many times, he has been more than a mentor to me, exposing me to the real world of research were results prove powerfull than words. I would also like to acknowledge the staff members at the DIMES cleanroom, especially Luigi Mele and Bruno Morana for assisting us during the fabrication phase of the project, and Silvana Milosavljević and Charles de Boer for giving me the training and the safety course to enter inside the cleanroom respectively.

Finally, I would like to thank my father, mother and my brothers for their endless love and exceptional support during the three years of my stay in Holland. By looking upto the life of my parents has helped to view the difficulties during the course as a challenege and not as a paralyzing event. I am grateful for them for sharing with me the stress and hardships of my studies for the last three years. There are many people who have shared a shoulder with me during the ups and downs of my research work: Fr. Avin, Gracy John, Gerda Rytz, Sriganesh A, Pranjal Gupta and Nijesh K. James for their unrelenting support to help me to dream and achieve the end goal.

Tittu Varghese Mathew
June 2011

Contents

TRANSDUCERS 2011 conference

MEMS SILICON-BASED RESISTOJET MICRO-THRUSTER FOR ATTITUDE CONTROL OF NANO-SATELLITES

M. Mihailovic[1], T.V. Mathew[2], J.F. Creemer[1], B.T.C. Zandbergen[2] and P.M. Sarro[1]
[1]Delft Institute of Microsystems and Nanoelectronics, Delft University of Technology, the Netherlands
[2]Chair Space Systems Engineering, Delft University of Technology, the Netherlands

This paper presents a miniaturized thruster device with an integrated thin-film heater, capable of delivering thrusts in the μN-mN range. Its small size (25 mm × 5 mm × 1 mm), low mass (162 mg), low power and propellant consumption make it very attractive for attitude control of nano-satellites (mass 1-10 kg).

Recently there has been a strong interest in the space community towards low-thrust propulsion systems, i.e. capable of delivering small thrust levels in the millinewton and micronewton range [1-4]. For such propulsion systems to be used in nano-satellites, they should be small, lightweight and have a limited power consumption (less than 1 W). Resistojet is one such option which is simple in design as it requires only a heater element to heat up stored propellant , and a nozzle to expand the hot gas to produce thrust. Presented device, fabricated in silicon MEMS technology, is designed to provide thrust levels in order of 1 mN and less, as required for fine attitude control of nano-satellites. The integrated heater is used to reduce propellant consumption.

A schematic view of the micro-thruster is shown in Figure 1. Design details are shown in Figure 2. It essentially consists of a heater channel connected to a linear (slit) nozzle. The channel is 50 μm wide and 150 μm deep. The length of the channel is 2 cm in order to have thermally fully developed flow (Fig. 2.a). The nozzle is designed with an expansion ratio of 25:1 (Fig. 2.b). Three different configurations were considered: single-channel devices with the nozzle throat height of 10 μm and 5 μm, and a three-channel device with the nozzle throat of 10 μm.

The devices were fabricated in a four masks process, using one double-side polished silicon wafer and one glass wafer anodically bonded after processing. On the front side of the silicon wafer, Al layer was sputtered on an insulating SiO_2 and patterned to define the heater and the contact pads. On the back side, three-step deep reactive ion etching (DRIE) procedure was employed to etch the channel (150 μm), the inlet hole (350 μm) and the etch-through area to thermally insulate the device (550 μm). After the wafer bonding, devices were diced and packaged (Fig. 3).

The measurements were performed in a vacuum chamber (~50 mbar), in a setup which is schematically shown in Figure 4. First, the measurements were performed without heating, with the propellant at room temperature (RT), which corresponds well to the normal satellite on-board temperatures (-10 – 40 °C). System pressure (P_S) was measured at the inlet of the thruster device (Fig. 4), based on which the pressure at the nozzle (P_C) was calculated (Fig. 5). Other relevant parameters are shown in Table 1. As expected, multi-channel devices have the same performance compared to the single-channel devices with the same nozzle, but exhibit lower pressure drop.

During heating, four-point measurements of the heater resistance provide the information on the heater temperature, based on the known TCR value of the heater material. In order to heat the gas flow to the desired working temperature, heating power is required (only e.g. 0.36 mW/K for the mass flow rate of 0.35 mg/s) which increases the chamber pressure (P_C) while the mass flow is kept constant (Figure 6).

The presented concept can be expanded to pico- and femto-satellites with the further miniaturization of the channel and nozzle dimensions. By using other propellants, such as water, thruster performance should increase. Water can be stored on-board in a liquid phase, thus limiting the storage volume. In the heater the water is gasified after which it attains a high velocity in the nozzle.

Word Count: 605

REFERENCES:

[1] J. Mueller, "Thruster options for microspacecraft: a review and evaluation of existing hardware and emerging technologies", in: AIAA97-3058.

[2] M.S. Bartsch, M.H. McCrink, R.W. Crocker, B.P. Mosier, K.A. Peterson, K. Wally, K.D. Patel, "Electrokinetically Pumped Liquid Propellant Microthrusters For Orbital Station Keeping", Transducers 2007, Lyon, France

[3] R. Krpoun, H.R. Shea, "Microfabricated Out-of-Plane Arrays of Integrated Capillary Nano-Electrospray Emitters", Transducers 2009, Denver, USA

[4] D. Briand, L. Guillot, U. Bley, S. Danninger, V. Gass, N.F. de Rooij, "Digital Micro-thrusters with simplified architecture and reliable ignition and combustion", PowerMEMS 2008

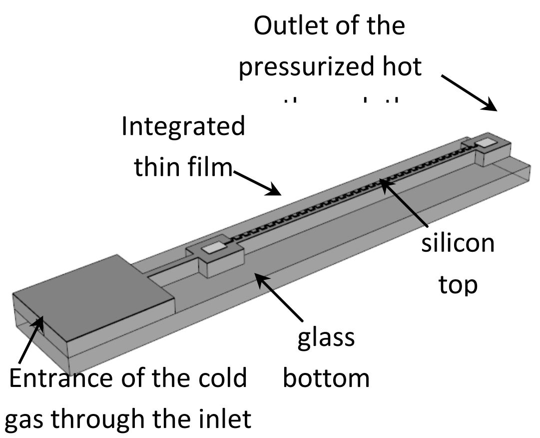

Figure 1: Sketch of the MEMS Resistojet. For test purpose, cold gas nitrogen is used as the propellant. It enters the device through the inletand is heated by the integrated thin-film heater. Bulk silicon has good thermal conduction properties and acts as heat spreader, providing the elevated temperature at the channel walls.

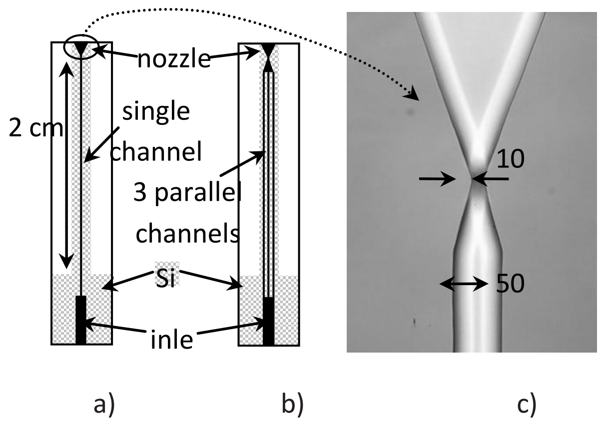

Figure 2. a) Schematic top view of the channel geometry. b) An alternative geometry (with 3 parallel channels) to further increase the performance is also considered. c) Optical image (top view) of the fabricated nozzle throat. All the channels and nozzles are 150 μm deep.

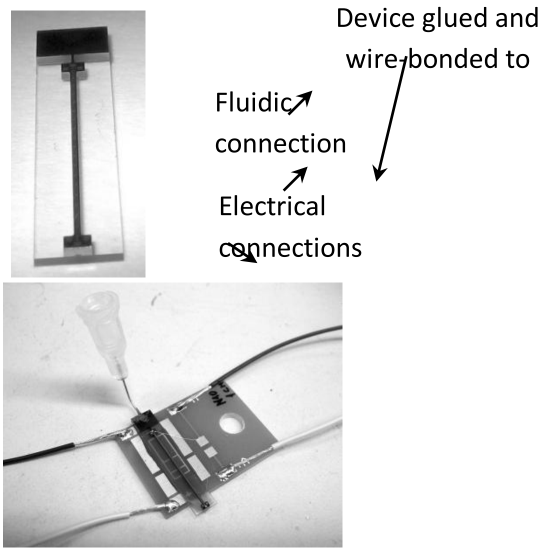

(a) (b)

Figure 3. Micro-thruster devices (25 mm x 5 mm x 1 mm) a) after fabrication and dicing and b) after packaging to the customized PCB.

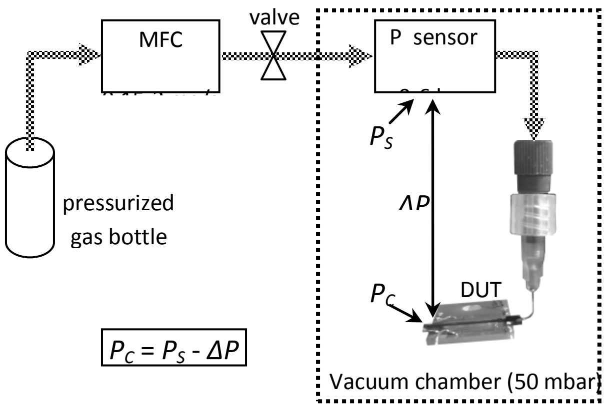

Figure 4. Schematic of the measurement setup, consisting of vacuum chamber, mass flow controller and pressure transducer. Equation used for calculating pressure at the nozzle throat (P_C) from measured P_S is also shown.

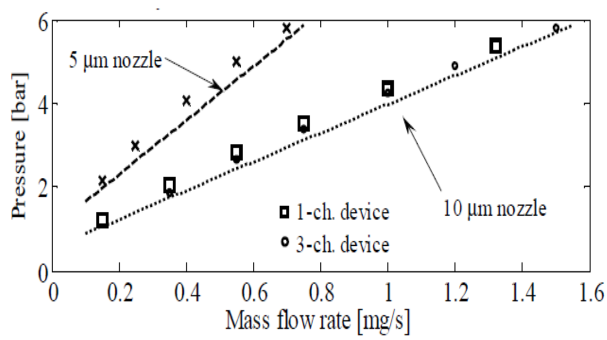

Figure 5: Measure P_s (data points) and calculated and fitted P_c (lines) for different geometries and different mass flow rates.

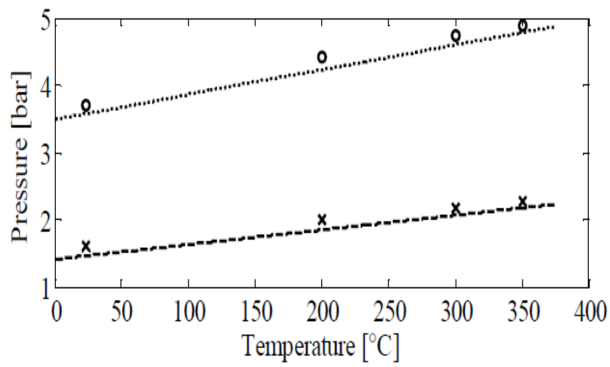

Figure 6: Change of pressure (points-P_s; line-fitted P_c) caused by heating, for mass flow rates of 0.3 mg/s (x) and 0.85 mg/s (o), for the device with the 10 µm wide nozzle throat.

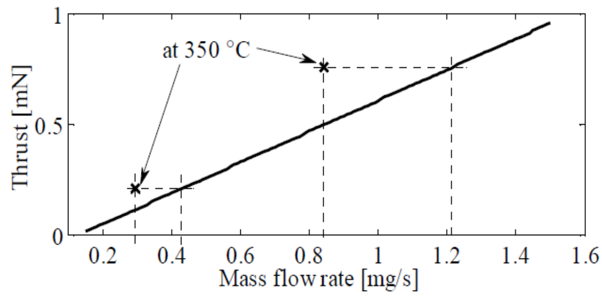

Figure 7: Thrust calculated for gas flow without heating, from the measured P_S shown in figure 5 (devices with 10 µm) nozzle), and ambient pressure (50 mbar), assuming adiabatic expansion of the gas in the nozzle and no losses. Increase of the thrust by heating (as in figure 6) is also shown.

IAC 2011 conference

62nd International Astronautical Congress 2011

SPACE PROPULSION SYMPOSIUM (C4)
Propulsion Technology (3)

Author: Mr. Tittu Varghese Mathew
Delft University of Technology (TU Delft), Rijswijk, The Netherlands, t2varghese@gmail.com
Mr. Barry Zandbergen
Delft University of Technology (TU Delft), Delft, The Netherlands,
B.T.C.Zandbergen@tudelft.nl
Mr. Marko Mihailovic
ECTM Laboratory (DIMES), TUDelft, Delft, The Netherlands, m.mihailovic@tudelft.nl
Prof. P.M. Sarro
ECTM Laboratory (DIMES), TUDelft, Delft, The Netherlands, p.m.sarro@tudelft.nl
Dr. J.F. Creemer
ECTM Laboratory (DIMES), TUDelft, Delft, The Netherlands, j.f.creemer@tudelft.nl

A SILICON-BASED MEMS RESISTOJET FOR PROPELLING CUBESATS

Abstract

Over the last decade, the space community has been showing increased interest in cubesat projects, thereby aiming to provide small spacecraft with the same capabilities as now found on larger satellites. With this comes the challenge of providing cubesats with highly integrated and miniaturized sub-systems. Of these sub-systems the miniaturization of the propulsion system is a very challenging one, because of the limitation of conventionally used space qualified Commercial off-the-shelf components to scale down with satellite size.

Here, we present a novel resistojet, realized in silicon-based MEMS technology. The design of resistojet-based systems is intrinsically simple, requiring only a heater to heat up the propellant flow before it expands in the nozzle. It is considered the step to make after cold gas propulsion as it not only offers higher performance, but also a higher propellant density and hence reduced system mass. In the same time it enables an adequate safety level, and good performance in terms of specific impulse and electric power consumption.

Our MEMS resistojet thruster has an integrated thin-film heater capable of heating propellant flow of 1 mg/s to 350°C. With nitrogen, it was demonstrated to produce a thrust between 20 μN and 1 mN. Chamber pressure values in the range of 1 - 5 bars were obtained for a propellant flow rate of 0.15 - 1.5 mg/s at cold gas mode. The discharge factor for the micro-nozzle was found to be 0.8 at higher end of mass flow range and was found to decrease by a factor of 1.6 at lower end of mass flow range. However, it is also suitable for use with water or ammonia, which will increase the propellant density. Its small size (25 x 5 x 1 mm), low mass (162 mg) and low power consumption (< 3 W) are very attractive for application on cubesats.

This paper will describe the specification of requirements, the performed analysis and the choices made. We will also outline the fabrication steps, as well as the test setup and strategy. The experimental results will be compared with the theoretical ones.

Nomenclature

A	-	area
d	-	moment arm; depth
c_p	-	specific heat capacity at constant pressure
C_d	-	discharge coefficient
C_F	-	thrust coefficient
D	-	diameter
e	-	roughness height
E_b	-	black body energy
f	-	Fanning friction factor
F	-	thrust; view factor used in radiation analysis
g	-	acceleration due to gravity (= 9.81 m/s^2)
h	-	heat transfer coefficient
H	-	enthalpy, height
I	-	current
I_{SP}	-	specific impulse
J	-	radiosity
k	-	thermal conductivity
K	-	contraction loss coefficient
Kn	-	Knudsen number
L	-	characteristic dimension, slanted divergent length
m	-	mass
M	-	molar mass, Mach number
$\dot{m}$	-	mass flow rate of propellant
N	-	number of channels
Nu	-	Nusselt number
p	-	pressure
P	-	power; perimeter
Pr	-	Prandtl number
q''	-	heat flux
r	-	radius of curvature
R	-	characteristic gas constant, electric resistance; thermal resistance
Ra	-	Rayleigh number
Re	-	Reynolds number
s	-	satellite typical dimension
t	-	silicon substrate thickness
T	-	temperature
U	-	velocity
V	-	voltage
W	-	width
x	-	axial location
z^*_{th}	-	thermodynamic development length constant
z^+	-	hydro-dynamic development length constant

List of Subscripts

a	-	ambient
b	-	bulk
c	-	chamber, channel
compr	-	compressible
cond	-	conduction
conn	-	connecting wires
constr	-	constriction
conv	-	convergent; convection
div	-	divergent
e	-	nozzle exit
eff	-	effective
el	-	electric
eq	-	equivalent
f	-	fluid; fin; film
fd	-	fully developed
g	-	Pyrex glass wafer
h	-	hydraulic; heater
i	-	inlet
incompr	-	incompressible
max	-	maximum
o	-	initial (t=0); outlet
p	-	propellant
s	-	surface
sub	-	substrate
t	-	throat
turb	-	turbulent
vap	-	vapourisation
w	-	silicon wafer; wall

List of Mathematical Symbols

$\ddot{\theta}$	-	angular acceleration
Δ	-	change
γ	-	specific heat ratio
Γ	-	vandenkerckhove function
ε	-	area ratio of the nozzle; emissivity of hot surface
ϱ	-	density; resistivity of heater material
μ	-	dynamic viscosity
α	-	nozzle half-expansion angle; temperature coefficient of resistance; aspect ratio of channels
λ	-	mean free path of gas molecules
β	-	nozzle half-contraction angle
η	-	efficiency
ξ	-	nozzle quality factor
δ^*	-	displacement thickness due to boundary layer formation
τ	-	shear stress
σ_v	-	tangential momentum accomodation coefficient
σ	-	Stefan-Boltzmann constant (= 5.67E-8 W/m^2K^4)

List of Figures

List of tables

List of Abbreviations

CFD	-	Computational Fluid Dynamics
COTS	-	Commercial Off The Shelf
CTE	-	Coefficient of Thermal Expansion
DAQ	-	Data Acquisition
DI	-	Distilled
DIMES	-	Delft Institute of Microsystems and Submicron Technology
DRIE	-	Deep Reactive Ion Etching
EDM	-	Electric Discharge Machining
ET	-	Etch Through
EWI	-	Faculteit Elektrotechniek, Wiskunde en Informatica (dutch).
FAST	-	Formation for Atmospheric Science & Technology demonstration
FLUENT	-	Computational software for fluid flow analysis
FMMR	-	Free Molecular Micro Resistojet
LABVIEW	-	LABoratory Virtual Instrumentation Engineering Workbench
LEO	-	Low Earth Orbit
MEOP	-	Maximum Expected Operating Temperature
MFC	-	Mass Flow Controller
MEMS	-	Micro Electro Mechanical Systems
MSExcel	-	Microsoft Excel program
MoI	-	Mass moment of Inertia
NIST	-	National Institute of Standards and Technology
OD	-	Outer diameter
OLFAR	-	Orbiting Low Frequency Antennas for Radio astronomy
PECVD	-	Plasma Enchanced Chemical Vapor Deposition
PCB	-	Printed Circuit Board
SEM	-	Scanning Electron Microscope
STP	-	Solar Thermal Propulsion
S/C	-	Spacecraft
TCR	-	Temperature Coefficient of Resistance
TNO	-	Netherlands Organisation for Applied Scientific Research
TU Delft	-	Delft University of Technology
VI	-	Virtual Instrument
VLM	-	Vaporising Liquid Micro-thruster

Chapter 1

INTRODUCTION

1.1 Role of micro-spacecraft

The space odyssey of the human race began way back in the 1960s with the launch of Sputnik, a "micro-satellite" weighing less than hundred kilograms carrying on-board a single payload. Later satellites became much larger with handful of instruments fitted onto a single platform to meet several mission requirements. As a result, not only the cost of spacecraft and the risk of spacecraft failure have risen to a strenuous level, but also the launch costs. As per the cost statistics, launch cost accounts for nearly one-third of total mission cost [1.16]. To address both the issues of cutting down on launch costs and increase the mission output, the space community has plans for future missions that give more emphasis on distributed space-platforms, with each platform manufactured with high degree of miniaturization and modularity. By scaling down conventional spacecraft components, mass reduction can be achieved and satellites can be made to meet launch vehicle constraints easier. Figure 1.1 shows a model of a 1-U (read as one unit) cubesat with dimensions of 10x10x10 cm.

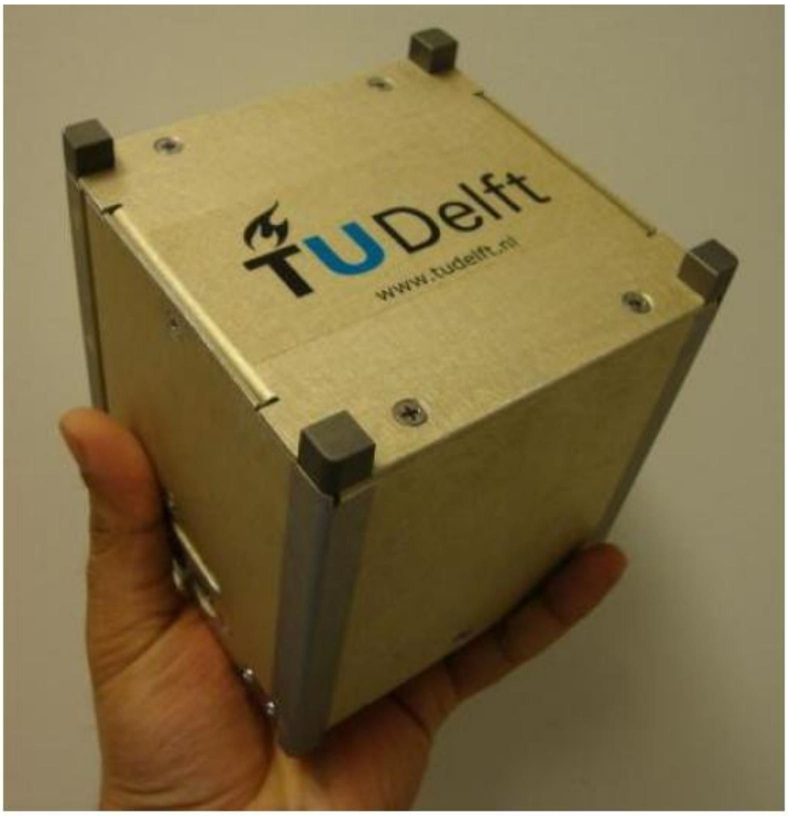

Figure 1.1: Model of 1-U cubesat.

Various categories of micro-spacecraft exist. An overview of these categories is given in table 1.1.

Table 1.1: Classification of micro-spacecrafts based on mass, on-board power and satellite dimensions [1.17].

Designation	Mass (kg)	Power (W)	Dimension (m)	Comment/Picture
Micro-spacecraft	10-100	10-100	0.3-1	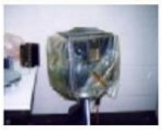
Class I micro-spacecraft	5-20	5-20	0.2-0.4	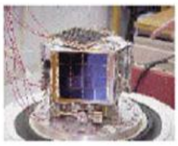
Class II micro-spacecraft	1-5	1-5	0.1-0.2	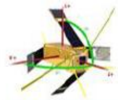
Class III micro-spacecraft	<1	<1	<0.1	

The table above shows that by scaling down the spacecraft both the mass and the available electrical power decreases. The latter is because most electrical power stems from solar panels and their size is reduced when reducing the size of the spacecraft.

TU-Delft is contributing to the development of micro-spacecraft through the Delfi series of satellites, like Delfi-C3 (launched in 2008) and Delfi-n3Xt (to be launched in 2012) [1.29]. These are Class II micro-spacecraft. In addition, TU-Delft is also joining forces with international partners like for example, the QB50 [1.27] and FAST [1.28] missions and is promoting a mission to the Moon using Class II microsatellites (OLFAR mission). One of the direct implications of small size satellites is the need for scaling down its systems, out of which miniaturization of propulsion system is found to be the most challenging. In [1.36], it is shown that the propulsion hardware makes up about 50% of the mass of a micro-satellite whereas for a conventional spacecraft, this is less than 10%. As part of the ongoing investigations in various fields at TU-Delft, the faculty of aerospace engineering is investigating amongst others the use of micro-propulsion for use on such spacecraft.

So far, TU-Delft has participated in the development of the cold-gas based T3-μps, a joint development by TNO, TU-Delft and UTwente. In addition, TU-Delft is investigating the possibility of extending the performance of this system by heating the gaseous propellant to a high temperature. This could be for instance through electrical heating and/or by solar heating as already researched in the past for larger thrusters [1.30,1.31]. Key is that sufficiently small thrusters can be manufactured.

One of the advantages of scaling down thrusters is the gain in thrust-to-weight ratio, a measure of how effective a thruster can act as an actuator as it is made clear in relation given below:

$$\frac{Thrust}{Mass_{eng}} \alpha \frac{P_c L^2}{P_c L^3} \alpha \frac{1}{L} \tag{1.1}$$

Where P_c is the chamber pressure and L is a characteristic dimension, such as the throat width [1.15]. But on the other side, a component having smaller mass makes it more vulnerable to large amplitude of acceleration during launch phase, because of its very high dynamic response [1.9,1.10,1.15]. This makes them more vulnerable to crack formations which in turn can alter their mechanical properties.

1.2 The best approach to small thrusters

In 2010 a literature study [1.1] has been performed by the author of this work to find out the best approach to fabricate such small thrusters and three choices were identified and they are: 1) MEMS (Micro-Electro-Mechanical Systems), 2) Micro-milling and 3) EDM (Electric Discharge Machining). With the rapid advancements made in MEMS technology applications in the field of micro-electronics during the last few decades, space system engineers are cashing in on the lessons learned from different MEMS manufacturing techniques to find a solution to miniaturize a conventional spacecraft component at hand to micro-level so as to fit into a cube-sat of 10x10x10 cm size [1.4]. Chief advantages of using MEMS for micro-propulsion purposes are its lightweight feature, possibility of high degree of integration between different components, robust performance with solid-state reliability and the ability to batch fabricate thereby bringing down the manufacturing cost [1.5,1.10,1.14]. All the more TU Delft has an excellent reputation in MEMS silicon technology.

It can be argued why micro-milling, which is another common method to fabricate small features, be used for scaling down spacecraft components, especially micro-thrusters. Kuan Chen [1.12] points out that due to the size of end mills used in his work, the size of minimum throat width achieved was one order of magnitude larger than that achieved by the DRIE (Deep Reactive Ion Etching) technique (DRIE is a MEMS fabrication technique and will discussed in chapter 4 on MEMS fabrication). At the same time, micro-milling will cause considerable amount of surface roughness on the micro-geometric features. The effect of surface roughness on the fluid flow will be studied in-depth in chapter 2 (nozzle flow) and 3 (heater chamber wall).

Conventional micro-machining techniques like EDM can easily achieve dimensions of 10 μm with an acceptable degree of surface quality. But there exists many limitations when compared to MEMS manufacturing [1.32]. First of all, when making a conical nozzle using EDM, it is not possible to make both the propellant flow channel and the nozzle in one single metal piece due to manufacturing setup used for EDM. Secondly, EDM can be carried out only on conductive material like aluminium, copper or steel. Cutting depths of upto any dimensions can be achieved irrespective of the thickness of the metal sheet (normally, EDM cuts through the entire metal sheet). It is possible to make micro-fluid channels and a flat nozzle of rectangle cross-section in one single sheet, but not enclosed from the top and bottom to form a closed fluidic passage. In that case, laser welding should be used to bond the metal sheets together. But, employing such high-temperature metal joining process can distort the micro-structural dimensions. With respect to surface quality that can be achieved with EDM, smoother surface can be achieved as harder materials like steel are used for machining. Also, the surface quality can be controlled by adjusting the machining setup. In short, EDM was found to be a good candidate for making the micro-fluid channels and nozzles out of conductive metals but there exists a lot more limitations compared to MEMS manufacturing to which certain solutions does not exist within TU Delft.

Therefore, it was concluded from the literature study to go with the MEMS approach to fabricate the small thruster and hence was born the opportunity to work in collaboration with the Delft Institute of Microsystems and Nanoelectronics (DIMES) department of TU Delft.

But with such a choice, comes certain challenges. Out-gassing is an issue that can hinder the application of MEMS technology in space as it may act as a source of contamination for sensitive payloads like lenses of cameras. Herbert Shea [1.8] says that this issue can be circumvented by proper hermetic sealing of MEMS devices. Satellite structure experiences large temperature gradient when it traverses from the day-light part of its orbit to the earth-shadowed stretch of the orbit. Typical thermal cycling falls in the range of 16 cycles from -80 to +100 ^{o}C for low earth orbits (LEO). Such thermal cycling can create thermal shocks in MEMS devices [1.8]. Another challenge with regard to usage of MEMS in space, as pointed out in [1.17], is to match the CTE (coefficient of thermal expansion) of structural materials used. Shea [1.8] suggests the usage of monolithic process for MEMS fabrication so that all materials have the same CTE.

1.3 Possible applications for micro-propulsion

A wide range of mission scenarios are envisioned for micro-satellites with the aim of performing useful science mission, while reducing cost and development time. Mission like rendezvous with a near Earth orbit asteroid, or an earth-observation platform with distributed satellites flying in formations [1.10] are to mention a few.

Micro-satellites require precise pointing requirements for their payloads and means of cancelling out disturbance torques produced by solar pressure, gravity gradients and earths oblateness. Thrusters, magneto-torquers and reaction wheels are some of the commonly used attitude control actuators depending on the mission orbit and mission lifetime. Though the reaction wheels are found to be more precise in achieving accurate pointing of the satellite, there exists certain disadvantage like higher cost, lower reliability due to mechanical parts and the problem of desaturation that makes it less preferable when compared to opting for thrusters. In the work of E. Razzarno [1.13], a comparative study was made between an attitude control system based on propulsion system and a reaction wheel based system in terms of mass and power. Another way of attitude control is by using magneto torquers but their usage is limited to only low earth orbits where earth's magnetic field is strong.

Two primary functions are foreseen for an on-board micro-propulsion system [1.17]:

(1) To provide slew capability to meet different mission scenarios, and
(2) To maintain the attitude within a dead-band so as to make steady scientific measurements.

The force required to meet mission derived slew requirements with one couple of thrusters firing is given by the relation [1.16]:

$$F = \frac{MoI \times \ddot{\theta}}{d} \tag{1.2}$$

where MoI is the mass moment of inertia of the satellite about the rotating axis, $\ddot{\theta}$ is the resulting angular acceleration from slew and 'd' is the moment arm.

[1] When the spacecraft's control system is being used to hold a particular attitude, there is a small range of attitude error around the ideal which is deemed acceptable and within which the thrusters do not fire. This error band is called the deadband and is usually set to be either ±5 degrees or ±0.5 degrees, depending on how accurately the spacecraft needs to be pointed. A narrower deadband will use more RCS fuel, as the thrusters will tend to fire more often when the spacecraft drifts through the small range.

From the above relation, it is clear that for a given satellite, the longer the time for the slew maneuver, the lower the force required from the thruster [1.3,1.7]. Janson [1.7] shows that the thrust required for slew (for fixed acceleration) scales with the 4th power of the satellite/spacecraft typical dimension 's'.

$$F \alpha \frac{MoI}{d}$$

$$\Leftrightarrow F \alpha \frac{Ms^2}{s} \alpha \frac{s^3.s^2}{s}$$

$$\Leftrightarrow F \alpha s^4$$

Apart from the generation of low thrust for slew requirements, another important thruster parameter is the minimum impulse bit required for precise attitude control. Impulse is defined as force (here thrust) integrated over time. When thrusting in a pulsed mode, impulse bit is the impulse generated per pulse.

Reference [1.17] provides first-hand numbers for the attitude control and slew requirements for micro-spacecraft and they are presented in table 1.2.

Table 1.2: Minimum impulse bit and thrust required for micro-spacecraft of 3 different classes [1.17]; Slew maneuver is 180 deg in 1 minute with dead band of 40 seconds.

			Required I bit, N-s						
S/C mass (kg)	S/C typical dimension (m)	Moment of inertia (kg.m2)	17 mrad (1 deg)		0.3 mrad (1 arc min)		0.02 mrad (5 arcs)		Minimum thrust for slew (mN)
			20 s	100 s	20 s	100 s	20 s	100 s	
1	0.1	0.017	1.4E-4	2.9E-5	2.5E-6	5.1E-7	1.7E-7	3.4E-8	0.06
10	0.3	0.150	4.3E-4	8.5E-5	7.5E-6	3E-6	1.0E-6	1.0E-7	1.75
20	0.4	0.533	1.1E-3	2.3E-4	2E-5	4E-6	1.3E-6	2.7E-7	4.65

All values could be reproduced (see sample calculation #1 in appendix 1) except the value for the minimum thrust for slew maneuver of 1-U cubesat. The correct value should be 0.6 mN.

Shown in table 1.2 are different pointing requirements and the time interval between the thruster firings. One can observe that the longer the time between the thruster firings (meaning large dead bands for the onboard instruments to take steady measurements), smaller will be the impulse bit that shall be imparted to the spacecraft. It can also be seen that the impulse bit requirements ranges from milli-newton-second range for coarse attitude control of large spacecrafts to micro and nano-netwon-second range for precise attitude control of very small spacecrafts. The required slew rate requirement of 180 $^{\text{deg}}/_{\text{min}}$ drives the thrust required from milli-newton range for 10-kg satellites to less than 0.1 milli-newton for 1-kg satellites [1.6].

When a thruster produces constant thrust, small impulse bits are obtained by having fast actuating valves. During the literature study [1.1], a number of micro-valves for propellant flow control have been studied. They can be mainly grouped into 4 types based on valve actuation mechanism: 1) Thermo-pneumatic, 2) Bimorph, 3) Shape memory alloy actuation and 4) electro-magnetic actuation and 5) piezoelectric actuation. For more information, the reader is referred to [1.1]. Most of the micro-valve concepts are still at their research stage. But some research groups in the Netherlands like the one at University Twente [1.33] have come up with a gas micro-valve with an actuation time of less than 30 milliseconds (actuation mechanism is by an electromagnetic mini-motor) that can be easily integrated to MEMS components. This would mean that a single cycle of opening and closing would take minimum 60 ms. Taking now the impulse bit duration as half this value, we find for the thrust (F = I bit/Δt with Δt = 30 ms) required for attitude control of satellites based on the impulse bit values given in table 1.2.

Table 1.3: Thrust required for attitude control of cubesats.

Required thrust, mN									
S/C mass (kg)	S/C typical dimension (m)	Moment of inertia (kg.m2)	17 mrad (1 deg)		0.3 mrad (1 arc min)		0.02 mrad (5 arcs)		
			20 s	100 s	20 s	100 s	20 s	100 s	
1	0.1	0.017	4.67	0.97	0.083	0.017	0.006	0.001	
10	0.3	0.150	14.33	2.83	0.25	0.1	0.033	0.003	
20	0.4	0.533	37.67	0.77	0.67	0.133	0.043	0.009	

By observing the range of thrust values for attitude control of cubesats (highlighted in table 1.3) and the thrust values required for slew maneuvers from table 1.2, it is immediately made clear that the thrust values we should aim for shall be less than or equal to 1 mN.

Another possible application of micro-propulsion is in orbit-raising maneuver of micro-satellites to prevent them from orbital decay due to atmospheric drag and thereby extend the useful science mission period. Also in the near future, space engineers plan to fly a swarm of cubesats in formation at low earth orbits for high resolution earth observation missions. In that case, apart from keeping each individual satellite in its designated orbit, an onboard propulsion system is planned to be used to maintain a precise formation by continuously correcting the relative position and velocity between two satellites and to safely make the satellites re-enter the atmosphere once the mission lifetime is over. Relative positioning is also considered for the two TU-Delft satellites proposed for the QB-50 mission [1.2] in order to improve the mission return.

Such maneuvers require total velocity increment in the range of 20 m/s. For a spacecraft of 2 kg mass, this translates to a propellant load of 4 % with a propulsion system operated in cold gas mode having an Isp of 50 seconds (Note: Cold gas mode refers to a propulsion system where the propellant is stored on-board at high pressure and is expanded through the nozzle to produce certain amount of thrust). The propellant load can be calculated by using the relation given in [1.16]:

$$m_p = m_o\left[1 - e^{\frac{-\Delta V}{I_{SP}g}}\right] = 2kg\left[1 - e^{\frac{-20 m/s}{50s \times 9.81 m/s^2}}\right] = 0.08kg \tag{1.3}$$

One can see that for a given satellite mass and total velocity increment from the mission requirements, the propellant mass to be stored on-board is a function of specific impulse of the propulsion system I_{SP}. Increasing the value of I_{SP} of the propulsion system by a factor of 8 can bring down the propellant load by an order of magnitude [1.2]. By cutting down the propellant mass, it will only provide more room to add new instruments to the spacecraft.

1.4 Why resistojets?

According to Ideal Rocket Motor theory [1.32], the specific impulse of a propulsion system is directly proportional to the velocity at which the propellant flow exits the rocket, which in turn is a function of the propellant used and the temperature to which the propellant will be heated. Figure 1.2 shows how the exit velocity (limit case) changes with gas temperature for different propellants. The term limit exhaust velocity refers to the highest possible exhaust velocity achieved when the propellant gas expands adiabatically to vacuum [1.32].

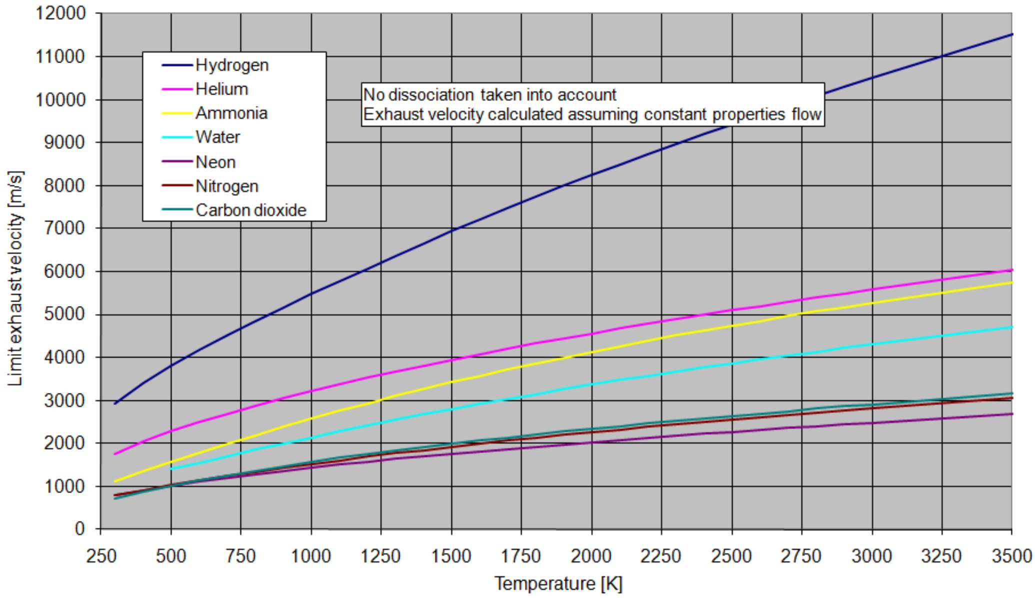

Figure 1.2: Limit exhaust velocity for non-chemical propellants [1.32].

There exist different concepts to heat up a propellant; to name a few are resistojets, solar thermal propulsion (STP) and electric propulsion. Resistojet and STP offer Isp of maximum 800 to 900 s using hydrogen as propellant. Electric thrusters offer Isp of several thousands of seconds but they require large amount of power for operation [1.11]. High voltage requirements in the order of kilo-Volt for electric propulsion systems like colloid thrusters requires bulkier power processing units to be fitted inside a small satellite. STP is too complicated to be used as it requires a large deployable collector to collect and focus the solar rays to heat up the propellant in a small space. Hence resistojets are found to be the most suitable candidate when aiming for high values of specific impulse.

A simple schematic of a resistojet is shown in figure 1.3. It consists of mainly a heater chamber where the input propellant flow is heated to a high temperature with the required heating power provided by an external power supply and finally exhausted through a converging-diverging nozzle to produce certain amount of thrust.

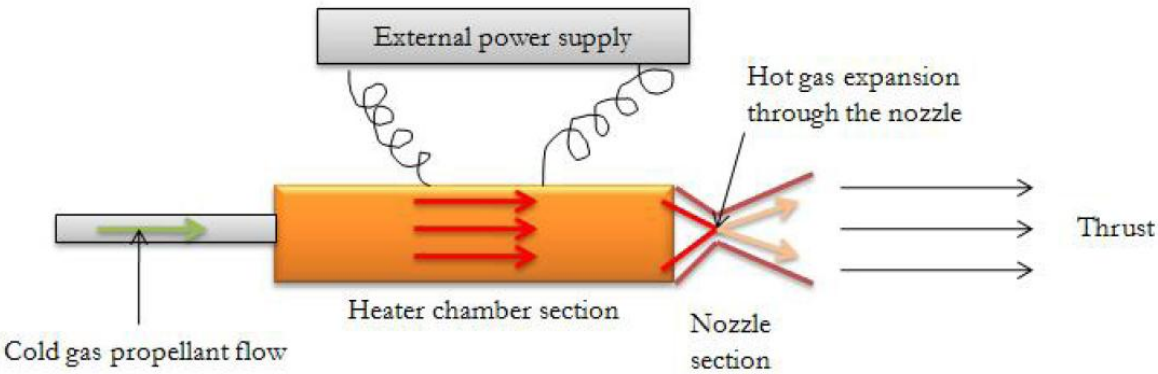

Figure 1.3: Schematic of a resistojet showing the important elements.

1.5 Design concept studies for MEMS heater chamber

In literature study [1.1], several design options were considered for MEMS resistojet heater chamber and they were compared based on design simplicity and maturity of MEMS fabrication techniques. Conventionally, there are two main concepts for heater chamber: (1) using porous medium and (2) by using small circular and non-circular ducts. The former design is used to decompose mono-propellants like hydrogen peroxide and to heat the decomposed products to high temperature, while the later design is used in the experimental electro-thermal thruster concepts like VLM (Vaporizing Liquid Microthruster) and FMMR (Free Molecular Micro Resistojet) where the propellant flow gets heated up by an electric heater placed within the channel walls [1.17]. The mode of heating can be in two different ways: one is by direct heating by applying a voltage across the heater layer deposited along the channel walls over which the propellant flows and the other is indirect heating where the heater chamber is heated indirectly using an external heat source like resistor wires. Table 1.4 contains a list of different heater chamber concepts. The final selected concept for heater chamber will be presented at the end of this section.

Table 1.4: MEMS heater chamber concepts.

#	Description of the concept	Figure
1	Concept 1 is taken from the research work of Jun Hao and Marko Mihailovic [1.18], developed and tested at DIMES. It's a MEMS based micro-evaporator to vaporize water at MEMS scale. From the figure to the right, it is clear that this concept consists of two layers, both made out of silicon wafers. Inlet and divider manifold, deep fin structures and the outlet manifold are etched in to the bottom silicon wafer. On top of upper silicon wafer, two aluminum contact pads are bonded, across which voltage is applied. Due to the electrical resistance of silicon, the whole substrate gets heated up. The heated channel wall then heat up and vaporize the fluid flow. Hence this concept comes under the category of indirect heating using non-porous medium. It is simple in fabrication and DIMES has already got expertise in such MEMS heaters.	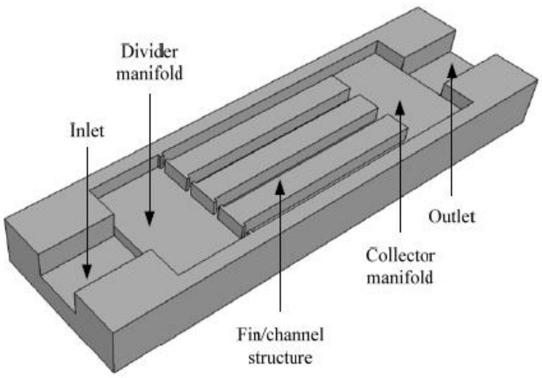 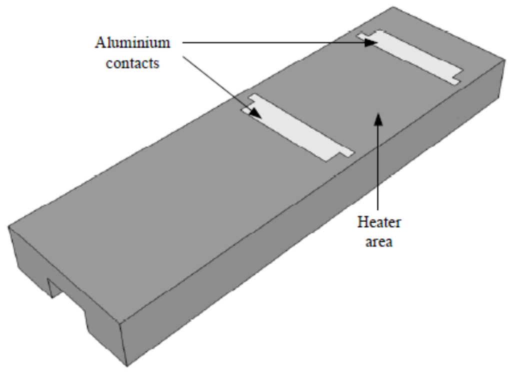

#	Description of the concept	Figure
2	The concept 2 is similar to the concept 1. It consists of two wafers; one made of silicon and the other is Pyrex glass. Instead of fin structures used in concept 1, shrouded staggered micro-pillars are etched onto silicon substrate [1.19]. Aluminum heater layer is deposited on top of silicon substrate. On careful observation, it can be seen that an air gap has been etched onto both sides of silicon channel walls as a measure to reduce heat loss. This design is achievable at DIMES by accordingly modifying the etch mask used for MEMS fabrication. But there is a danger that the silicon micro-pillars may break at high pressures which inturn can create violent pressure variations in the chamber which is not good for stable operation of a thruster.	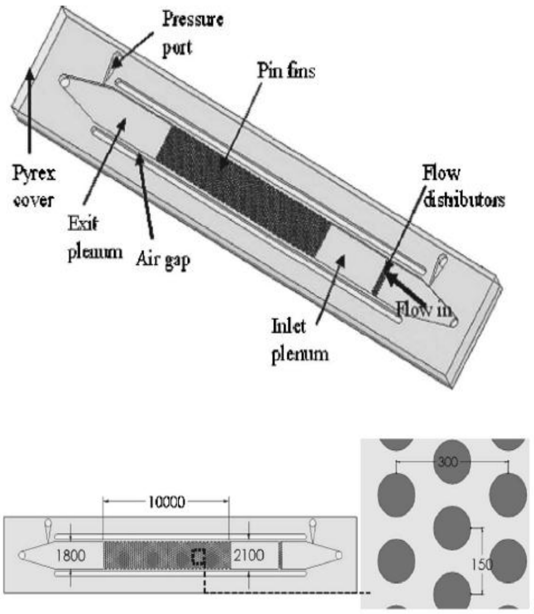
3	Concept 3 has been widely used in high temperature micro-gas sensors developed at DIMES department [1.20, 1.21]. A high temperature resistive heater material like Titanium Nitride (TiN) is deposited on to a flat Silicon nitride (SiN) membrane, suspended across silicon substrate. Maximum operating pressure is 1 bar due to low stress characteristic of SiN membrane. The same concept used in micro-gas sensors where temperature of hot gas flows are sensed by measuring the resistance drop across the heater wire, can be used the other way around for our MEMS electro-thermal thrusters. Such heater concept falls under the category of direct heating.	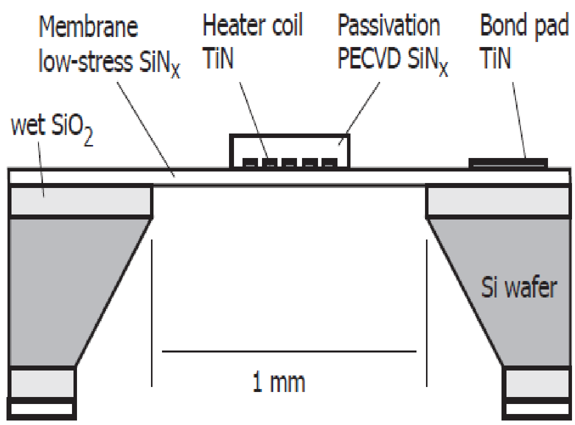

#	Description of the concept	Figure
4	This concept is similar to concept 1 with integrated fin structures parallel to the fluid flow. The difference between the two concepts lies in that fact that in this concept, current is forced to flow through the whole silicon substrate [1.8]. This concept provides localized heating rather than heating the whole silicon substrate as in concept 1. This design falls under the category of direct heating with non-porous medium.	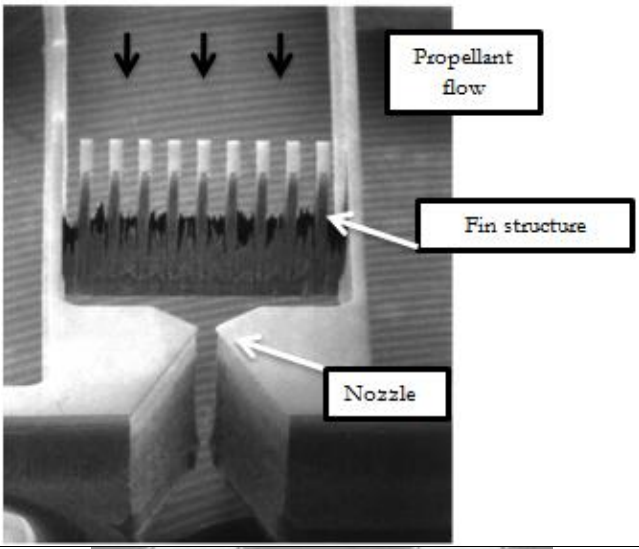
5	Concept 5 falls under the category of direct heating. Such heater concepts are commonly found in MEMS thrusters using solid propellant [1.22]. Here, resistive wires are suspended across the silicon channel wall and they are connected to an external electric power supply through contact pads. Such a design does not heat up the entire substrate. But fabricating such suspended features is costly and time consuming. Also, it has been found that thermal cycling at high temperatures during pulsed mode of thruster operation can lead to its faster rupture.	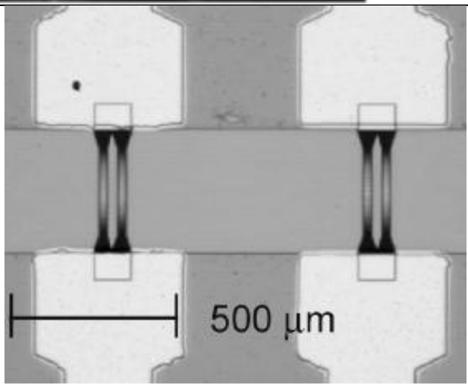
6	This concept falls under the category of direct heating. It makes use of micro-coil heaters made out of carbon or tungsten coated carbon. Each end of the micro-coil is connected to an external voltage supply. Fabrication techniques for such micro-coils are available in DIMES department. Only one research team from angstrom laboratory in Sweden has developed such micro-coils specifically for MEMS thruster applications [1.23, 1.24]. They had reported that such micro-coils showed some degrading features at high temperature operation. Such MEMS-heater concepts are difficult to fabricate and integrate as they have a suspended feature within a flow duct.	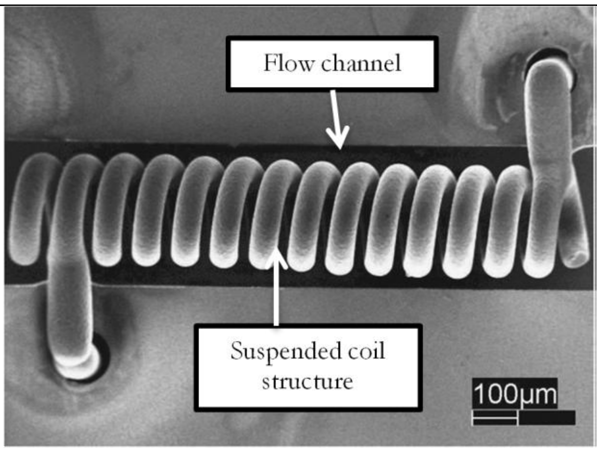

#	Description of the concept	Figure
7	This concept is quite similar to concept 3, except that the heater resistor layer is deposited onto a solid silicon substrate than onto a suspended silicon-nitride layer. Hence such heater chamber designs can withstand a pressure greater than 1 bar [1.25]. This concept falls under the category of direct heating. Internal leads are connected to the deposited heater layer and voltage is applied from an external power supply.	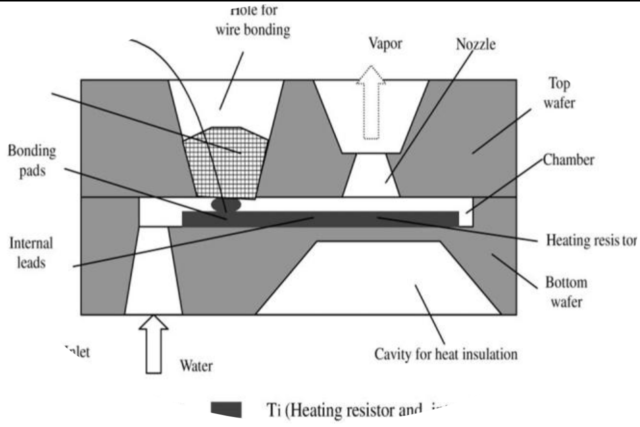
8	This concept uses a porous medium, like porous silicon to increase the surface area of micro-channel. Fabricating porous features in the channel requires special fabrication set-up which leads to more cost. Though the heat transfer efficiency is increased through larger heater surface area, the pressure drop across the porous insert will be much higher.	 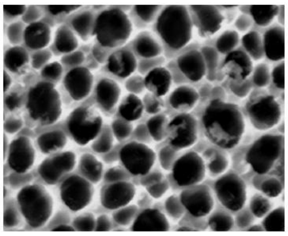

From all the concepts presented in table 1.4, it is clear that the flexibility in design at MEMS scale is not an option. The concept of "plug-and-play" as with Commercial Off The Shelf (COTS) components is not possible at MEMS scale. Concept 5, 6 and 8 are ruled out for the demonstrator model as their fabrication process is extremely complex and costly. The DIMES department has already got an expertise with the design used in concept 1 and 3. For possible chamber pressures values greater than 1 bar, the concept of suspended microheaters (concept #3) can be neglected. Although concept #7 seems to be more attractive with direct heating, according to Marco [1.26], depositing thin layers of resistive heater material on the bottom etched part of flow channel requires a complex fabrication step. Out of the remaining three concepts (concept # 1, 2 & 4) with indirect heating, concept #1 was found to be the most attractive for the purpose of the demonstrator model, as it was simple in design with less complex parts or geometric shapes that could be achieved using well-defined MEMS fabrication techniques.

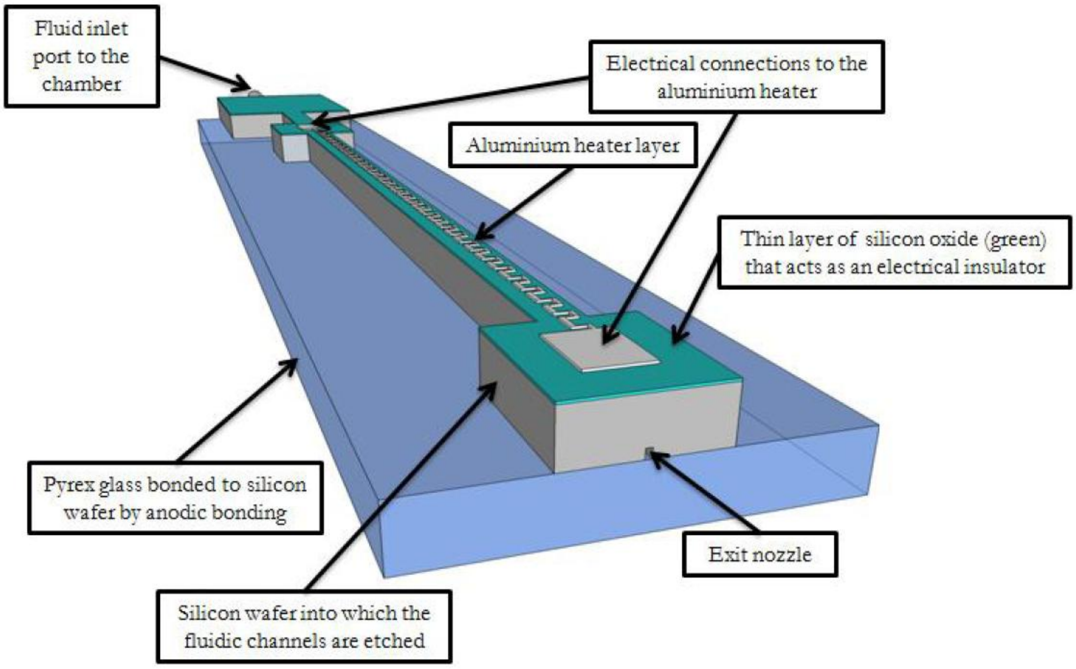

Figure 1.4: Schematic diagram of a MEMS resistojet concept based on the initial proposal.

In figure 1.4, the proposed design for a MEMS resistojet is presented. It consists of a silicon wafer layer bonded to pyrex glass. The fluidic channels for the propellant flow are etched into the silicon wafer before bonding. The propellant (to be selected in section 1.6) shall be fed through the inlet manifold at one end of the chip and expands through the nozzle at the other end of fluidic channel. The chip shall be heated by passing current through the aluminium layer deposited on top of the chip. A thin layer of silicon oxide electrically isolates the silicon bulk from the aluminium layer. The design details and fabrication procedure are provided in chapter 4.

1.6 Propellant selection

Once the heater chamber concept is selected, the next question is upto what temperature can be achieved with this concept, because this in turn determines the maximum temperature to which a propellant flow can be heated. The maximum temperature of the heater chamber is determined by the structural material; from figure 1.4 it is clear that silicon, pyrex and aluminium are the main structural material. Among these three, aluminium has got the lowest melting temperature at 660 ^{o}C (933.47 K).

Many different substances can be used as a propellant in non-chemical thermal propulsion systems. However, for a qualitative analysis we restrict the analysis to five propellants as given in table 1.5. We assume that the propellant flow can be heated upto a maximum chamber temperature T_c of 800 K using the MEMS heater concept just before the flow entry to the nozzle (refer to figure 1.3).

Table 1.5: Candidate propellants for the MEMS resistojet concept along with their properties.

Propellant	Molar mass, M [gm/ mole]	Specific heat ratio, γ** [-]	Γ*	R [J/kg/K]	Enthalpy change, $\Delta H_{298.15\text{-}800K}$ [kJ/mole]+	Propellant phase during storage	H_{vap} [kJ/kg]
Hydrogen	2.016	1.4	0.6847	4124.22	14.702	Gas	-
Helium	4	1.67	0.727	2078.61	10.43	Gas	-
Nitrogen	28.01	1.384	0.682	296.83	15.14	Gas	-
Carbon dioxide	44.01	1.24	0.656	188.92	22.81	Gas	-
Water	18.02	1.29	0.665	461.4	$\Delta H_{298->373K} + \Delta H_{vap} + \Delta H_{373->800K}$	Liquid	2258.4

Γ = vanderkerchove function (it is a function of specific heat ratio; see [1.32] for definition)
+= values taken from NIST [1.35]
***=specific heat ratio is taken as the average of the values of propellant species from 298 to 800 K.*

Once the interested thrust range of ≤ 1 mN and the maximum propellant temperature of 800 K are selected, the next step is to trade these propellants based on following parameters:

1) Specific impulse:
   As mentioned earlier, this performance parameter of a thruster is directly connected to the molar mass of the propellant; lower the molar mass, higher the Isp as it can be seen in the relation below:

$$I_{SP} \alpha \sqrt{\frac{1}{M}}$$

2) Heat input required to heat the propellant :
   A thruster is said to be more efficient when it requires less energy to heat up the propellant flow to a certain temperature.
3) Propellant mass required for the calculated Isp and the QB50 delta-V requirements:
   Based on the QB50 mission requirements discussed in section 1.3, we try to derive the propellant mass based on the I_{SP} and ΔV requirement.
4) Volume of propellant storage tank:
   Volume is an extremely scarce resource on a micro-spacecraft. Considering a Maximum Expected Operating Pressure (MEOP) of 5 bar for cubesat applications [1.33,1.37], we try to determine the volume and the dimension of propellant storage tank assuming a spherical shape.

The chamber pressure just before the nozzle entry is taken as 2 bar and the ambient pressure is taken as the minimum vacuum pressure that can be achieved using the vacuum oven in the cleanroom facility, i.e. 10 millibar [1.34]. A sample calculation for nitrogen gas is given in appendix 1 (see sample calculation #2), using the ideal rocket motor theory from the lecture notes [1.32].

Table 1.6 summarizes the values of parameters for the selected propellant candidates based on which trade-off will be performed.

Table 1.6: Calculated values of propellant parameters.

Propellant		H_2	He	N_2	CO_2	H_2O
Parameter	**Unit**	**Values**				
Characteristic velocity	[m/s]	2652.87	1773.77	174.52	592.62	913.61
Thrust coefficient	[-]	1.59	1.52	1.59	1.67	1.64
Mass flow rate	[mg/s]	0.24	0.37	0.88	1.01	0.67
Specific impulse	[s]	424.74	275.5	115.83	100.93	152.14
Propellant mass*	[grams]	9.58	14.75	30	40	26.62
Thermal power	[W]	1.75	0.96	0.48	0.52	2.29
Electric or input power**	[W]	2.19	1.21	0.6	0.65	2.86
Diameter of spherical storage tank	[m]	0.48	0.33	0.22	0.2	0.04$^+$

* Mission characteristic velocity is taken from [1.2] and is 20 m/s

** Efficiency of the thruster is taken as 80%

$^+$ Density of water is taken as 1000 kg/m^3.

Based on the calculated values for propellant parameters from table 1.6, following can be inferred:

1) Specific impulse: Highest value for specific impulse was calculated for hydrogen gas as it has the lowest molar mass among the propellant candidates.

2) Heat input required to heat the propellant: Power required to heat the propellant to a certain temperature is calculated by multiplying the mass flow rate with the required change in enthalpy. From table 1.5, we see that carbon dioxide requires the highest change in enthalpy among the gaseous propellants. But a propellant stored in liquid phase will require much larger change in enthalpy since power is required for both heating up the fluid to its boiling temperature and also for the phase change from liquid to vapor. This is made clear from the numbers presented in table 1.6. The least amount of power is required for heating up the nitrogen gas. For 1-U cubesat applications where the on-board satellite power is roughly 1 W (assuming a specific power of 1 W/kg), lighter propellants like hydrogen and helium as well as liquid propellants find limited application because they require larger amount of heating power than what the satellite can provide.

3) Propellant mass required for the calculated Isp and the QB50 delta-V requirements: For a given ΔV requirement and satellite mass, propellant mass will be the lowest for the one having the highest I_{SP}. This point is made clear from the numbers in table 1.6.

4) Volume of propellant storage tank:
Considering the size of tank for propellant storage at room temperature, we see that the lighter propellants like hydrogen and helium require tank dimensions larger than the cubesat dimensions (see table 1.1 and 1.2).

Different propellant candidates were analyzed based on mission requirements and satellite constraints. Nitrogen gas is found to be a good propellant to demonstrate the feasibility of MEMS resistojet concept. Also, the Space engineering department has got experience in handling with nitrogen gas as it has been used extensively as the test gas during test campaigns of previous resistojet concepts.

1.7 Conclusion and requirement generation

From this chapter, we can arrive at the following conclusions:

1) The selected MEMS micro-thruster resistojet concept shall be able to produce a thrust of less than or equal to 1 mN inorder to meet the thrust requirements for cubesats (from section 1.3).
2) The thruster shall operate using cold gas nitrogen stored at a maximum operating pressure of 5 bars (from section 1.6).
3) The MEMS heater concept shall be able to heat the nitrogen gas to a maximum chamber temperature of 600 K so as to aim for a 30 % reduction in propellant load based on the delta-V requirements of QB50 mission (from section 1.3).
4) The maximum input electric power to the MEMS thruster is limited to 1 W based on the typical power budget for a 1U cubesat.

Table 1.7 below summarizes the requirements for the development of the first prototype of MEMS micro-resistojet:

Table 1.7: Requirements table.

Thrust	≤1 mN
Electric input power	≤ 1 W
Propellant	Nitrogen
MEOP	5 bar
Hot gas temperature, T_c	≤ 600 K

1.8 Reference

[1.1] Tittu V Mathew; Study on MEMS Micro-resistojet; Literature study.
[1.2] E. Gill, P. Sundaramoorthy, J. Bouwmeester, B. Sanders; Formation flying to enhance The QB50 space network.
[1.3] Barry Zandbergen; Micropropulsion; Propulsion for microspacecraft (lecture slides)
[1.4] Koji Takahashi; Micro thruster for miniaturised space systems- need and perspective; The fourth international workshop on micro and nano-technology for power generation And energy conversion applications; PowerMEMS 2004.
[1.5] Tor-Arne Gronland, Pelle rangston, Martin Nese, Martin Lang; Miniaturisation of Components ans systems for space using MEMS-technology.
[1.6] Juergen Mueller, Colleen Marrese, John Ziemer, Amanda Green, Eui-Hyeok Yang, Mohammad Mojarradi, Travis Johnson, David Bame; JPL Micro-thruster propulsion Activities; AIAA-2002-5714.
[1.7] Siegfried W. Janson, Henry Helvajian, William W. Hansen, Lt. John Lodmell; Microthrusters for nano-satellites; The second international conference on integrated Micro nanotechnology for space applications (MNT99), Pasadena, CA, April 11-15,1999.
[1.8] Herbert R. Shea; Reliability of MEMS (Microsystems) for space applications.
[1.9] L. Muller, M. H. Hecht, L.M. Miller, H.K. Rockstad, J.C. Lyke; Packaging and qualification of MEMS based space systems.
[1.10] Lilac Muller; Microelectromechanical systems (MEMS) technology integration into Microspacecraft; Jet propulsion laboratory, Pasadena, California.
[1.11] M.N. Sweeting, T. Lawrence, J. Leduc; Low cost orbit manoeuvres for mini-satellites Using novel resistojet thrusters; Proc Instrn Mech Engrs Vol 213 Part G.
[1.12] Donald Pratt; A monopropellant milli-newton thruster system for attitude control of Nano-satellites; 16th annual USU conference on small satellites.

[1.13] E. Razzano and M. Pastena; A novel AOCS Cold-gas micro-propulsion system design And applications to micro and nano-satellites; Small satellite missions for earth Observation.
[1.14] Alina Alexeenko, Dmitry A. Fedosov, Sergey F. Gimelshein, Deborah A. Levin; Transient heat transfer and gas flow in a MEMS based thruster; Journal of microelectro Mechanical systems, Vol 15, No 1, February 2006.
[1.15] Robert.L. Bayt; Analysis, fabrication and testing of a MEMS based micropropulsion System; MIT PhD Thesis; June 1999.
[1.16] James R. Wertz and Wiley J. Larson; Space mission analysis and design; Microcosm press; Third edition.
[1.17] Dr. Michael M. Micci & Dr. Andrew D. Ketsdever: Micro-propulsion for small spacecrafts.; AIAA Book series.
[1.18] Jun Hao; Silicon MEMS micro-evaporator; MSc thesis; TUDelft.
[1.19] Yoav Peles, Ali Kosar, Chandan Mishra, Chih-Jung Kuo, Brandon Schneider; Forced Convective heat transfer across a pin fin micro heat sink; International journal of heat And mass transfer 48 (2005) 3615-3627.
[1.20] J.F. Creemer, P.M. Saro, M. Laros, H. Schellevis, T. Nathoeni, L. Sttenweg, V. Svetchniko H.W. Zandbergen; Titanium nitride for MEMS hotplates.
[1.21] J.F. Creemer, D. Briand, H.W. Zandbergen, W. Van der Vlist, C.R> de Boer, N.F. de Rooij, P.M. Sarro; Microhotplates with TiN heaters; Sensors and actuators A 148 (2008) 416-421.
[1.22] B. Larangot, C. Rossi, T. Camps, A. Berthold, P.Q. Pham, D. Briand, N.F. de Rooij, M. Puig-Vidal, P. Miribel, E. Montane, E. Lopez, J. Samitier; Solid propellant micro-Rockets- towards a new type of power MEMS.
[1.23] K.L. Williams, A.B. Eriksson, R. Thorslund, J. Kohler, M. Boman and L Stenmark; The electrothermal feasibility of carbon micro-coil heaters for cold/hot gas micro-thrusters. Journal of Micromechanics and Micro-engineering 16 1154.
[1.24] K.L. Williams, K. Jonsson, J. Kohler, M. Boman; Electrothermal characterization of tungsten-coated carbon microcoils for micropropulsion systems. Carbon 45 (2007) 484-492.
[1.25] X.Y. Ye, F. Tang, H.Q. Ding, Z.Y. Zhou; Study of a vaporizing water micro-thruster. Sensors and actuators A 89 (2001) 159-165.
[1.26] Technical discussion with Marko Mihailovic.
[1.27] www.vki.ac.be/QB50/project.php
[1.28] www.lr.tudelft.nl (Search for FAST Overview)
[1.29] www.delfispace.nl (Information on Delft-C3 and Delfi-n3Xt)
[1.30] Rodrigo Ferreira; Development and testing of a water micro-resistojet; MSc thesis; TUDelft.
[1.31] H.C.M. Leenders; Development of a solar thermal propulsion system; MSc thesis; TUDelft.
[1.32] Barry Zandbergen; Thermal rocket propulsion (Lecture notes).
[1.33] R.A. Ferreira; Development and testing of a water microresistojet; MSc thesis, TUDelft.
[1.34] F. Valente; Development and verification of test setup for microthruster testing.
[1.35] http://webbook.nist.gov/chemistry/
[1.36] J.L.P.A. Moerel, H.M. Sanders, M.C. Louwerse, H.V. Jansen, J. Boscher, B.T.C. Zandbergen, F La Torre, S. Kenjerens and C.R. Kleijn; Development of micropropulsion system technologies for minisatellites in the netherlands; 5th International spacecraft propulsion conference, Heraklion, Crete, Greece, 5-8 May, 2008.
[1.37] A.Migliaccio, B.T.C. Zandbergen, F.T. Nardini, M.C. Louwerse; Vacuum testing of a micropropulsion system based on solid propellant cool gas generators; 61st International Astronautical Congress, Prague, CZ (IAC-10.C4.3.12).

Chapter 2

MICRO-NOZZLE DESIGN ANALYSIS

As it was indicated in the previous chapter, the nozzle is instrumental in expanding and accelerating the high-pressure low-velocity gas inside the chamber to a low pressure high velocity gas at the exit, thereby producing useful thrust. The most commonly found nozzle shape is the converging-diverging de-laval nozzle. There exists a great depth of knowledge in the design of a macroscopic nozzle. But only a handful of research studies have been carried out in the field of micro-nozzle design. One of the recent studies on the performance characterization of micro-nozzles carried out at the space engineering department of TU Delft was the experimental work performed by Migliaccio et al [2.7] on cold gas thrusters using axi-symmetric micro-nozzles with circular cross-section made out of Pyrex glass. Figure 2.1(a) shows a Scanning Electron Microscope (SEM) image of the nozzle used in his work, showing the circular throat and nozzle exit region.

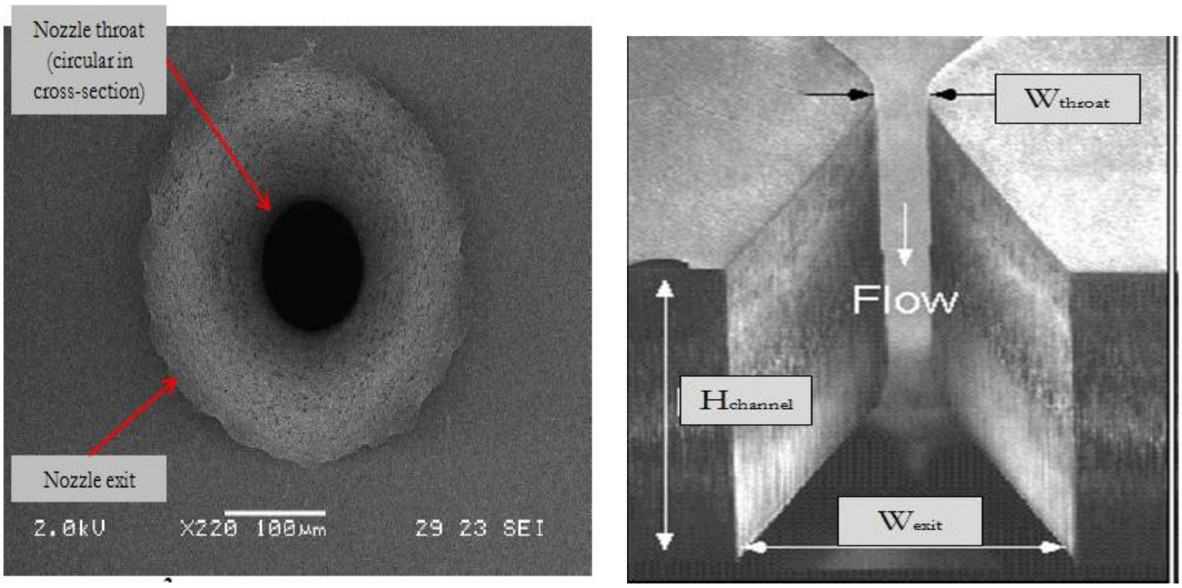

(a) (b)

Figure 2.1: SEM images of (a) a micro-nozzle having circular cross-section [2.7] and (b) a 2-D micro-nozzle etched in a silicon wafer [2.2].

But for our selected approach of using MEMS technology to fabricate micro-nozzles out of silicon, the nozzle shape is limited to a two-dimensional feature due to fabrication limitations. (see figure 2.1 (b)). The nozzle is no longer circular, but rectangular in cross-section with a constant channel height $H_{channel}$ throughout the nozzle length and the channel width W defining the nozzle profile. In figure 2.1(b), W_{throat} stands for the width of the channel at the throat and W_{exit} represents the width of the channel at nozzle exit.

Now that we know the basic nozzle shape, the next step is to dimension the nozzle based on the requirements. From the requirements table 1.7, the thrust range we are aiming for is 1 mN and lower. The maximum propellant storage pressure at cold gas mode is limited to 5 bars. As a first design approximation, we assume the chamber pressure, p_C (stagnation pressure of the fluid just before the nozzle entry) to be the same as the propellant storage pressure by neglecting any pressure drop in the feeding system and in the heater chamber. This assumption shall be verified during the comparison of experimental data with the theory in chapter 7. The maximum chamber temperature T_C (stagnation temperature of the fluid just before the nozzle entry) is limited to 600 K.

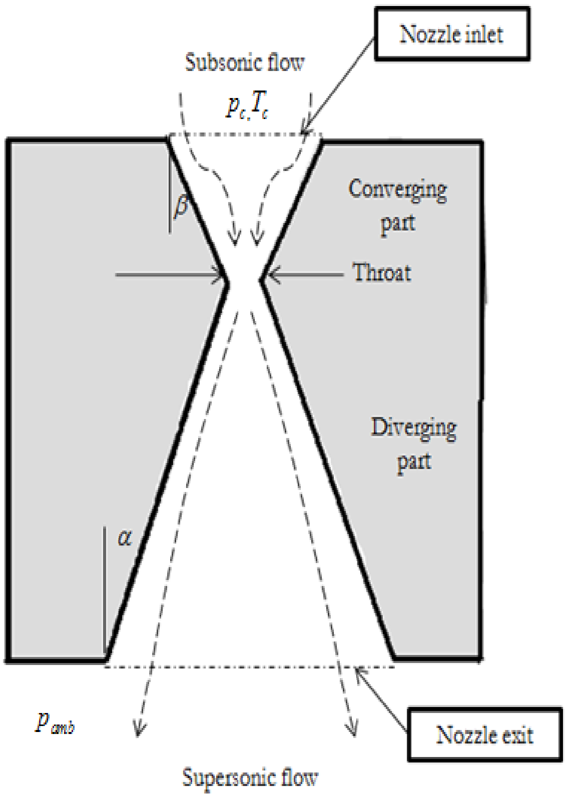

Figure 2.2: Schematic diagram of a nozzle →

Figure 2.2 shows the schematic diagram of a converging-diverging nozzle where α represents the half-divergence angle, β represents the half-convergence angle, p_c and T_c the stagnation or chamber conditions and p_{amb} the ambient pressure. Area ratio, ε of the nozzle is defined as the ratio of the nozzle exit area to the nozzle throat area.

In section 2.1 we will show using ideal rocket theory that for a given nozzle area ratio, ideal thrust and Reynolds number at the throat mainly depends on chamber pressure and throat geometry. Factors affecting the ideal thrust performance are discussed in section 2.2. In section 2.3 a preliminary nozzle performance study in terms of deliverable thrust and specific impulse as a function of chamber pressure at cold gas mode operation is performed. During the literature study, we had pointed out the effect of low Reynolds number on thruster performance and this will be discussed in section 2.4. In section 2.5, influence of any changes in the nozzle geometry on nozzle efficiencies will be addressed. The thruster performance at higher chamber temperature will be discussed in section 2.6 followed by the conclusion in section 2.7. Section 2.8 contains the list of references used in this chapter.

2.1 Thrust and Reynolds number

An important performance parameter for a nozzle is the amount of thrust it can produce. The thrust produced F can be expressed as [2.1]:

$$F = \dot{m}U_e + (p_e - p_a)A_e \tag{2.1}$$

where $\dot{m}$ being the propellant mass flow rate, U_e the velocity of gas at nozzle exit, p_e the stagnation pressure of the flow at nozzle exit, p_a the ambient pressure and A_e the nozzle exit area. From equation 2.1, we can see that the thrust produced by a nozzle consists of two parts: the momentum component $\dot{m}$ U_e and the other being the pressure component. If we assume that the nozzle is operating at optimum expansion (meaning p_e=p_a), then the thrust becomes only a function of mass flow rate of propellant through the nozzle and the jet exhaust velocity. The mass flow rate through the nozzle at which the flow in the throat becomes sonic (Mach number, M=1) is referred to as the "chocked" mass flow rate and is given by [2.1]:

$$\dot{m} = \frac{\Gamma p_c A_t}{\sqrt{RT_c}} \tag{2.2}$$

where R being the characteristic gas constant (for nitrogen, R=296.8 J/kg/K) and Γ the Vandenkerchove function defined as [2.1]:

$$\Gamma = \sqrt{\gamma}\left(\frac{2}{\gamma+1}\right)^{\frac{\gamma+1}{2(\gamma-1)}} \tag{2.3}$$

where γ being the specific heat ratio of the propellant (for nitrogen, γ=1.4). The exhaust velocity U_e is given by [2.1]:

$$U_e = \sqrt{\frac{2\gamma}{\gamma-1} RT_c \left(1-\left(\frac{p_e}{p_c}\right)^{\frac{\gamma-1}{\gamma}}\right)} \tag{2.4}$$

The pressure ratio, p_e/p_c is calculated iteratively for a given nozzle area ratio, ε by using the following relation from [2.1]:

$$\varepsilon = \frac{A_e}{A_t} = \frac{\Gamma}{\sqrt{\frac{2\gamma}{\gamma-1}\left(\frac{p_e}{p_c}\right)^{\frac{2}{\gamma}}\left(1-\left(\frac{p_e}{p_c}\right)^{\frac{\gamma-1}{\gamma}}\right)}} \tag{2.5}$$

Substituting relations (2.2) and (2.3) in (2.1), we see that for a nozzle with a fixed area ratio and given propellant, the thrust produced becomes a function of chamber pressure p_c and throat area A_t:

$$F = f(p_c, A_t)$$

Reynolds number of fluid flow is a dimensionless number which is a measure of the ratio of inertial forces to viscous forces. In the case of a nozzle, the flow Reynolds number at the throat can be defined as:

$$\mathrm{Re}_t = \frac{\rho_t U_t D_{h_t}}{\mu_t} \tag{2.6}$$

where ρ being the fluid density, U the fluid velocity, μ the dynamic viscosity and D_h the hydraulic diameter, all defined at the nozzle throat. By substituting the relation for critical mass flow rate (relation 2.2) in relation 2.6, we can relate the Reynolds number at the throat to the chamber pressure, throat diameter and chamber temperature:

$$\mathrm{Re}_t = f\left(p_c D_t \big/ T_c^{\,x} \right)$$

(Note: The value of 'x' is between 1.2 and 1.5 depending on the gas)

From relation 2.6, we see that the Reynolds number at the throat is directly proportional to the throat diameter; that should tell us that at micro-scale geometries for a MEMS thruster, the Reynolds number should be proportionately low. Low Reynolds number implies that the fluid becomes more viscous as per the definition. The viscous effects on the thruster performance will be addressed in section 2.4.

2.2 Factors that affect ideal thruster performance

In section 2.1, we presented the ideal rocket thrust equation. In reality, there are various factors that make the thrust to deviate from ideal case. Hence they should be taken into account for better prediction of nozzle performance. Some factors have been taken from [2.1], but some new factors were identified during the literature study. All of them are presented in table 2.1. Effect of low Reynolds number on the thruster performance will be discussed separately in section 2.4.

Table 2.1: Factors affecting ideal thrust performance.

Sl. No.	Factor	Effect on ideal thrust performance
1	Nozzle half-expansion angle, α	For relation 2.1, we assumed that the entire flow at the nozzle exit flows parallel to the nozzle axis having no radial component. But from figure 2.2, we see that as the nozzle half-divergence angle α is increased, this assumption does no longer hold since the radial component of the exit momentum increases with this angle. Hence, the effective thrust by taking into account the flow divergence loss is given by: $$F = \left(\frac{1+\cos\alpha}{2}\right)\dot{m}U_e + \left(p_e - p_a\right)A_e \qquad (2.7)$$
2	Exit pressure to ambient pressure ratio, p_e/p_a	For relation 2.1, we assumed that there exists no discontinuities like shock formation or flow separation within the nozzle. To prevent, such flow discontinuities from occurring, the following criterion must be observed: $$\frac{p_e}{p_a} > 0.35 \text{ to } 0.45 \quad \text{or}$$ $$\frac{p_e}{p_a} = \left(1.88M_e - 1\right)^{-0.64} \qquad (2.8)$$ Here p_e and M_e stands for the stagnation pressure and Mach number of the flow at the nozzle exit respectively and p_a the ambient pressure.
3	Nozzle throat edge	During the literature study, it was learned that the throat radius of curvature r_t can have an influence on the effective mass flow through the nozzle. Typical values are: $$\frac{r_t}{D_{h_t}} = 0.5 - 1$$ where D_{ht} stands for the hydraulic diameter at the nozzle throat. For the preliminary study in this chapter and for the nozzles fabricated in chapter 4, the throat edge is kept sharp.
4	Surface roughness of nozzle wall	The size of surface irregularities gets magnified at micro-scale. From the literature study it was found that surface roughness can produce shocks in the expanding nozzle flow giving rise to loss in flow momentum and thereby reduce the thrust. But the effect of surface roughness starts to play a role only when its height is in the order of flow boundary layer thickness along the wall. For the preliminary study in this chapter, we assume the nozzle channel walls to be perfectly smooth.
#	Factor	Effect on ideal thrust performance

5	Flow Knudsen number, Kn	Knudsen number is a dimensionless number that tells whether the gas flow is in continuum or rarified and it is defined as: $$Kn = \frac{\lambda}{D_h} = \frac{\mu\sqrt{\frac{\pi}{2p\rho}}}{D_h} \quad (2.9)$$ where D_h being the hydraulic diameter of the flow channel, λ the mean free path of the gas molecules defined as the average distance covered by moving gas molecules in between their collision and p and ρ representing the local gas pressure and density respectively. When the flow Knudsen number is in between 0.01 and 0.1 (slip flow), the fluid flow is no longer stationary at the channel walls (velocity slip) and the fluid temperature is no longer equal to that of the wall temperature (temperature jump). The velocity slip factor increases with decrease in flow Reynolds number. Lin [2.4] tried to understand the difference between slip and no-slip conditions at the nozzle wall on the thruster performance using numerical approach. He found that a no-slip condition predicts a higher Mach number near the wall region compared to a slip flow condition. On the other hands, presence of temperature jump at the channel wall translates to an additional thermal resistance to any heat flow from fluid to the walls. Hence, any loss in kinetic energy of flow due to heat transfer to the nozzle walls is minimal in case of slip flows.

2.3 Nozzle performance study for fixed geometry

Once the various factors affecting the ideal performance of a thruster are presented, in this section we will perform a preliminary nozzle performance study in terms of deliverable thrust and I_{SP} as a function of chamber pressure at cold gas mode. The effect of flow Reynolds number on the nozzle performance is not taken into account in this section and will be dealt separately in section 2.4. For this study, we will be using the ideal rocket motor theory as presented in amongst others [2.1, 2.3] as a starting point.

Ideal rocket motor theory is based on the following assumptions:

1) The working substance is homogenous.
2) All the species are gaseous.
3) The gas products obey the perfect gas law.
4) Adiabatic flow expansion; meaning no heat transfer across the nozzle walls.
5) Friction and all boundary layer effects are neglected.
6) No shock waves or discontinuities occur in the nozzle flow.
7) Nozzle flow is steady and constant. Transient effects can be neglected.
8) Gas velocity, pressure, temperature and density are all uniform across any section normal to the nozzle axis.
9) Frozen flow is achieved in the nozzle; meaning that the gas composition remains constant throughout the nozzle.

Table 2.2 summarizes the different parameters that are taken into account for this study. The only variable is the chamber pressure p_C varied from 5 to 1 bar. Gas compressibility factor effect need not be taken into account as the maximum chamber pressure for analysis is less than 6 bars [2.1].

Table 2.2: List of parameters that are taken fixed for the thruster performance study.

Sl. No.	Parameter	Symbol	Value	Unit	Comment and reasoning
1	**Fixed nozzle geometry parameters** (refer to figure 2.1, 2.2 and 2.3)				
	Throat width	W_t	10	μm	Arbitrary
	Channel height	H_c	150	μm	Aspect ratio at the throat, $\alpha_t^* = H_c/W_t = 150/10 = 15$; High aspect ratios are required to minimize the effect of boundary layers from end walls of a micro-nozzle as shown in figure 2.4 [2.2]. Therefore, 2-D simplification is applicable only when aspect ratio is greater than 5 [2.8].
	Nozzle expansion ratio	ε	25:1	[-]	Arbitrary; Larger the expansion ratio, more the gas flow gets expanded.
	Nozzle half-expansion angle	α	20	deg	The analysis on optimum expansion angle for a given expansion ratio is presented in appendix 2 under the section "Determination of optimum expansion angle for a given expansion ratio of a nozzle".
	Nozzle contraction angle	β	15	deg	Arbitrary
	Nozzle contraction ratio	$\frac{A_{in}}{A_t}$	5	[-]	To reduce the losses of flow velocity of gases within the chamber, the chamber geometry should be at-least three times larger than the throat width [2.1]
2	**Stagnation conditions at the chamber** (refer to figure 2.2)				
	Chamber pressure	p_C (max)	5	bar	Assuming negligible pressure drop in the feeding system, we take the maximum chamber pressure to be equal to that of MEOP
		p_C (min)	1	bar	Arbitrary; Lower limit for the chamber pressure is better determined from the flow separation criterion
	Chamber temperature	T_C	298	K	We assume a cold gas mode operation of thruster for this present study.
3	**Propellant properties**				
	Propellant	Nitrogen gas			Propellant selection was performed in section 1.6
	Propellant properties	R, γ, R, Γ			Propellant properties are provided in table 1.5
4	**Ambient properties**				
	Ambient pressure	p_a	0.0767	mbar	Ambient pressure in space at Low Earth Orbit (LEO) [2.3]

*-Aspect ratio of a rectangular fluidic channel α, is defined as the ratio of channel height (or depth) to channel width.

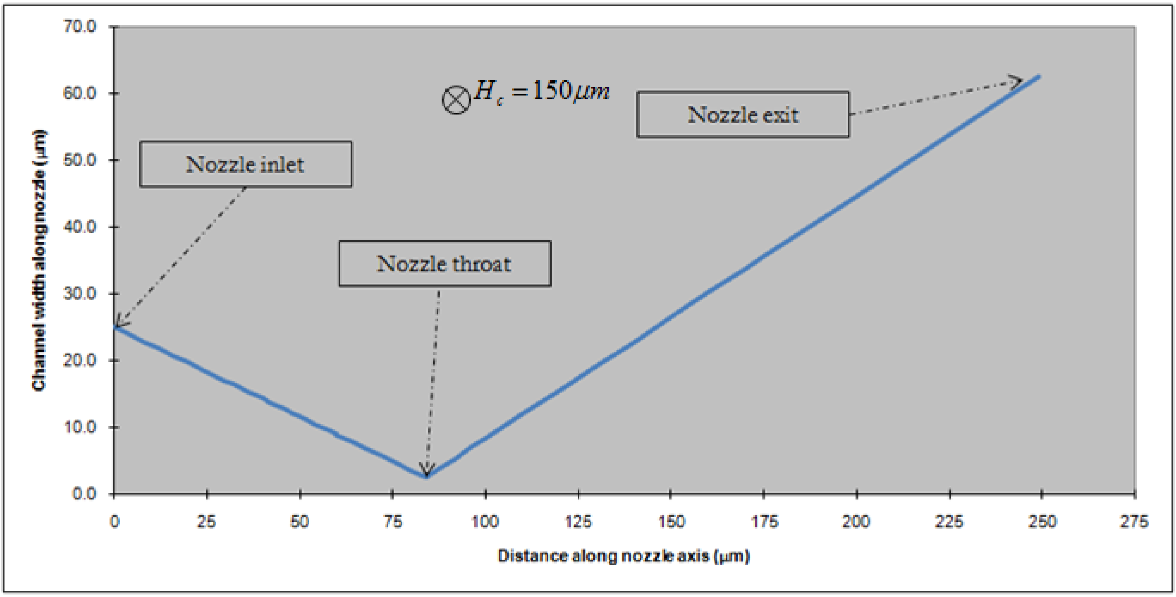

Figure 2.3: 2-D nozzle wall contour based on the selected geometry parameters from table 2.2.

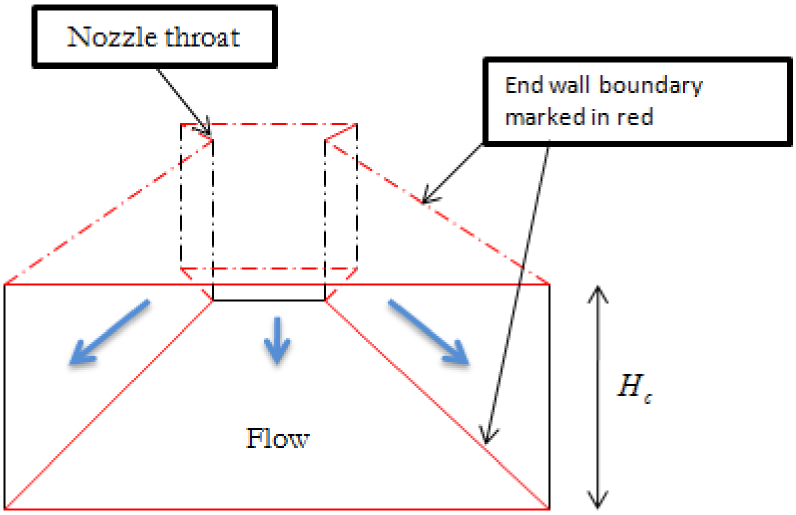

Figure 2.4: Representation of the end walls in a 2-D nozzle.

All the calculations done for the micro-nozzle design are included in the excel spreadsheet developed by the author. The spreadsheet can be accessed from the following folder: k:/lr/spe/sse/sse-shared/3.PersonalDirectories/TittuMathew/Excelsheets/Micro-nozzle design analysis.

Table 2.3: Nozzle performance at different chamber pressures.

Sl. No.	**Chamber pressure,** p_C [bar]	**Mass flow rate,** $\dot{m}\left[{}^{mg}/_{s}\right]$ (using relation 2.2)	**Thrust,** F [mN] (using relation (2.5))	**Specific impulse,** I_{SP}* [s]
1	5	1.73	1.24	~ 73
2	4	1.38	0.99	
3	3	1.04	0.75	
4	2	0.69	0.49	
5	1	0.35	0.25	

From table 2.3, it follows that the ideal thrust values are ≤ 1 mN. The specific impulse remains about constant (73 s) in cold gas mode. This is because it is a function of effective exhaust velocity which is constant for a fixed nozzle expansion ratio as it can be seen in relation 2.4. In table 2.4, the calculated flow Reynolds number at the throat and the Knudsen number at both the throat and exit are presented.

Table 2.4: Fluid flow properties at both the throat and exit conditions.

Sl. No.	**Chamber pressure,** p_C [bar]	**Flow Reynolds number at throat,** Re_t [-]	**Knudsen number at throat,** Kn_t [-]	**Knudsen number at nozzle exit,** Kn_e [-]
1	5	1402	0.001	0.008
2	4	1122	0.001	0.010
3	3	841	0.002	0.014
4	2	561	0.003	0.020
5	1	280	0.005	0.041

From table 2.4, we can observe the following points:

1) We find that the throat Reynolds number decreases linearly with chamber pressure. Such a correlation had already been predicted in section 2.1 for a given nozzle geometry and chamber temperature. But is the flow laminar or turbulent? For that, we need to know the critical Reynolds number for a rectangular cross-sectional channel with an aspect ratio of 15. In table 3.2 in chapter 3, it will be shown that the critical Reynolds number for such geometry is 2500. Hence, from table 2.4, we can conclude that for all values of chamber pressure, the flow at the throat is laminar.
2) Flow at the throat is in continuum regime with Kn < 0.01 for all chamber pressures. But by observing the flow Knudsen number at the nozzle exit, we see that the flow switches from continuum to slip flow (Kn > 0.01) for chamber pressures ≤ 4 bars. Such a trend of slip flow at the nozzle "lip" vicinity has also been observed in the work of Wang.*et.al* [2.8].

In near vacuum conditions of space, the effect of ambient pressure on the fluid flow through the nozzle can be neglected. But this will not be the case when a MEMS thruster prototype is tested in the vacuum chamber facility available at the Space engineering department of TU Delft , where the minimum pressure is limited to 10 mbar [2.5]. To prevent any flow separation within the nozzle, we have seen from table 2.1 that the minimum criterion for p_e/p_a is a function of exit Mach number. The exit Mach number is in turn a function of the nozzle area ratio, ε as shown below:

$$\varepsilon = \frac{A_e}{A_t} = \left(\frac{\gamma+1}{2}\right)^{\frac{-(\gamma+1)}{2(\gamma-1)}} \left(1+\frac{\gamma-1}{2}M_e^{\,2}\right)^{\frac{\gamma+1}{2(\gamma-1)}} / M_e \tag{2.10}$$

For the selected area ratio of 25:1, the exit Mach number is calculated to be 5. Substituting this value of exit Mach number in relation 2.8), we get p_e/p_a=0.256. For a test ambient condition of 10 mbar, then the minimum nozzle exit pressure to prevent any flow separation should not be less than 2.56 mbar. For a fixed nozzle expansion ratio of 25:1, we get the pressure ratio across the nozzle, p_e/p_c as 0.00189 using relation 2.5. From these two values, we can calculate the minimum chamber pressure in order to avoid any flow separation within the nozzle and this comes out to be 1.35 bars. This is slightly larger than the minimum chamber pressure of 1 bar which was taken for the preliminary nozzle performance study.

Also from table 2.4, we see that the flow Reynolds number at the throat drops by a factor of 5 with decrease in chamber pressure. For Reynolds number greater than 10000, the viscous losses are not considered of great effect on the thruster performance [2.1]. But since the calculated values for Reynolds number at the throat are in the range of 300 to 1400, the effect of viscous losses on the thruster performance must be investigated further and this is done in the following section.

2.4 Effect of low Reynolds number on thruster performance

In table 2.4, we have seen that the throat Reynolds number for all the chamber pressure cases were in the laminar regime. Such low values of Reynolds number means that the fluid flow will be highly viscous in nature as per the definition. As a result of increasing viscous effects at micro-scales, boundary layer starts building up along the nozzle walls as shown in figure 2.5 (boundary layer is highlighted in orange). Comparing this figure with that of 2.2, the effect of boundary layer on the nozzle fluid flow is immediately striking. Both the throat area and the nozzle expansion ratio get reduced by the blockage from the boundary layer formation. This in turn leads to a reduced mass flow through the nozzle and lower exhaust velocity and lower flow expansion due to reduced area ratio.

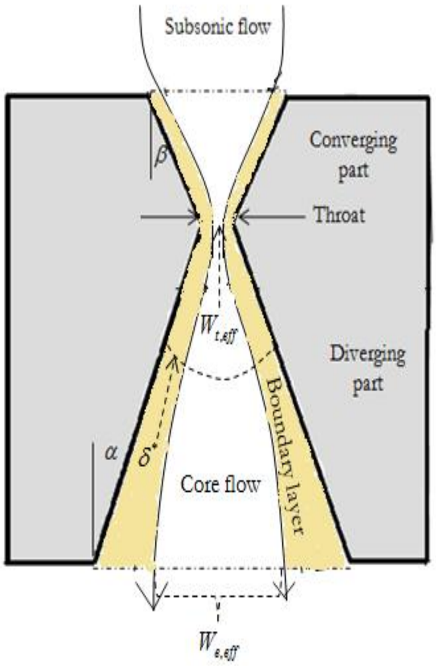

Figure 2.5: Boundary layer formation in micro-nozzles along the nozzle wall →

As a result, the effective thrust from the nozzle and the specific impulse of the system decreases with throat Reynolds number. By plotting the two thruster efficiency parameters, namely the thrust efficiency and the Isp efficiency against the throat Reynolds number, it can tell us how effectively the stored energy in a highly pressurized gas gets converted to kinetic energy of flow exiting the micro-nozzle. All the efficiency terms and nozzle quality factor are presented in table 2.5. The terms with 'eff' as suffix refers to the case considering viscous losses whereas the ones with 'ideal' as suffix refers to the case without considering viscous losses.

Table 2.5: Losses in thrust performance parameter due to boundary layer formation.

Sl. No.	Efficiency / Quality factors of a nozzle	Comments
1	Discharge coefficient, C_D $$C_D = \frac{\dot{m}_{viscous\_losses}}{\dot{m}_{ideal}} \quad (2.11)$$ or $$C_D = \frac{A_{t,eff}}{A_{t,ideal}} \quad (2.12)$$	Figure 2.6 shows how the discharge coefficient C_D varies with inverse square root of the throat Reynolds number.

Sl. No.	Efficiency / Quality factors of a nozzle	Comments
		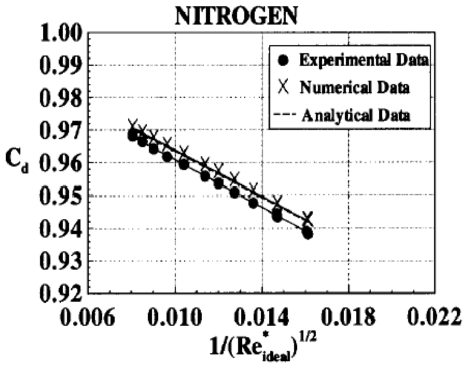 Figure 2.6: Discharge coefficient vs. inverse square root of throat Reynolds number for nitrogen gas [2.6]. Assuming that the trend continues to be linear even in lower values of abscissa, we can derive the following relation using a simple linear fit to the experimental data. $$C_D = -3.625\left(\frac{1}{\sqrt{\mathrm{Re}_t}}\right) + 0.997 \quad (2.13)$$ By substituting the discharge coefficient from equation 2.13 into equations 2.11 and 2.12, we can determine the effective mass flow and effective throat area respectively.
2	Thrust efficiency, η_F $$\eta_F = \frac{F_{viscous\_losses}}{F_{ideal}} \quad (2.14)$$	Effective thrust after viscous losses is given as: $$F_{viscous\_losses} = \left(\frac{1+\cos\alpha}{2}\right)\dot{m}_{eff}\, U_{eff,e} + (p_{eff,e} - p_a)A_{eff,e} \quad (2.15)$$ where $\dot{m}_{eff}$ is calculated using relation 2.11. $A_{eff,e}$, $p_{eff,e}$ and $U_{eff,e}$ are calculated after taking into account the boundary layer thickness at the nozzle exit. F_{ideal} is calculated using relation 2.7.
3	Specific impulse efficiency, $\eta_{I_{SP}}$ $$\eta_{I_{SP}} = \frac{I_{SP_{viscous\_losses}}}{I_{SP_{ideal}}} \quad (2.16)$$	$$I_{SP_{viscous\_losses}} = \frac{U_{eff,e}}{g} \quad (2.17)$$
4	Nozzle quality, ξ_F $$\xi_F = \frac{C_{F_{vicous\_losses}}}{C_{F_{ideal}}}^{*} \quad (2.18)$$	$$C_{F_{viscous}} = \frac{F}{p_c A_t} \quad (2.19)$$ $$C_{F_{ideal}} = \Gamma\sqrt{\frac{2\gamma}{\gamma-1}\left(1-\left(\frac{p_e}{p_c}\right)^{\frac{\gamma-1}{\gamma}}\right)} + \left(\frac{p_e-p_a}{p_c}\right)\frac{A_e}{A_t} \quad (2.20)$$

*- Thrust coefficient, C_F denotes the thrust amplification due to gas expansion in micro-nozzle when compared to thrust that would be exerted when the chamber pressure acts over the throat area [2.1].

But before we determine the thruster efficiencies and nozzle quality factor, we need to calculate the local boundary layer thickness δ^* as shown in figure 2.5 along the nozzle length, starting from the nozzle throat to the nozzle exit plane. We consider only boundary layer growth along the nozzle contour wall and neglecting any boundary layer effects from the end walls (refer back to table 2.2 for the reason). Based on the throat Reynolds number, the nozzle discharge factor C_D is calculated by using the relation 2.13. From this discharge coefficient value, we calculate the effective throat area (relation 2.12) and the actual mass flow rate through the nozzle (relation 2.11). The effective throat width is then calculated as:

$$W_{t,eff} = W_t - 2\delta^* \tag{2.21}$$

To study the boundary layer growth along the diverging section of the nozzle, we take the simple approach of modelling it as flow over a flat plate. The local flow Reynolds number is then calculated as a function of the slanted divergent length L (figure 2.7):

$$\mathrm{Re}_L = \frac{\rho U L}{\mu} \tag{2.22}$$

where, $L = \dfrac{x}{\cos 20^o}$ (2.23)

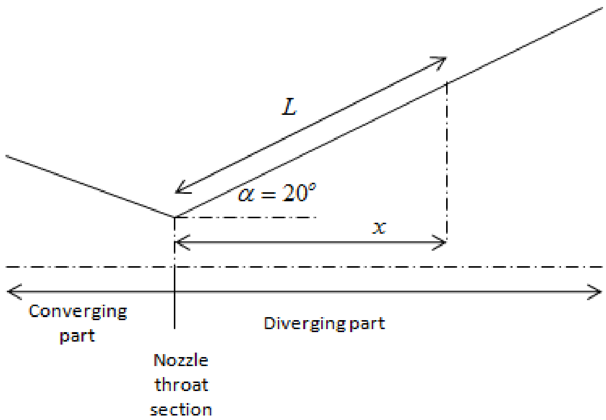

Figure 2.7: Representation of slanted divergent length L of the nozzle.

Table 2.6 gives the relation for calculating the displacement thickness δ^* depending on the flow regime.

Table 2.6: Displacement thickness formula for laminar and turbulent flow regime

Property	Laminar	Turbulent
Displacement thickness, δ^*	$\dfrac{\delta^*}{L} = \dfrac{1.72}{\sqrt{\mathrm{Re}_L}}$	$\dfrac{\delta^*}{L} \cong \dfrac{0.020}{(\mathrm{Re}_L)^{1/7}}$

Then the local channel width is calculated by using relation 2.21. The calculated effective nozzle size for flow expansion at different operating pressures is given in table 2.7.

Table 2.7: Effective nozzle size for flow expansion at different operating points.

Sl. No.	**Throat Reynolds number,** Re_t	**Discharge coefficient** C_D [-]	**Viscous mass flow rate** $\dot{m}_{viscous\_losses}$ [mg/s]	**Effective throat width** $W_{t,eff}$ [μm]	**Reduction in nozzle exit area** [%]
1	1402	0.900	1.557	9.00	11.71
2	1122	0.889	1.227	8.89	13.08
3	841	0.872	0.907	8.72	15.10
4	561	0.844	0.582	8.44	18.51
5	280	0.780	0.273	7.80	26.18

It follows that at lowest Reynolds number, boundary layer occupies roughly 26 % of the nozzle exit area and 22% of the nozzle throat area. This in turn leads to a reduction in mass flow rate through the nozzle by 22% and reduction in expansion ratio by ~5%. With the new mass flow rate and effective nozzle cross-section for flow expansion after taking into account boundary layer from viscous effects, we then calculate the thrust and Isp efficiency of the nozzle along with the nozzle quality factor and the results are presented in table 2.8.

Table 2.8: Efficiency of nozzle against the throat Reynolds number.

Sl. No.	**Throat Reynolds number,** Re_t [-]	**Thrust efficiency** η_F [%]	**Specific impulse efficiency** η_{Isp} [%]	**Nozzle quality factor** ξ_F [-]
1	1402	89.97	99.95	0.873
2	1122	88.83	99.94	0.862
3	841	87.14	99.93	0.846
4	561	84.32	99.91	0.818
5	280	77.92	99.86	0.756

From the calculated values presented in table 2.8, it is worth to note that both the thrust efficiency and the nozzle quality factor decreases by 13% and 15% respectively, with a drop in flow Reynolds number at the throat by a factor of 5. Such a trend of decreasing thruster performance with throat Reynolds number can also been observed in the work of Bayt.*et.al* [2.2] and La Torre [2.5]. The effect of any changes in the nozzle geometry on its efficiency will be discussed in following section.

2.5 Effect of nozzle geometry parameters on nozzle efficiency

In this section, we study the effects of any changes made to the nozzle geometry on its efficiency. Referring back to figure 2.1 and 2.2, we see that a number of parameters can be played around with, but certain parameters are limited due to the selected MEMS fabrication technique. All of these geometrical parameters and their limitations, if any, are presented in table 2.9.

Table 2.9: Nozzle geometry parameters and their limitations.

Sl. No.	Nozzle geometry parameter	Symbol	Limitation	Values selected for study
1	Channel height	H_c	The standard thickness of the silicon wafer used is 550 μm. This limits the maximum channel height for a not fully etch through channel in our selected concept.	150 μm 50 μm
2	Throat width	W_t	The minimum throat width is limited to 5 μm because of the fabrication limitation and pronounced effect of any surface roughness on fluid flow.	10 μm 5 μm
3	Nozzle expansion ratio	$\varepsilon = \frac{A_e}{A_t}$	No limitation	25:1 (fixed for all designs)
4	Half contraction and expansion angle	$\beta \,\&\, \alpha$	No limitation from fabrication point of view.	$\beta = 15^o$ $\alpha = 20^o$ (fixed for all designs)

Based on the limitations on nozzle geometry parameters and to perform a qualitative performance study of a MEMS thruster within a short time, 6 different variants of nozzles were fabricated. They are listed in table 2.10.

Table 2.10: Design case studies.

Design variant #	Throat width W_t [μm]	Channel height H_c [μm]	Throat area A_t [μm^2]	Converging length L_{conv} [μm]$^+$	Divergent length L_{div} [μm]$^{++}$	Aspect ratio at throat, α
1	10	50	500	74.64	329.70	5
2	5	50	250	83.97	164.85	10
3	10	50	500	634.45	329.70	5
4*	10	150	1500	74.64	329.70	15
5	5	150	750	83.97	164.85	30
6	10	150	1500	634.45	329.70	15

**- This was the design that was used in nozzle performance study in section 2.3.*
$^+$- Convergent length is the axial length along the nozzle from the nozzle inlet to the throat section.
$^{++}$- Diverging length is the axial length along the nozzle from the throat section to the nozzle exit plane. Note that both these lengths are not the slant length as represented in figure 2.7.

The six nozzle design variants are studied at different chamber pressures, similar to what we did in section 2.3 and 2.4. Figure 2.8 plots the *ideal* thrust values for each design at different chamber pressures. It follows that with these six designs, we can cover a thrust range of 1.2 mN to 0.04 mN; i.e. a thrust range varying two orders of magnitude. The specific impulse for all the designs is the same at 73 s. This is because the nozzle expansion ratio is kept the same for all variants.

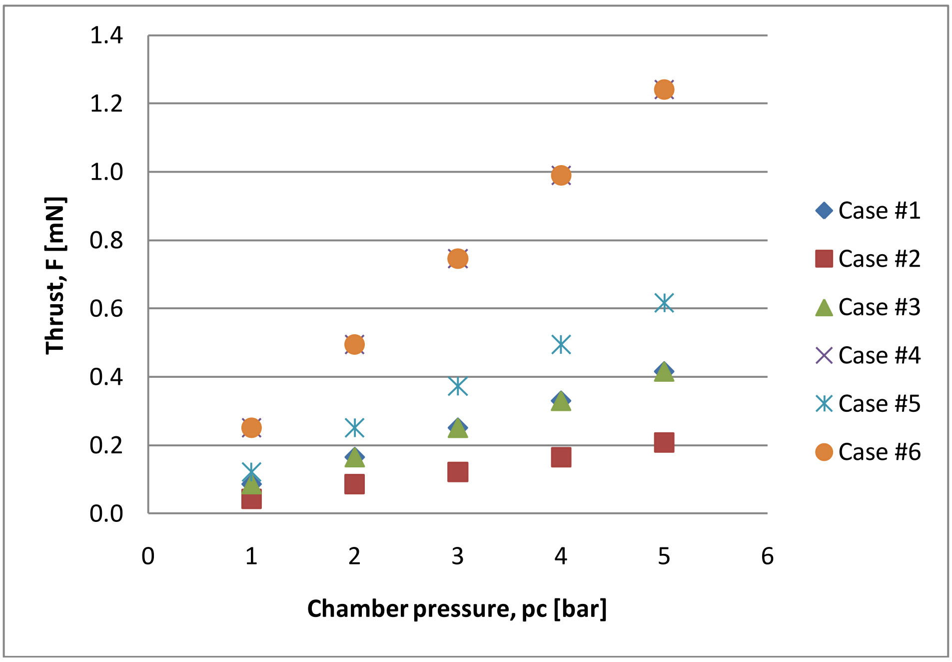

Figure 2.8: Ideal thrust values for six nozzle design variants as a function of chamber pressure.

Figure 2.9 plots the thrust efficiency as a function of the throat reynolds number for each variant after considering the viscous losses. From the figure, it is very clear that the throat reynolds number in all the design cases at operating points is within the laminar flow regime. It can also be seen that the thrust efficiency decreases dramatically at low throat reynolds number as it was concluded from table 2.8. The lowest thrust efficiency of 68 % coincides with the lowest throat reynolds number observed in the nozzle having the smallest throat area (case #2).

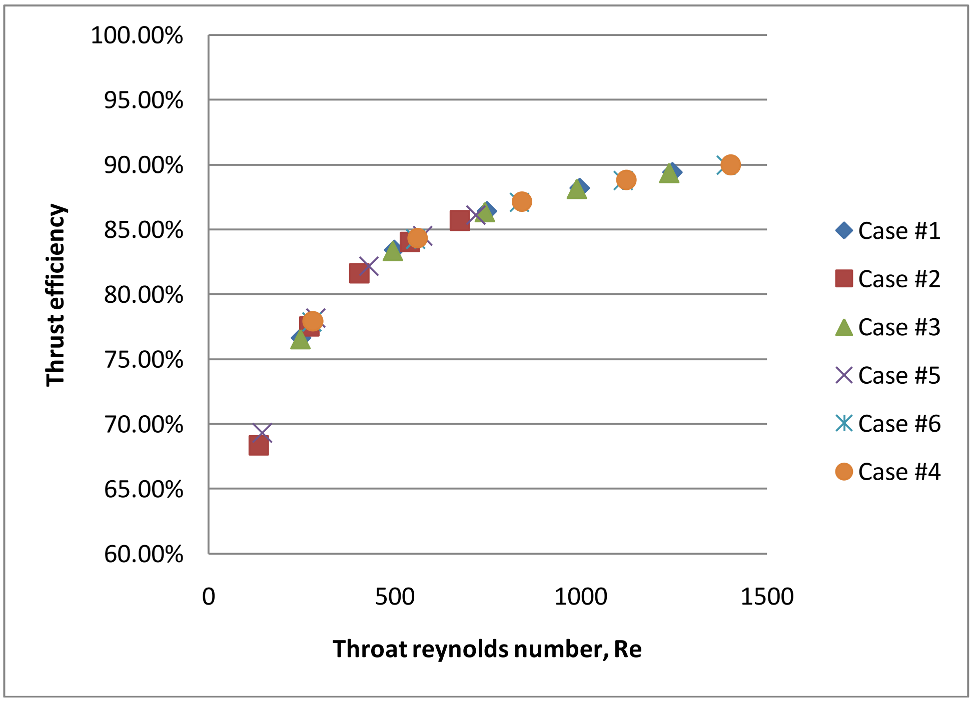

Figure 2.9: Thrust efficiency as a function of throat reynolds number for the six design variants.

Figure 2.10 plots the Isp efficiency as a function of the throat reynolds number for each variant. From the figure, it follows that the Isp efficiency too decreases with the throat Reynolds number. But the drop in performance with flow reynolds number is more or less negligible. This leads us to the conclusion that the effect of boundary layer formation on micro-nozzle performance is more pronounced in the effective thrust produced.

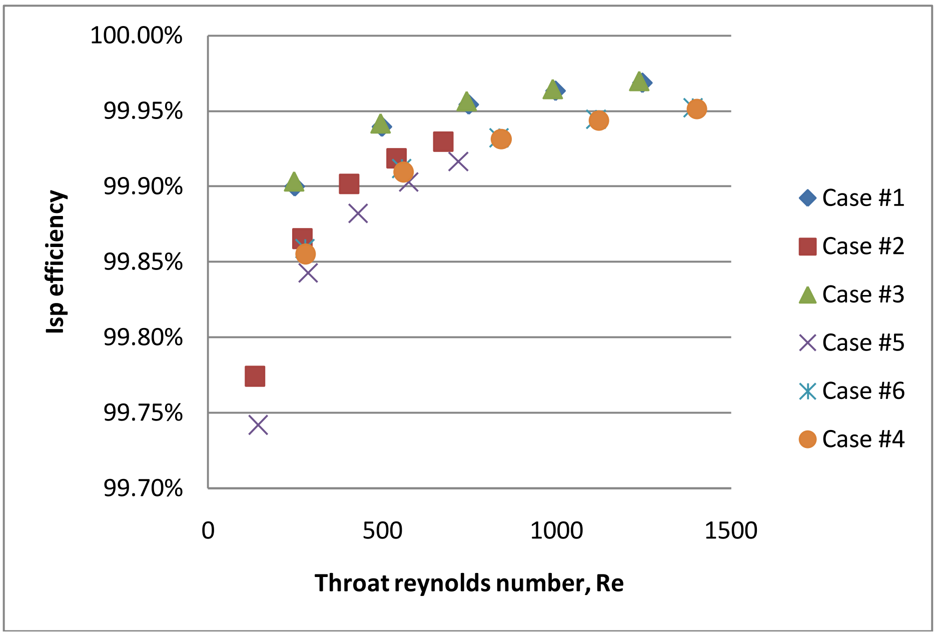

Figure 2.10: Isp efficiency as a function of throat reynolds number for the six design variants.

Figure 2.11 plots the nozzle quality factor for all the design variants. The trend followed is similar to what we saw with the thrust efficiency curves (figure 2.9). It can be seen that for throat Reynolds number below 550, the nozzle quality factor starts dropping quite drastically (a decrease of 20 % within the lower Reynolds number range of 135 – 550). This marks the onset of the effect of boundary layer formation on the nozzle flow.

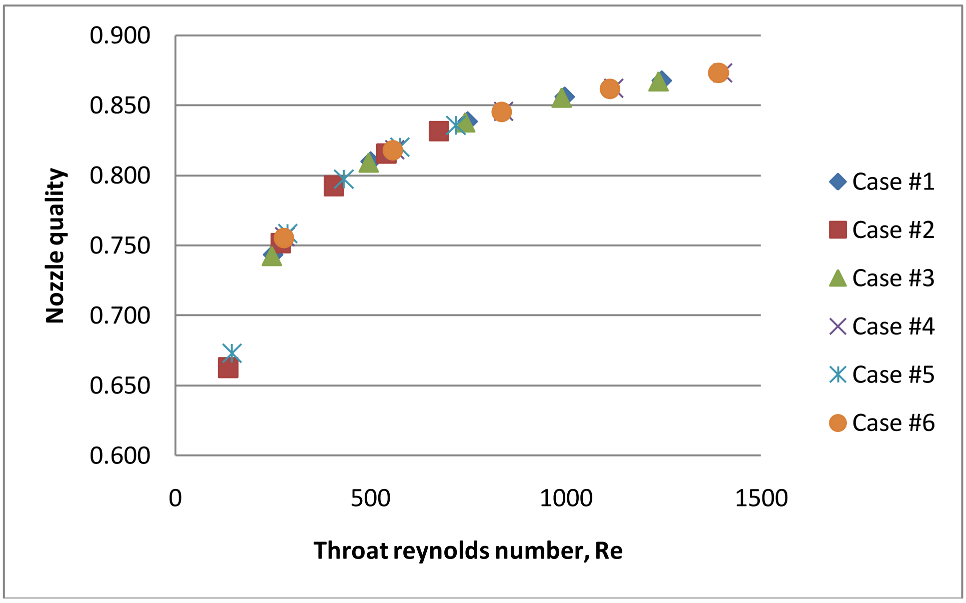

Figure 2.11: Nozzle quality factor for all designs as a function of throat Reynolds number.

Summarizing the main findings in this section, both the thrust efficiency and the nozzle quality factor drops significantly by 25 % with decreasing flow Reynolds number irrespective of different nozzle geometries considered for the study.

2.6 Thruster performance at high chamber temperatures

The MEMS resistojet concept shall be able to heat up the propellant flow to a maximum temperature of T_C = 600 K. Hence, it is legitimate to ask the question how does the thrust and Isp change with increasing gas temperature. From ideal theory we expect that the effect on thrust is negligible since exhaust velocity is proportional to the square root of the gas temperature, whereas mass flow rate is inversely proportional to the square root of the gas temperature.

For gases, the viscosity increases with temperature [2.9]. From the definition of Reynolds number (relation 2.6), this increase in viscosity translates to a proportional decrease in flow Reynolds number. Based on the studies performed in section 2.4, we must expect larger viscous losses at hot gas mode operation due to much lower values of Reynolds number. As an example, we take the design case #4 and calculate and compare ideal thrust, ideal specific impulse and throat Reynolds number at a chamber temperature of 600 K with those at 298 K. The results are presented in table 2.11.

Table 2.11: Comparison of thruster performance parameters at both cold and hot gas mode.

Chamber pressure p_c [bar]	**Throat Reynolds number** Re_t [-]		**Ideal thrust** F [mN]		**Ideal specific impulse** I_{SP} [s]	
	T_c=298 K	T_c=600 K	T_c=298 K	T_c=600 K	T_c=298 K	T_c=600 K
5	1402	665	1.24	1.24	73.08	103.73
4	1122	532	0.99	0.99	73.09	103.75
3	841	399	0.75	0.74	73.07	103.74
2	561	266	0.49	0.50	73.06	103.72
1	280	133	0.25	0.24	72.99	103.78

From the table, we see that the thrust remains the same at both modes of operation. But the specific impulse of the nozzle improves by 42 % when the propellant flow is heated from 298 K to 600 K. From the throat Reynolds number presented in the above table, it is easy to visualize how viscous the fluid will be at the throat in hot gas mode when compared to cold gas mode. The viscous nature of the flow at high temperature will be made clearer once we plot the thrust efficiency as a function of chamber pressure for hot gas mode and compare the result with that of cold gas mode. This is done in figure 2.12 for taking the nozzle design #4 using nitrogen as the propellant.

From figure 2.12, we can observe the following:

1) The thrust efficiency during hot gas mode of thruster is consistently lower than its value at the cold gas mode for all values of chamber pressure.
2) The hot gas thrust efficiency decreases with the chamber pressure. But if we compare the difference between the thrust efficiencies at cold and hot gas mode for high pressure and low pressure points, we see that the difference in the former is only 5 % whereas in the latter, the difference increases to 14 %. Such a faster decrease in thrust efficiency can be attributed to the viscous losses getting further augmented at high temperatures.

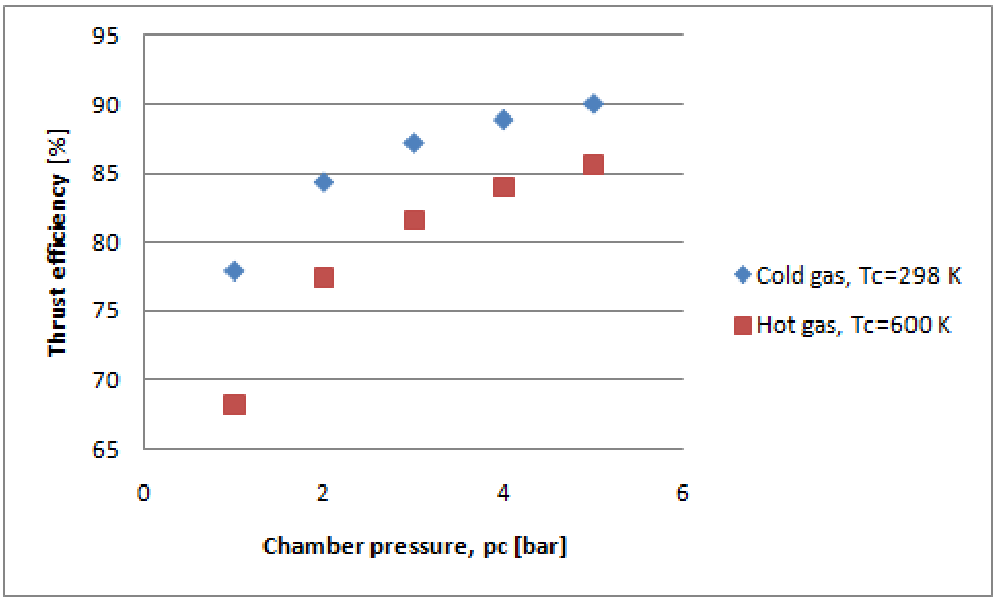

Figure 2.12: Thrust efficiency vs chamber pressure at both cold and hot gas mode.

2.7 Conclusion

The nozzle geometry for a MEMS micro resistojet was presented in this chapter. Six different nozzle design variants are planned to be fabricated and tested so as to cover a thrust range of two orders of magnitude. Increasing viscous nature of the flow at micro-scales has been the main highlight of this chapter and its effect on micro-thruster performance has been studied in detail by using a simple modeling approach. A significant drop in thruster performance was observed with decreasing Reynolds number, correlating well with similar studies performed by other authors. The viscous losses was further augmented by hot gas mode operation.

2.8 Reference

[2.1] Barry Zandbergen; Thermal rocket propulsion; Lecture notes.
[2.2] Robert L. Bayt; Analysis, fabrication and testing of a MEMS based micropropulsion System; MIT PhD Thesis.
[2.3] George P. Sutton and Oscar Biblarz; Rocket propulsion elements; Eighth edition.
[2.4] C.X. Lin and V.V.V. Gadepalli; A computational study of gas flow in a de-laval micro Nozzle at different throat diameters; International journal for numerical methods in Fluids; Int. J. Numer. Meth. Fluids 2009; 59: 1203-1216.
[2.5] Federico La Torre, Sasa Kenjeres, Jean-Luc P.A. Moerel, Barry T.C. Zandbergen and Chris R. Kleijn; Influence of boundary layer formation and surface roughness on the Thrust of micro-nozzles.
[2.6] A.N. Johnson, P.I. Espina, G.E. Mattingly, J.D. Wright and C.L. Merklet; Numerical Investigation of the discharge coefficient in critical nozzles; NCSL Workshop & Symposium, Session 4E, 1998.
[2.7] A. Migliaccio, B.T.C. Zandbergen, F.T. Nardini, M. C. Louwerse; Vacuum testing of a micropropulsion system based on solid propellant cool gas generators (IAC-10.C4.3.12); 61st International Astronautical congress, Prague, CZ.
[2.8] M.R. Wang and Z.X. Li; Numerical simulations on performance of MEMS-based nozzles at moderate or low temperatures; Microfluid Nanofluid (2004) 1:62-70.
[2.9] M.M. Rathore and Raul R.A. Kapuno, Jr; Engineering heat transfer; Second edition; ISBN-13:978-0-7637-7752-4.

Page intentionally left blank

Chapter 3

DESIGN OF HEATER CHAMBER FOR MEMS RESISTOJET

The purpose of a heater chamber is to heat up the propellant from its initial temperature to the required chamber temperature just before the nozzle entry. In practice, this heating can be accomplished in various ways. Here we limit ourselves to resistance heating. The requirements for the chamber design are that it shall be able to heat up nitrogen gas flow to a maximum temperature of 600 K with maximum input electric power of 1 W.

The heater chamber concept used in previous research works on resistojets at the chair of space engineering, like the DUR-1 [3.23], DUR-1.2 [3.24] and DUR-1.0H_2O [3.25] is shown graphically in figure 3.1. It consists of a helically coiled hollow steel tube through which the propellant flow is passed. The steel tube is resistively heated by passing electric current through it and the propellant flow which is in direct contact with the heat source gets heated up by means of forced convection.

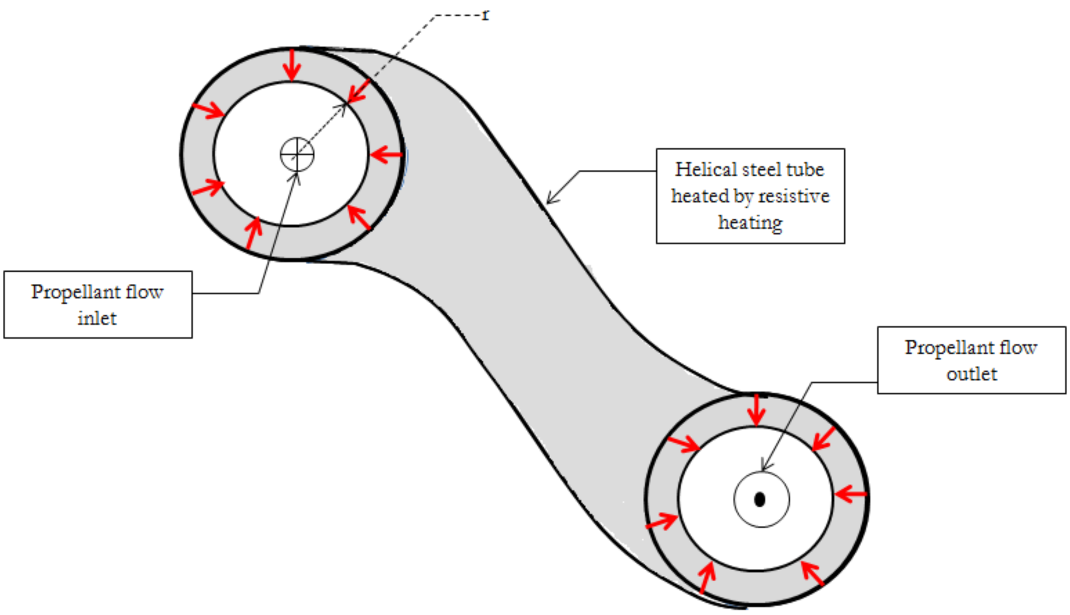

Figure 3.1: Helically coiled tube heater chamber concept.

But for the present selected concept of MEMS heater chamber (figure 3.2), the main heat source is the thin aluminium heater layer deposited on top of the silicon chip. The aluminium layer is resistively heated by passing current through it. This heat then conducts through the silicon subtrate (the grey shaded portion in figure 3.2) and heats up the propellant that flows through the micro-fluidic channel (highlighted with green boundary). This concept is very similar to MEMS heat sinks which is widely used in cooling electronic circuits.

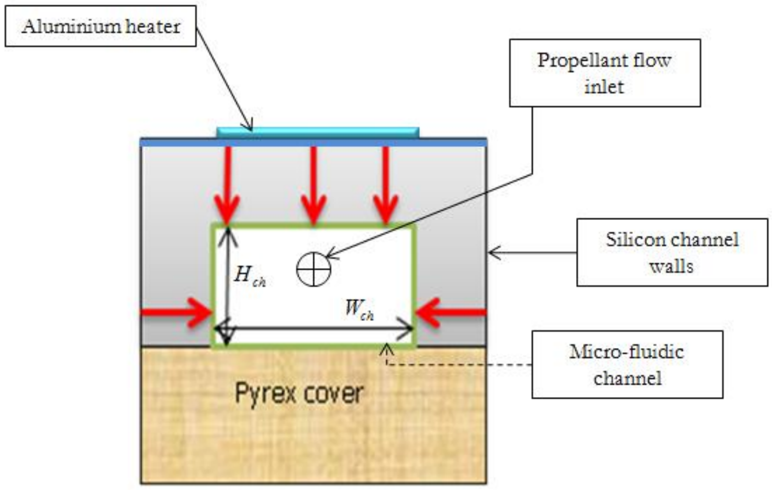

Figure 3.2: MEMS heater chamber concept.

Now, part of the input electrical input power P_{el} is used to heat up the propellant flow P_{heat} and the rest is lost to the environment P_{loss}.

$$P_{el} = P_{heat} + P_{loss} \tag{3.1}$$

In section 3.1, the total electric input power is discussed. The power that goes into heating up the nitrogen gas flow is discussed in section 3.2. In section 3.3, both the heater material and gas properties that play a role in heat transfer are discussed. Pressure loss in fluid flow as it flows through a micro-fluidic channel is addressed in section 3.4. In section 3.5, four design cases are presented and they are compared with each other with respect to the pressure drop. The power loss from a MEMS thruster chip to its ambient by means of convection, conduction and radiation is discussed in section 3.6 followed by conclusion in section 3.7. Section 3.8 contains a list of all the references used in this chapter.

3.1 Electrical input power

The electric properties of the heater are fundamental in order to know the amount of electric current required to achieve a certain power. The heater resistance is an important property since a high value of resistance for the same input current leads to a high value of power (see relation (3.2)). Also the resistance of a metal like aluminium is temperature dependent and can be represented in the form of a linear relation as shown in relation 3.3.

$$P_{el} = I^2 R = \frac{V^2}{R} \tag{3.2}$$

$$R = R_o(1+\alpha.(T-T_o)) \tag{3.3}$$

$$R_o = \frac{\rho_o L}{A} \tag{3.4}$$

where R_0 is the heater resistance at reference room temperature (296 K), L the heater length, A the heater cross-sectional area, α the temperature coefficient of resistance (CTE) for aluminium (=0.0043) and ΔT the temperature difference. We assume an initial heater resistance of 60 Ω at room temperature (to be verified in chapter 6 dealing with test result discussion). Considering the fact that for a microsatellite like delfi-n3Xt, the voltage level is more or less constant at 12 V

[3.22], the input electric power to achieve a heater temperature of 660 K (Heater temperature is taken as 10% higher than the chamber temperature) will be 1 W.

3.2 Propellant heating power

Convection is a mode of heat transfer between a surface and moving fluid. When a propellant is forced to flow through a micro-channel under a feed pressure, heat gets transferred from the hot silicon channel walls to the flow by means of forced convection. To study about this forced convective heat transfer, we start with Newton's law of cooling where the fluid properties are taken at the bulk fluid temperature, T_b as they are defined below:

$$P_{heat} = \dot{m}\, c_p \Delta T = \dot{m}\, \Delta H = hA(T_S - T_f) \tag{3.5}$$

$$h = \frac{Nu \times k}{D_h} \tag{3.6}$$

$$T_b = \frac{T_i + T_o}{2} \tag{3.7}$$

$$D_h = \frac{2H_{ch}W_{ch}}{H_{ch} + W_{ch}} \tag{3.8}$$

where $\dot{m}$ is the mass flow rate, ΔH the change in enthalpy required, h the convective heat transfer coefficient, k the thermal conductivity of propellant at the bulk temperature, D_h the hydraulic diameter of the channel, Nu the Nusselt number, A the surface area of channel for heat transfer, H_{ch} the channel height, W_{ch} the channel width, T_S the surface temperature, T_i and T_o the inlet and outlet fluid temperature respectively. From relation 3.5, we see that a much higher heat transfer coefficient can be achieved with smaller heat transfer area A, for a fixed propellant heating power. The concept of hydraulic diameter D_h for non-circular channels is applicable for rectangular channels only when its aspect ratio, defined as the ratio of channel height to its width, is in the range of ¼ to 4 [3.34]. Heating power P_{heat} required to raise the temperature of a given mass flow rate of gas from an initial temperature of 298 K to a higher temperature T is calculated by:

$$P_{heat} = \frac{\dot{m}\left[{}^{mg}\!/_{s}\right].\Delta H\left[{}^{kJ}\!/_{mole}\right]}{M\left[{}^{gm}\!/_{mole}\right]} \quad [\mathrm{W}] \tag{3.9}$$

where M is the molar mass of the propellant (for nitrogen gas, M=28.01 gm/mole [3.19]). For ideal gas like nitrogen, enthalpy is a function of temperature only [3.5]. The change in enthalpy for nitrogen gas can be calculated by one of the two relations given below depending upon the final gas temperature [3.7]. For final gas temperatures less than 500 K, the required change in enthalpy is:

$$\Delta H = 28.98641t + 1.853978\frac{t^2}{2} - 9.647459\frac{t^3}{3} + 16.63537\frac{t^4}{4} - \frac{0.000117}{t} - 8.671914 \tag{3.10}$$

For final gas temperatures greater than 500 K, the required change in enthalpy is:

$$\Delta H = 19.50583t + 19.88705\frac{t^2}{2} - 8.598535\frac{t^3}{3} + 1.369784\frac{t^4}{4} - \frac{0.527601}{t} - 4.935202 \tag{3.11}$$

where t =T/1000 in Kelvin and ΔH in kJ/mole.

Figure 3.3 plots the heating power P_{heat} required as a function of mass flow rate for different chamber temperature T_c using nitrogen gas as the propellant.

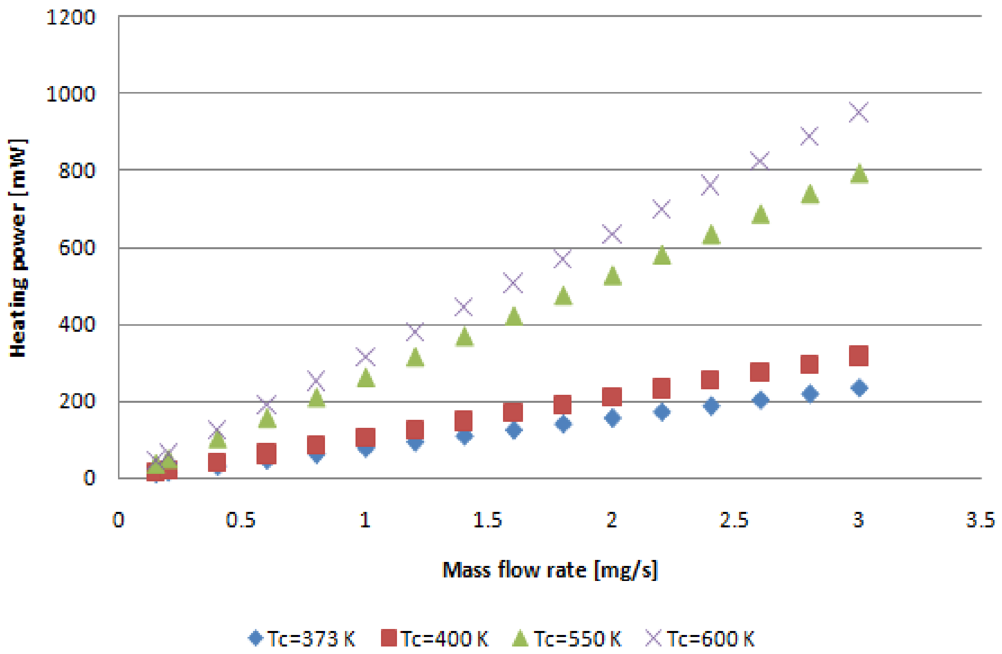

Figure 3.3: Heating power as a function of mass flow rate for different chamber temperature.

From figure 3.3, it can be seen that a maximum nitrogen gas flow rate of 3 mg/s can be heated upto a maximum chamber temperature of 600 K with a heating power of less than 1 W. Assuming ideal heating conditions with no heat losses to the environment, this maximum heating power can be treated the same as the electric input power from an onboard power supply to the MEMS thruster.

3.2.1 Nusselt number correlations

How much heat flows to the gas is determined amongst others by the Nusselt number, as we saw in relation 3.5 and 3.6. There exist a number of readily available correlations for Nusselt number in the literature, depending on the channel geometry, flow regime (fully developed flow, simultaneously developing flow, thermally developing flow, transitional flow) and thermal boundary condition applied on the heater channel wall (constant heat flux or constant wall temperature). Constant wall temperature may be used as the thermal boundary condition based on the argument that the silicon is a very good thermal conductor. But since a majority of work on MEMS heat sink design is done by taking constant heat flux as the thermal boundary condition, we shall take the same approach for our MEMS heater chamber design. Nusselt number correlations for a 3-side heated channel wall (the 4^{th} side of a rectangular channel in our MEMS heater chamber design is made of Pyrex glass as it was highlighted in figure 3.2; since Pyrex is a bad thermal conductor, we assume it to act like a thermal insulator layer) are presented in table 3.1.

Table 3.1: Nusselt number correlations for a 3-side heated channel wall.

Flow regime	**Nusselt number correlations**	**Eq.**	**Ref.**
Fully developed laminar flow	Nu_{Dh}=-1.047+9.326G where $G=\dfrac{1+\left(\dfrac{1}{\alpha}\right)^2}{\left(1+\dfrac{1}{\alpha}\right)^2}$ and α=H_{ch}/W_{ch} is the aspect ratio of the channel.	(3.12)	[3.3]
Thermally developing, hydraulically developed flow	$Nu=8.24-16.8\left(\dfrac{1}{\alpha}\right)+25.4\left(\dfrac{1}{\alpha}\right)^2-20.4\left(\dfrac{1}{\alpha}\right)^3+8.7\left(\dfrac{1}{\alpha}\right)^4, z^*_{th}\geq 0.1$ $Nu=3.35z^{*\,-0.130}_{th}\left(\dfrac{1}{\alpha}\right)^{-0.120}\Pr^{-0.038}, 0.013\leq z^*_{th}<0.1$ $Nu=1.87z^{*\,-0.300}_{th}\left(\dfrac{1}{\alpha}\right)^{-0.056}\Pr^{-0.036}, 0.005<z^*_{th}<0.013$ where z^*_{th} is the thermal entrance length constant and Pr the Prandtl number of the fluid defined as: $\Pr=\dfrac{c_p\mu}{k}$ (3.13) where c_p, μ and k are the specific heat, dynamic viscosity and thermal conductivity of the fluid, all taken at the bulk fluid temperature.	(3.14)	[3.4]
	For single channel design; Nu=5.39, $z_{th}^* \geq 0.1$, $Nu=5.16+0.02(z_{th}^*)^{-1.035}$, $0.01 \leq z_{th}^* < 0.1$ $Nu=1.17(z_{th}^*)^{-0.401}Pr^{-0.044}$, $0.001 < z_{th}^* < 0.01$	(3.15)	[3.4]
Fully developed turbulent flow	$Nu_{fd,Turb}=\dfrac{(f/2)(\mathrm{Re}-1000)\Pr}{1+12.7\sqrt{f/2}(\Pr^{2/3}-1)}$, where f is the fanning friction factor defined as $f=(1/4)[1.82\log(\mathrm{Re})-1.64]^{-2}$ This equation is applicable for $0.5 \leq Pr \leq 2000$ and $2300 \leq Re \leq 5E6$.	(3.16)	[3.30]

Flow regime	Nusselt number correlations	Eq.	Ref.
Thermally developing turbulent flow	$\frac{Nu_{Dh}}{Nu_{fd,Turb}} = 1 + 0.48\left(L_{ch}/D_h\right)^{-0.25}\left[1 + \frac{3600}{Re_{Dh}\sqrt{L_{ch}/D_h}}\right] \times \exp\left(-0.17\, L_{ch}/D_h\right)$, where $4000 \le Re_{Dh} \le 5E5$, $0.7 \le Pr \le 1.0$ and $L_{ch}/D_h \ge 0.06$. $Nu_{fd,Turb}$ is calculated using relation 3.16.	(3.17)	[3.3]

$$z^*_{th} = \frac{L_{ch}}{D_h \operatorname{Re} \Pr} = -1.27E-6\alpha^6 + 4.709E-5\alpha^5 - 6.902E-4\alpha^4 + 5.014E-3\alpha^3 - 1.769E-2\alpha^2$$
$$+1.845E-2\alpha + 5.691E-2$$

3.2.2 Flow regime characterization based on flow Reynolds number

It is fundamental to understand whether the flow through a channel is laminar or turbulent, since the Nusselt number to be used for heat transfer analysis from table 3.1 depends on the type of flow regime. It is characterized by the flow Reynolds number, which depends on the channel hydraulic diameter, fluid velocity, density, fluid viscosity and mass flow rate. It is expressed as follows:

$$\operatorname{Re} = \frac{\rho U D_h}{\mu} = \frac{4\dot{m}}{\pi D_h \mu} \tag{3.18}$$

For flow through a smooth square or rectangular micro-channels, the critical Reynolds number for flow transition from laminar to turbulent flow is found to be a function of channel aspect ratio α as given in table 3.2 [3.1]:

Table 3.2: Critical Reynolds number for different aspect ratios.

Aspect ratio	Critical Reynolds number
$\alpha = 1.0$	2200
$\alpha \le 0.2$ or $\alpha \ge 5.0$	2500
Other values of α	Linear interpolation

3.2.3 Conductive heat transfer through the silicon chip

Under ideal conditions, conductive heat transfer from aluminium heater layer through the chip should equal the convective heat transfer from the channel walls to the fluid flow. The parameters that govern a MEMS heater chamber design can be classified into two: 1) parameters that govern convective heat transfer from the channel walls to the fluid flow which includes fin spacing W_{ch}, channel height H_{ch}, channel length L_{ch} and the number of channels N and 2) parameters that govern heat dissipation from the heat source which includes the fin width W_f, substrate thickness t and thermo-physical properties of silicon [3.20]. All the geometric parameters can be traced in figures 3.4-3.6 using a schematic diagram of MEMS heater chamber having three channels.

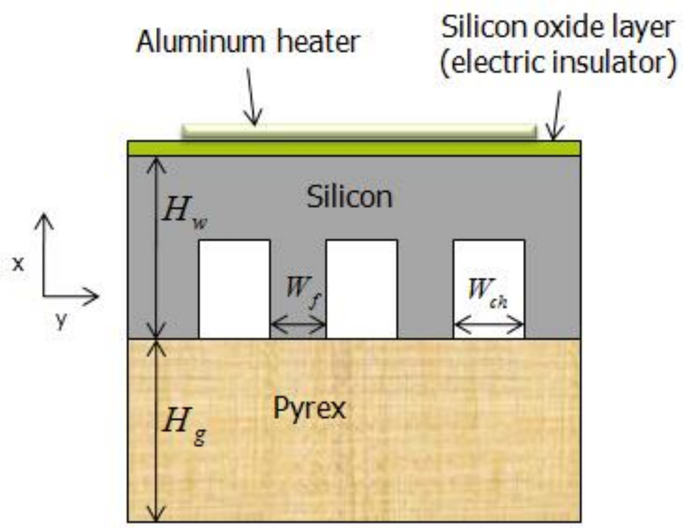

Figure 3.4: Lateral cross-sectional view of a MEMS heat heater chamber (left).

In figure 3.4, H_W represents the standard height or thickness of silicon wafer (550 μm) and H_g represents the standard thickness of pyrex glass wafer (500 μm).

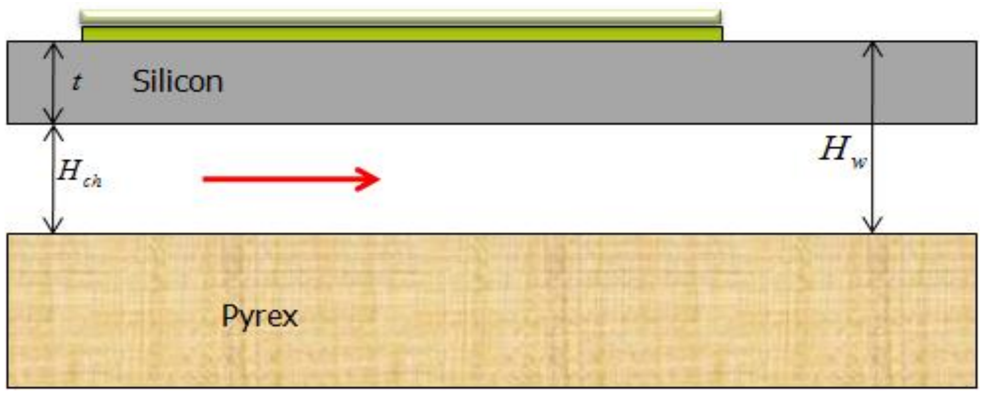

Figure 3.5: Cross-sectional top view of a MEMS heater chamber showing the three channels and the nozzle (top)

In figure 3.5, L_{ch} stands for the length of the channel and W the total width of the heat sink base.

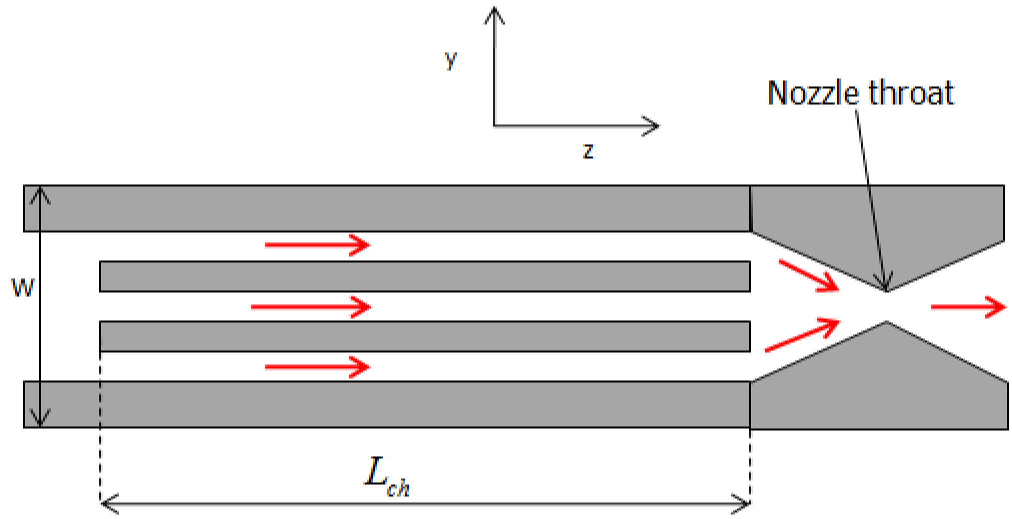

Figure 3.6: Longitudinal cross-sectional view of a MEMS heater chamber (top)

In figure 3.6, t represents the silicon substrate thickness between the heat source and the channel walls.

The thermal resistance to heat flow from the heat source to the fluid is analogous to the electric resistance to current flow when a potential is applied across an electric circuit. From various studies performed on MEMS heat sink design, we see that this total thermal resistance is the sum of four different types of thermal resistance, each of them defined in table 3.3.

Table 3.3: Types of thermal resistance in a MEMS heat sink.

Sl. No.	Type of thermal resistance	Relation	Eq.	Unit	Ref
1	Conduction resistance through silicon substrate, R_{sub}	$R_{sub} = t/(k_{Si}\, L_{ch}\, W)$ This is the thermal resistance to the heat flow through the silicon substrate of thickness t.	(3.19)	[k/W]	[3.10, 3.11, 3.12, 3.13, 3.14]
2	Constriction thermal resistance, R_{constr}	$R_{constr} = \frac{(W_{ch}+W_f)}{\pi k_{Si}} \ln\left(\frac{1}{\sin\left[\frac{\pi W_f}{2(W_{ch}+W_f)}\right]}\right)$ This is the thermal resistance to the heat flow as it gets funneled from the silicon substrate to the fin section of the heat sink.	(3.20)		

Sl. No.	Type of thermal resistance	Relation	Eq.	Unit	Ref
3	Convection thermal resistance, R_{conv}	$R_{conv}=\left[1/R_{fin}+1/R_{base}\right]^{-1}$ $=\left[\eta h 2L_{ch}H_{ch}(N-1)+hW_{ch}L_{ch}N\right]^{-1}$ $\eta_f=\dfrac{\tanh(m.H_{ch})}{m.H_{ch}}$; (3.22) $m=\sqrt{\dfrac{h.(P_f)}{(A_f).k_{Si}}}=\sqrt{\dfrac{h.(2.L_{ch})}{(L_{ch}.W_f).k_{Si}}}$ (3.23) where N is the number of the channels, η is the fin efficiency and h is the convective heat transfer coefficient. This is the thermal resistance to the convective heat transfer from the channel walls to the fluid flow.	(3.21)	[k/W]	[3.10, 3.11, 3.12, 3.13, 3.14]
4	Bulk thermal resistance, R_{heat}	$R_{heat}=\dfrac{1}{\dot{m}c_p}$ This is the thermal resistance to the propellant heating as it flows through hot micro-fluidic channels.	(3.24)		

The heating power P_{heat} can then be defined as follows:

$$P_{heat}=\frac{T_{s,\max}-T_{g,i}}{R_{total}} \tag{3.25}$$

where $T_{surf,max}$ is the maximum surface temperature of the silicon wall at the end of a micro-fluidic channel for a constant heat flux boundary condition, $T_{g,in}$ the gas temperature at the inlet of the micro-channel and R_{total} the total thermal resistance defined as:

$$R_{total}=R_{sub}+R_{heat}+R_{conv}+R_{constr} \tag{3.26}$$

3.3 Material and gas properties

From previous sections on convective and conductive heat transfer, we find that apart from the geometrical parameters, the effective heat transfer also depends on the thermo-physical properties of both the structural material and the fluid.

Silicon is the structural material of the micro-fluidic channels. Due to its high thermal conductivity (k=157 W/mK at room temperature [3.32]), it acts as an excellent thermal conductor between the aluminium heater and the micro-fluidic channel. But from literature, we found that the thermal conductivity of silicon varies with the temperature [3.8]. This in turn means that the thermal resistance of a given heat sink designs can change with temperature. Table

3.4 contains the curve-fitting equation for the thermal conductivity of silicon as a function of temperature.

Table 3.4: Silicon properties as a function of temperature.

Material	Property	Formula	Eq.	Ref.
Silicon	Thermal conductivity k_{Si}	$k = 252098T^{-1.296}$ R^2=0.9994; Unit of k is W/mK Unit of T is K	(3.27)	[3.8]

The gas properties are evaluated at the bulk temperature, T_b defined as the average of inlet and outlet gas temperature. It is essential to know how then certain fluidic properties vary as a function of temperature like for example; the heat capacity which is an important fluidic parameter that tells us how much energy is required to raise the temperature of unit mass of gas by unit temperature. Table 3.5 contains the curve-fitting equations for certain thermo-physical properties of nitrogen gas as a function of temperature.

Table 3.5: Nitrogen gas properties as a function of temperature.

Gas	Property	Formula	Eq.	Ref.
Nitrogen	Specific heat capacity $c_{p,N2}$	$c_p = -4E-7T^3 + 0.0009T^2 - 0.439T + 1103.5$ R^2=0.999 Unit of c_p is in J/kgK Unit of T is K	(3.28)	[3.7]
	Gas viscosity, μ_{N2}	$\mu = 3E-8T + 8E-6$ R^2=0.9948 Unit of μ is in Ns/m^2 Unit of T is K	(3.29)	[3.28]
	Thermal conductivity, k_{N2}	$k = 6E-5T + 0.0084$ R^2=1 Unit of k is in W/mK Unit of T is K	(3.30)	[3.9]
	Prandtl number, Pr	$\mathrm{Pr} = \frac{c_p \mu}{k} = 0.7$	(3.31)	[3.5]

3.4 Pressure losses

Calculating the pressure drop in a heater chamber right till the nozzle inlet is important to know what the feed pressure should be to achieve a certain chamber pressure [3.5]. Any fluid flowing through a channel will experience a drop in its pressure head due to shear force acting at the walls against the flow. This shear stress can be expressed in the form of Fanning friction factor 'f' defined as [3.2]:

$$f = \frac{\tau_w}{\frac{1}{2}\rho U^2} \tag{3.32}$$

where τ_w is the shear stress at the channel wall, ρ the fluid density and U the fluid velocity. Though Darcy friction factor is more commonly used in the lecture notes (Darcy friction factor = 4 x Fanning friction factor), for the current MEMS heater chamber design the fanning friction factor will be used since most of the pressure drop analysis in a MEMS heat sink have been carried out with this friction factor definition. This friction factor is then used to deduce the pressure drop Δp that occurs across a channel of length L_{ch} and hydraulic diameter D_h when a fluid with velocity U and density ρ flows through it:

$$\Delta p = p_i - p_o = 2f\frac{L_{ch}}{D_h}\rho U^2 \tag{3.33}$$

There exist a number of correlations for fanning friction factor constant in the literature, depending on the channel geometry, flow regime (fully developed flow, hydraulically developing flow laminar or turbulent flow), flow compressibility and slip flow (table 3.6). The effects of compressibility starts showing up when the flow Mach number, M becomes greater than 0.3. Compressibility effects increases the mean velocity in stream-wise direction and thus brings an additional pressure drop due to flow acceleration. According to theory, surface roughness of the channels has negligible effect on friction factor for laminar flow, but it does have an effect in case of turbulent flow. Friction factor is also influenced by the flow rarefaction especially when dealing with micro-fluidic flow problems.

Table 3.6: Fanning friction factor constant for a rectangular/square fluidic channel.

Flow condition	**Fanning friction factor relation**	**Eq.**	**Ref.**
Fully developed laminar incompressible flow	$f.\mathrm{Re} = 4.7 + 19.64G$ where, $G = \dfrac{1+\left(\frac{1}{\alpha}\right)^2}{\left(1+\frac{1}{\alpha}\right)^2}$	(3.34)	[3.21]
Hydraulically developing laminar flow	$f\,\mathrm{Re} = 11.3(z^+)^{-0.202}\left(\frac{1}{\alpha}\right)^{-0.094}, 0.02 \le z^+ < 0.1$ $f\,\mathrm{Re} = 5.26(z^+)^{-0.434}\left(\frac{1}{\alpha}\right)^{-0.010}, 0.001 < z^+ < 0.02$ where z^+ is the hydro-dynamic development length constant defined as: $z^+ = L_{ch}/(D_h.\mathrm{Re}) = 0.055$. Entrance effects can be neglected when the value of z^+ is higher than 0.1 [3.17].	(3.35)	[3.4]
Hydraulically developing turbulent flow	$f = B.\mathrm{Re}^C$, where $B = 0.09290 + 1.01612/(L_{ch}/D_{eq})$, $C = -0.26800 - 0.31930/(L_{ch}/D_{eq})$, D_{eq} is the equivalent diameter of the channel defined as: $D_{eq} = \left[\frac{2}{3} + \frac{11}{24}\frac{1}{\alpha}\left(2 - \frac{1}{\alpha}\right)\right]D_h$ This equation is applicable for 2300 < Re < 28000 and for aspect ratio, $\alpha > 1$	(3.36)	[3.6]

Flow condition	Fanning friction factor relation	Eq.	Ref.
Friction factor for turbulent flow as function of roughness	$f_{turb}^{-1} = 3.474 - 1.564\ln\left[\left(\frac{2e}{GD_h}\right)^{1.11} + \frac{63.64}{G\,\mathrm{Re}}\right]$ where $G = \frac{2}{3} + \left(\frac{11}{24}\right)\left(\frac{1}{\alpha}\right)\left(2 - \frac{1}{\alpha}\right)$, e the roughness height.	(3.37)	[3.4]
Friction factor for turbulent incompressible flow through a smooth tube	$f = 0.079\,\mathrm{Re}^{-0.25}$	(3.38)	[3.29]
Friction factor for compressible isothermal flow	$f = \frac{D_h}{4L_{ch}}\left(\frac{M_o^2 - M_i^2}{\gamma M_i^2 M_o^2} + \ln\frac{M_i^2}{M_o^2}\right)$ where γ is the specific heat ratio of fluid, M_i the inlet Mach number of the flow and M_o the outlet Mach number of the flow. The first term in the brackets represents the friction pressure drop and the second term represents the flow acceleration effect.	(3.39)	[3.29]
Friction factor for compressible adiabatic flow	$f = \frac{D_h}{4L_{ch}}\left[\frac{p_i^2}{RT_i\left(\rho U^2\right)}\left(1 - \frac{p_o^2 T_i}{p_i^2 T_o}\right) + \ldots\right.$ $\left.\frac{\gamma+1}{2\gamma}\ln\left[\frac{T_i}{T_o}\frac{2p_o^2\gamma + (\gamma-1)\rho U^2 RT_o}{2p_i^2\gamma + (\gamma-1)\rho U^2 RT_i}\right]\right]$ where R is the characteristic gas constant, ρ and U are the fluid density and velocity respectively, p and T are the fluid pressure and temperature respectively with suffix 'i' representing the inlet condition and 'o' representing the outlet condition.	(3.40)	[3.29]
Friction factor constant ratio between compressible and incompressible laminar flow	$\frac{(f\,\mathrm{Re})_{comp}}{(f\,\mathrm{Re})_{incomp}} = \left[1 - 0.143M + 1.273M^2\right]$ where M is the mean Mach number between the inlet and the outlet of the channel and f_D is the Darcy friction factor. The friction factor constant increases by 15 % at Mach number M=0.4 [3.31], which shows that the pressure drop increases with the compressibility of the flow.	(3.41)	[3.31]
Friction factor for rarefied flow	$f = \frac{16}{\mathrm{Re}\left(1 + 8Kn\frac{(2-\sigma_v)}{\sigma_v}\right)}$, where σ_v is the tangential momentum accomodation coefficient (equals to 0.2 for nitrogen gas [3.31]) and Kn is the Knudsen number of the flow representing its degree of rarefaction. A slip flow (0.01 < Kn < 0.1) leads to a decrease in shear stress at the channel walls due to velocity slip; this in turn translates to a lower pressure drop for rarefied flows.	(3.42)	[3.31]

3.5 Chamber geometries

From figures 3.4 to 3.6, we have seen that a number of geometrical parameters can be played around with in-order to achieve an optimum heater chamber design. But we restrict the number of variable geometric parameters to two, namely the height of the channel H_{ch} and the number of channels, N. In table 3.7, we present four different heater chamber geometries. In section 3.5.1, a comparative study of their pressure drop at cold gas mode is performed. In section 3.5.2, a comparative study of their pressure drop along with their heat transfer performance as a function of mass flow rate at hot gas mode is performed. All the calculations done for the MEMS heat transfer analysis are included in the excel spreadsheet developed by the author. The spreadsheet can be accessed from the following folder: k:/lr/spe/sse/sse-shared/3.PersonalDirectories/TittuMathew/Excelsheets/MEMS heat transfer analysis.

Table 3.7: Geometrical parameters of heater chamber geometries fabricated.

Design case #	W_{ch} [μm]	L_{ch} [cm]	W_f [μm]	H_{ch} [μm]	N	D_h [μm]	α	L_{ch}/D_h [-]
1	50	2	100	150	1	75	3	266.67
2	50	2	100	150	3	75	3	266.67
3	50	2	100	50	1	50	1	400
4	50	2	100	50	3	50	1	400

3.5.1 Performance of chamber geometries at cold gas mode

In this section, the performance of chamber geometries in terms of pressure drop versus mass flow at cold gas mode is carried out. For that, we take a fixed value for the inlet pressure and gas temperature as 5 bars and 298 K respectively, with nitrogen as the propellant gas. We assume that the channel walls are smooth, the flow remains isothermal with no viscous heating and that a given mass flow gets equally divided among the channels in case of a multichannel design (design #2 and #4 from table 3.7).

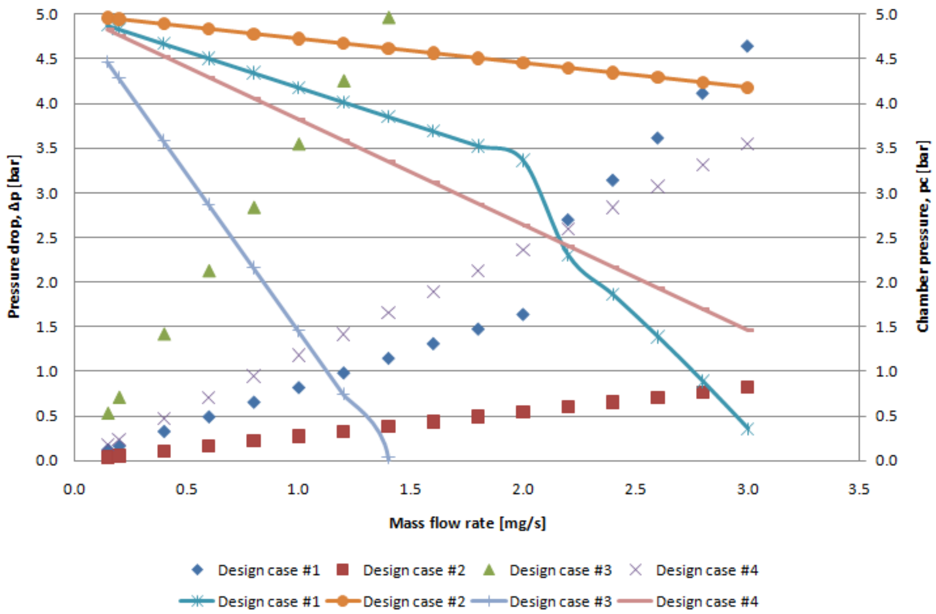

Figure 3.7: Pressure drop (non-solid line) and pressure at the nozzle inlet p_c (solid line) versus mass flow rate for four different chamber geometries at a regulated inlet pressure of 5 bars and cold gas temperature of 298 K.

In figure 3.7, both the pressure drop and pressure at the outlet (same as the chamber pressure, p_c calculated as $p_c=p_i-\Delta p$) for each chamber geometry, are plotted as a function of mass flow rate (0-3 mg/s). From the figure, we see that with increasing mass flow rate, the pressure drop increases and as a result the pressure at the nozzle inlet decreases for all chamber geometries. On a closer look, we see that the rate of increase in pressure drop in #3 is the maximum, whereas the minimum is seen for #2. This is because for a given mass flow rate and a fixed inlet pressure, the total flow cross-sectional area for #2 is three times larger than that for #3 resulting in flow velocity which is three times lower for #2 by using the mass conservation principle. A flow velocity which is three times higher leads to a pressure drop in the channel which is six times larger according to relation 3.33. This explains the steeper rise in pressure drop for #3.

By saying this, we also see that the slope of rise in pressure drop changes at a mass flow rate of 2 mg/s for the single channel design #1. This marks the flow transition from laminar to turbulent flow regime. By looking at large values of length-to-diameter ratios for all the geometries given in table 3.7, it's made clear that we are dealing with fully developed flows. Inlet Mach number of the flow was calculated for each design cases and it was found to be less than 0.3 at all mass flow rates (when M>0.3, compressibility effects has to be taken into account for pressure drop calculations [3.5]), except for the design case #3 when mass flow rate becomes greater than 1.2 mg/s. Knudsen number calculated at the channel inlet tells us that we are dealing with continuum flow (Kn<0.01).

3.5.2 Performance of chamber geometries at hot gas mode

In this section, the performance of heater chamber geometries in terms of pressure drop vs mass flow at hot gas mode is carried out, similar to what we did in the previous section. The only difference is that for hot gas mode, the propellant gas is heated to a maximum temperature of 600 K for all mass flows. The fluid properties are taken at the bulk temperature, defined as the average of inlet and outlet temperature.

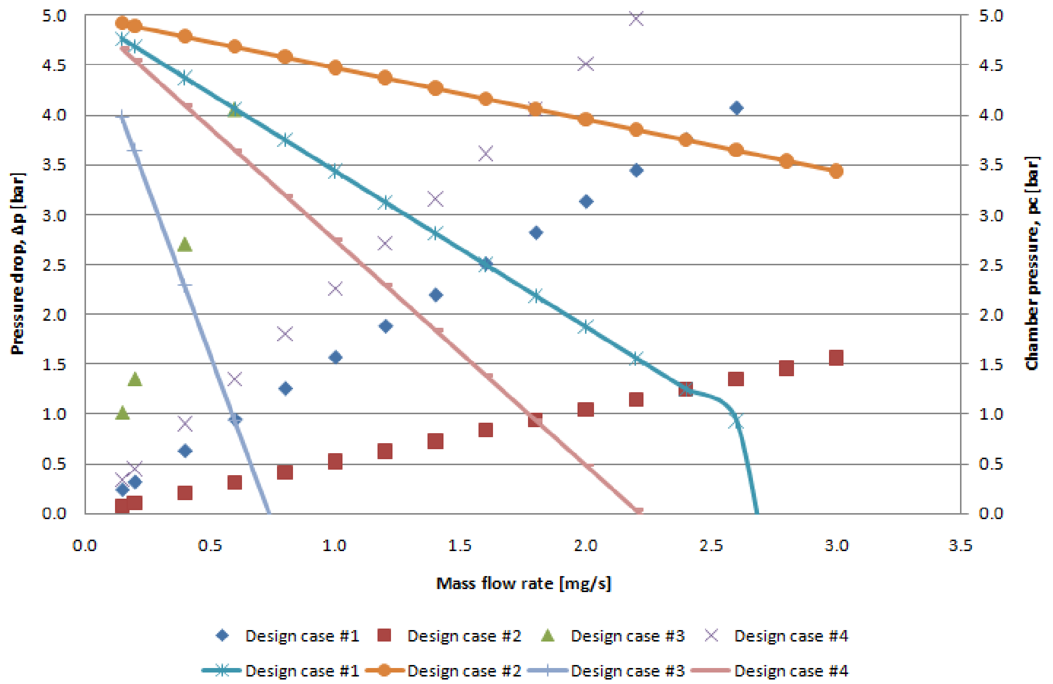

Figure 3.8: Pressure drop (non-solid line) and pressure at the nozzle inlet p_c (solid line) versus mass flow rate for four different chamber geometries at a regulated inlet pressure of 5 bars and chamber temperature T_c of 600 K.

In figure 3.8, both the pressure drop and the chamber pressure p_c for all chamber geometries are plotted as a function of mass flow rate (0-3 mg/s). Maximum propellant flow rate of 3 mg/s is chosen because this was found to be the maximum nitrogen gas flow rate that can be heated to the maximum temperature of 600 K with a maximum input electric power of 1 W under ideal conditions. From the figure, we see that with increasing mass flow rate, the pressure drop increases and as a result the pressure at the nozzle inlet decreases for all chamber geometries, similar to what we observed for cold gas mode. But when comparing the pressure drop and the pressure at the outlet curves for each of the geometries at hot gas mode with their corresponding curves in figure 3.7, we observe some differences as:

1) Slope of increase in pressure drop with mass flow is higher in case of hot gas compared to the cold gas for all geometries. This is because of lower gas density for a given inlet feed pressure as the flow gets heated to a high temperature. This low gas density translates to a high value of flow velocity through the channels leading to larger pressure drop.
2) There appears a sudden increase in pressure drop at a mass flow of 2.6 mg/s for design # 1. As it was reasoned in section 3.5.1, this point corresponds to the flow transition from laminar to turbulent flow. But on closer look, we see that such a transition in flow regime happens at a higher mass flow rate at hot gas mode, compared to that in cold gas mode. This is because as the gas gets heated up, their viscosity increases which in turn translate to a low flow Reynolds number for a given mass flow rate as per the relation 3.18.

In the second half of this section, a comparative study of thermal performance in terms of total thermal resistance for the four chamber geometries is performed as a function of mass flow rate. We take the temperature of the gas flow at the channel inlet as 298 K and the maximum temperature to which the flow gets heated as 600 K, using nitrogen as the propellant. All the fluidic properties are evaluated at the bulk temperature of 449 K using relations in table 3.5 and the thermal property of the structural material, namely the thermal conductivity of silicon is calculated at the maximum temperature of 600 K. Certain assumptions had to be made to simplify the study and they are listed below:

1) Axial heat conduction along the chamber walls is neglected except for the 1-D heat conduction from the heat source to the channel surface.
2) Axial heat conduction along the gas due to the presence of large temperature gradient is neglected.
3) Gas flow is heated under ideal conditions with no heat losses from the chip to its environment.
4) Pyrex glass is treated as a thermally insulating layer due to its very low thermal conductivity compared to silicon (k_{pyrex} = 1.2 W/mK [3.27] compared to k_{Si} = 157 W/mK at room temperature [3.32]).
5) Mass flow gets equally divided among the channels for a multi-channel design.

From table 3.3, we have seen that the total thermal resistance of a MEMS heat sink consists of four types. From equation 3.20, we see that the conduction resistance through the silicon substrate of thickness 't' will be fixed for a given heater chamber geometry irrespective of the mass flow through the channels. The same is the case with the constriction thermal resistance according to relation 3.21. On the other hand, the bulk heating thermal resistance remains the same for all the chamber geometries for a given mass flow and fluid property, as per the relation 3.22. Whereas, the convection thermal resistance depends both on the chamber geometry and the heat transfer efficiency from the "finned" structures to the fluid flow.

A sample calculation for the design case #2 at a mass flow rate of 2 mg/s is provided in appendix 3 under the section "sample calculation #1". In table 3.8, the calculated values for the four different types of thermal resistance are given.

Table 3.8: Values for different types of thermal resistances for design #2 at mass flow of 2 mg/s and T_c =600 K.

Types of thermal resistances	Value	Unit
R_{sub}	0.648	K/W
R_{const}	0.011	K/W
R_{conv}	27.21	K/W
R_{heat}	475.46	K/W

One can see that the thermal resistance due to channel constriction constitutes the least resistance to the heat flow from the heat source to the propellant. The next higher resistance comes from the silicon substrate, which is one order of magnitude larger compared to the resistance from channel constriction. As we had mentioned earlier, these two values will remain the same for this specific design #2, irrespective of the propellant mass flow rate. The convection thermal resistance constitutes the third largest thermal resistance and it is three orders of magnitude larger than the constriction thermal resistance. The bulk thermal resistance is the largest among the four types of thermal resistance for a MEMS heater chamber and this value is the same for all four design cases at a given mass flow rate. Figure 3.9 plots the total thermal resistance for all the four design cases as a function of propellant mass flow rate taking T_c=600 K and nitrogen gas as the propellant.

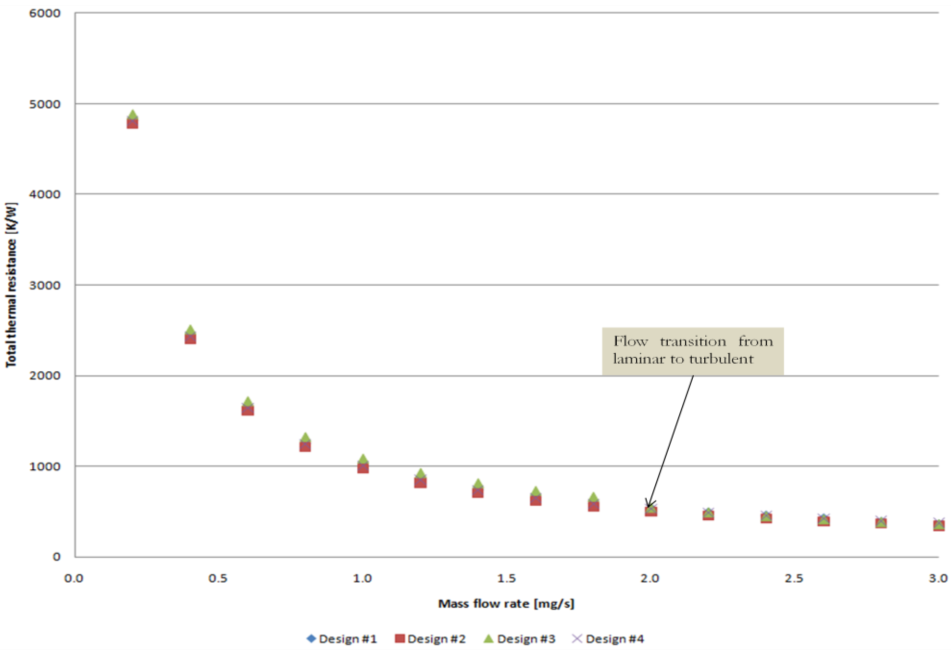

Figure 3.9: Total thermal resistance vs mass flow rate for four different chamber geometries with nitrogen as the propellant and T_C=600 K.

From figure 3.9, certain points are made clear and they are discussed below:

1) First of all, the most striking point is that the total thermal resistance for all the design cases decreases in an asymptotic manner with increasing mass flow. Also we see that there is negligible difference between the total thermal resistance values for the four design cases at a given mass flow rate. The reason for such a trend can be found in the

elaboration of the results from table 3.8 and also having a look on the relation for bulk thermal resistance (relation 3.24).

2) On careful observation, we see that the total thermal resistance for design #3 is consistently higher than those values for other designs until a mass flow rate of around 2 mg/s. Beyond this value, we observe a slight drop in the total thermal resistance for design #3 and thereafter becomes the same as the resistance values for other chamber designs. This slight drop in total thermal resistance is due to a decrease in convection thermal resistance as the heat transfer coefficient improves when the flow undergoes transition from laminar to turbulent flow regime.

To summarize the findings in section 3.5, four different heater chamber geometries having different number of channels and channel depth were considered for a comparative study of their pressure drop as a function of mass flow with and without heating and their heat transfer performances in terms of thermal resistance to the heat flow, P_{heat}. From the pressure drop results, we see that a single channel shallow design shows the highest increase in pressure drop with mass flow, while a three channel deeper design shows the lowest. Heating the fluid flow to a high chamber temperature further augments the pressure drop for all the designs. Comparing the thermal performance as a function of propellant mass flow rates, we see that all the chamber geometries display the same trend.

3.6 Heat loss from MEMS heater chamber

In equation 3.1, we had illustrated that not all input power into the system is used to heat the propellant flow as some heat will be lost to the environment. This heat loss can be through a number of mechanisms like in the form of conduction, convection or radiation. For example, we might have conduction losses through the silicon substrate to the pyrex glass wafer, radiative heat transfer from the hot chip to its surroundings and heat loss due to free convection during ambient condition testing. Most of the theory used in the sections hereafter has been taken from the work of Bejan [3.21, 3.2] and Holman [3.19].

3.6.1 Heat loss by natural convection

One of the modes of heat loss from a micro-heater chip to its environment is by free convection. This mode of heat loss gets more highlighted especially when testing at atmospheric conditions. The power loss due to natural convection follows from:

$$P = q'' A \tag{3.43}$$

where $q'' = h\Delta T = h(T_h - T_a)$, T_h the heater temperature, T_a the ambient temperature, h the natural convective heat transfer coefficient which is a function of L the characteristic dimension of the hot surface, k the thermal conductivity of ambient air and Nu the Nusselt number (table 3.9) which in turn is a function of Rayleigh number, Ra defined as:

$$Ra = \frac{g\beta L^3 (T_h - T_a)\,\mathrm{Pr}}{\gamma^2} \tag{3.44}$$

$$\beta = \frac{1}{T_f},\ T_f = \frac{T_a + T_h}{2},\ \rho = \frac{p_a}{RT_f},\ \gamma = \frac{\mu}{\rho},\ g = 9.81\ \mathrm{m/s^2},\ \mathrm{Pr} = \frac{c_p \mu}{k}$$

All properties of ambient air are determined at the film temperature, T_f defined as the average of ambient and heater temperatures. To predict the convective heat losses from a MEMS heater section, we model the top side as a horizontal hot plate with the hot surface facing upwards and the side walls of the chip as vertical hot plates as it is shown in figure 3.10. We also take constant heat flux as the thermal boundary condition. In figure 3.10, L_{ch} represents the channel length which is 2 cm for all the four chamber designs and 'W' stands for the total width of the heater geometry which varies according to the number of channels in the design (for single channel, W= 400 μm and for a three channel, W=500 μm). For the vertical side walls, standard silicon wafer thickness of 560 μm is taken as the characteristic length L (see relation 3.44) to calculate the heat losses.

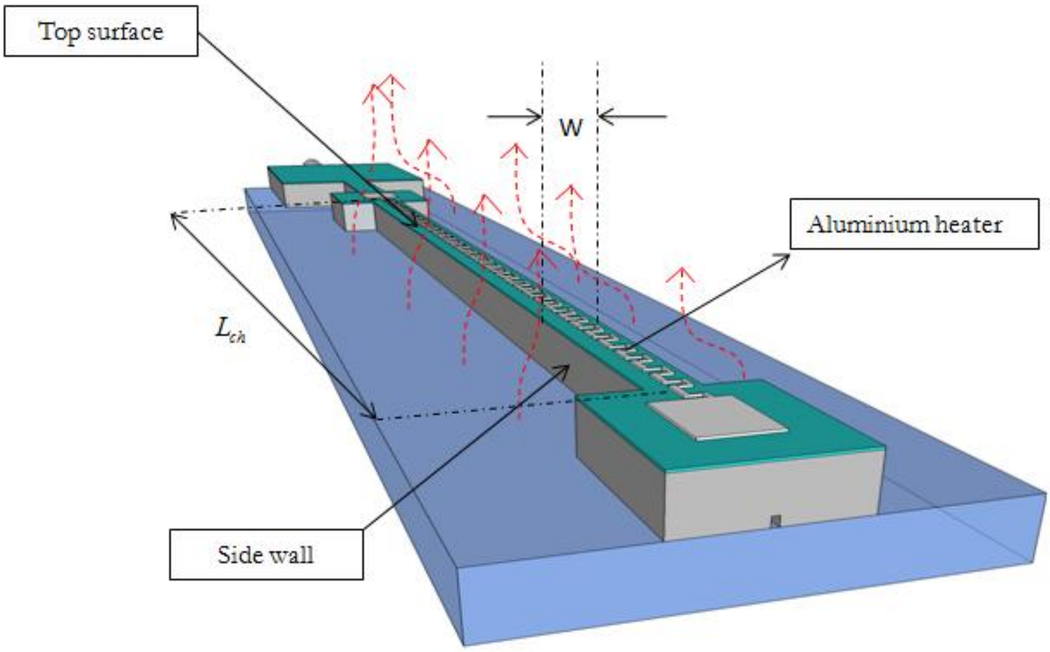

Figure 3.10: Schematic diagram showing heat loss by natural convection from a MEMS thruster.

In table 3.9, the relations for the Nusselt number are presented for both the horizontal and vertical plates.

Table 3.9: Nusselt number correlations for the heat transfer by natural convection.

Chip surface	Relation	Eq.	Ref
Top surface	Average Nusselt number, $\bar{Nu}_L = 0.13 Ra_L^{1/3}$, for $Ra_L < 2\times10^8$. Characteristic length, L from relation 3.44 is defined as L=A/P, where $A=W.L_{ch}$ and $P=2(L_{ch}+W)$.	(3.45)	[3.19]
Vertical side wall	Average Nusselt number, $\bar{Nu} = 0.68 + \dfrac{0.67 Ra^{1/4}}{\left[1+\left(0.492/\Pr\right)^{9/16}\right]^{4/9}}$, for $Ra_L < 10^9$	(3.46)	[3.19]

Figure 3.11 plots the natural convection heat losses from a three channel design as a function of heater temperature at three different ambient pressures: 1 bar corresponding to atmospheric testing conditions, 10 millibar corresponding to the minimum achievable vacuum pressure using the testing facility at the SSE cleanroom and an additional vacuum pressure of 50 millibar.

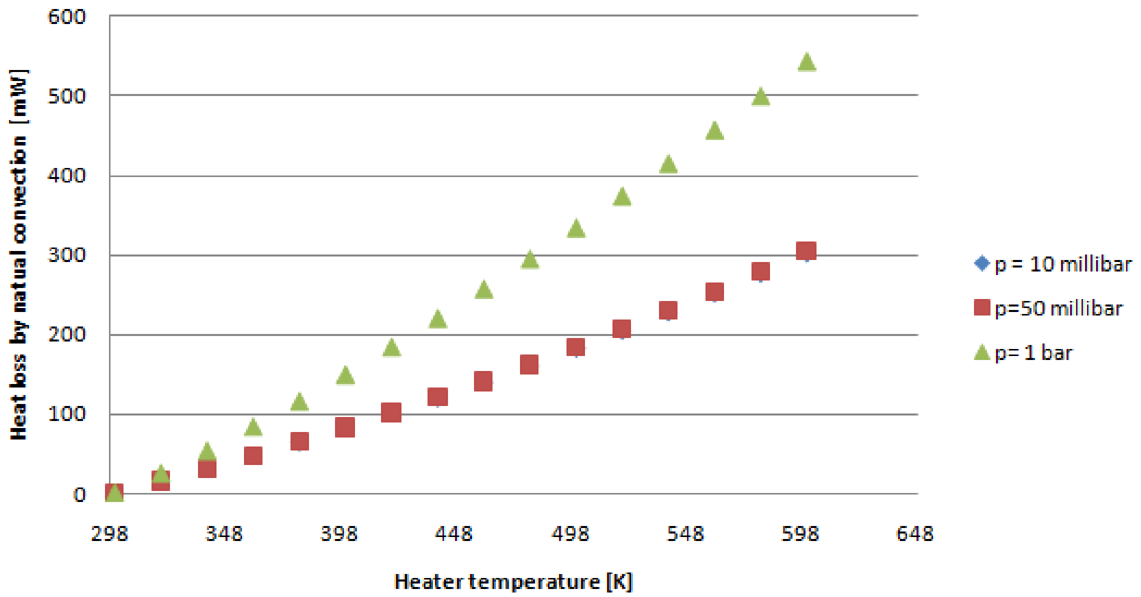

Figure 3.11: Heat loss by natural convection from a three channel design as a function of heater temperature at three different ambient pressures.

From figure 3.11, it is made clear that:

1) The heat loss from the heater chip by natural convection increases with the heater temperature. The trend is not linear but can be fitted with a polynomial of 2nd order.
2) The difference between the heat loss at near vacuum conditions of 10 and 50 millibar is negligible. But the difference between the heat loss at ambient and vacuum test conditions is striking which increases with the heater temperature. At the maximum heater temperature of 600 K, this difference is roughly about 79 %. Therefore, inorder to heat a maximum nitrogen gas flow rate of 3 mg/s to a maximum chamber temperature of 600 K, the total input electric power should be 1.3 W (=1 W for the heating power + 0.3 W accounting for the heat losses by natural convection alone) when testing at vacuum conditions.

Similarly, the heat loss from a single channel design was calculated as a function of heater temperature and the difference in convective heat losses from that of a three channel heater chamber design was found to be negligible.

3.6.2 Heat loss by radiation

Thermal radiation is a form of electromagnetic radiation that a body emits as a result of its temperature. This radiative heat loss is a function of the fourth power of heater surface temperature. Since silicon is a very good thermal conductor, we assume it to be at a constant temperature as a first approximation inorder to simplify the modeling of radiation heat loss. For a given heater surface area, the net radiative heat loss as a function of its temperature can be calculated using the relation given below:

$$P = F_{h\text{->}Ambient} A_h \varepsilon \sigma (T_h^4 - T_a^4) \quad (3.47)$$

where A_h is the surface area of the hot radiating surface, σ the Stefan Boltzmann constant (=5.67E-8 $W/m^2/K^4$), T_h the heater temperature or the chip temperature, T_a the ambient temperature, $F_{h\text{->}ambient}$ the view factor from the heater to its ambient and ε the surface emissivity. A value of 0.09 is taken for the surface emissivity of highly polished aluminium [3.19] whereas the surface emissivity of a highly polished surface such as silicon is about 0.1 [3.20]. To model the radiative heat loss from the top surface of the heater chip to the ambient is relatively easy since the view factor between the aluminium heater layer and the ambient can be taken as 1. To calculate the view factor between the silicon side walls and the ambient, the problem can be modeled as shown in table 3.10 as two rectangular plate's perpendicular to each other with a common edge. The view factor between the silicon side wall and the ambient was calculated to be 0.58.

Table 3.10: View factor between the vertical side wall and ambient.

View factor	Schematic diagram	View factor values	Ref.
View factor for the vertical side wall.	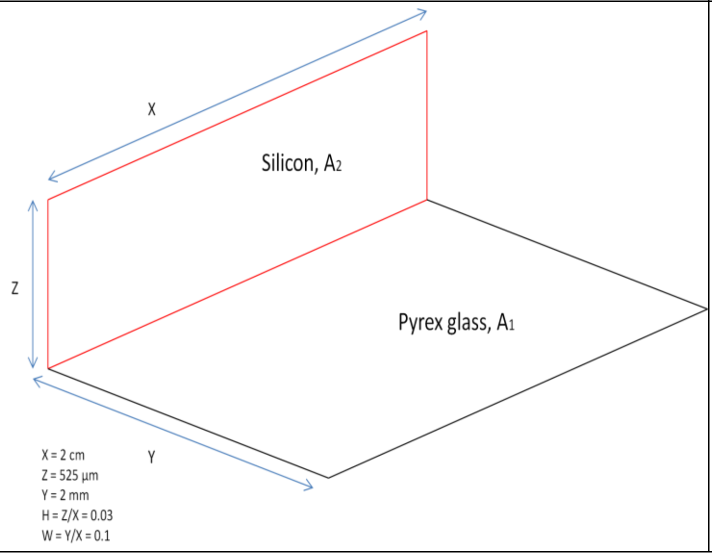	$F_{pyrex\text{->}Si}$= 0.13 $F_{pyrex\text{->}ambient}$= 0.87 $F_{Si\text{->}pyrex}$ =0.42 $F_{Si\text{->}ambient}$ =0.58	[3.19]

Once the view factor is calculated, the next step is to develop a thermal network for the radiative heat transfer analysis between the silicon side wall and the ambient, as shown in figure 3.12. As shown in the figure, node 1 stands for the silicon side wall, node 2 for the pyrex glass and node 3 for the ambient. For the simplification of the modelling, the temperature of the pyrex glass T_2 is taken to be equal to that of the ambient temperature T_3 (=298 K) at all cases of heater temperature. The surface resistance to radiative heat transfer for atmosphere $(1\text{-}\varepsilon_3)/(\varepsilon_3 A_3)$ can be treated as negligible due to its large surface area compared to the small chip size.

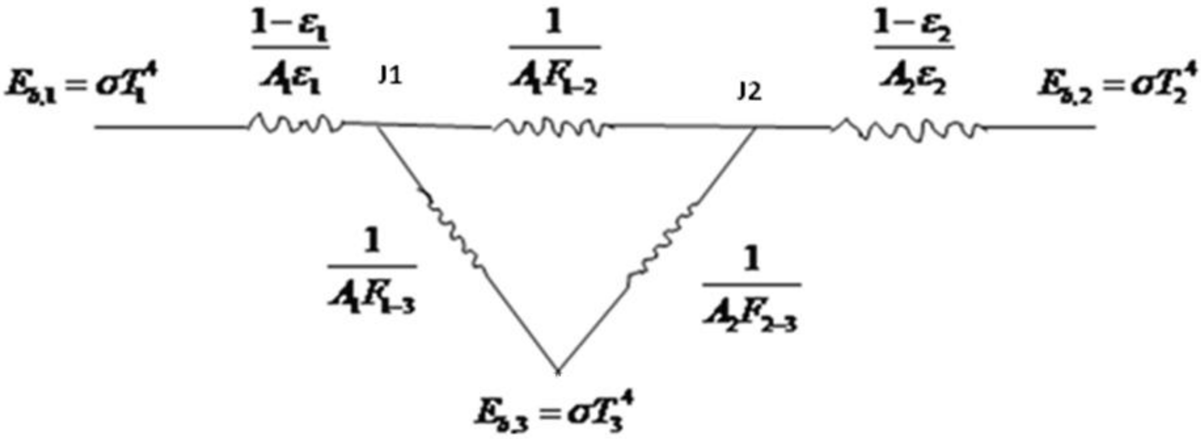

Figure 3.12: Thermal network for radiative heat loss modelling from the silicon side walls to the ambient.

In figure 3.13, the total radiative heat loss from a MEMS heater chip having a 3 channel design is plotted as a function of heater temperature.

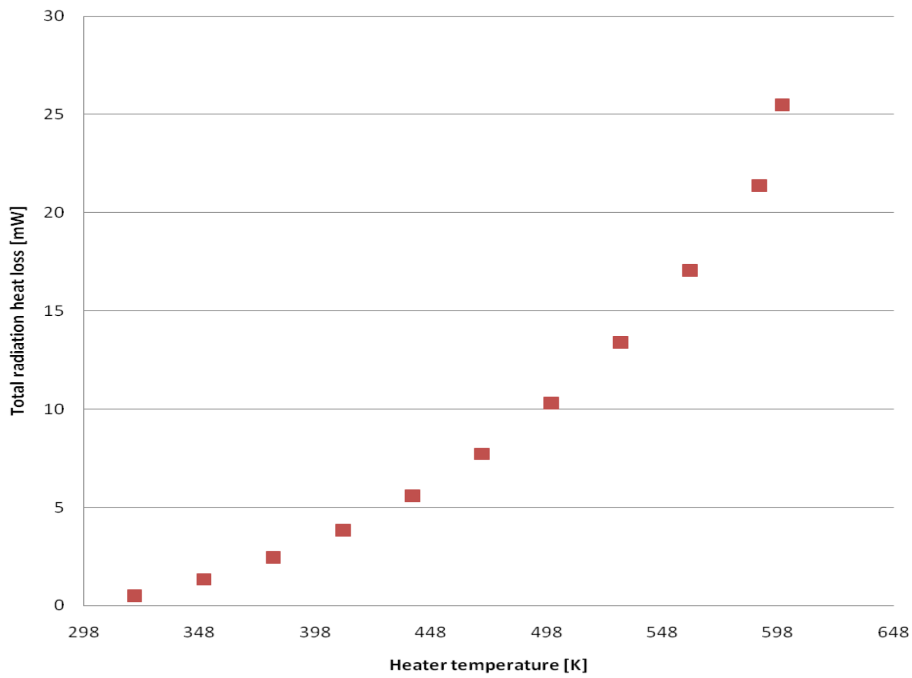

Figure 3.13: Radiative heat loss for a three channel design as a function of heater temperature.

From figure 3.13, it can be seen that the radiation heat loss increases with temperature but in an asymptotic manner (to the 4th power of heater temperature). By comparing the results in figure 3.11 and 3.13, it can be concluded that the natural convection losses play a predominant role in heat loss mechanism from a MEMS heater chip to its ambient. At the maximum heater temperature of 600 K, the net radiative heat loss is 12 times lower than the heat loss by natural convection.

3.6.3 Heat loss by conduction

For the heat transfer analysis in section 3.5, the pyrex glass was treated as a thermally insulating layer due to its very low thermal conductivity. But in reality, conduction losses can occur through this thin layer of Pyrex (standard thickness of 500 μm [3.27]) when a high temperature gradient is applied across its thickness. To calculate the one-dimensional heat loss by conduction, we model the Pyrex glass as a slab with a temperature difference of ΔT ($=T_h-T_a$) applied across its thickness of L as shown in figure 3.14. Thus, the conduction loss Q_{cond} can be calculated as:

$$Q_{cond} = kA\frac{\Delta T}{L} \tag{3.48}$$

where $\Delta T=T_h-T_a$, T_h the heater temperature on one side of the glass layer, T_a the ambient temperature on the other side (=298 K) and 'A' the contact area between the hot silicon chip and the Pyrex glass ($A=WL_{ch}-NW_{ch}L_{ch}$). Calculated value of conduction heat loss through Pyrex glass at a maximum heater temperature of 600 K was found to be 5.1 W. Comparing this value with that of convection and radiation losses, it is very clear that the conduction loss is the most predominant form of heat loss mechanism for a MEMS heater chamber.

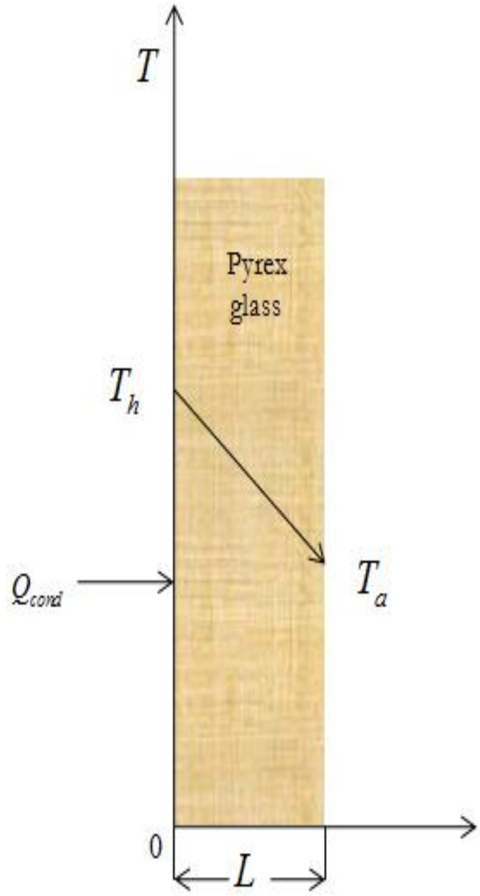

Figure 3.14: One-dimensional heat transfer by conduction [3.19] ↑.

3.7 Conclusion

The geometry of a MEMS heater chamber was presented at the beginning of this chapter. With the current concept using an aluminium resistive heater, it was found that a heater temperature of 600 K can be achieved with an electric input power of roughly 1 W. In the propellant heating power analysis, it was concluded that a maximum nitrogen gas flow rate of 3 mg/s can be heated to the maximum required chamber temperature of 600 K within the constraint of total electric input power of 1 W under ideal heating conditions. Four different chamber geometries were considered to carry out a performance study in terms of pressure drop at both cold and hot gas mode. The sharp increase in pressure drop with increasing propellant mass flow rate at the micro-fluidic scale was highlighted in the results, especially in the case of single channel design having square cross-sections. It was concluded that such a trend was due to compressibility of the flow and its transition from laminar to turbulent flow regime. The total thermal resistance to the heat flow for all the heater chamber geometries was found to be within 5% at a given propellant mass flow rate. Out of the three heat loss mechanisms for a MEMS heater chamber, conduction heat loss was found to be the most predominant form and it was found to be one order of magnitude larger than the convection and radiation heat losses at the maximum heater temperature of 600 K. As a result, to heat a nitrogen gas flow rate of 3 mg/s to the maximum chamber temperature of 600 K, the total input electric power should be 6.5 W when testing at vacuum conditions.

3.8 Reference

[3.1] Gian Luca Morini; Laminar to turbulent flow transition in micro-channels.
[3.2] Adrian Bejan; Heat transfer; Wiley.
[3.3] Roy W. Knight, Donald J. Hall, John S. Goodling, Richard C. Jaeger; Heat sink Optimization with application to micro-channels; IEEE transactions of components, Hybrids, and manufacturing technology, Vol 15, No. 5, October 1992.
[3.4] Todd M. Harms, Michael J. Kazmierczak, Frank M. Gerner; Developing convective heat Transfer in deep rectangular micro-channels; International journal of heat and fluid flow; Vol 20, issue 2, april 1999, 149-157.
[3.5] Barry Zandbergen; Thermal rocket propulsion [Lecture notes].
[3.6] R.J. Phillips, L.J. Missaggia, J,N, Walpole, Z.L. Liau; Microchannel heat sinks for two Dimensional high power-density diode laser arrays; IEEE J. Quantum Electron. 25 (9) (1989) 1988-1992.
[3.7] www.webbook.nist.gov/chemistry
[3.8] Chandra Prakash; Thermal conductivity variation of silicon with temperature; Microelectron. Reliability, Vol 18, p 333. Pergamon press. Printed in Great Britaain.
[3.9] E.W. Lemmon and R.T. Jacobsen; Viscosity and thermal conductivity equations for Nitrogen, oxygen, argon and air; International journal of thermophysics, Vol 25, No.1, January 2004.
[3.10] Wen Zhimin and Choo Kok Fah; The optimum thermal design of microchannel heat Sinks; 1997 IEEE/CPMT Electronic Packaging technology conference.
[3.11] Pradeep Dixit, Nay Lin, Jianmin Miao, Wai Kwan Wong, Teo Kiat Choon; Silicon Nanopillars based 3D stacked microchannel heat sinks concept for enhanced heat Dissipation applications in MEMS packaging; Sensors and actuators A 141 (2008) 685-694.
[3.12] G.A. Quadir, Anvar Mydin, K.N. Seetharamu; Analysis of microchannel heat exchangers Using FEM; International journal of numerical methods for heat and fluid flow; Vol 11 No. 1, 2001, pp 59-75.
[3.13] Weilin Qu and Issam Mudawar; Thermal design methodology for high-heat-flux single Phase and two-phase micro-channel heat sinks; IEEE transactions on components and Packing technologies, Vol 26, No 3, September 2003.
[3.14] Yoav Peles, Ali Kosar, Chandan Mishra, Chih-Jung Kuo, Brandon Schneider; Forced Convective heat transfer across a pin fin micro heat sink; International journal of Heat and mass transfer 48 (2005) 3615-3627.
[3.15] S.V. Garimella and Vishal Singhal; Single phase flow and heat transport and pumping Considerations in microchannel heat sinks; Heat transfer engineering 25 (1): 15-25,2004.
[3.16] Gnielinski, V., New equations for heat and mass transfer in turbulent pipe and channel Flow, International chemical engineering; Vol 16, pp. 359-368, 1976.
[3.17] Puzhen Gao, Stephane Le Person, Michel Favre-Marinet; Scale effects on hydro-dynamic and heat transfer in two-dimensional mini and micro-channels; International journal of thermal sciences 41 (2002) 1017-1027.
[3.18] O. Barlay Ergu, O.N. Sara, S. Yapici, M.E. Arzutug; Pressure drop and point mass Transfer in a rectangular micro-channel; International communications in heat and mass Transfer 36 (2009) 618-623.
[3.19] Heat Transfer; J.P. Holman (Ninth edition)
[3.20] Robert. L.. Bayt, Analysis, fabrication and testing of a MEMS based micro-propulsion system; PhD thesis; MIT.
[3.21] A. Bejan; Convection heat transfer. New York: Wiley, pp. 75-82.
[3.22] Technical communication with Japer Boumeester.

[3.23] K.J.A Rycek, L. Bisi, it. B.T.C. Zandbergen (MSc); Preliminary performance characterization of a 1N laboratory resistojet DUR-1. IAC-05-C.4.4.01.
[3.24] R. Tijsterman and B.T.C. Zandbergen; Performance analysis and development of a micro-resistojet (draft).
[3.25] R.A. Ferreira; Development and testing of a microresistojet using water as propellant; MSc thesis, TUDelft.
[3.26] I. Tiselj, G. Hetsroni, B. Mavko, A. Mosyak, E. Pogrebnyak, Z. Segal; Effect of axial Conduction on heat transfer in micro-channels; International journal of heat and mass Transfer 47 (2004) 2552-2565.
[3.27] www.schott.com/borofloat.
[3.28] http://www.lmnoeng.com/Flow/GasViscosity.htm
[3.29] K. Vijayalaksmi, K.B. Anoop, H.E. Patel, P.V. Harikrishna, T. Sundararajan, Sarit K. Das; Effects of compressibility and transition to turbulence on flow through microchannels; International Journal of Heat and Mass transfer 52 (2009) 2196-2204.
[3.30] Wahib Owhaib and Bjorn Palm; Experimental investigation of single –phase convective heat transfer in circular microchannels; Experimental thermal and fluid science 28 (2004) 105-110.
[3.31] G.H. Tang, Zhuo Li, Y.L. He, W.Q. Tao; Experimental study of compressibility, roughness and rarefaction influences on microchannel flow; International Journal of heat and mass transfer 50 (2007) 2282-2295.
[3.32] Frank P. Incoprera and David P. DeWitt, Theodore L Bergman, Adrienne S Lavine; Introduction to heat transfer; 5th edition.
[3.33] Ali Kosar; Effect of substrate thickness and material on heat transfer in microchannel heat sinks; International Journal of thermal sciences 49 (2010) 635-642.
[3.34] Fox and McDonald; Introduction to fluid mechanics; Fifth edition.

Chapter 4

FABRICATION OF MICRO-THRUSTER

After the previous chapters on micro-nozzle design analysis and MEMS heater chamber design based on the requirements, this chapter takes you through the fabrication procedure that needs to be followed to produce a micro-thruster using MEMS technology. The production process, i.e. from the process flow design to the final packaged device, was performed inside the cleanroom of class 100 and MEMS laboratory at the Delft Institute of Microsystems and Nanoelectronics (DIMES) by Marko Mihalovic. At the very beginning of the fabrication phase, it was jointly decided that the author shall be allowed to witness and record the fabrication process. Therefore, inorder to enter the clean room of class 100 wh, the author had to take a 2-day safety course which was conducted by Charles de Boer in July 2010. To assist Marko with the fabrication, a short course on wafer cleaning (this process will be discussed in section 4.1) was also undertaken under the guidance of Silvana Milosavljevic. Meanwhile, whatever fabrication steps that were performed in a day including any anomalies, where recorded in a cleanroom logbook that was assigned specific to our fabrication sequence. The log-book can be accessed only within the cleanroom.

This chapter on fabrication is divided into four sections. In section 4.1, the fabrication sequence to be followed inorder to produce a micro-thruster using MEMS technology is explained coupled with illustrations using figures. The same fabrication sequence is to be followed for all the thruster chips except for differences in certain steps like etching time and the masks used depending on the heater chamber geometry and the nozzle throat size. Towards the end of this section, the device packaging (mechanical interface) and wire bonding steps (electrical interface) are presented. They were performed in MEMS laboratory which is located outside the clearoom 100. In section 4.2, all variants of MEMS thruster chips fabricated are presented and discussed along with some Scanning Electron Microscope (SEM) images to verify the dimensions produced in section 4.3. Finally we conclude this chapter in section 4.4.

4.1 Fabrication of device

A flowchart must be prepared before the start of any fabrication process using MEMS technology. The flowchart was prepared by Marko Mihailovic and was agreed to by Prof Lina Sarro. In table 4.1 is shown the flowchart for the MEMS fabrication of micro-thrusters.

Table 4.1: Flowchart for MEMS fabrication process of a micro-thruster.

Step #	Fabrication sequence	Purpose of fabrication step
Starting material	The fabrication of micro-thruster begins with double-side polished silicon wafers. The wafers were p-type, <100> crystallographic orientation, 550 μm thick and 100 mm in diameter	-
Step 1	Thermal oxidation of silicon (500 nm thickness)	To protect the bonding surface and to provide electrical insulation
Step 2	Patterning and etching of alignment marks	To provide alignment marks on the wafer
Step 3	Metallization (Sputter deposition of aluminium (with 1 % Si) - thickness of 675 nm)	To provide the heater material
Step 4	Lithography with mask 1 followed by wet etching of aluminium	To pattern the heater along with the dicing lines
Step 5	Plasma Enhanced Chemical Vapor Deposition (PECVD) silicon oxide deposition on both sides of wafer to thickness of 6 μm	For the protection of aluminium on top side + mask for Deep Reactive Ion Etching (DRIE) of silicon on back side
Step 6	Lithography with mask 2 followed by dry etching of silicon oxide layer on the back side	For patterning and etching 220 μm of etch-through area- first part
Step 7	DRIE to a depth of 220 μm on the back side	
Step 8	Lithography using spray coating with mask 3 followed by dry etching of silicon oxide in the back side	For patterning and etching of 300 μm of etch-through area plus the inlet area
Step 9	DRIE to a depth of 300 μm on the back side of wafer	
Step 10	Lithography using spray coating with mask 4 followed by dry etching of silicon oxide on the back side of the wafer	For patterning and etching of 50 μm of etch through inlet + channel
Step 11	DRIE to a depth of 50 μm on the back side of the wafer	
Step 12	Wet stripping of silicon oxide layer from the bonding surface. This process is called unwrapping	To expose the bonding surface
Step 13	Anodic bonding of the silicon wafer to a glass wafer	To seal the micro-fluidic channel
Step 14	Dry stripping of silicon oxide on the front side to access the Aluminium heater layer	To expose the bond pads
Step 15	Dicing along the saw-lines that were included in mask 1.	To seperate the chips fabricated on a single wafer
Step 16	Packaging which includes gluing the needle to the chip and the chip to the Printed Circuit Board (PCB) and wire-bonding.	Final product

Four masks are required for pattern transfer at different stages of fabrication sequence. Table 4.2 contains the mask number along with its designation. They can be accessed inside the cleanroom under the mask-set designated as LR 1658, which is specific to our fabrication sequence.

Table 4.2: Mask number and its designation.

Mask number	Mask designation as in Box LR 1658
Mask_1	METAL
Mask_2	ET
Mask_3	ET_IN
Mask_4	ET_IN_CH

In the following paragraphs, the various steps from table 4.1 are explained in detail.

Starting material

The micro-thruster was fabricated using a four mask process, starting with five double-side polished silicon wafers as process wafers and 5 single-side polished wafers as test wafers. Process wafers are the ones used for fabricating the actual device, while the test wafers are used to know about certain test parameters like for example, the time required to etch a certain channel depth. All the wafers were p-type single crystal silicon wafers with a crystallographic orientation of <100> , 100 mm in diameter and standard wafer thickness of 550 µm (see figure 4.1). But we needed to know the exact wafer thickness to determine the etch rate; hence this parameter was measured and was found to be 560 µm.

Figure 4.1: P-type single side polished silicon wafers.

Step 1

A 500 nm thick thermal silicon oxide layer was grown on both sides of the wafer to protect the wafer surface during processing (see figure 4.2).

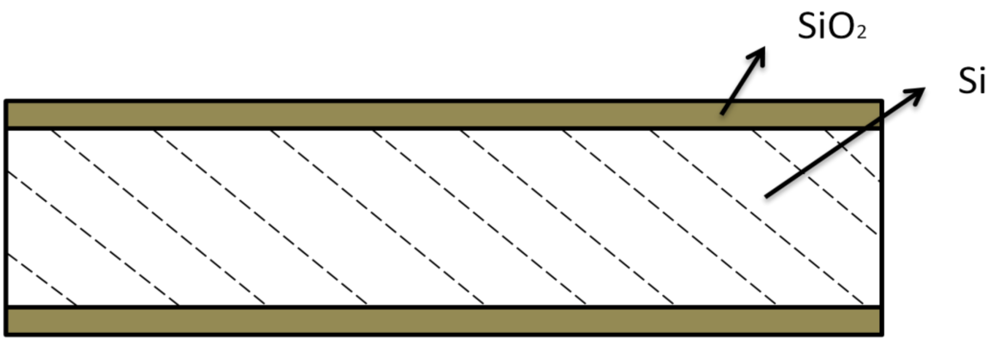

Figure 4.2: A 500 nm thick thermal silicon oxide on both sides of silicon wafer.

Step 2

The thermal silicon oxide layer was stripped off from the top side of wafer. After this step, alignment marks which are crucial for aligning the wafer with lithography masks were then etched through the silicon oxide layer and into the silicon. Then the wafers were cleaned in 99% nitric acid HNO_3 solution for 10 minutes to remove any organic contaminants, followed by 5 minutes of cleaning in distilled water, followed by 5 minutes of rinsing in 69.5% HNO_3 solution to remove any metal contaminants and 5 minutes of further rinsing in the DI water. This cleaning process is termed as "silicon sequence" . The thermal silicon oxide layer thickness was checked on the bottom side of wafer using Leitz interferometer system and it was found to be roughly 616.7 nm.

Steps 3

On the top side of the wafer, aluminium layer of 675 nm was deposited at 350 °C in the Trikon Sigma sputter-coater.

Step 4

To pattern this aluminium layer inorder to form the heater, the wafers were first treated with the Hexa-Di-Methyl-Solizane (HMDS) vapor to improve the adhesion of photoresist onto the wafer (this step is always performed in all forthcoming lithography steps). It was then spin coated with a photoresist (SPR 3012) to a thickness of 1.4 µm which is a standard thickness. Then the heater pattern was transferred to the photoresist layer using mask 1 by exposing to ultra-violet radiation in the contact aligner. Once the exposure was done, it was developed in an automatic coating/development station.

Aluminium layer was then patterned by wet etching process in H_3PO_4 at a temperature of 35 °C. To etch a depth of 675 nm in the aluminium layer which is a standard value, total etch time was calculated to be 5 minutes including 30 seconds of over-etching, based on the etch rate data of 1500 Å/min, previously measured in DIMES cleanroom (see figure 4.3 and 4.4). This step was followed by 30 seconds of poly-silicon etching in HNO_3/HF solution to remove any poly-silicon grains originating from the 1% Si in aluminium. Once the etching of aluminium layer was done, the remaining photoresist was removed by treating the wafer in acetone solution at 40 °C for about 1 minute. As the last process as part of step 4, the wafers were cleaned, this time avoiding the cleaning step in 69.5% HNO_3 solution due to presence of aluminium layer on one side of wafer. This cleaning process is termed as "metal sequence".

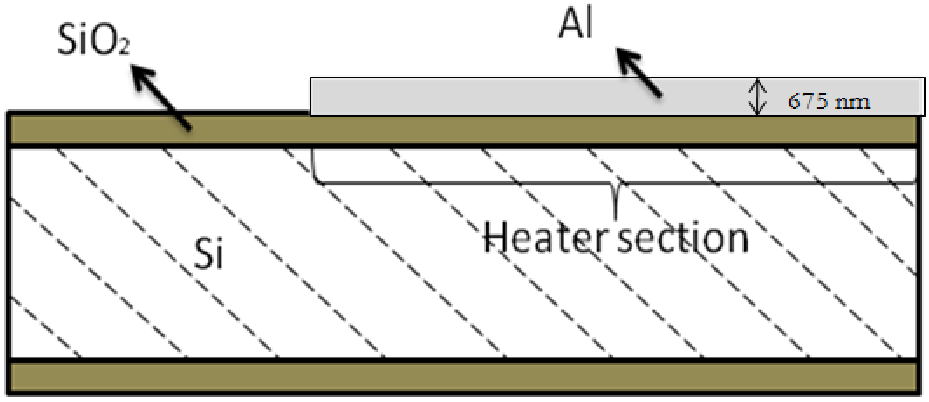

Figure 4.3: Aluminium layer of 675 mm thickness deposited on the top side of silicon wafer.

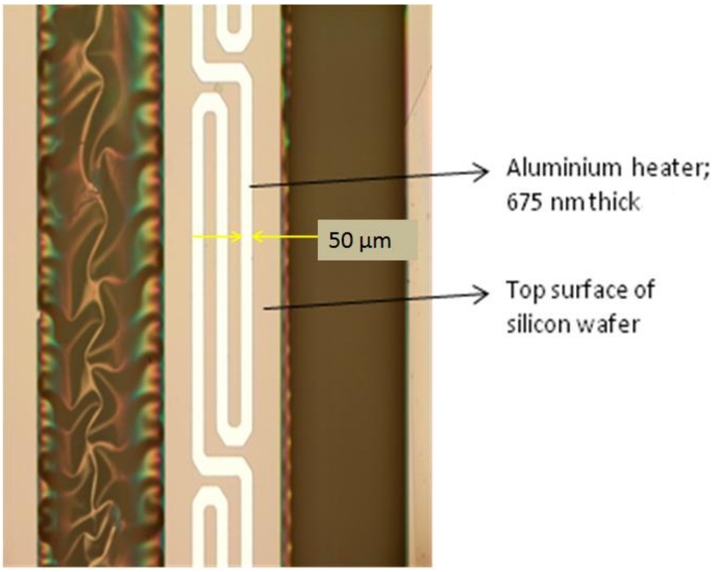

Figure 4.4: Optical image showing the patterned aluminium heater layer on top of silicon wafer.

The portion of the image shown in figure 4.4 in brown color is the etch-through area.

Step 5

A 6 µm thick PECVD silicon oxide layer was then deposited on both the top and bottom side of wafers (see figure 4.5). This PECVD silicon oxide layer thickness was later measured and was found to be slightly thicker than 6 µm with a maximum value of 6.44 µm.

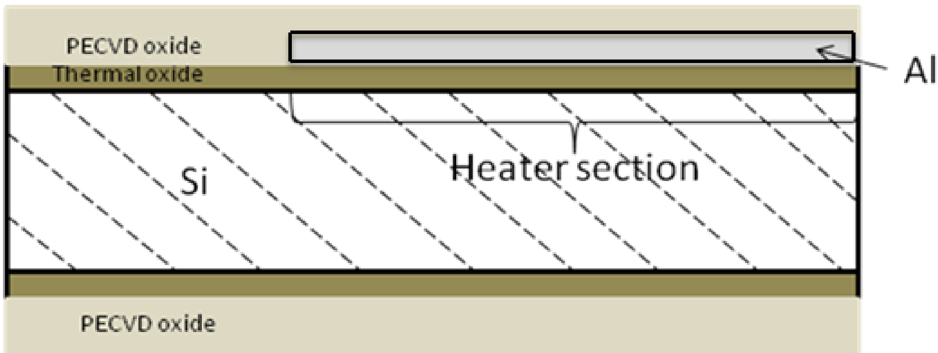

Figure 4.5: PECVD silicon oxide deposition on both sides of wafer.

Step 6 & 7

The back side of the wafer was coated with photoresist with a thickness of 3 µm and was exposed and developed. This was followed by the dry etching of silicon oxide layer in Drytek etcher machine using silicon oxide etching recipe for 21 minutes at a power of 200 W. The thickness of silicon oxide layer was later measured after the RIE step only to confirm that it was completely removed. The photoresist layer was later removed by oxygen plasma washing using the PVA Tepla machine. After removing the photo resist, wafer was cleaned again using the "metal sequence".

Now the total wafer thickness must be equal to etch depth of the mask 2 plus the etch depth using mask 3 (i.e. 300 µm) and etch depth due to mask 4 (i.e. 50 µm). From the measured total wafer thickness of 560 µm, the etch depth for mask 2 was calculated to be:

$$d1 = 560 - 50 - 300 = 210\ \mu m.$$

An etch rate of 6 µm/min was determined by performing etching in one of the test wafers in Adixen machine for 10 minutes. Therefore, to etch a depth of 220 µm from the bottom side of wafer (+10 µm to be sure), a total etching time of 36 minutes was required including an additional one minute for etching 6 µm of silicon oxide mask. The etched depth was later measured using Dektak profilometer both at the centre (217 µm) and a bit far away from the centre of wafer (213.5 µm) (see figure 4.6).

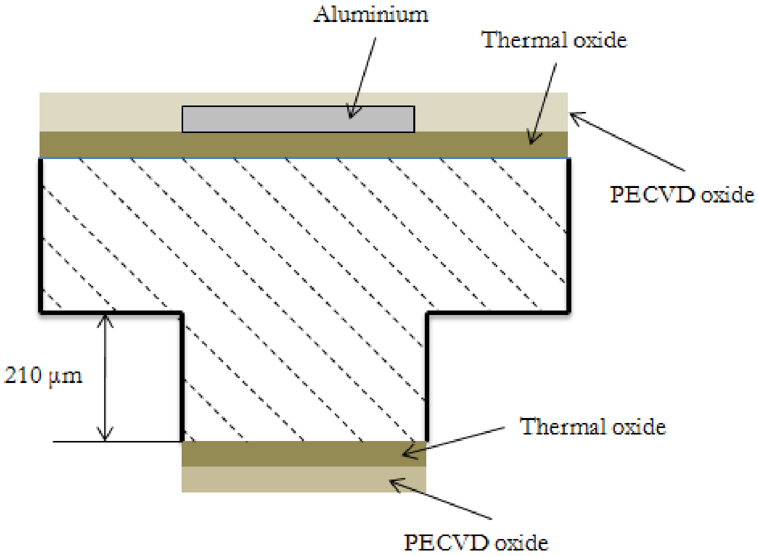

Figure 4.6: 210 µm DRIE etch through [side-view cross-section]

<u>Step 8 & 9</u>

To etch a depth of 300 µm for the inlet cavity together with further etching of the etch-through cavity at the bottom side of wafer using mask 3, the wafer is then spray coated with photoresist followed by baking at 115 ^{o}C for hardening the photoresist.. Because of the high topography, spin-coating technique cannot completely coat the entire wafer; hence the spray-coating technique was used. Once the spray coating was done, the wafers were exposed using mask 3 for a time of 60 seconds and later on manually developed using AZ400K as the developer (ratio of 1:2; 2 parts of water)

The masking PECVD silicon oxide layer on the back side of the wafer was etched in DryTek machine using the same recipe as in the previous patterning step. After removing the photoresist using TEPLA, the wafers were cleaned in metal line and etched in Adixen etcher machine for 50 minutes to create a 300 µm etch depth for the inlet. The wafers were again cleaned in metal sequence (see figure 4.7).

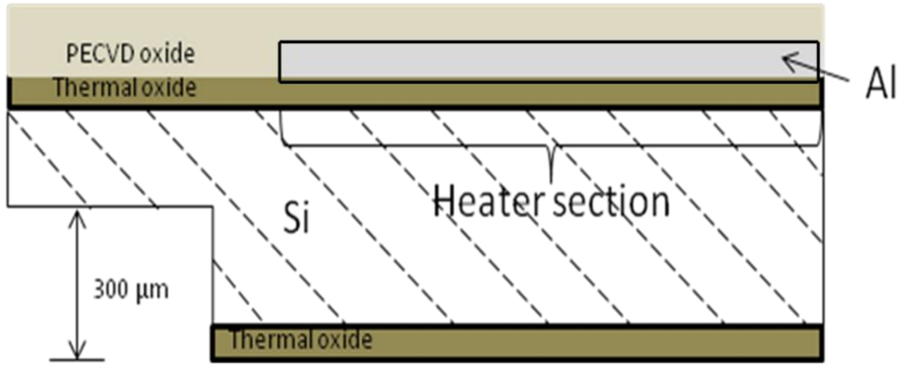

Figure 4.7: 300 µm DRIE etch at the inlet.

Step 10 & 11

To etch the micro-fluidic channel on the bottom side of wafer, first the wafer is spray coated with photoresist. To determine the etch rate for a micro-channel dimension of 50 µm, a test wafer is applied with a photoresist and is exposed and developed using mask 4. Mask thickness was found to be approximalty 6.40 µm. After performing etching for 10 minutes in the Adixen machine, the etch depth together with the mask was found to be 34.5 µm including 6 microns of thermal silicon oxide layer. Therefore the etch rate for the fluidic channel was calculated to be 2.85 µm/min (= (34.5 - 6)/10 µm/min). Therefore to etch a channel of depth 50 µm (see figure 4.8), a total etching time of 19 minutes was needed. This etching process was done in Adixen using "aspect-ratio independent" etching recipe.

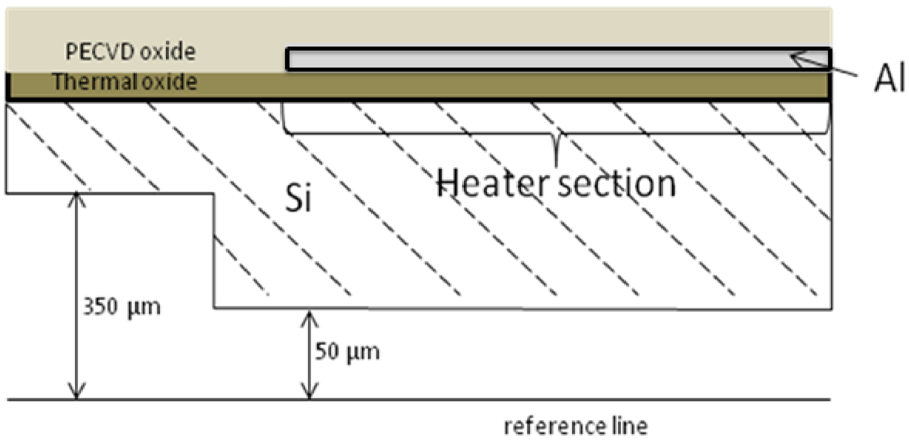

Figure 4.8: 50 µm DRIE of micro-fluidic channel.

After this etching step, the inlet hole was 350 µm deep and the etch through area was fully done.

Step 12, 13 & 14

Then the protective silicon oxide layer on the bottom side of wafer was "unwrapped" using Buffered HydroFlouric acid (BHF) solution. Once the bottom side of wafer was clean from silicon oxide layer, it was anodically bonded to a BOROFLOAT glass wafer in EVG machine at temperature of 400 ^{0}C and voltage of 1000 V, for 1 hour (figure 4.9). Once the anodic bonding was done, silicon oxide on the top side of wafer was measured and 800 nm was found to be the thickness of silicon oxide on top of aluminium. This was removed by dry etching of silicon oxide (see figure 4.10).

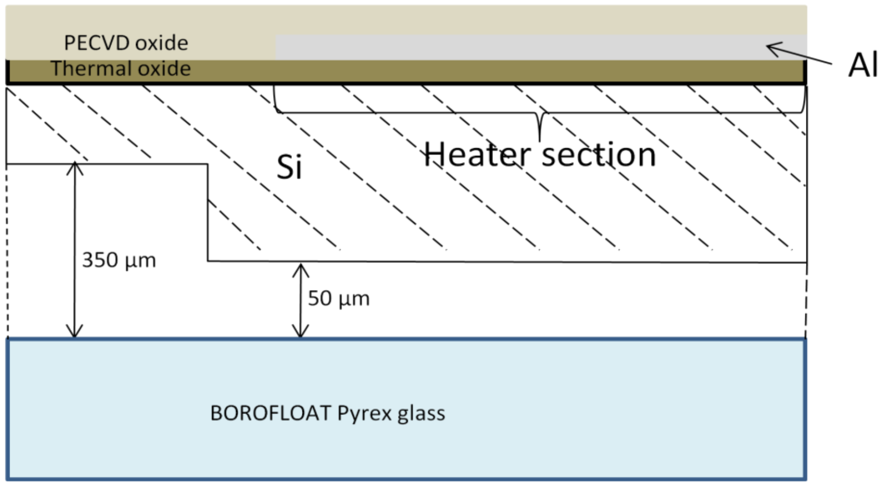

Figure 4.9: Stripping of protective silicon oxide layer on the bonding surface and anodic bonding of processed silicon wafer to a Pyrex glass layer.

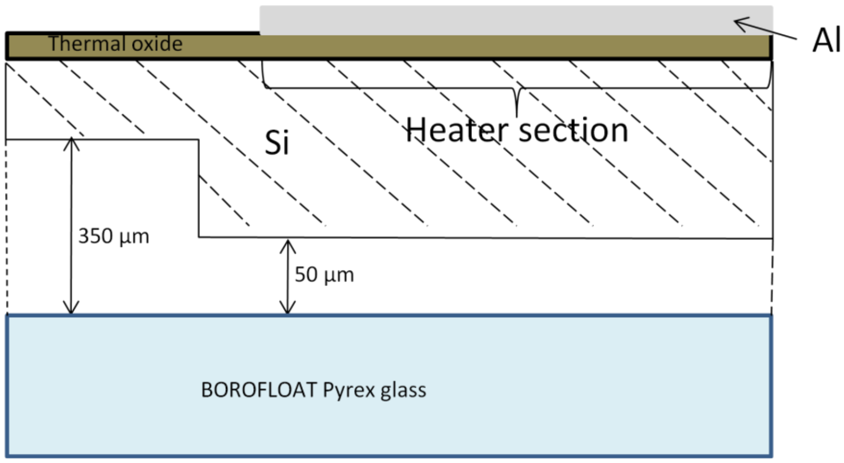

Figure 4.10: Stripping of protective silicon oxide layer on the aluminium heater.

<u>Step 15</u>

Before dicing of the chips, the whole wafer was deposited with a layer of photoresist in order to prevent the aluminium layer from peeling off during dicing. This was the last fabrication step performed inside the cleanroom 100 facility.

In order to proceed with the further packaging, first the whole wafer had to be diced along the dicing line. This dicing line was transferred to the wafer while using the mask 1 in step 4. The dicing step was performed by Loek Steenweg who was the technician in charge. Figure 4.11 shows the devices after dicing.

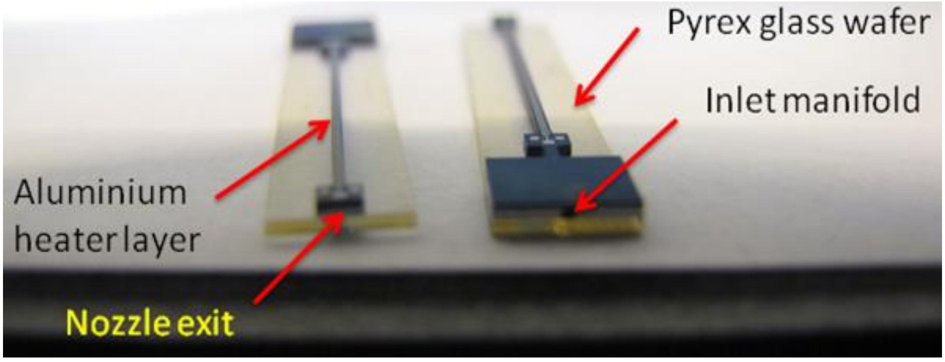

Figure 4.11: Diced MEMS micro-thruster chip with no silicon islands.

Step 16

The diced chips were then glued on to a Printed Circuit Board (PCB) with a special glue made by mixing ARALDITE AV 138M and HARENER HV 998 in the proportion 1:4 (mass ratio). The glue was selected for its 1) temperature resistance upto 120 °C and 2) low outgassing property. Also the DIMES had prior experience in handling with such epoxy materials. The same epoxy mix was used to glue the needle into the inlet manifold of the chip. The tip of the needle that goes into the inlet manifold of the thruster chip was first cleaned with acetone. Once after the needle tip was pushed into the full length of inlet manifold, the mixed epoxy was applied around the periphery, at the point where the needle first touches the chip. Care was taken not to use excess adhesive as there were chances for the glue to seep into the inlet manifold and block the fluidic passage. You would have noticed that the maximum temperature which the glue can resist is 393 K whereas the maximum heater temperature that we aim for is 600 K. Hence inorder to prevent the glue from disintegrating at high temperatures, the inlet manifold was kept away from the main heater section by a distance of 1 mm in all the designs.

Now with the needle glued to the chip and the chip glued to the PCB, the next step was to cure the epoxive bonding. Curing was done at a temperature of 80 °C for 15 minutes in an oven at the MEMS laboratory.

After curing of the epoxive bonding, wire bonding (electrical interface) was performed with aluminium wires, between the aluminium contact pads on the chip and the gold pads on the PCB. This step was performed by Loek Steenweg, the technician at DIMES specific for this job. Figure 4.12 shows the schematic diagram for wire-bonding of MEMS thruster chip with no silicon islands while figure 4.13 shows that for MEMS thruster chips with silicon islands.

For the first time, we introduce the concept of silicon islands. Basically, they are fabricated along with the main thruster chip body for 2 purposes: 1) for providing additional structural integrity while handling the thruster chips made using brittle material like silicon and 2) for simplifying the electrical connections between the aluminium heater layer and the gold pads on the PCB. On the other hand, those silicon islands are independent structures that neither takes part in the propellant flow nor in the heat transfer.

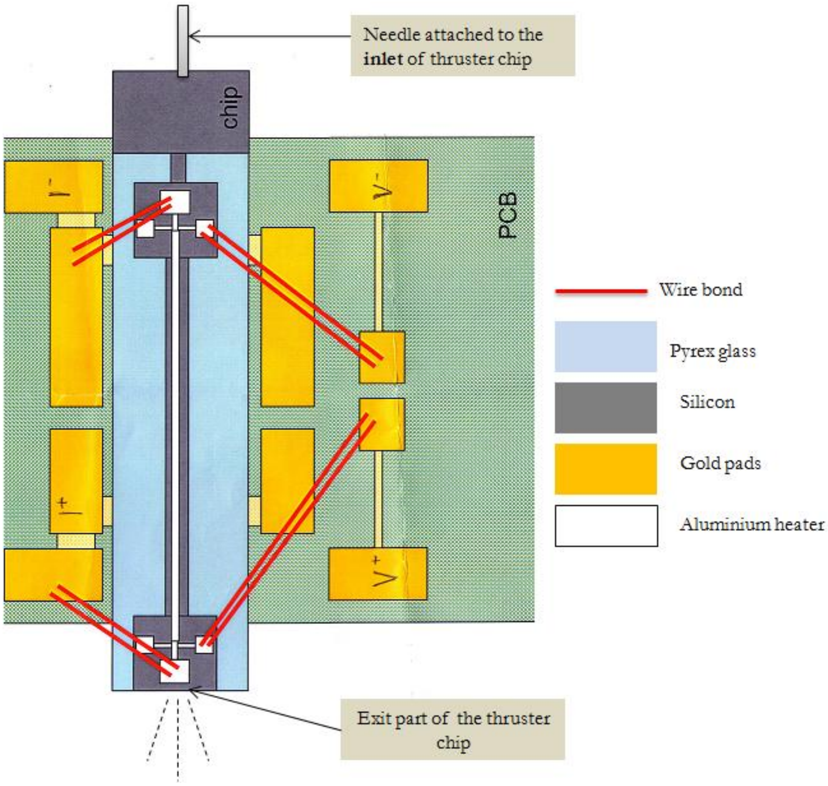

Figure 4.12: Wire bonding schematic diagram for the MEMS thruster chip with no silicon islands.

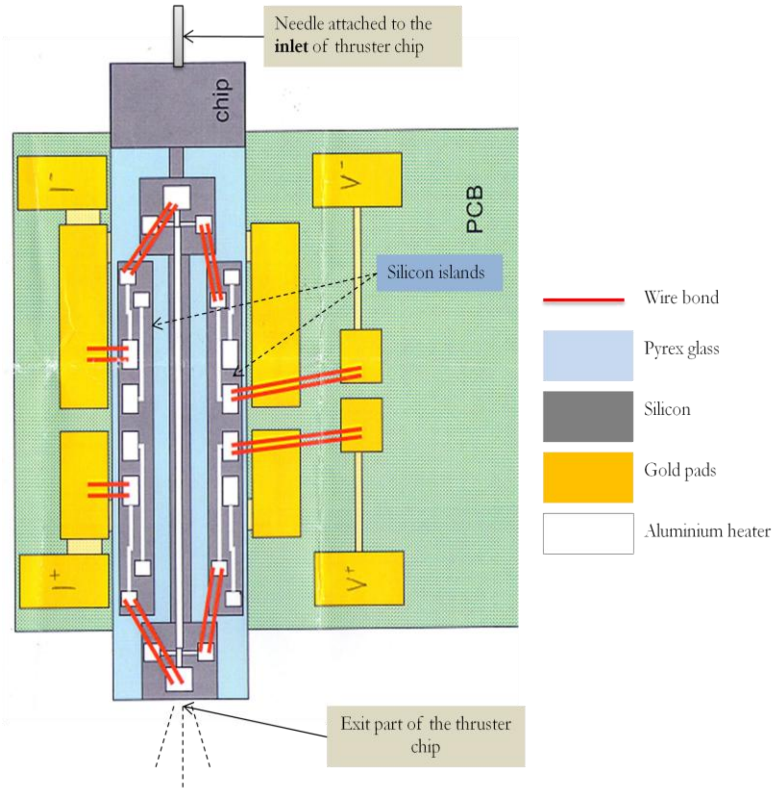

Figure 4.13: Wire bonding schematic diagram for the MEMS thruster chip with silicon islands.

4.2 Devices / thrusters chips produced

In total, 19 thruster chips were fabricated out of three process wafers. All the chips were numbered from #1 to #19 and they are listed in table 4.3. For thruster chips from wafer #1 and wafer #2, three different thruster configurations were proposed: 1) single channel heater chamber with 10 µm width at the nozzle throat (figure 4.15 & 4.16), 2) three channel heater chamber with 10 µm width at the nozzle throat (figure 4.14 & 4.16) and 3) single channel chamber with 5 µm width at the nozzle throat (figure 4.15 & 4.16). The heater channel depth and width were fixed at 50 µm. For thruster chips from wafer #3, both single channel and three channel concept were tried out, but this time with a deeper channel with a depth of 150 µm and keeping the channel width the same at 50 µm (figure 4.17) The length of heater section was fixed at 2 cm for all the designs.

For the nozzle design, apart for the two different throat widths, the remaining nozzle design parameters like the nozzle half-contraction angle (15°), the nozzle half-expansion angle (20°) and the nozzle expansion ratio (25:1) were kep the same for all the designs.

The maximum size of only the micro-heater section was 2 cm x 500 µm (length x width of heater section for a 3 channel design); hence, seven different thruster chips could be made out of one single wafer. Since wafer #2 got broke during the fabrication sequence, two of the thruster chips had to be discarded which is the reason why only 19 thruster chips are presented in table 4.3.

Table 4.3: List of fabricated thrusters chips.

ID	Wafer #	Channel depth H_{ch} [µm]	Number of channels, N	Nozzle throat width W_t [µm]	Si islands (Yes/No)
1	**2**	50	1	10	No
2	**2**	50	1	10	Yes
3	**2**	50	1	5	Yes
4	**2**	50	3	10	No
5	**2**	50	3	10	Yes
6	**1**	50	1	10	No
7	**1**	50	1	10	No
8	**1**	50	1	10	Yes
9	**1**	50	1	5	No
10	**1**	50	1	5	Yes
11	**1**	50	3	10	No
12	**1**	50	3	10	Yes
13	**3**	150	1	10	No
14	**3**	150	1	10	No
15	**3**	150	1	10	Yes
16	**3**	150	1	5	No
17	**3**	150	1	5	Yes
18	**3**	150	3	10	No
19	**3**	150	3	10	Yes

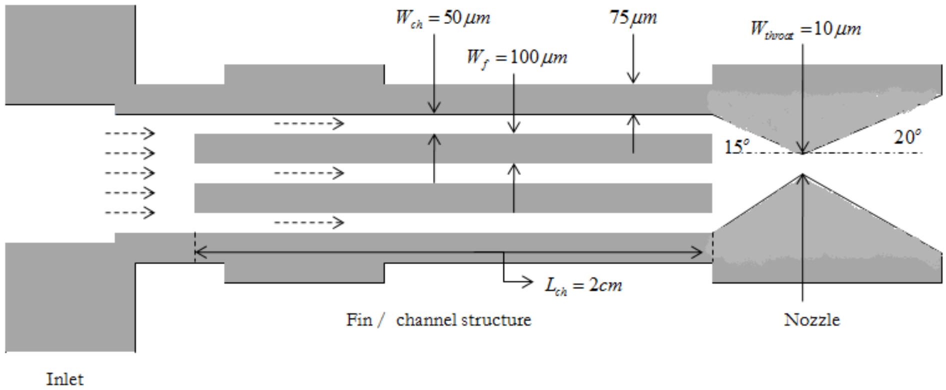

Figure 4.14: Schematic top view of the device with 3 channel design and 10 µm throat width.

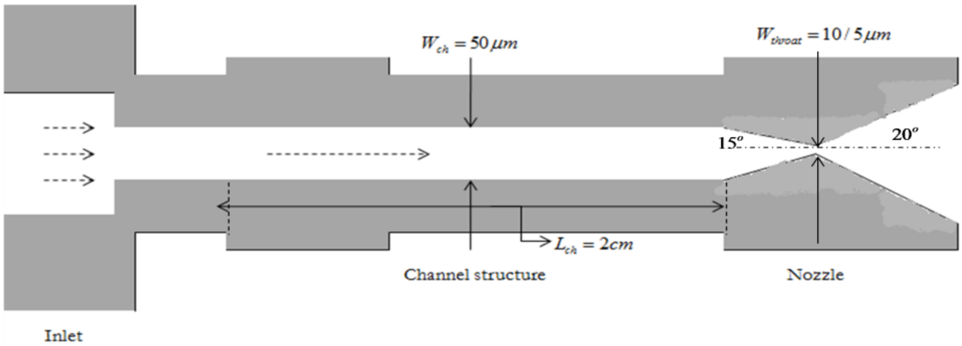

Figure 4.15: Schematic top view of the device with single channel design and 10 (or 5) µm throat width.

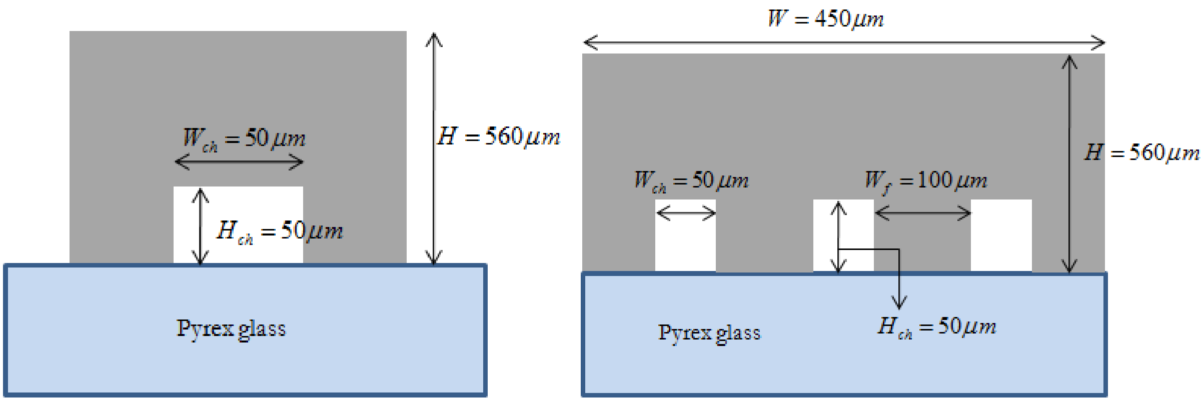

Figure 4.16: Cross-section view of the devices (single channel (left) and 3 channel design (right)) with 50 µm as the channel depth

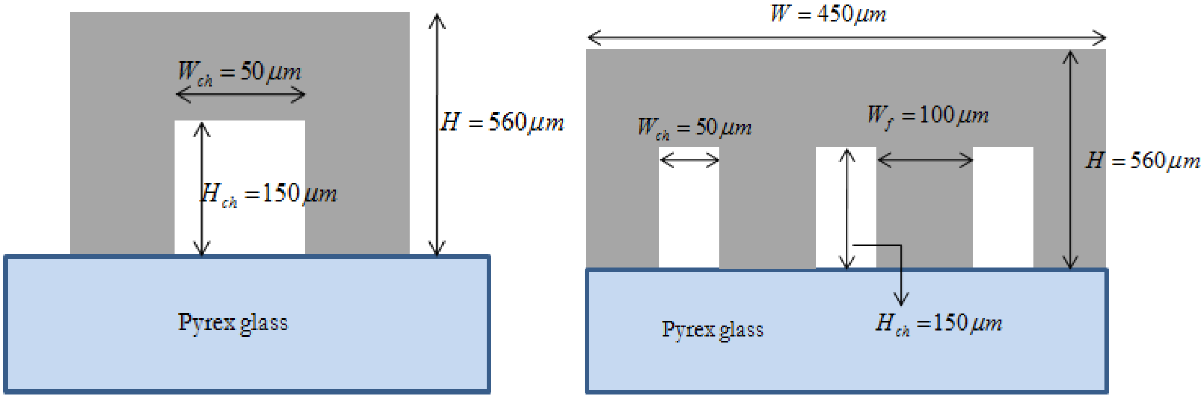

Figure 4.17: Cross-section view of the devices (both single channel (left) and 3 channel design (right)) with 150 µm as the channel depth

4.3 SEM images of thruster chips

In this section, the SEM images of micro-channels and the nozzle are presented to show the reader how much the fabricated geometry differs from the design value. Some of the images show the top-view of the nozzle (figure 4.18 and 4.19), while figures 4.20 to 4.22 show the tilted samples to visualize the third dimension as well. The SEM image captury was performed by Marko at the DIMES facility. All the SEM images can be accesed from the following archive: K:\spe\sse\sse-shared\3.Persoanl Directories\Tittu Mathew\Images\SEM images of thruster.

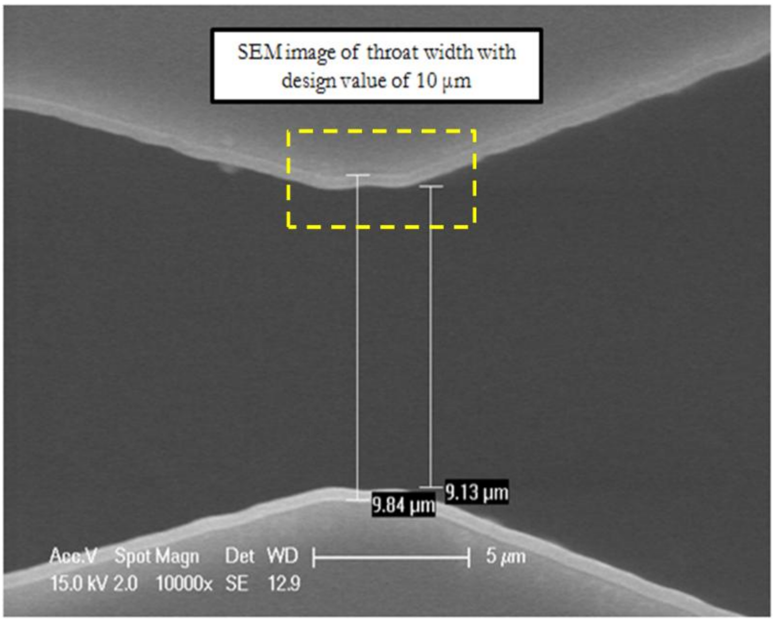

Figure 4.18: SEM image of throat width with design value of 10 µm.

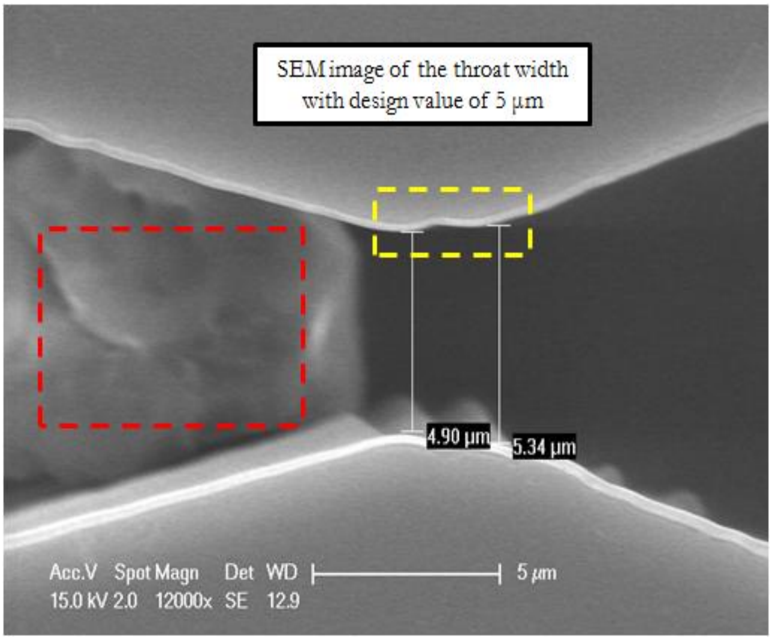

Figure 4.19: SEM image of throat width with design value of 5 µm.

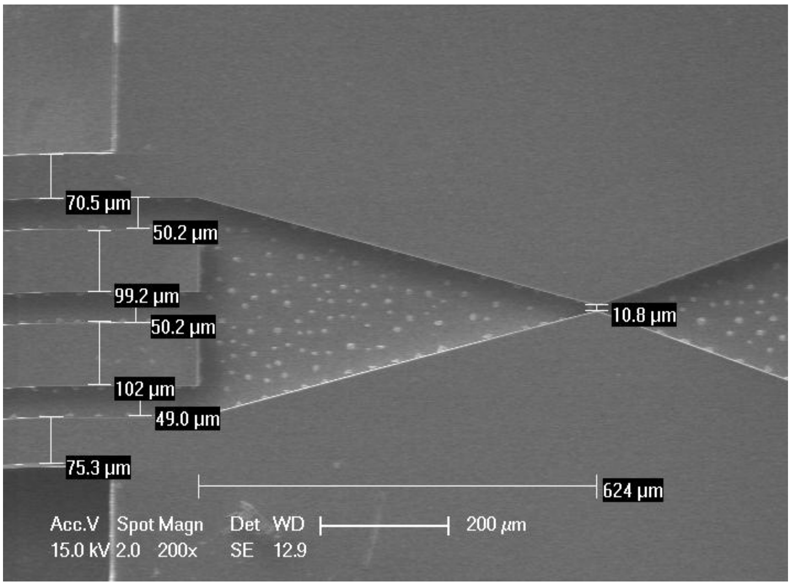

Figure 4.20: SEM image of the device with three channel and throat width of 10 µm.

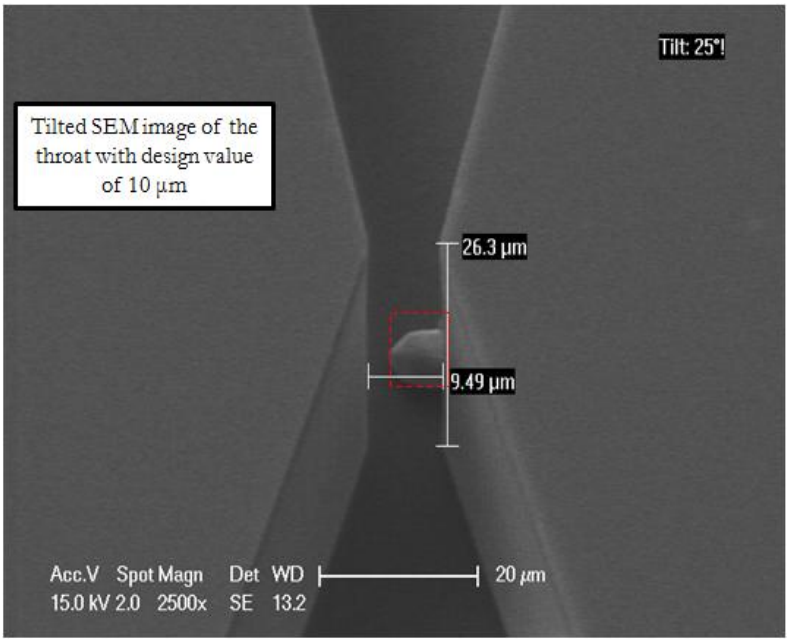

Figure 4.21: Tilted SEM image of nozzle with throat width of 10 μm.

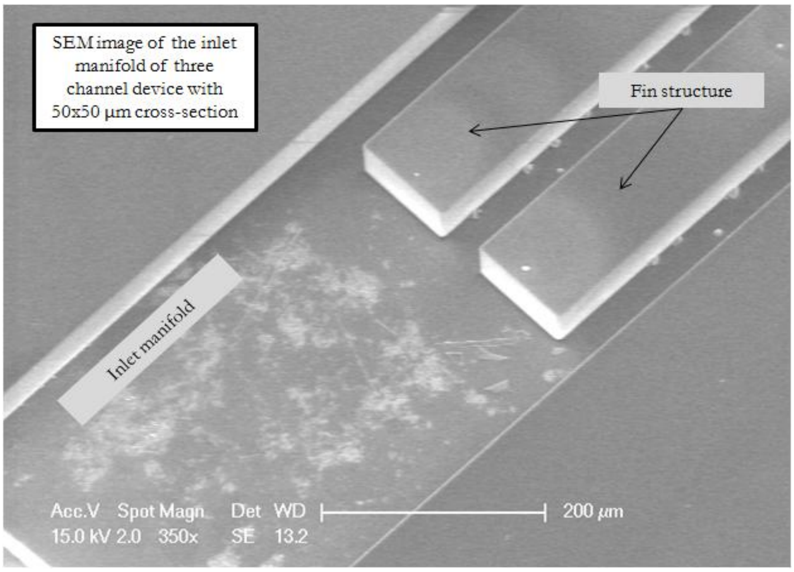

Figure 4.22: Tilted SEM image of the inlet manifold for the three channel device.

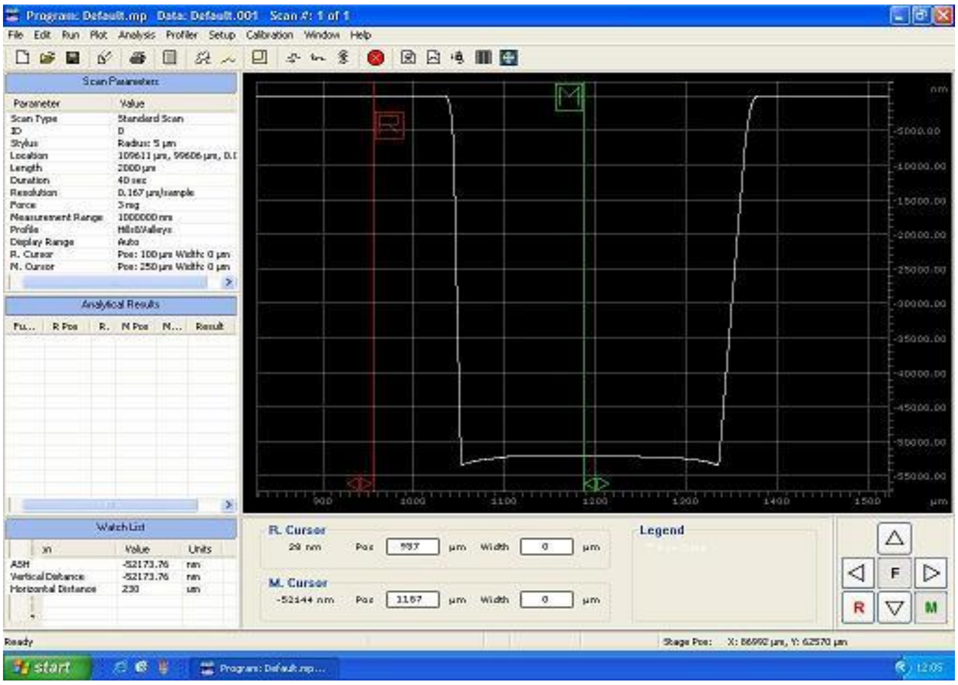

Figure 4.23: Screenshot of channel depth measurement by using a scanning probe profilometer.

Certain remarks about these SEM images are given below:

1) From the SEM images, we see that smooth and vertical channel walls can be etched in silicon using MEMS technology. From the measurements, we observe a maximum deviation of ±10% in the fabricated geometry from the actual design value.
2) Some irregularities can be observed inside the etched cavities (see figure 4.18 and 4.19; highlighted using a yellow box). These features are caused due to not properly drying the wafer after the removal of silicon oxide mask. In the tilted image (figure 4.21), certain contaminants are found sticking onto the bottom side of nicely etched cavities (highlighted using a red box).
3) The measured depth of the channel as shown in figure 4.21 is not correct. Instead of the design value of 50 μm, the measured value shown is 26.3 μm. This error was due to certain changes in SEM settings which were not taken into account during the measurements. Later on, the depth measurement was performed using a scanning probe profilometer. Figure 4.23 shows the screenshot of channel depth measurement. The typicall depth measured at the center of the channel was 52.2 μm with a slight increase by 1.3 μm towards the corner. The channel walls shown in the screenshot are found to be not vertical. This is due to the limitation of the scanning technique which uses a probe tip.

4.4 Conclusion

Fabrication sequence of a micro-thruster starting from the process flow design to fully packaged device using MEMS technology was presented in this chapter. It consists of 16 steps which include the fabrication of the heater layer, patterning of the micro-fluidic channel, the nozzle and the inlet manifold, and the anodic bonding of the silicon chip to the Pyrex glass. A total of 19 thruster chips having different chamber geometries and nozzle throat size were produced out of three process wafers. With the help of SEM images, we could observe a maximum deviation of ±10% in the fabricated geometry using state-of-the-art fabrication technology from the actual design value.

Chapter 5

TEST SETUP FOR MEMS THRUSTER CHARACTERIZATION

Once the MEMS thruster chips are fabricated, the next step is to develop a test setup to perform characterization testing of the chips both in cold gas and in hot gas mode. In order to study the performance of a MEMS micro-resistojet, we need to measure the propellant mass flow rate through the chip, the chamber pressure p_C and chamber temperature T_C just before the nozzle inlet.

But with the micro-geometries we are dealing with, it was quickly found out that it would be extremely difficult to measure the chamber pressure; therefore special steps had to be taken to measure the pressure in the system (hereafter referred to as the system pressure p_S) just before the flow enters the thruster chip. The method of calculating chamber pressure from this measured system pressure will be presented in this chapter. It also became obvious that the chamber temperature could not be directly measured due to the same reason of micro-scale geometry. Hence a work around solution was agreed upon to determine this parameter and it will also be addressed in this chapter.

To perform a characterization test of a MEMS micro-thruster, the test setup should include atleast a Mass Flow Controller (MFC) that controls and measures the propellant mass flow rate and a pressure sensor that measures the system pressure upstream of the chip as shown in figure 5.1.

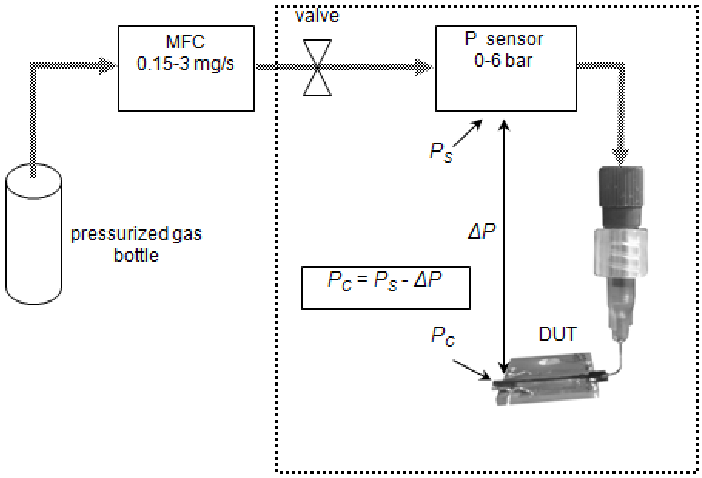

Figure 5.1: Schematic of the measurement setup.

It was also planned to conduct thrust measurements using a newly developed thrust bench to further characterize the performance of MEMS micro-resistojets in terms of thrust and Isp efficiency. Unfortunately, when preparing for testing, it quickly became clear that both the bench and the data Acquisition system (DAQ) were not operating as they should be. Contact with National Instruments showed that identifying the error in the DAQ would take quite some time, which was not available for this study. It is for this reason that thrust measurements were omitted as part of this research. For the time being, the anomaly found with the DAQ has been reported in appendix 6.

In section 5.1, the selection of the sensors is discussed. The calibration of the selected instruments is discussed in section 5.2. In section 5.3, the test setup for both the cold and hot gas testing of thruster chips is discussed with explanation of each component in the test setup. The Labview program developed for the test campaign is discussed in section 5.4. The chamber pressure is calculated from the measured system pressure using the relation $p_C=p_S-\Delta p$ where Δp is the pressure drop which includes the minor losses in the feeding system and the major loss in the micro-fluidic channels. While the major losses have already been discussed in chapter 3, the method to calculate the minor losses in the feed system is discussed in section 5.5, followed by conclusion of this chapter in Section 5.6. Section 5.7 contains a list of references used in this chapter.

5.1 Selection of the sensors

As it was mentioned in the introduction, we need a mass flow controller that can input and measure a certain amount of mass flow through the system, a pressure transducer to measure the system pressure at a point upstream of the thruster chip and an external power source to heat up the propellant flow during the hot gas testing of thruster chips. Characterization tests on MEMS thrusters are to be performed in vacuum conditions; for that the vacuum chamber available at the cleanroom facility of the Space Engineering department is used. From chapters on nozzle and heater design, it was shown how the ambient pressure influences the performance of the thruster and heater respectively. Therefore, a sensor is required to measure this parameter. To measure the ambient temperature inside the vacuum chamber, a temperature sensor is required. A solenoid valve is needed to switch on and off the propellant flow through the chip. Table 5.1 lists the selected sensors along with information on their range and accuracy of measurement provided by the respective manufacturer.

Table 5.1: Sensors selected for the testing of MEMS thruster chips.

Sl. No.	Sensor	Selection of sensor	Range and accuracy
1	Mass flow controller	Mass flow controller from Brooks instruments (Model: 5850S). This sensor was already available in the cleanroom facility.	Range: 0-3 mg/s Accuracy: ± 0.2% F.S.
2	System pressure sensor	OMEGA pressure transducer. Model: PXM209-006A10V. This sensor had to be purchased.	Range: 0-6 bars (absolute) Accuracy: 0.25% F.S. (including linearity, hysteresis and repeatability)
3	External power source	Keithley sourcemeter. Model: 2611/2612. This instrument was borrowed from the DIMES facility.	Range: 0-1 A Accuracy: 0.05%+1.8 mA.
4	Pressure sensor for the vacuum chamber	Kulite pressure sensor. Model: LE-30-125-100A. This sensor was already available in the clean-room facility.	Range: 0 – 7 bars. Accuracy: ± 0.5% F.S.O.
5	Temperature sensor for the vacuum chamber	K-type thermocouple.	Range: -200 to +1350 °C. Accuracy: 1%

Sl. No	Sensor	Selection of sensor	Range and accuracy
6	Solenoid valve	Normally closed ON/OFF valve from Clippard. Model: E210C-2W-012. This valve was already available in the cleanroom facility.	-NA-

5.2 Calibration of sensors

In real world the physical quantities are represented in numbers, for example "5 bars of system pressure". But when it comes down to the instrument level, these physical quantities are represented either in voltage or in current. To perform this conversion, each sensor had to be calibrated. Table 5.2 contains the calibration equation for each sensor.

Table 5.2: Calibration equation for the sensors.

Sl. No.	Sensor	Calibration equation	Range of calibration	Date of calibration	Reference
1	MFC (input command)	$V = 3.87.\dot{m}$	0-3 mg/s	24.09.2010	[5.6]
2	MFC (output signal)	$\dot{m}$ =0.90V-0.78	0-3 mg/s	24.09.2010	[5.6]
3	System pressure sensor	p=0.60V	0-6 bars	17.08.2010	[5.10]
4	Vacuum pressure sensor	p=-((Vx1000)x1.01)x0.07	0-7 bar	-	Borrowed from [5.2]

5.3 Test setup for both cold and hot gas testing

Once the sensors are selected and calibrated, the next step is to design and built the test setup. Figure 5.2 shows a schematic diagram of the test setup used for both cold and hot gas testing of a MEMS thruster chip, highlighting each component and the mechanical and electrical interfaces between the thruster chip and the test environment. Not shown in the schematic diagram of the test setup are: 1) KULITE pressure sensor used to measure the pressure in the vacuum chamber and 2) the K-type thermocouple to measure the temperature inside the vacuum chamber.

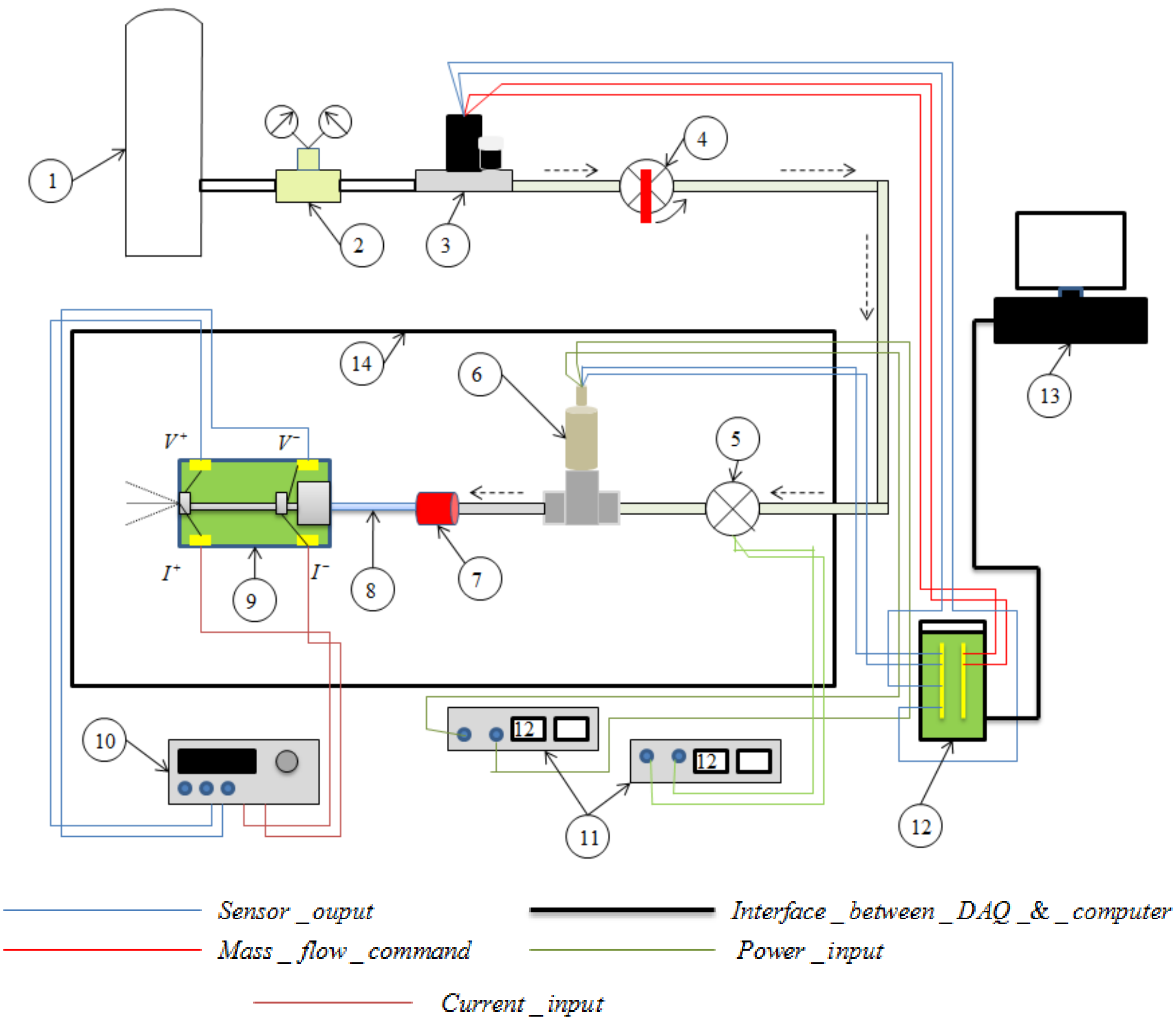

1-Nitrogen storage tank (p_{max} =200 bar), 2-Pressure regulator (p_{outlet}=5±0.5 bars), 3-Mass Flow Controller, 4-Swagelok gate valve, 5-Clippard solenoid valve, 6-Pressure sensor, 7-Tube-needle adaptor, 8-Needle, 9-MEMS thruster chip, 10-Power sourcemeter, 11-Power supply units for the sensors and valve, 12-Data Acquisition System (DAQ), 13-Test control PC, 14-Vacuum chamber.

Figure 5.2: Schematic diagram of the test setup showing the components, mechanical and electrical interfaces between the test chip and the test environment.

Nitrogen gas is stored in high pressure cylinder with a maximum storage pressure of 200 bars. A coarse pressure regulator then steps down this high pressure to a lower relative pressure of 5±0.5 bar, so as to comply with the inlet pressure specification of the selected MFC. Using a LABVIEW program developed for the test campaign (discussed in section 5.4), the user can set a certain value of mass flow through the system. The mass flow controller also has an integrated sensor that measures the actual mass flow flowing into the system. Flexible vinyl tubing then connects the output of mass flow controller and guides the gas into the vacuum chamber. Just outside the vacuum chamber, there is a Swagelok gate valve. It is a quarter turn gate valve and is normally kept open during the entire test campaign. Once inside the vacuum chamber, the propellant flow through the micro-thruster is turned on or off by the selected Clippard valve. It is kept closed during the de-pressurization of vacuum chamber before the start of each test campaign. After the valve, comes the pressure transducer which measures the system pressure. This pressure sensor is mechanically interfaced with the feeding system using a Tee junction from Swagelok (Model: SS-4T).

Vinyl tubing with an outer diameter of 1/4" runs in-between the pressure transducer and the needle glued to the inlet of the MEMS thruster chip. To achieve a fluidic interface between the vinyl tubing and the needle hub, a special type of tube size reducer/adaptor had to be thought off. Upon consultation with people from DIMES and with Upchurch scientific instruments, the tube adaptor as shown in figure 5.3 was procured and used for the whole test campaign. It's basically made up of three components as highlighted in the figure, with the feed system inlet to the left and the connection to the needle to the right hand side of the figure.

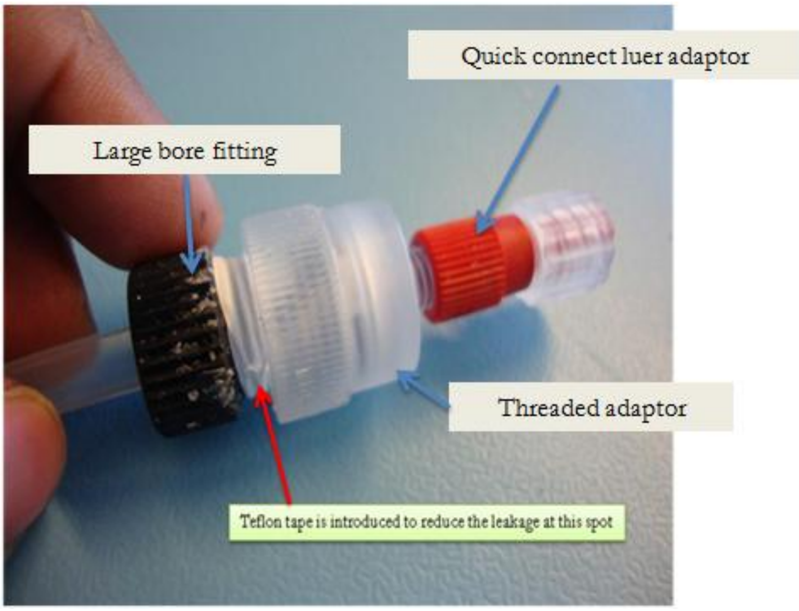

Figure 5.3: Tube-to-needle adaptor that connects the feed system to the chip.

Two types of needles are used. One type has a 90^{o} bend with an inner diameter of 0.152 mm whereas the other has a straight tip with an inner diameter of 0.160 mm. The straight needles are used for thruster chips fabricated from wafer #3 and bend tip needles are used for thruster chips fabricated from wafer #1.

Selection of an external power source that can simultaneously feed a set current and measure the voltage across the aluminium heater was discussed in section 5.1. This input current is manually set and controlled, without any Labview interface. Steps on how to operate the sourcemeter is provided in appendix 5. We are interested in determining the heater temperature for a set input current. From the very beginning of the test setup design, we realized that the heater temperature cannot be measured directly using a thermocouple due to the small size of the heater chamber section and presence of thin delicate electric bond wires in the vicinity. Hence it was decided to determine this parameter from the calculated heater resistance for a set input current. For that, the following relation is used:

$$T_h = \frac{1}{TCR}\left(\frac{R(T_h)}{R(T=0^0C)} - 1\right) \tag{5.1}$$

where TCR is the temperature coefficient of resistance of the heater material (=0.0043 for aluminium), $R(T_h)$ the measured heater resistance and $R(T=0^0C)$ the calculated heater resistance at a reference temperature of 0^0C. There are two ways to calculate the heater resistance as shown in figure 5.4: 1) Two point probe method and 2) Four point probe method [5.5].

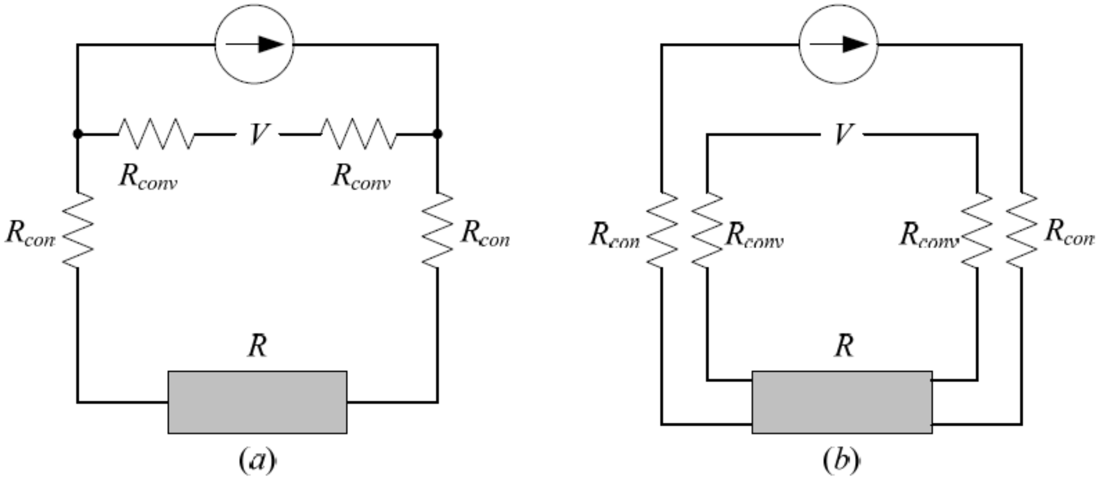

Figure 5.4: Schematic diagram of (a) a two-point probe method and a (b) four-point probe method.

In the figure above, R stands for the heater resistance, R_{conv} the resistance of connecting wires to the voltmeter and R_{con} the resistance of connecting wires to the current source. To calculate the heater resistance of MEMS micro-thrusters, we will be going with the four-point probe method. The reason why a two point measurement method was not used is because then the measured resistance will be $R+R_{con}$ which will not be the actual resistance of the heater and hence not the right value of heater temperature. This problem is overcome in a 4 point measurement method since the amount of current going through the voltmeter will be very small due to its high resistance.

Since it was not possible to directly measure the chamber temperature T_C at the nozzle inlet, a work around solution had to be agreed upon as it was mentioned in the introduction. Under cold gas conditions, the chamber temperature is taken to be identical to the ambient temperature. Under hot gas conditions, the chamber temperature is calculated from the amount of input electric power that goes into heating up the gas flow at a certain mass flow and heater temperature. This will be further discussed in detail in chapter 6 during the test procedure description and test data elaboration for the hot gas testing of thruster chips.

Table 5.3 contains a list of all the components in the feed system starting from the outlet of mass flow controller to the inlet of the MEMS thruster chip, along with their length, the inner diameter and the calculated flow area and volume. While the inner diameter of all the components was either measured using a vernier caliper or taken from the product catalogue, the length of special components like the valves and bends in the feed system had to be calculated by using the concept of equivalent length, as taught in the lecture notes [5.3]. The length of vinyl and metal tubes was measured using a ruler.

Table 5.3: Volume of the feed system.

Sl. No.	**System component**	**I.D** [mm]	**Length** L [cm]	**Flow area** A [mm^2]	**Volume** V [m^3]
1	Vinyl tubing outside the vacuum chamber (connecting the MFC to vacuum chamber inlet)	5.04	220 / 90*	19.95	4.39E-5 / 1.80E-5
2	Swagelok gate valve (outside the vacuum chamber)	5.00	19.50+	19.63	3.83E-6
3	Metal tube	5.00	27.00	19.63	5.30E-6
4	90^0 bend	3.13	17.84++	7.69	1.37E-6
5	Vinyl tubing (connecting the vacuum chamber inlet to the valve and from valve to pressure transducer)	3.13	52.50	7.69	4.04E-6
6	Clippard valve	0.76	76.20^^	0.46	3.48E-7
7	T-junction (flow through)	7.14	14.28**	40.04	5.72E-6
8	Vinyl tubing (connecting the pressure sensor outlet to thruster inlet)	4.75	60.00	17.72	1.06E-5
9	Threaded adaptor	3.30	1.24	8.55	1.06E-7
10	Quick connect luer adaptor	1.30	1.17	1.33	1.55E-8
11	Needle (straight tip)	0.16	1.80	0.02	3.62E-10
12	Needle (bent tip)	0.15	1.95	0.02	3.45E-10
	90^0 bend in the needle	0.15	0.86++	0.02	1.51E-10

**- The length of the vinyl tubing outside the vacuum chamber was cut short to 90 cm in a later stage of test campaign in order to reduce the volume of feed system and thereby the time required to achieve a stable pressure.*
+- Swagelok gate valve is modeled as a gate valve with a quarter turn closed. Its equivalent length is taken as 39 times the inner diameter.
++- There exist two 90 degree bend in the feed system: one just at the inlet part of the vacuum chamber and the other is the 90 degree bend in the needle. They are modeled as square bend with an equivalent length of 57 times the inner diameter.
***- T-junction (flow straight through type) is used to install the pressure transducer in the feed system. Its equivalent length is taken as 20 times its inner diameter.*
^^-The clippard valve in the feed system is modeled as a needle valve with an equivalent length of 1000 times its inner diameter.

Initially, silicon tubing was used in the section between the system pressure transducer and the thruster inlet because of its better flexibility, lesser rigidity and good stability at vacuum conditions. But we quickly realized that silicon tubes cannot withstand high pressures of 6 bars. Therefore, silicone tubing was no longer used in the feed system; instead it was replaced by rigid vinyl tubing that can withstand such high pressures.

5.4 LABVIEW program

To perform the test campaign, a LABVIEW program had to be developed to carry out certain functions like commanding the MFC to provide certain mass flow rate through the system, to acquire the output signals from the sensors like system pressure transducer and so forth. Reference 5.7 is a good source to learn about the basics of programming using LABVIEW. A LABVIEW program basically consists of two parts: 1) a front panel through which a user interacts with the instruments/sensors and 2) a block diagram where behind-the-scene actual control flow of the program takes place. Screenshots of both these parts are given in appendix 4. The calibration equation for each sensor is inserted into their respective Formula VI as highlighted in the screenshot of block-diagram.

The program used for the test campaign was originally made by Alessandro Migliaccio [5.2]. Slight modifications were made with respect to the mass flow range (0-3 mg/s) and a new VI was developed to measure the system pressure. The LABVIEW program can be accessed from the following folder: k:/lr/spe/sse/sse-shared/3.PersonalDirectories/Tittu Mathew/Labview programs/steadystate.vi. The data acquired through the DAQ were the system pressure, vacuum chamber pressure, mass flow rate and the vacuum chamber temperature. All the raw data were saved in the following folder and was later on processed using MATLAB during the data elaboration phase of the thesis: k:/lr/spe/sse/sse-shared/3.Personal Directories/Tittu Mathew/Test data/Raw data.

Now to predict a stabilized pressure in the system for a set mass flow, a criterion had to be developed. Since we are dealing with vacuum test conditions where no physical access to the test section is possible, we had to incorporate a separate VI within the same LABVIEW program that can tell when the stable system pressure is reached for a set mass flow rate. This stabilization criterion is in turn influenced by the accuracy of the selected system pressure sensor. From table 5.1, we see that the accuracy of the selected sensor is 0.25 % of full scale, meaning 0.025 V(=0.25 % x 10V). Substituting this value in the calibration equation for the pressure sensor, we get the accuracy of the pressure transducer as 0.015 bar. Hence, the stabilization criterion for the system pressure is defined as follows:

> *"The system pressure shall be considered stable for a set mass flow rate, when the relative change in pressure reading within a time period of 1.5 minutes does not exceed more than 20 millibar"*

Figure 5.5 shows the screenshot of that part of the block diagram that contains the stability criterion code. During every loop execution of the program, the system pressure reading gets stored as elements in a one-dimensional array. From this array, an array subset is created by taking the readings during the last 90 seconds (or 1.5 minutes) of measurements. The standard deviation and the mean value of this subset are calculated and from these two values, the relative change in the measurements is calculated as:

$$relative\_change = \frac{std\_deviation}{mean\_value} \times 100 \tag{5.2}$$

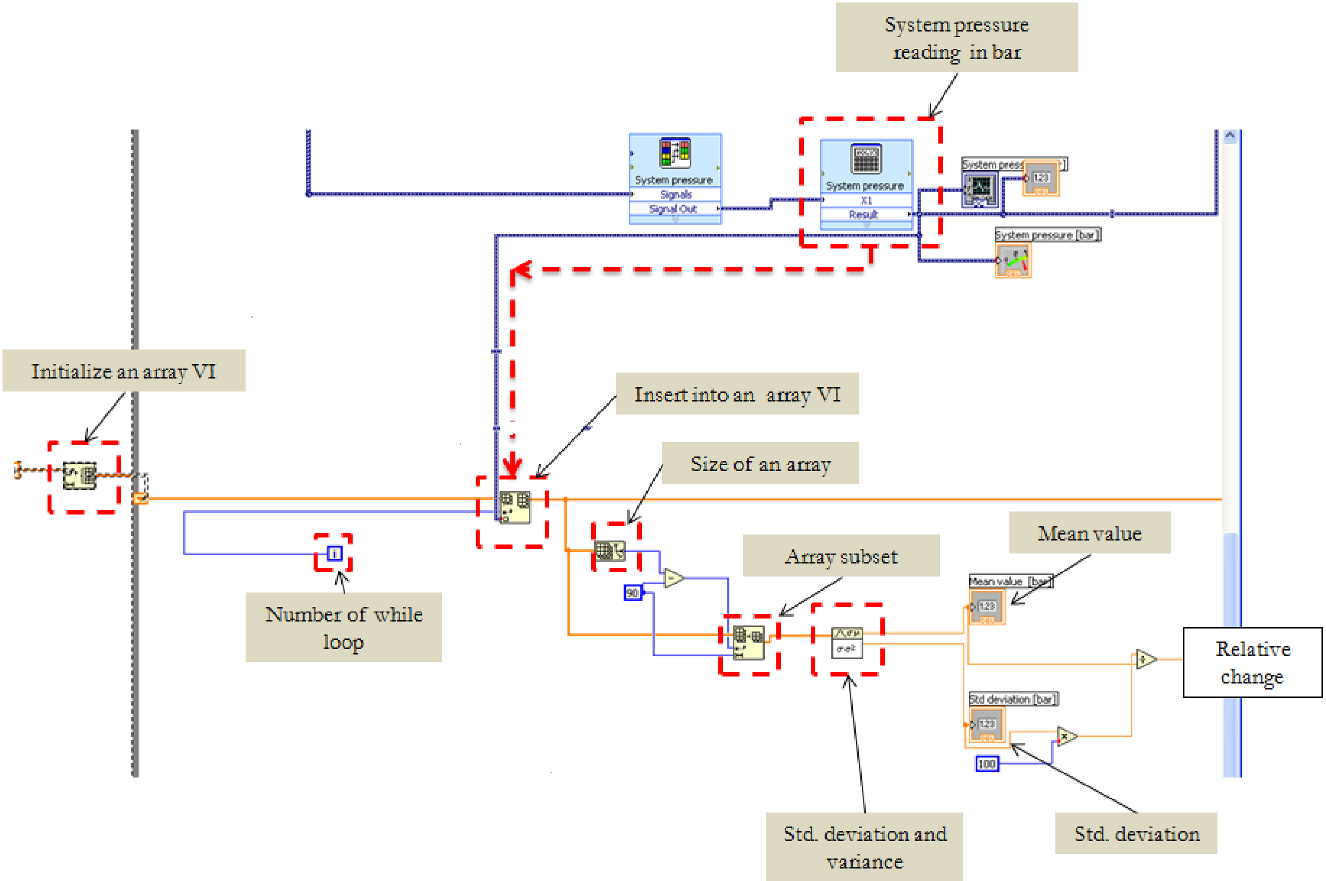

Figure 5.5: Screenshot of the block diagram containing the stability criterion code.

5.5 Minor losses in the feed system

From the MEMS thruster performance characterization point of view, we are interested in the chamber pressure p_C for a set mass flow rate. Since it was not possible to measure this parameter directly, an indirect approach had to be taken by recording the system pressure for a set mass flow rate and then subtracting from it the pressure drop in the feeding system (minor losses) and that within the micro-fluidic channel (major loss) to theoretically calculate the chamber pressure. The major loss in the micro-fluidic channel had already been discussed in chapter 3. In this section, we will be focusing on the minor losses in the feed system like for example, the loss in pressure head at sudden channel contractions (section 5.5.1), at bends in channel and along a tube of certain length (section 5.5.2).

5.5.1 Pressure drop due to channel contraction

There exist a number of channel contractions in the feed system. For example, when looking only at the tube-to-needle adaptor, the area reduction from a tube size of 4.75 mm I.D. to a needle is carried out in 3 steps as shown in figure 5.6.

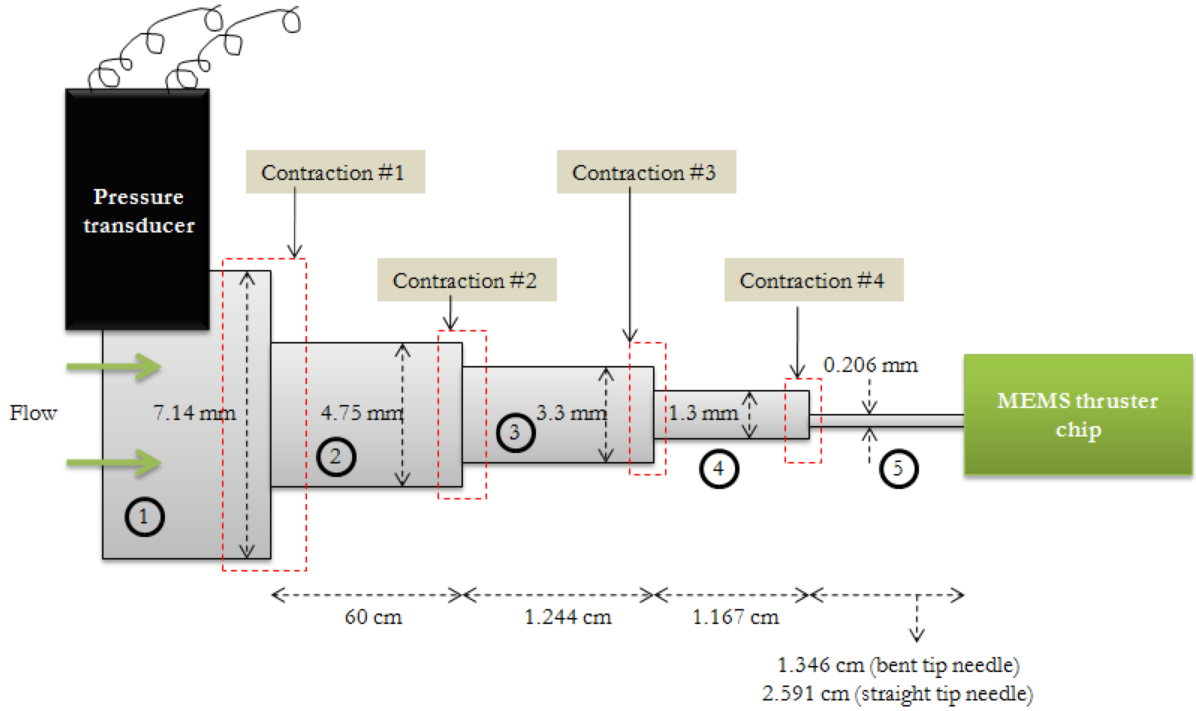

1- T junction, 2-Vinyl tubing, 3-Threaded adaptor, 4-Luer lock adaptor, 5-Needle.

Figure 5.6: Flow channel contractions from the pressure transducer port to the MEMS thruster inlet.

The pressure drop due to sudden contraction in the channel is given by:

$$\Delta p = K.\ \tfrac{1}{2}\ .\rho U^2 \qquad (5.3)$$

where K is the contraction loss coefficient which depends on the contraction ratio (see table 5.4), ρ the fluid density and U the fluid velocity in the constricted channel.

Table 5.4: Contraction loss coefficient K at different contraction spots in the feed system [5.1].

Contraction #	D [mm]	d [mm]	d/D [-]	K [-]
1	7.14	4.75	0.67	0.23
2	4.75	3.30	0.69	0.22
3	3.30	1.30	0.39	0.36
4	1.30	0.15/0.16^{+}	~0.12	0.50

$^{+}$- *Taking into account the inner diameter of both the straight and bent tip needles. We approximate the contraction ratio values for both the cases to 0.12. .*

Also, we have to take into account the channel contraction that happens in between the needle outlet and the inlet manifold of the MEMS heater chamber. As we have seen in table 3.7 in chapter 3, there are four different heater chamber concepts. In table 5.5 below, we present the contraction factor depending on the contraction ratio for each of the four chamber design cases.

Table 5.5: Contraction loss coefficient K at the channel contraction between the needle and inlet manifold for four different heater chamber designs.

Design case #	D [μm]+	d_h [μm]	d_h/D [-]	K [-]
1	160	75	0.47	0.32
2	160	210	1.31*	0.19**
3	152	50	0.33	0.39
4	152	87.5	0.58	0.27

+ - Needles with straight tip were used for thruster chips with deeper channels (depth of the channel = 150 μm), whereas needles with 90° bend tip were used for thruster chips with shallow channels (depth of the channel = 50 μm).
**-For design case #2, we see that the gas flow undergoes a sudden expansion soon after the needle since the hydraulic diameter of the inlet manifold of the thruster chip is greater than the inner diameter of the needle used.*
***- The expansion loss coefficient value corresponding to the area ratio is taken from figure 8.15 of reference [5.11].*

5.5.2 Pressure drop in a straight tube and at bents

The pressure drop across a straight tube is formulated as in reference [5.4] as:

$$\Delta p = 2\rho U^2 f \frac{L}{D} \tag{5.4}$$

where U is the flow velocity, f the fanning friction factor, L the tube length and D the tube inner diameter. For the needle with 90° bent, the equivalent length from table 5.3 is used. In case of a non-circular channel like in the case of inlet manifold of a MEMS heater chamber, 'D' will be its hydraulic diameter.

5.5.3 Pressure drop at the entrance of a multi-channel geometry

In case of three channel design for heater chamber, additional pressure drop occurs when the flow gets distributed to multiple passages at the entrance. Then the loss coefficient K_C, similar to the contraction factor K in equation 5.3, depends on the value of σ which is defined in reference [5.1] as:

$$\sigma = A_2/A_1 \tag{5.5}$$

where A_2 is the sum of cross-sectional area of 'N' number of channels and A_1 is the cross-sectional area of the channel just before the fluid front crosses the plane of entrance of the channel. Figure 5.7 shows the flow constriction in a 3 channel design.

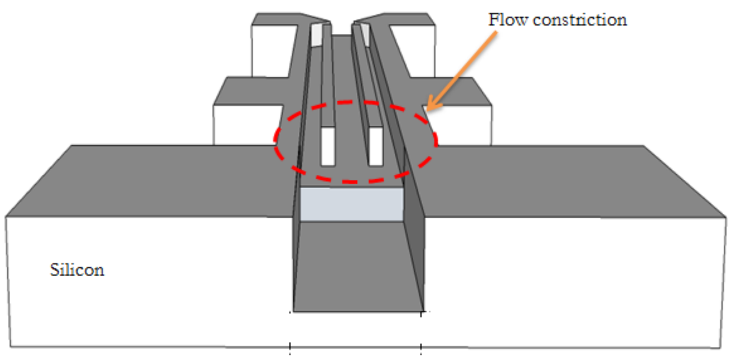

Figure 5.7: Flow constriction in a 3-channel design.

The loss coefficient for the chamber design variants 2 and 4 (design #2 refers to a 3 channel design with depth of 150 μm and design variant #4 refers to a 3 channel design with 50 μm depth; channels in both the cases have a width of 50 μm) is given in table 5.5.

Table 5.6: Loss coefficient in a multi-channel chamber geometry.

Chamber design #	**Flow cross-sectional area** A_2 [μm^2]	**Frontal area** A_1 [μm^2]	σ [-]	**Loss coefficient** K_c [-]
2	7500	17500	0.43	0.73
4	22500	52500	0.43	0.73

5.5.4 Sample calculation for pressure drop in the feed system and analysis

In this section, we present a sample calculation showing the pressure head loss in the feed system starting from the pressure sensor location till the entrance of the MEMS heater channels for a regulated pressure of 5 bars and propellant mass flow rate of 1 mg/s taking chip #19 as the thruster chip. All the calculations pertaining to the pressure loss in the feed system are included in the excel spreadsheet developed by the author. The spreadsheet can be accessed from the following folder: k:/lr/spe/sse/sse-shared/3.PersonalDirectories/TittuMathew/Excelsheets/Pressure loss in the feed system. First, the gas density ρ is calculated using the ideal gas law and taking 23°C as the gas temperature:

$$\rho = \frac{p_{sys}}{RT} = \frac{5E5 \, {}^{N}\!/\!_{m^2}}{296.8 \, {}^{J}\!/\!_{kgK} \, 296.15K} = 5.69 \, {}^{kg}\!/\!_{m^3}$$

The flow velocity U follows from the mass conservation principle by taking the inner cross-sectional area of the T-junction from table 5.3:

$$U = \frac{\dot{m}}{\rho A} = \frac{1E-6 \, {}^{kg}\!/\!_{s}}{5.69 \, {}^{kg}\!/\!_{m^3} \times 40.04E-6m^2} \times 100 = 0.44 \, {}^{cm}\!/\!_{s}$$

To determine the friction factor, we need to determine the flow Reynolds number as follows:

$$\mathrm{Re} = \frac{\rho U D}{\mu} = \frac{5.69 \, {}^{kg}\!/\!_{m^3} \, 0.44E-2 \, {}^{m}\!/\!_{s} \, 7.14E-3m}{1.76E-5 \, {}^{Ns}\!/\!_{m^2}} = 10.16 \quad [-]$$

where D is the inner diameter of the T-junction and μ is the nitrogen gas viscosity at the room temperature of 23°C. From this parameter, it is clear that we are dealing with laminar flow. We now calculate the fanning friction factor as follows:

$$f = \frac{16}{\mathrm{Re}} = \frac{16}{10.16} = 1.57$$

We next calculate the pressure drop in the T-junction using relation 5.4:

$$\Delta p = 2f\frac{L}{D}\rho U^2 = 2\times 1.57\times\frac{14.28E-2m}{7.14E-3m}\times 5.69\,{}^{kg}\!/_{m^3}\times(0.44E-2)^2\,{}^{m^2}\!/_{s^2} = 0.007Pa$$

Similarly, we calculate the pressure drop at each channel contractions and along channel length by assuming no leakage in the feed system. The results are given in table 5.7.

Table 5.7: Pressure loss values; p=5 bar, T=296.15 K and m=1 mg/s

Sl. No.	**Component/Contraction**	**Fanning friction factor** f [-]	**Pressure drop** Δp [Pa]
1	T-junction	1.58	0.01
2	Contraction 1	-	6.55E-5
3	Vinyl tubing	1.05	0.15
4	Contraction 2	-	2.64E-4
5	Threaded adaptor	0.73	0.01
6	Contraction 3	-	1.80E-2
7	Quick connect luer adaptor	0.29	0.52
8	Contraction 4	-	108.71
9	Needle	0.04	3461.59
10	Expansion loss	-	41.02
11	Inlet manifold	0.05	110.99
12	Contraction 5	-	367.86
Total pressure drop in the feed system			4091.88

In table 5.7, 'Contraction 5' refers to the channel contraction between the needle outlet and the inlet manifold of the heater chamber. From the table, we see that:

1) The calculated total pressure drop in the feed system starting from the point of system pressure measurement till the entrance of multi-channels is 4091.88 Pa which is 0.82% of the regulated pressure.
2) The maximum pressure drop happens in the straight needle due to its relatively large length-to-diameter ratio, followed by the second highest pressure drop at the entrance of the multi-channel geometry.

In figure 5.8, the pressure loss in the feed system is plotted against mass flow rate for four different heater chamber design cases. We keep the inlet pressure at 5 bars and the propellant temperature at 296.15 K.

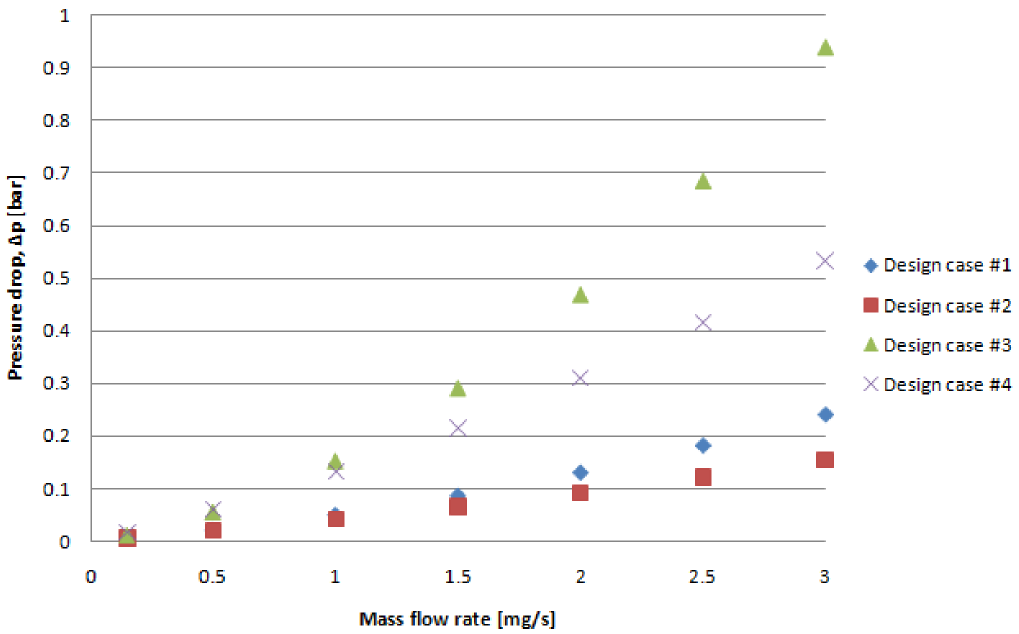

Figure 5.8: Pressure loss in the feed system as a function of mass flow rate for four different heater chamber design cases; p=5 bar, T=296.15 K.

From figure 5.8, we see that with increasing mass flow rate, the pressure drop increases for all the design cases. We came across a similar result while studying the pressure drop in the micro-channels in chapter 3.

1) When comparing the pressure drop trend for design case #1 and #2, we see that they follow the same trend till a mass flow rate of 1.5 mg/s. Beyond this value, the pressure drop in the feed system with chamber design #1 starts to increase faster and becomes 56% higher than that with chamber design #2 at a mass flow rate of 3 mg/s. The reason for such a trend is due to the larger effect of the pressure drop at the channel contraction between the needle outlet and chip inlet manifold for case #1.
2) When comparing the results of thruster chips having straight needle (#1 & #2) with those having a 90^{o} bend needle (#3 & #4), we see that the pressure drop in the later is larger at all mass flow rates. This highlights the additional pressure drop due to the sharp bend in the feed system.
3) At the maximum propellant flow rate of 3 mg/s, the pressure drop in feed system with chamber design #3 is the largest constituting roughly 19% of the regulated pressure, whereas the lowest value is shown in case of chamber design #2 constituting only 3% of the total regulated pressure.

5.6 Conclusion

The test setup to perform both cold gas and hot gas tests on a MEMS micro-thruster was discussed in this chapter. Due to the extremely small size of a MEMS micro-thruster, certain properties like the chamber pressure, chamber temperature and heater temperature could not be directly measured; therefore an indirect way of calculating those properties from other measurements had to be thought off and was presented in this chapter. It was decided to theoretically calculate the chamber pressure value for a given mass flow from the system pressure measured just outside the chip, by subtracting from it the head loss in feed system and across the micro-channels. In this chapter, special focus was given on the pressure head loss in feed system.

It was concluded from the sample calculations that the largest pressure drop occurs at the needle section. Relative change of less than 20 millibars was selected as the stabilization criterion for the system pressure at a given mass flow or at a given input heater current during the hot gas testing. It was decided to calculate the heater temperature from its electric resistance which was measured by using a four point probe method.

5.7 Reference

[5.1] Frank. M. White; Fluid Mechanics; Fourth edition; McGraw Hill international series.
[5.2] Alessandro Migliacciao; Test campaign of T3μPS: a microthruster based on solid thruster cool gas generators; Master thesis; TUDelft.
[5.3] Barry Zandbergen; Thermal rocket propulsion; Lecture notes.
[5.4] Adrian Bejan; Heat transfer; Wiley publications.
[5.5] Jun Hao; Silicon MEMS micro-evaporator; MSc thesis; TUDelft.
[5.6] Facility handbook-2, Clean room facility, Space systems engineering, TUDelft.
[5.7] Lisa K. Wells; Labview programming for instrumentation; Student edition user's guide.
[5.8] Federica Valente; Vacuum facility development and thrust bench improvement for micro-thruster testing, MSc thesis, TUDelft.
[5.9] Marko Mihailovic, T.V. Mathew, J.F. Creemer, P.M. Sarro, B.T.C. Zandbergen; MEMS Silicon-based resistojet micro-thruster for attitude control of nano-satellites.
[5.10] Omegadyne Inc. PX209/219 Final calibration report.
[5.11] Fox and Mc Donald; Introduction to Fluid Mechanics; Fifth edition.

Page intentionally left blank

Chapter 6

TEST RESULTS – PRESENTATION & DISCUSSION

Once we have discussed the design of test setup in the previous chapter, in this chapter we will be presenting the test results of MEMS micro-thrusters under both cases of with and without propellant heating, followed by data elaboration and comparison with the theory. In section 6.1, the cold gas test results of MEMS thrusters are dealt with. The hot gas test results are discussed in section 6.2. This chapter concludes in section 6.3 followed by a list of references used in this chapter in section 6.4.

6.1 Cold gas test results

In section 6.1.1, the test parameters and the sensors used to measure them are discussed. The test plan for the testing of a MEMS micro-thruster without propellant heating is given in section 6.1.2. In section 6.1.3, a sample test plot from the cold gas test campaign performed on one of the micro-thruster chips is presented and elaborated. Data presentation and elaboration of the cold gas test results is done in section 6.1.4. Apart from the propellant mass flow rate and the system pressure, the pressure and temperature inside the vacuum chamber were also measured during a cold gas test campaign and they are disussed in section 6.1.5. In section 6.1.6, the chamber pressure derived by using the procedure described in chapter 5 is compared with that calculated using the ideal rocket motor theory.

6.1.1 Parameters measured during cold gas tests

To study the performance of a micro-thruster at cold gas mode, we need to measure the mass flow rate through the chip, the system pressure, and the pressure and temperature inside the vacuum chamber. To perform measurements of these parameters, corresponding sensors from table 5.1 is used.

6.1.2 Test plan for cold gas testing of a micro-thruster

Controlled parameter during the cold gas testing is the propellant mass flow rate. By controlling the mass flow rate, the system pressure is set; this phenomenon will be explained with the help of test plot in section 6.1.3. In table 6.1, we focus on the test procedure to be followed for the cold gas testing of a MEMS micro-thruster. This test procedure is common for all the thrusters irrespective of their identity.

Table 6.1: Test plan for cold gas testing of a MEMS micro-thruster.

Test procedure #	Description
1	Connect the micro-thruster to be tested with the feed system inside the vacuum chamber by interlocking the needle hub with the tube adaptor of the feed system.
2	Close the vacuum chamber. Switch ON the power supply to all the sensors and the test control personal computer (PC). Before running the LabView program, a new folder is created using the VI to write the test data to a file in computer. The date on which the testing is performed is given as the name of the folder. All the test results can be retrieved using this directory path:

Test procedure #	Description
	k:\spe\sse\sse-shared\3.PersonalDirectories\Tittu Mathew\Test data\Raw data. Turn open the outlet of the pressurized gas cylinder and adjust the coarse pressure regulator manually in such a way that the mechanical pressure gauge at the outlet of the regulator shows a relative pressure reading of 5±0.5 bars.
3	Run the LabView program. Input a command of zero mass flow to the MFC using the front panel. Then turn OFF the power supply to the Clippard solenoid valve placed inside the vacuum chamber to shut off the feeding system part in between the MFC and the valve.
4	Start de-pressurising the vacuum chamber by powering ON the vacuum pump after manually opening the valve between the vacuum chamber and the pump and closing the gas escape passage. The reader is advised to refer to the manual on vacuum chamber operation that is made available inside the cleanroom. The vacuum chamber pressure p_a is constantly measured and displayed on the front panel of LabView program. Once this parameter become less than 50 millibar*, stop the depressurization by turning OFF the pump and manually closing the valve between the vacuum chamber and the pump. The temperature inside the vacuum chamber T_a is also measured by a K-type thermocouple throughout the test campaign.
5	Switch ON the power supply to the Clippard solenoid valve to fully open the feed system. Set a value for the input mass flow rate using the front panel of LabView program and press enter to forward this command to the mass flow controller (MFC). Keep the commanded mass flow rate constant until the system pressure stabilizes. The stability criterion for the system pressure has already been discussed in chapter 5.
6	Once the system pressure gets stabilized, a new value for the input mass flow rate is set and again the system pressure is allowed to stabilize. This step is repeated for different values of mass flow rates.
7	Once the cold gas test campaign of the thruster chip at different mass flow rates is done, input a command of zero mass flow to the MFC so that no further gas enters the system. Stop running the LabView program. Then turn off the power supply to the sensors. And finally, depressurize the vacuum chamber by opening the gas escape passage located on the side panel of the vacuum chamber.

* - The minimum vacuum pressure that can be achieved using the vacuum chamber at the SSE cleanroom is 10 millibar. But since the vacuum chamber pressure sensor was showing erratic reading for pressure levels lower than 50 millibar, we took this reading as the point to stop the chamber depressurization.

6.1.3 Sample test plot of a cold gas test campaign

In this section, we present a sample test plot from a cold gas test campaign performed on MEMS micro-thruster. All the test plots are provided in appendix 7. Each test plot is given a name in the format as follows: **AP_ (month of testing) _ (serial number of the test plot)** where AP stands for appendix. For example, test plot from the cold gas test campaign of chip #14 is given in figure 6.1. This test plot has its identification as **AP_NV_8** in appendix 7 which tells us that this particular test campaign was 8th in the row performed in the month of November.

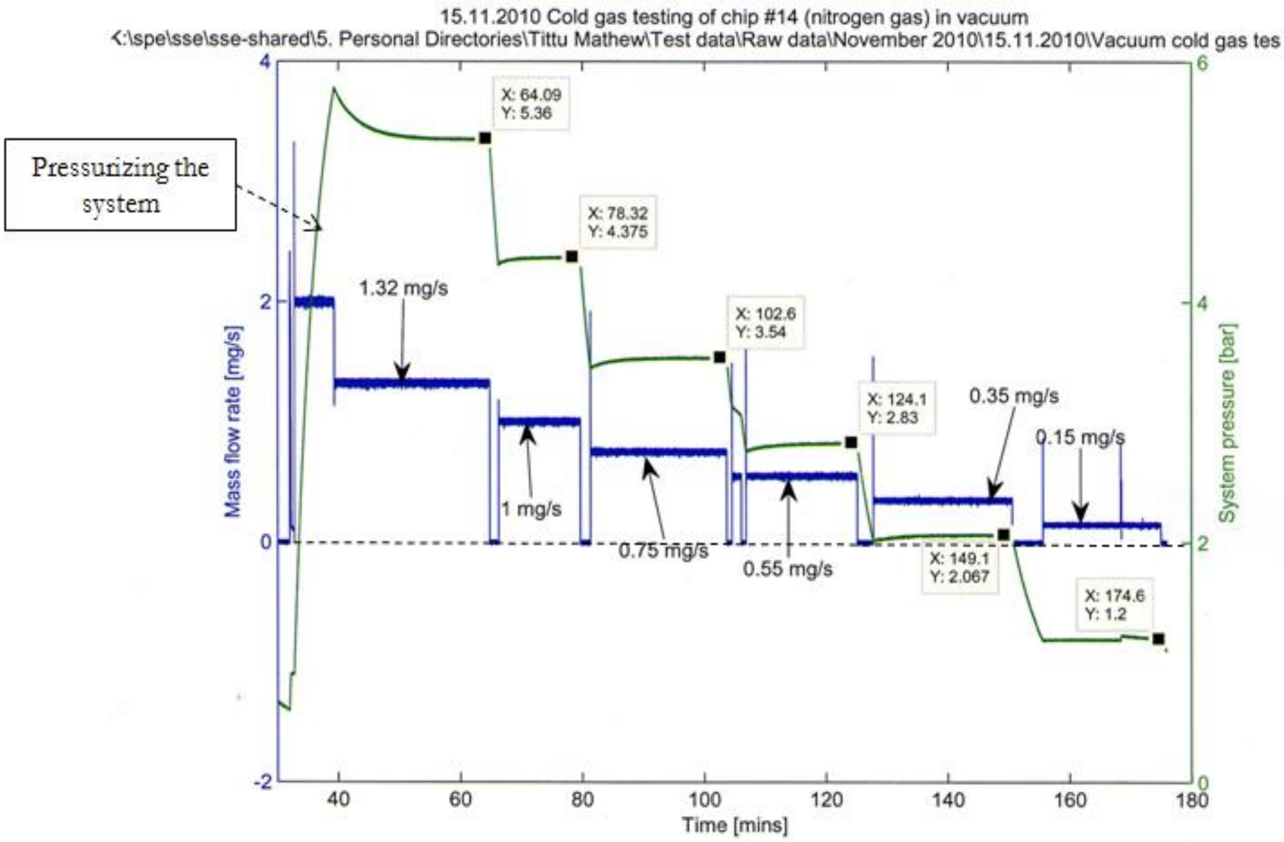

Figure 6.1: Cold gas test plot of thruster chip #14.

Figure 6.1 shows a plot of system pressure (represented by green line with its scale on the secondary Y axis) and mass flow rate (represented by blue line) measured versus time over a period of 3 hours. During the cold gas test campaign of chip #14, six different mass flow rates were tested, starting at a high mass flow rate of 1.32 mg/s and ending with a low mass flow rate of 0.15 mg/s. The minimum mass flow rate through the system is limited to 0.15 mg/s because the difference between the commanded and measured mass flow using the calibrated MFC becomes more than 1 % at lower values. The maximum mass flow rate through the system is limited by the maximum pressure range of 6 bars of the system pressure sensor. New setting for the mass flow rate was commanded using the Labview front panel after which the commanded mass flow rate was kept constant.

From figure 6.1, following points can be noted:

1) The time history (on the X axis) starts at 30 minutes and not from zero. It was during the first 30 minutes that the depressurization of vacuum chamber was carried out with the solenoid valve closed. One can also see the system pressure decreasing during depressurization phase. This is because any residual gas residing inside the feeding system after the solenoid valve, gets sucked out through the micro-nozzle and thereby resulting in a decrease in absolute pressure.
2) The sudden rise in the system pressure around t=32 minutes is due to switching on the solenoid valve soon after the vacuum chamber gets depressurized to 50 millibar.
3) From the plot of the measured mass flow rate, we find that the response of the mass flow rate to the command is nicely block shaped, meaning that the response of the mass flow rate to a change in commanded mass flow rate is quite fast.
4) With each step change in mass flow rate, we find that the system pressure changes. From the system pressure curve, we find that it takes some time for the pressure to adjust to the new mass flow rate before it shows a stable reading. Once a stable pressure reading was achieved, the input mass flow settings were changed and/or the test was ended.
5) We see that the mass flow setting was not immediately switched to a new value after a stable pressure reading; instead it was first switched to zero to quickly bring down the system pressure and thereby cut short the test duration.

6.1.4 Cold gas test data elaboration

Once we have discussed how a sample cold gas test plot looks like, in this section we present the cold gas test results followed by data elaboration. Table 6.2 lists all the thruster chips for which the cold gas testing was performed. Comparing this table with the table 4.3 in chapter 4 listing all the fabricated chips, it can be seen that all thruster chips from wafer #1 were tested with cold gas. Thruster chips from wafer #2 were not tested with cold gas, because of two reasons:

1) Chips fabricated from wafer #2 had the same geometrical features as that of chips from wafer #1, except for the fact that they were fabricated from two different wafers; hence performing any cold gas testing using thruster chips from wafer #2 will only be a case of repetition without gaining additional information from the tests.
2) Marco had pointed out that certain problems were encountered during the fabrication of thruster chips from wafer #2 and hence its geometrical features could be far from the ideal design, though we did not confirm it using Scanning Electron Microscope (SEM).

As a result, none of the chips from wafer #2 were used during the cold gas test campaign. On the other hand, only four thruster chips from wafer #3 were tested with cold gas (chip #14, 15, 17 and 19). Chip #13 was not used for testing as its geometrical features (both in the case of channel and nozzle design) were similar to that of chip #14, except that it had no silicon islands. The same reasoning goes with not performing any cold gas tests on chip #16 when compared with chip #17. Chip #18 got broke while handling during step 15 of the fabrication sequence.

Table 6.2: Thruster chips tested with cold gas along with their geometrical properties

ID	Channel depth H_{ch} [μm]	Number of channels N	Nozzle throat width W_t [μm]	Silicon islands (Yes/No)
	Chips from wafer #1			
6	50	1	10	No
7	50	1	10	No
8	50	1	10	Yes
9	50	1	5	No
10	50	1	5	Yes
11	50	3	10	No
12	50	3	10	Yes
	Chips from wafer #3			
14	150	1	10	No
15	150	1	10	Yes
17	150	1	5	Yes
19	150	3	10	Yes

In the following sub-sections, the presentation and elaboration of test results is done in three parts: section 6.1.4.1 deals with the test results of thruster chips from wafer #1 and section 6.1.4.2 deals with that of thruster chips from wafer #3. The comparison between the test results of thruster chips having deeper and shallow channels is made in section 6.1.4.3.

6.1.4.1 Cold gas test results for thruster chips from wafer #1

Figure 6.2 plots the trend of system pressure against the mass flow rate for all the thruster chips from wafer #1 with the test data presented in tabular form in table 6.3.

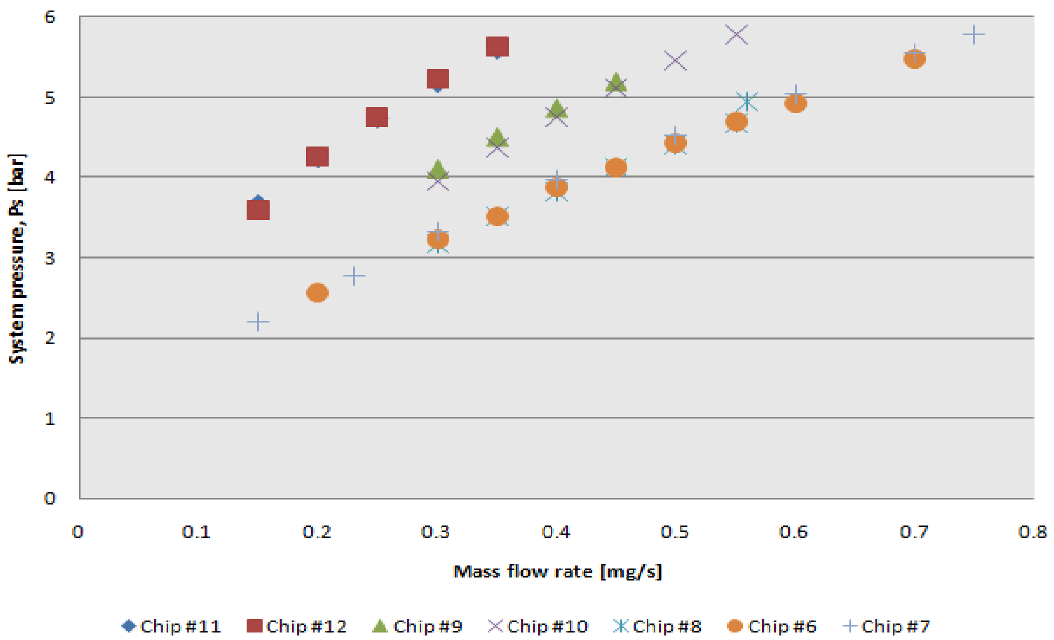

Figure 6.2: System pressure vs. mass flow rate for thruster chips from wafer #1.

Table 6.3: Test data from the cold gas testing of thruster chips from wafer #1.

Mass flow rate, $\dot{m}$ [mg/s]	**Chamber pressure,** p_c [bar]						
	Chip #6	**Chip #7**	**Chip #8**	**Chip #9**	**Chip #10**	**Chip #11**	**Chip #12**
	Reference graph						
	AP_NV_4, AP_NV_5, AP_NV_3	AP_NV_11, AP_NV_12	AP_NV_4	AP_OCT_10, AP_OCT_2	AP_NV_1, AP_NV_2, AP_OCT_5	AP_OCT_11, AP_OCT_12, AP_OCT_4	AP_OCT_9, AP_OCT_8, AP_OCT_3
0.15	-	2.20	-	-	-	3.66	3.59
0.2	2.57	-	-	-	-	4.23	4.25
0.23	-	2.78	-	-	-	-	-
0.25	-	-	-	-	-	4.73	4.75
0.3	3.22	3.33	3.17	4.10	3.96	5.17	5.23
0.35	3.51	-	3.51	4.50	4.37	5.59	5.63
0.4	3.87	3.97	3.83	4.86	4.76	-	-
0.45	4.12	-	4.12	5.19	5.11	-	-
0.50	4.42	4.52	4.40	-	5.45	-	-
0.55	4.69	-	4.69	-	5.78	-	-
0.6	4.93	5.04	-	-	-	-	-
0.7	5.48	5.54	-	-	-	-	-
0.75	-	5.77	-	-	-	-	-

From the bigger picture in figure 6.2, we can observe the following:

1) The system pressure increases with mass flow rate for all the thruster chips.
2) Three channel design gives a consistently higher system pressure for a given mass flow rate than for a single channel design.
3) Thruster chips with smaller throat width produce a consistently higher system pressure than for a larger throat.

By comparing the system pressures at the same mass flow rate for chip #11 and #12 (chips with three channel design and 10 µm nozzle throat width) from table 6.3, we see a maximum difference of less than 2% and within a range of 0.4 to 1.9 %. By performing the same comparison for chip #9 and #10 (chips with single channel design and 5 µm throat width), we see that the differences are in the range of 1.57 to 3.5 %. Similar analysis of the system pressures at a given mass flow rate for chip #6, 7 and 8 (chips with single channel design and 10 µm throat width) shows a maximum deviation of 5 %. These numbers helps us to conclude that the experimental measurements can be reproduced using multiple chips of the same geometry within a difference of less than 5 %.

Taking a deeper look into the test data, we see that among the chips with single channel 10 µm design, chip #7 shows a consistently higher system pressure compared to #6 and #8 for a given mass flow rate; the second highest value is from chip #6 followed by chip #8 showing the lowest. Such a consistent trend in the system pressures of the chips at all tested mass flows can be attributed to slight differences in their fabricated geometry while the same test setup is used. The same reasoning goes for chip #9 showing a consistently higher system pressure than chip #10 and chip #11 showing a consistently higher system pressure than chip #12.

Since we concluded that the system pressures can be repeated for chips with the same geometry within a certain acceptable amount of deviation, we can average those values at a given mass flow rate. In that case, the next step would be comparing the results between chips with different geometries. First we try to compare the system pressure values at the same mass flow rates for chips with single and multi-channel design (chip #11, 12 vs. chip #6, 7 and 8). The three channel design was found to be showing a consistently higher system pressure than the single channel design with difference in the range of 60 to 65%. But based on theory, it should be the other way around where a three channel design should show a lower system pressure compared to a single channel design at a given mass flow rate. Next, we compare the system pressure values at the same mass flow rates for chips with single channel 10 μm and single channel 5 μm designs. The single channel with 5 μm throat width was found to be showing a consistently higher system pressure than the chips with 10 μm throat width, but this time with differences in the range of 23 to 27%.

6.1.4.2 Cold gas test results for thruster chips from wafer #3

In a similar way, the cold gas test results for thruster chips from wafer #3 are plotted in figure 6.3 with the test data presented in table 6.4.

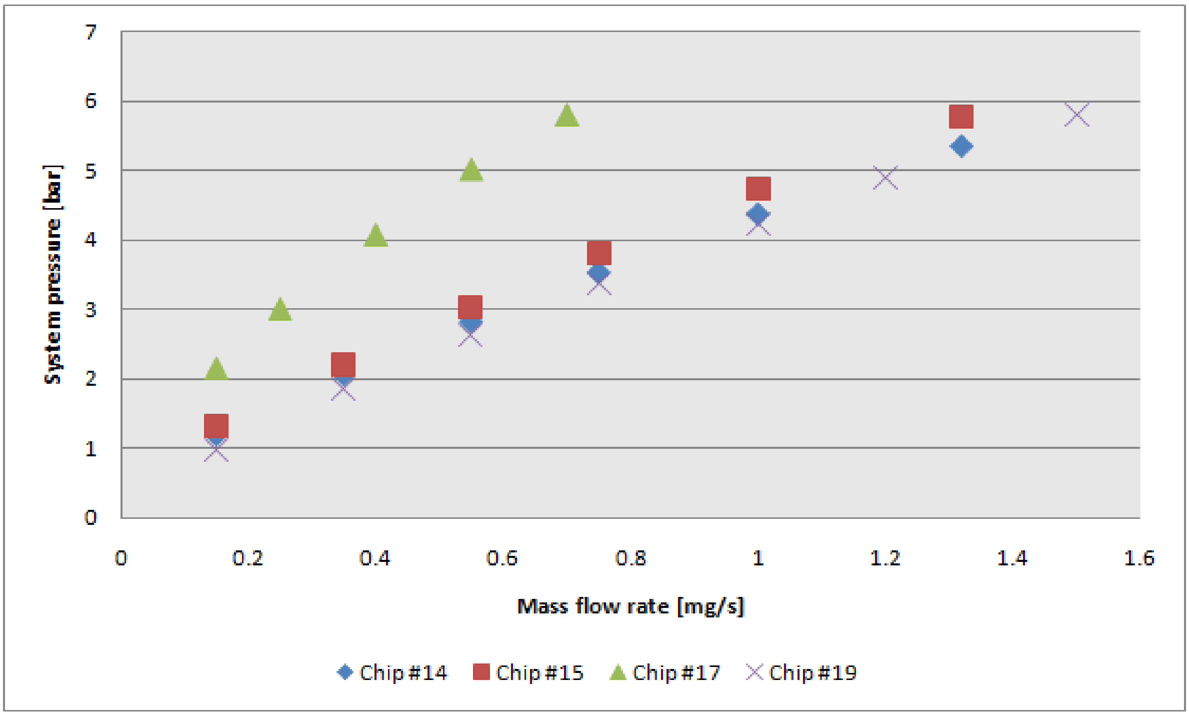

Figure 6.3: System pressure vs. mass flow rate for thruster chips from wafer #3.

Table 6.4: Test data for cold gas testing of thruster chips from wafer #3.

Mass flow rate, $\dot{m}$ [mg/s]	**Chamber pressure,** p_c [bar]			
	Chip #14	**Chip #15**	**Chip #17**	**Chip #19**
	Reference graph			
	AP_NV_8	AP_NV_6 & AP_NV_7	AP_NV_10	AP_NV_9
0.15	1.2	1.33	2.15	0.99
0.25	-	-	3.01	-
0.35	2.07	2.20	-	1.85
0.4	-	-	4.08	-
0.55	2.83	3.04	5.03	2.64
0.7	-	-	5.82	-
0.75	3.54	3.82	-	3.38
1	4.38	4.74	-	4.24
1.2	-	-	-	4.91
1.32	5.36	5.78	-	-
1.5	-	-	-	5.81

From the test data plot in figure 6.3, we can observe the following:

1) The system pressure increasing with mass flow rate for all the thrusters.
2) Micro-thrusters with smaller throat of 5 μm give a consistently higher system pressure than those with larger throat of 10 μm.
3) Three channel design gives a consistently lower system pressure for a given mass flow rate than for a single channel design.

Though we could observe the first and second findings in both cases of deeper and shallow channels, the third finding appears to contradict with what we observed in section 6.1.4.1. In theory, the three channel device should show a lower pressure drop for the same mass flow rate compared to a single channel design with the same cross-sectional area, hence a lower system pressure. Therefore, the test results from chip #19 appear to be more valid from the theoretical point of view.

Repeatability of test measurements could be confirmed only in case of chip #14 and #15. The repeatability was confirmed within a range of 6 to 11 %, which is slightly higher than what was observed for chips from wafer #1. Again, chip #15 was found to be showing a consistently higher system pressure than for chip #14 at all tested mass flow rates, which can be attributed to the slight difference in their fabricated geometry.

By averaging the system pressures for chip #14 and #15 and comparing that with chip #17 at same mass flow rate, we find the chip with smaller throat width shows consistently higher system pressure with the difference in the order of 70%. Next we compare the system pressure for chips with single and multi-channel design with 10 μm throat width. As it was mentioned earlier while discussing the test plot in figure 6.3, the three channel design shows a consistently lower system pressure compared to that of a single channel design at same mass flow rate, with the differences decreasing from 28 % to 8 % with increasing mass flow rate.

6.1.4.3 Comparison of cold gas test results for thruster chips from wafer #1 and #3

Once we have presented and elaborated on the test results of thruster chips from wafer #1 and #3 separately, in this section, we compare their test data to further investigate on the effect of channel depth on the test results. First, the chips with single channel design and 10 µm nozzle throat width are compared; chip #6, 7 and 8 with 50 µm deep channels and chip #14 and 15 with 150 µm deep channels. We find that the chips with deeper channels show consistently lower system pressure at same mass flow rate than for chips with shallow channels, with differences in the range of 57 to 74 %. The lower system pressure for chips with deeper channels can be attributed to their larger throat area for the same throat width, resulting in lower chamber pressure values for the same mass flow rate as per the theory from the lecture notes. Similar trend was also observed in case of chips with single channel and 5 µm throat width designs, but this time the difference was in the range of 15 to 18 %. The largest difference was observed when comparing the chips with multi-channel design with difference of more than 300 %.

6.1.5 Pressure and temperature inside the vacuum chamber

Apart from the system pressure and mass flow rate through the system, both the pressure and temperature inside the vacuum chamber were also measured during a cold gas test campaign. In figures 6.4 and 6.5, the plot history of measured temperature and pressure inside the vacuum chamber are given respectively.

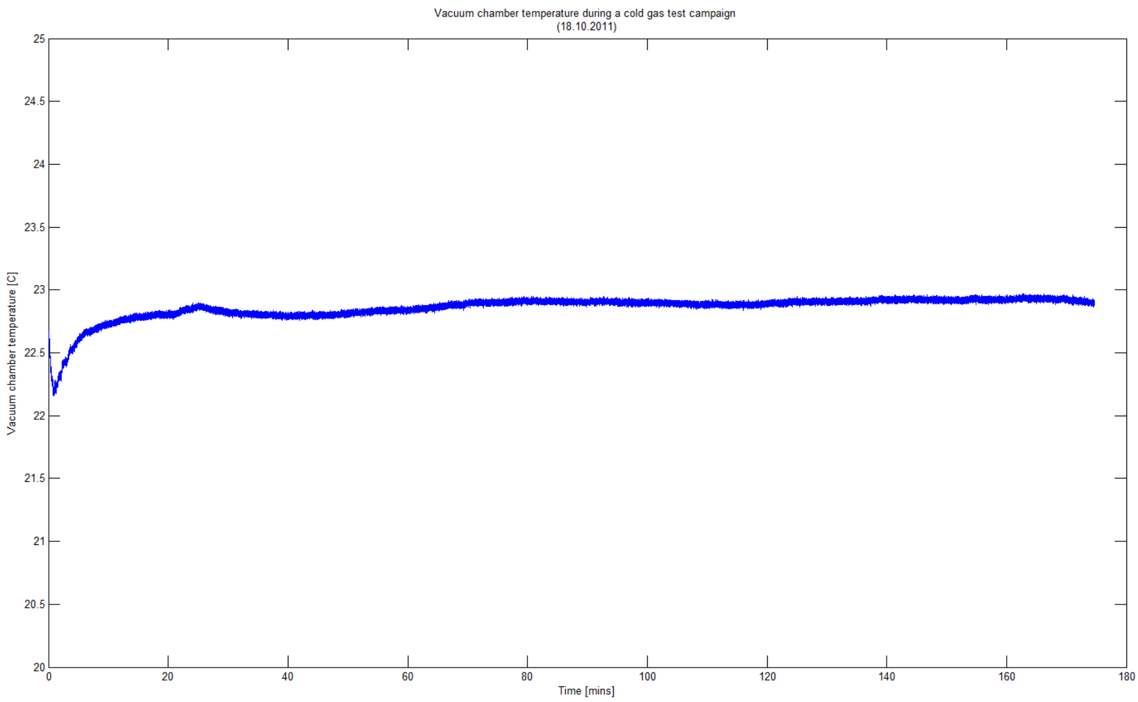

Figure 6.4: Plot history of measured temperature inside the vacuum chamber during a cold gas test campaign.

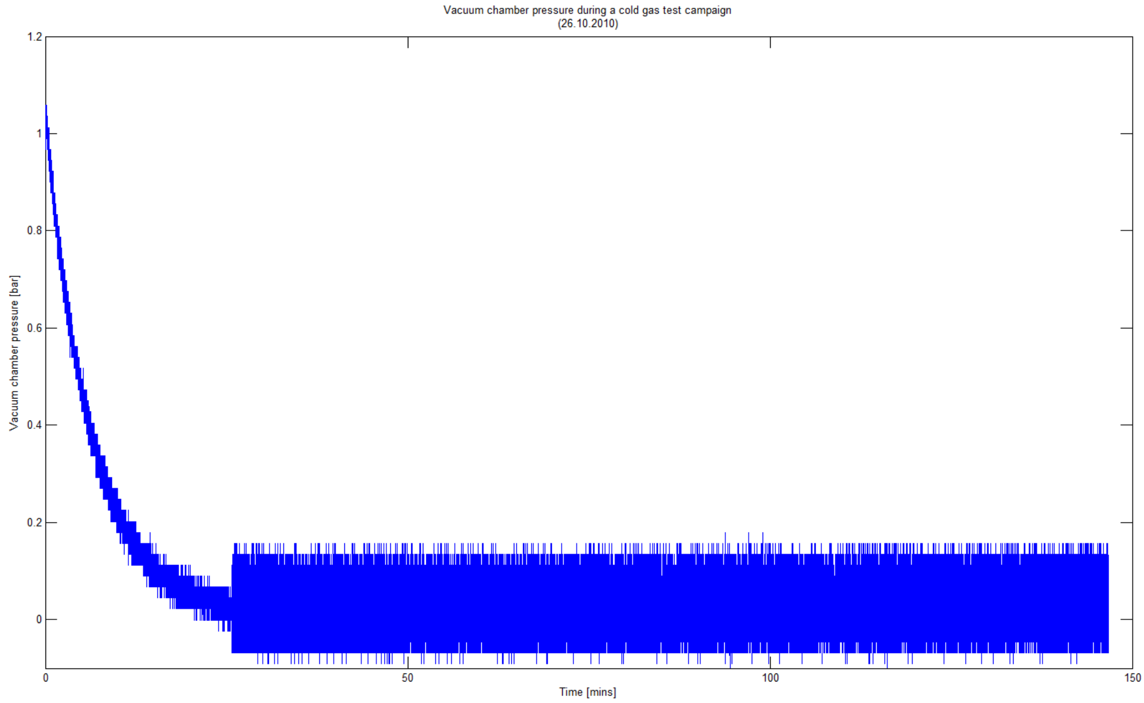

Figure 6.5: Plot history of measured pressure inside the vacuum chamber pressure during a cold gas test campaign.

From figure 6.4, we see that the temperature inside the vacuum chamber remains constant at 23^{o}C throughout the whole test campaign. Figure 6.5 shows the history of vacuum chamber pressure, starting from the point of depressurization when the sensor read-out shows a value of 1 bar at t=0. The sensor readout then decreases with time during the depressurization phase. It takes roughly 30 minutes to depressurize the vacuum chamber to 50 millibar. On the other hand, we see that the noise in the signal increases with decreasing absolute pressure value. Typical accuracy of the selected pressure sensor is given as 0.1% of full scale, which translates to 7 millibar. Hence, the selected minimum limit of 50 millibars is well above what the sensor can accurately measure. The large noise in the signal at low pressure values can be either due to electrical noise, vibrations in the surroundings or due to the selection of a larger range for sensor calibration (0-7 bars) instead of required 0-1 bar. The same trend in both vacuum chamber temperature and pressure measurements was seen in all other cold gas test campaigns.

6.1.6 Calculation of chamber pressure and comparison with the theory

In this section, we calculate the chamber pressure from the measured system pressure for some of the micro-thrusters using the procedure outlined in chapter 5 and later compare the results with its ideal value. Before we proceed, you might have noticed in the test setup shown in figure 5.2 in chapter 5 and also by looking at the simplified schematic diagram of the feed system in figure 6.6 that the MFC which controls the mass flow through the system is situated far from the micro-thruster and there exists a large volume of feed system comprising of flexible viny tubing. Till now for all the calculations, we assumed that the propellant flow rate through the micro-thruster is the same as the output mass flow from the MFC with no leakage in the feed system. But is the case in real scenario? Is there any leakage from the feed system? If yes, then how significant is the leakage? These questions will be answered in the following section.

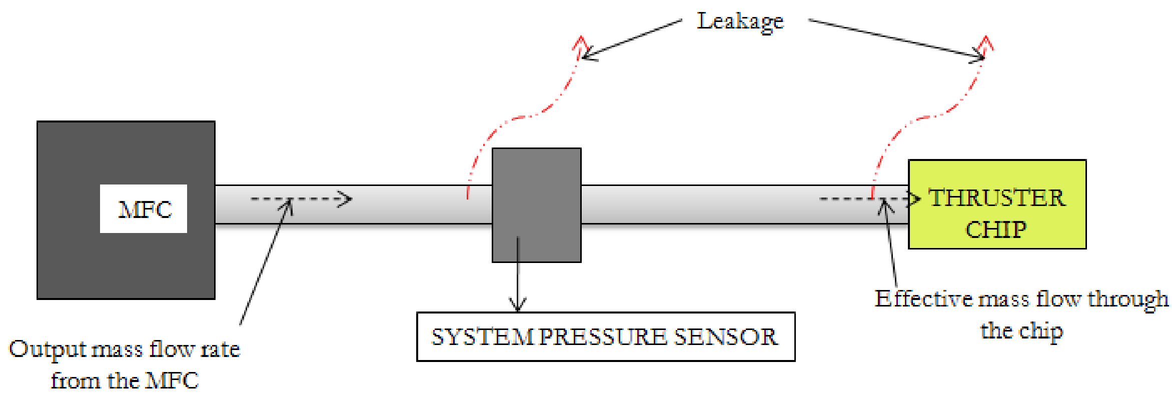

Figure 6.6: Schematic diagram of the feed system between the MFC and micro-thruster.

6.1.6.1 Leakage in the feed system

To find out if there is any leakage in the feed system section during pressurized phase, we did a simple test. For this test, the microthruster at the end of the feed system was replaced by a needle with its tip soldered inorder to prevent any propellant gas escaping from its outlet. The vacuum chamber was then depressurized. The feed system was later pressurized by inputing a certain amount of mass flow rate using the MFC. Once the system was pressurized to a pressure of less than 6 bars, the propellant flow rate into the system was cut off and the system pressure was recorded as a function of time. The plot history of system pressure during the leakage test is shown in figure 6.7. From figure, we see that with time the system pressure decreases. Also, we see that the system pressure decreases in a non-linear fashion, with the highest rate of drop at larger values of system pressures. To calculate the leakage rate at a given system pressure, following relation is used which is a first derivative of the ideal gas law with respect to time:

$$\frac{dp}{dt}V = \dot{m}RT \tag{6.1}$$

$$\Leftrightarrow Leakage = \dot{m} = \frac{\frac{dp}{dt}V}{RT}$$

where R is the characteristic gas constant of the nitrogen gas, T the gas temperature (taken to be the same as the temperature inside the vacuum chamber), V the volume of feed system (equal to 4.8E-5 m^3; refer back to table 5.3 in chapter 5) and dp/dt the instantenous rate of pressure drop at a given system pressure.

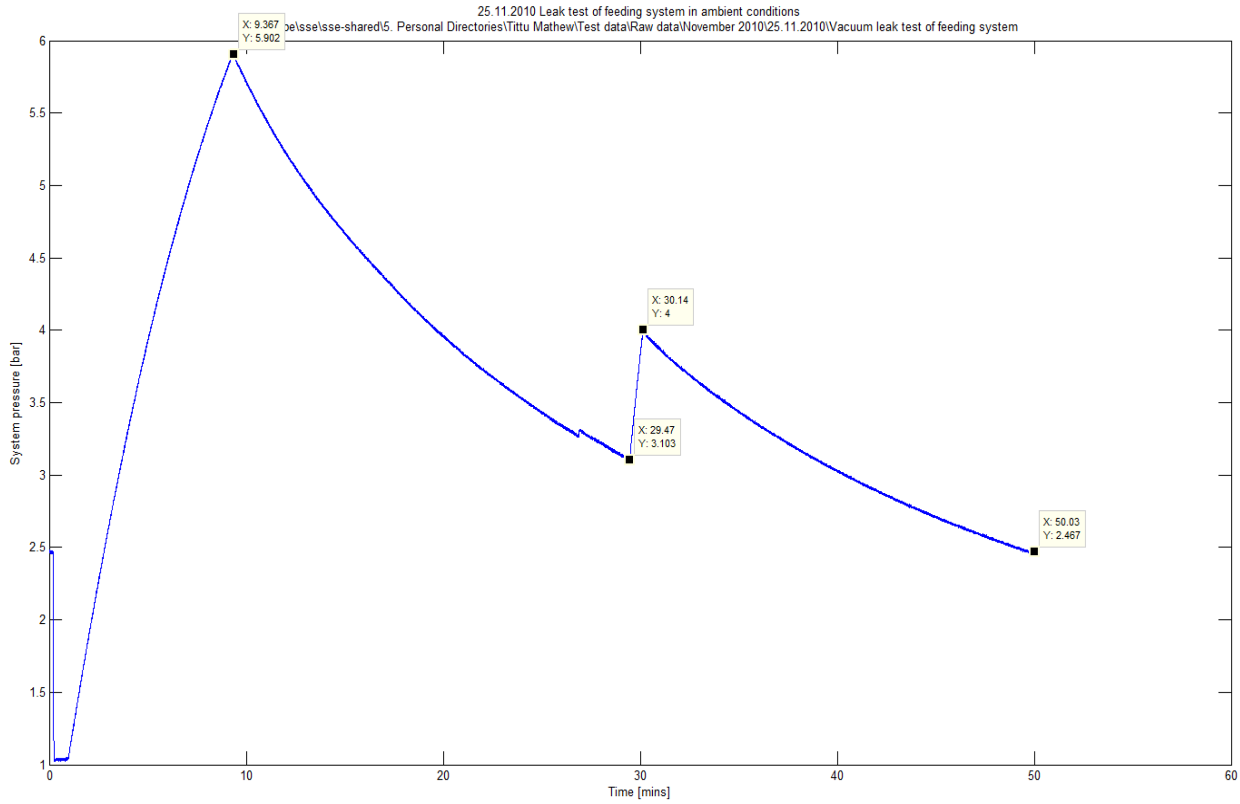

Figure 6.7: Plot history of system pressure during a leakage test of the feed system.

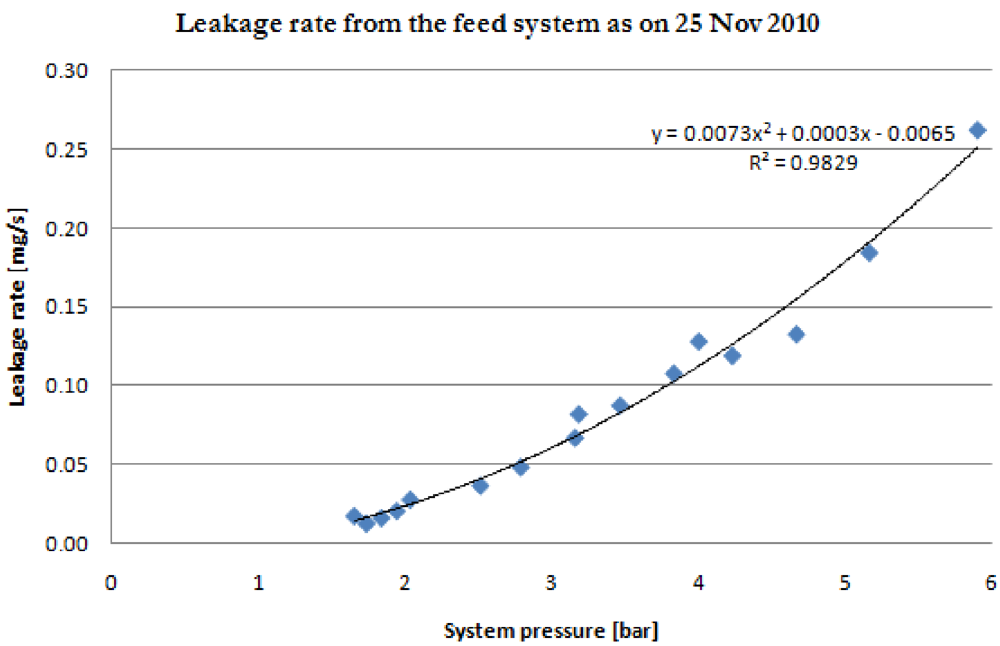

Figure 6.8: Leakage rate vs system pressure.

From the simple test performed, we could confirm that there is leakage in the feed system and its rate increasing with the system pressure. But how significant is the leakage? For that we take the cold gas test results of chip #6, 7 & 8 and calculate the percentage of leakage at each measured system pressure as shown in table 6.5.

Table 6.5: Percentage of leakage w.r.t. to the input mass flow rate at each measured system pressures for chip #6, 7 & 8 at cold gas mode.

Input mass flow rate $\dot{m}$ [mg/s]	**System pressure** p_s [bar]	**Leakage rate** [mg/s]*	**Percentage of leakage with respect to the input mass flow** [%]
0.15	2.18	0.03	19
0.23	2.78	0.05	22
0.3	3.30	0.07	25
0.4	3.97	0.11	27
0.5	4.52	0.14	29
0.6	5.04	0.18	30
0.7	5.54	0.22	31
0.75	5.77	0.24	32

**- Leakage rate at a measured system pressure is calculated by using the relation given in figure 6.8:* $y=0.0073x^2+0.0003x-0.0065$

By looking at the percentage of leakage rate, we see that it varies from 20 to 30% of the commanded input mass flow rate, which is significant and should be taken into consideration for further calculations. The effective mass flow rate through the micro-thruster is from now on determined by subtracting the leakage rate from the input mass flow rate.

6.1.6.2 Calculation of chamber pressure and comparison with the ideal case for Chip #6, 7 & 8

In this section, we calculate the chamber pressure as a function of effective mass flow rate for chip #6, 7 and #8 (single channel design with 10 μm throat width and 50 μm channel depth) and then compare them with the ideal case. The reason why we chose these chips for sample calculation is that we had previously measured their fabricated geometry using SEM technique. The measured values of geometrical features and their deviation from the design value are given in table 6.6.

Table 6.6: Measured values of fabricated micro-geometric features using SEM technique and their deviation from the design value.

Geometry parameter	**Design value**	**Measured value using SEM technique**	**Percentage deviation**	**Comment**
Throat width, W_t	10 μm	9.67 μm	3.4%	Quoted measure value is the average of 9.49 and 9.84 μm.
Channel width, W_c	50 μm	48.1 μm	~4%	-NA-
Channel height, H_c	50 μm	52.2 μm	4.4%	The channel depth value quoted here is that at the center of the channel and it is the same at the nozzle throat.

With the help of the measured values of micro-geometric features and the effective mass flow rate through the micro-thruster at a given system pressure, we calculate the pressure drop in the feed system and in the micro-channels using the excel sheets discussed in chapter 5 and 3 respectively. The ideal chamber pressure is calculated by using the following relation based on the ideal rocket motor theory [6.1]:

$$p_c = \frac{\dot{m}\sqrt{RT_c}}{\Gamma A_t} \tag{6.2}$$

where $\dot{m}$ is the effective mass flow rate, T_c the chamber temperature (taken to be the same as the measured temperature inside the vacuum chamber), A_t the nozzle throat area and Γ the vandenkerckhove function (for nitrogen gas, Γ=0.6847 [6.1]). Figure 6.9 plots the calculated and ideal p_c as a function of effective mass flow rate for micro-thrusters 6, 7 and 8.

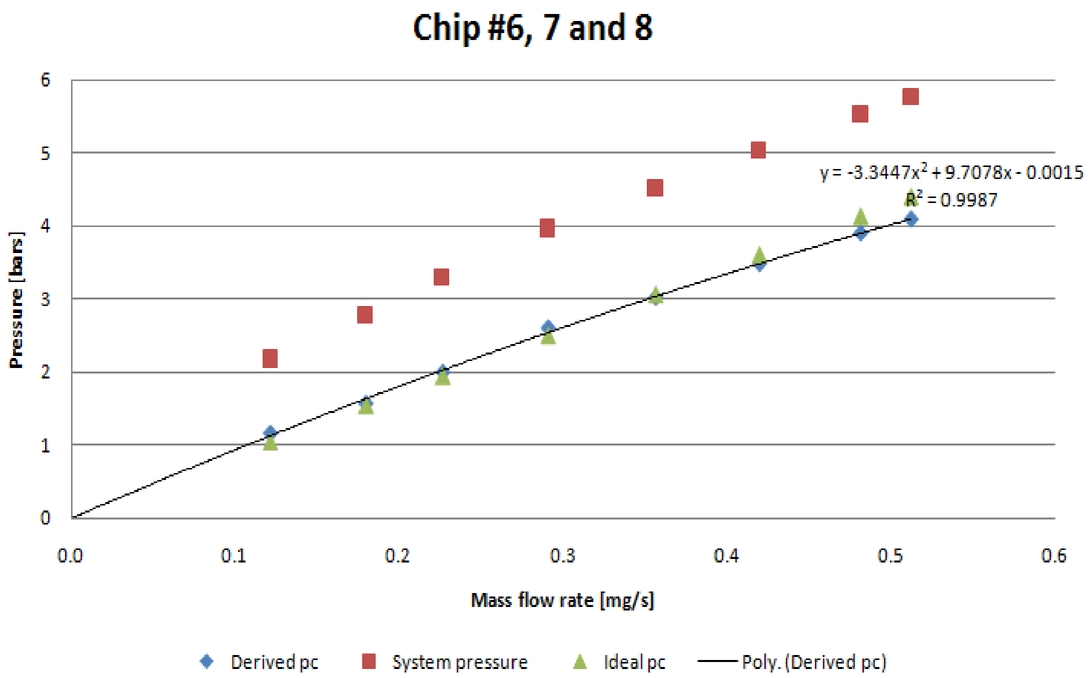

Figure 6.9: Calculated and ideal chamber pressure as a function of propellant flow rate for chip #6, 7 and 8.

From figure 6.9, we notice the following:

1) The difference between the measured system pressure and the derived chamber pressure, or in other words the calculated pressure drop in the feed system is increasing with mass flow rate, from 1 bar at 0.15 mg/s to 1.68 bar at 0.51 mg/s.
2) The derived chamber pressure plot can be best fitted with a second order polynomial which gives a zero chamber pressure when propellant mass flow rate becomes zero. But according to the ideal rocket motor theory, for a given nozzle throat dimensions, chamber temperature and propellant, the mass flow rate should increase linearly with the chamber pressure.

In table 6.7, we compare the derived and the ideal chamber pressures values for the same effective mass flow rates. From the table, we see that the percentage deviation is within a range of 1 to 11%.

Table 6.7: Comparison of derived and ideal chamber pressure for chip # 6, 7 and 8.

Effective mass flow rate $\dot{m}$ [mg/s]	**Derived chamber pressure** p_c [bar]	**Ideal chamber pressure** p_c [bar]	**Percentage deviation** [%]
0.12	1.16	1.04	11
0.18	1.57	1.54	2
0.23	2.00	1.94	3
0.29	2.60	2.49	4
0.36	3.02	3.05	1
0.42	3.48	3.60	3
0.48	3.90	4.13	6
0.51	4.09	4.39	7

6.1.6.3 Calculation of chamber pressure and comparison with the ideal case for chip #19, 17, 14 and 15

In this section, we follow the same procedure outlined in the previous section for comparing the derived and ideal chamber pressure values, but this time for micro-thrusters #19, 17, 14 and 15 having deeper channels. There fabricated micro-geometric features were not measured by using SEM technique. Hence, we will be using their design values for the chamber pressure calculations. In figure 6.10, we compare the derived and ideal chamber pressures of chip #19 (three channel design with 10 μm throat width), while figures 6.11 and 6.12 are for thruster chips with single channel and 10 μm (chip #14 and 15) and 5 μm throat width (chip #17) respectively.

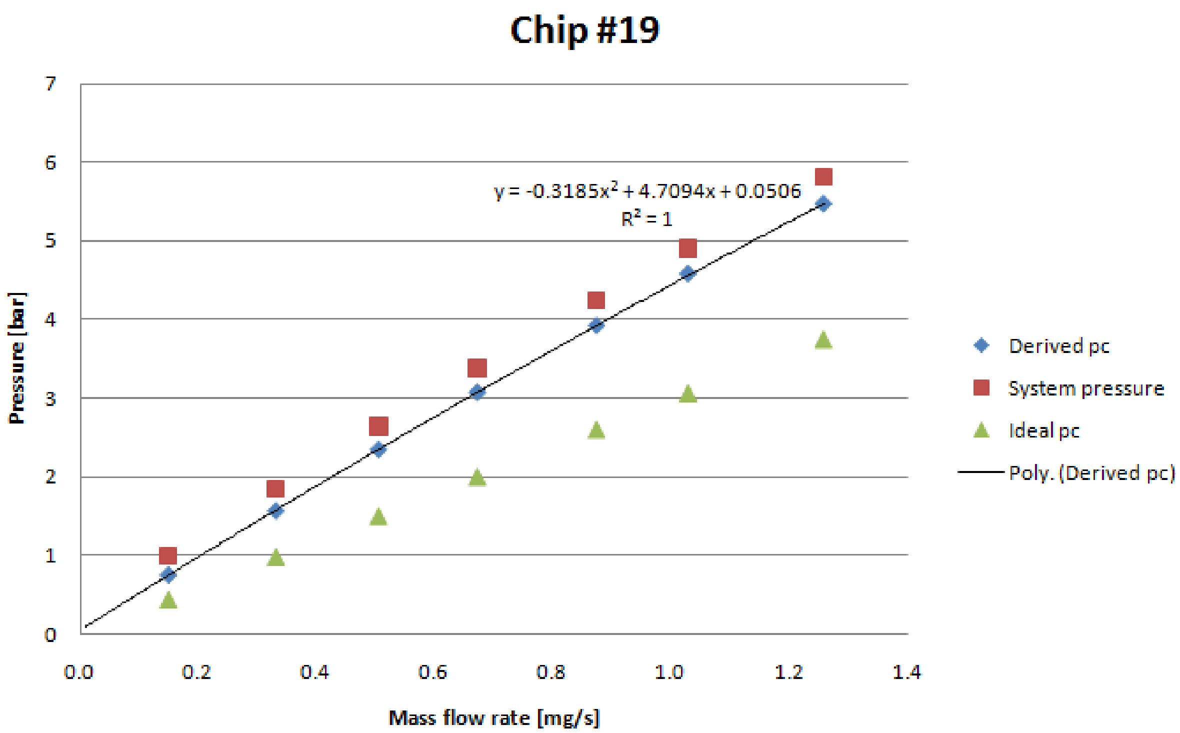

Figure 6.10: Derived and ideal chamber pressure as a function of propellant flow rate for chip #19.

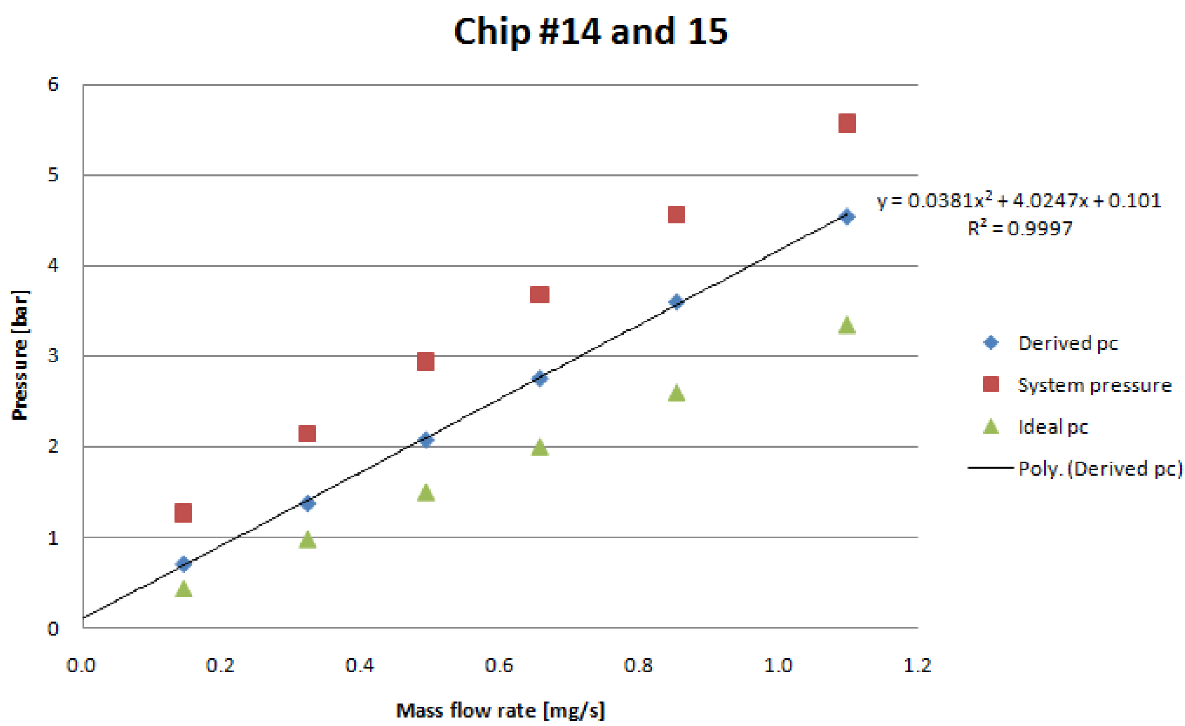

Figure 6.11: Derived and ideal chamber pressure as a function of propellant flow rate for chip #14 and 15.

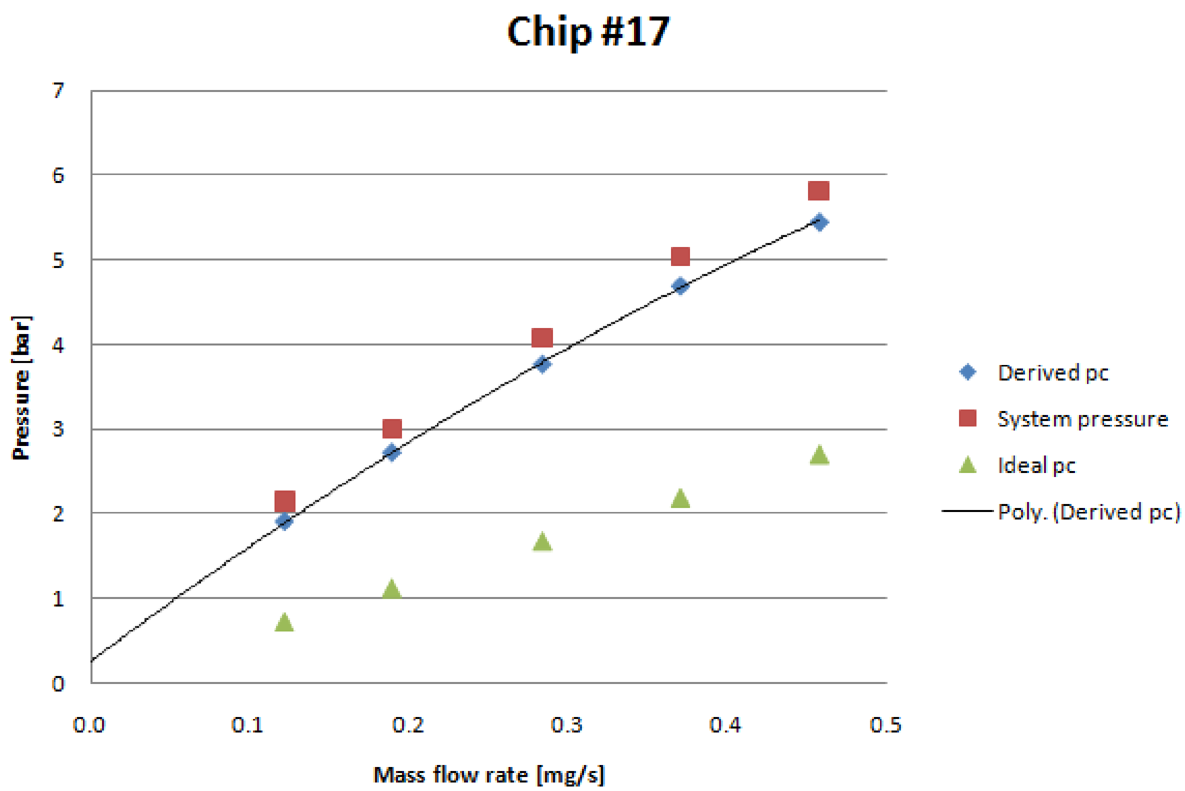

Figure 6.12: Derived and ideal chamber pressure as a function of propellant flow rate for chip #17.

First of all, when comparing the results from the above three figures with that in figure 6.9, we see that the pressure drop or the difference between the measured system pressure and derived chamber pressure is found to be less in case of micro-thrusters having deeper channels and with straight tip needles in the feed system. On the other hand, the difference between the derived and the ideal chamber pressure is increasing with the mass flow rate for all micro-thrusters.

Hereafter, we define this ratio of the ideal to derived chamber pressure as the discharge coefficient of the micro-nozzle, represented as C_d. From the lecture notes [6.1], this nozzle quality factor is defined as the extent to which the effective throat area differs from the geometric throat area due to the formation of boundary layer at the throat, as shown below:

$$C_d = \frac{A_{t,eff}}{A_{t,ideal}} \tag{6.3}$$

Since the mass flow through the micro-thruster was the controlled parameter during the test campaign, the definition of the discharge coefficient can be slightly modified as follows:

$$C_d = \frac{A_{t,eff}}{A_{t,ideal}} = \frac{\dfrac{\dot{m}\sqrt{RT_c}}{\Gamma p_{c,calc}}}{\dfrac{\dot{m}\sqrt{RT_c}}{\Gamma p_{c,ideal}}} = \frac{p_{c,ideal}}{p_{c,calc}} \tag{6.4}$$

The flow Reynolds number at the throat of an extruded nozzle is defined as [6.2]:

$$\mathrm{Re} = \frac{\dot{m}}{H_t \mu} \tag{6.5}$$

where $\dot{m}$ is the mass flow rate, H_t the throat height and μ the propellant gas viscosity at the throat temperature, T_t. The throat temperature is calculated from the chamber temperature T_c by using the relation given below [6.1]:

$$T_t = T_c \frac{2}{\gamma + 1} \tag{6.6}$$

In figure 6.13, the discharge coefficient for micro-thruster chips with deeper channels is plotted against the throat Reynolds number. By looking at the throat Reynolds number, it tells us that the flow is laminar for all designs. We also see that the discharge coefficient is below 1 as per the definition and varies with the Reynolds number. The discharge coefficient for thruster chips with 10 μm throat width is found to be larger than that for 5 μm throat width. Discharge coefficient C_d as low as 40% at Reynolds number less than 100 has been reported in the work of Kuluva et al [6.3]. Such low values of discharge coefficient is due to increased blockage from boundary layer displacement at the nozzle.

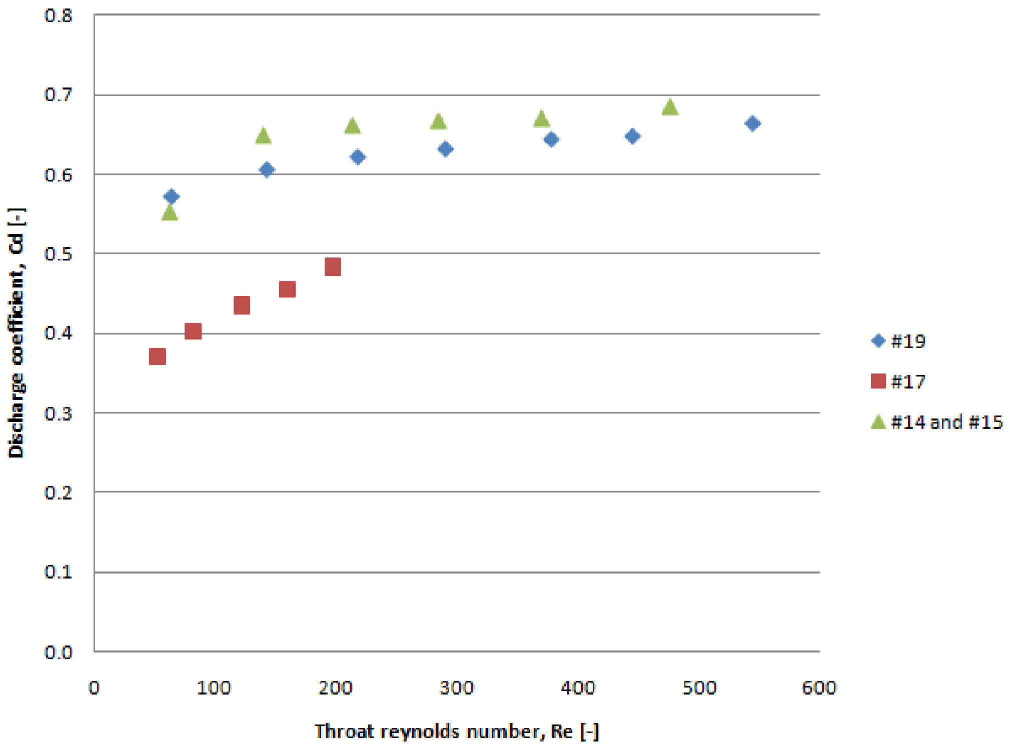

Figure 6.13: Discharge coefficient vs. throat reynolds number for micro-thrusters with deeper channels.

6.2 Hot gas test results

In section 6.2.1, the test parameters and the sensors used to measure them are discussed. The test plan for the testing of a MEMS micro-thruster with propellant heating is given in section 6.2.2. In section 6.2.3, a sample test plot from the hot gas test campaign performed on one of the micro-thruster chips is presented and elaborated. Data presentation and elaboration of the hot gas test results is done in section 6.2.4.

6.2.1 Parameters measured during hot gas tests

For the hot gas testing of a MEMS micro-thruster, apart from knowing the mass flow rate through the chip, system pressure, pressure and temperature inside the vacuum chamber, both the input current and heater voltage has to be measured to quantify the input electric power. To perform these measurements, their corresponding sensors or instruments from table 5.1 is used.

6.2.2 Test plan for hot gas testing of a micro-thruster

Controlled parameters during the hot gas testing are the propellant mass flow rate and the current input to the heater. While the former is controlled using the LABVIEW interface, the later is controlled manually. In this section, we focus on the test procedure to be followed for the hot gas testing of MEMS micro-thrusters. This test procedure is common for all the thrusters irrespective of their identity.

Table 6.8: Test plan for hot gas testing of MEMS micro-thrusters.

Test procedure #	Description
1	Connect the thruster chip to be tested with the feed system inside the vacuum chamber by interlocking the chip needle hub with the tube adaptor of the feed system. Then make electric connections between the gold pads on the thruster chip and the external sourcemeter to supply a set current and to measure the voltage across the heater simultaneously.
2	Close the vacuum chamber. Switch ON the power supply to all the sensors and the test control PC. Before running the LabView program, a new folder is created using the VI to write the data to a file in computer. The date of testing is given as the name of the folder. All the test results can be retrieved using this directory path: k:\spe\sse\sse-shared\3.PersonalDirectories\Tittu Mathew\Test data\Raw data. Turn open the outlet of the pressurized gas cylinder and adjust the pressure regulator manually in such a way that the mechanical pressure gauge at the outlet of the regulator shows a relative pressure reading of 5±0.5 bars.
3	Run the LabView program. Input a command of zero mass flow to the MFC through the front panel. Then turn OFF the power supply to the Clippard solenoid valve placed inside the vacuum chamber to fully close the feeding system part in between the MFC and the valve.
4	Start de-pressurising the vacuum chamber by powering ON the vacuum pump after manually opening the valve between the vacuum chamber and the pump and closing the gas escape passage. The vacuum chamber pressure p_a is constantly measured and displayed on the front panel of LabView program. Once this parameter become less than 50 millibar stop the depressuration by turning OFF the pump and manually close the valve between the vacuum chamber and the pump. The temperature inside the vacuum chamber T_a is also measured by a K-type thermocouple throughout the test campaign and is also displayed in the front panel of the LABVIEW program.
5	Set an input current of 0.1 mA using the sourcemeter and input that to the aluminium heater by pressing on the "OUTPUT ON/OFF" button on the front side of the Keithley sourcemeter. The calculated heater resistance from the measured voltage and set input current will be displayed on the front panel of the sourcemeter. Manually record the the heater resistance $R(T_a)$ and the vacuum chamber temperature T_a into an EXCEL spreadsheet. A seperate spreadsheet is created for the hot gas testing of each micro-thruster with the chip number as the name of the file. All the excel spreadsheets for hot gas tests can be retrieved using the following directory path: k:\spe\sse\sse-shared\3.PersonalDirectories\Tittu Mathew\Test data\Excel sheets. Using the measured heater resistance $R(T_a)$ from step 5 and vacuum chamber temperature T_a from step 4, calculate the heater resistance at 0^oC by using the relation*:

Test procedure #	Description
	$$R\left(T=0^{0}C\right)=\frac{R(T_{a})}{\left(1+\alpha T_{a}\right)} \quad (6.7)$$ Using this value of resistance and a reference temperature of 0°C, develop a linear temperature model of heater temperature as a function of heater resistance by using relation 5.1.
6	Start the measurements by inputing a current of 10 mA using the sourcemeter and increment the current level in steps of 10 mA for each measurement. Record the measured heater voltage, calculated heater resistance, electric input power and heater temperature for each set current into the excel spreadsheet. Plot the recorded input power as a function of heater temperature.
7	Cut off the current supply to the heater by turning off the "OUTPUT ON/OFF" button on the front side of the Keithley sourcemeter. Switch on the power supply to the Clippard solenoid valve to fully open the feed system. Set a value for the input mass flow rate using the front panel of LabView program and press enter to forward this command to the MFC. Keep the commanded mass flow rate constant until the system pressure stabilizes.
8	Then switch on the power supply to the heater and manually set the input current level using a control knob in Keithley sourcemeter until the heater resistance corresponding to a pre-defined heater temperature is reached. Keep the commanded mass flow rate the same as in step 7 while the system pressure stabilizes for the new heater temperature**. This step is repeated for different value of heater temperatures.
9	Once the hot gas test campaign of the thruster chip at different mass flow rates and heater temperatures is done, turn off the power supply to the heater and input a command of zero mass flow to the MFC. Stop running the LabView program. Then turn off the power supply to the sensors. And finally, depressurize the vacuum chamber by opening the gas escape passage located on the side panel of the vacuum chamber.

* -In a linear temperature model, both $R(T_0)$ – resistance at reference temperature T_0 and TCR – temperature coefficient of resistance are dependent on the reference temperature level – T_0. TCR gives the relative change (the first derivative) of the resistance at the T_0. In a linear model, first derivative is constant and same for all the points in a valid range. However, R_0 is always calculated for the reference T_0. In most of the cases, T_0 is chosen to be 0°C, rather than the room temperature level; because the latter one is not standardized (room temperature can be 20°C, 23 °C and 25 °C). In our case, TCR value was provided for the model with T_0=0°C, and therefore, we needed to take 0°C for the reference value as well.

** - While carrying out similar tests in future in a much more efficient manner, the author advices to control the external sourcemeter using a LabView program and develop a Proportional-Integral-Derivative (PID) control to automatically adjust the input current level to achieve the required heater resistance.

6.2.3 Sample test data and plot of a hot gas test campaign

In this section, we present the test data and test plots from the hot gas test campaign performed for chip #19. In figure 6.14, the heater temperature is plotted against its resistance. We see that it follows a linear trend and the corresponding equation is:

$$T_h=4.5312\ R - 232.56 \tag{6.8}$$

where R is the heater resistance in ohms and T_h the heater temperature in ^oC. Heater output voltage, resistance, temperature and electric input power are tabulated in table 6.9 for each input current level. Input electric power is plotted as a function of heater temperature in figure 6.15 and the data fits well with a 2nd order polynomial as given below:

$$P_{el}=9E\text{-}6.T_h^{\,2}+0.0043.T_h-0.1097 \tag{6.9}$$

where P_{el} is the electric input power in Watts and T_h the heater temperature in ^oC.

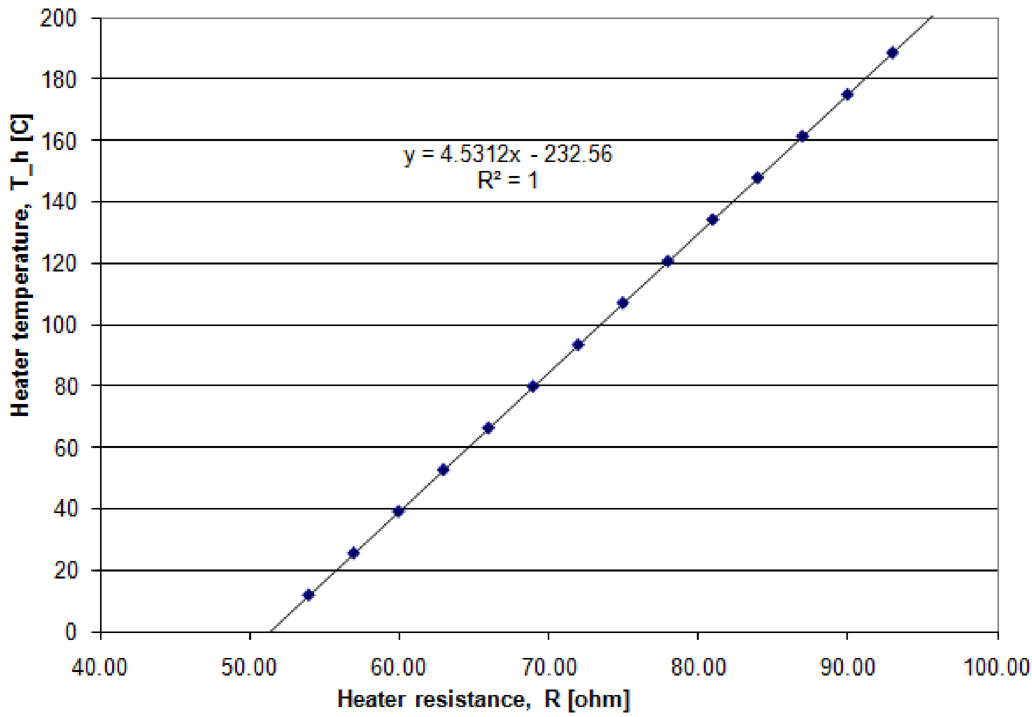

Figure 6.14: Heater temperature Vs electric resistance for chip #19.

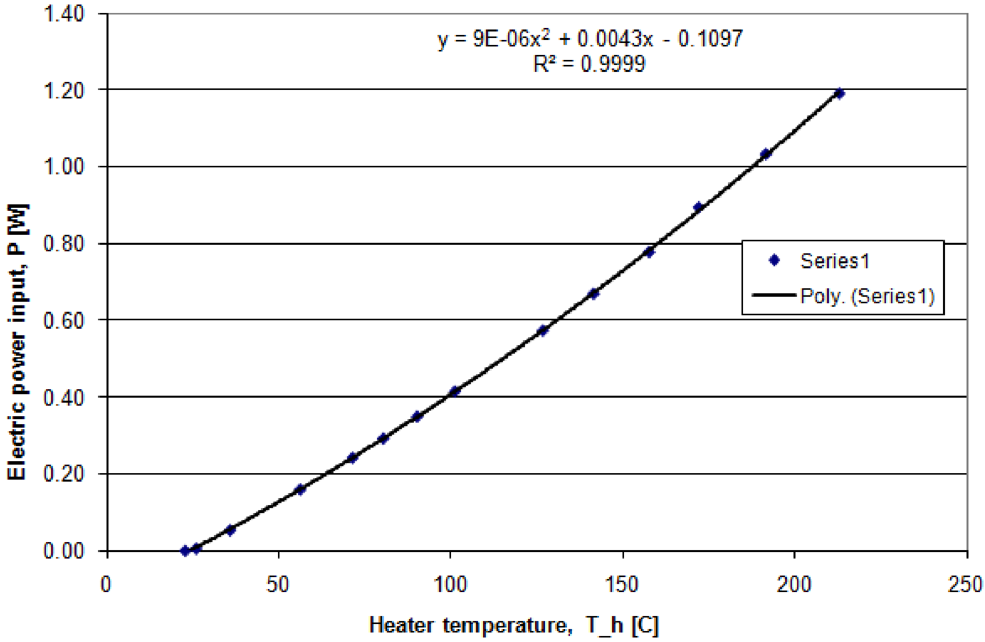

Figure 6.15: Electric input power as a function of heater temperature for chip #19.

Table 6.9: Measured heater output voltage, calculated heater resistance and temperature and electric input power for each input current level for chip #19.

Input current I [mA]	**Heater resistance,** R [Ω]	**Output voltage,** V	**Heater temperature,** T_h [°C]	**Electric input power,** P [W]
0.1	56.40	0.01	23.00	0.00
10	57.09	0.57	26.13	0.01
30	59.27	1.78	36.00	0.05
50	63.76	3.19	56.35	0.16
60	67.11	4.03	71.53	0.24
65	69.08	4.49	80.46	0.29
70	71.26	4.99	90.33	0.35
75	73.67	5.53	101.25	0.41
85	79.31	6.74	126.81	0.57
90	82.55	7.43	141.49	0.67
95	86.11	8.18	157.62	0.78
100	89.30	8.93	172.08	0.89
105	93.60	9.83	191.56	1.03
110	98.30	10.81	212.86	1.19

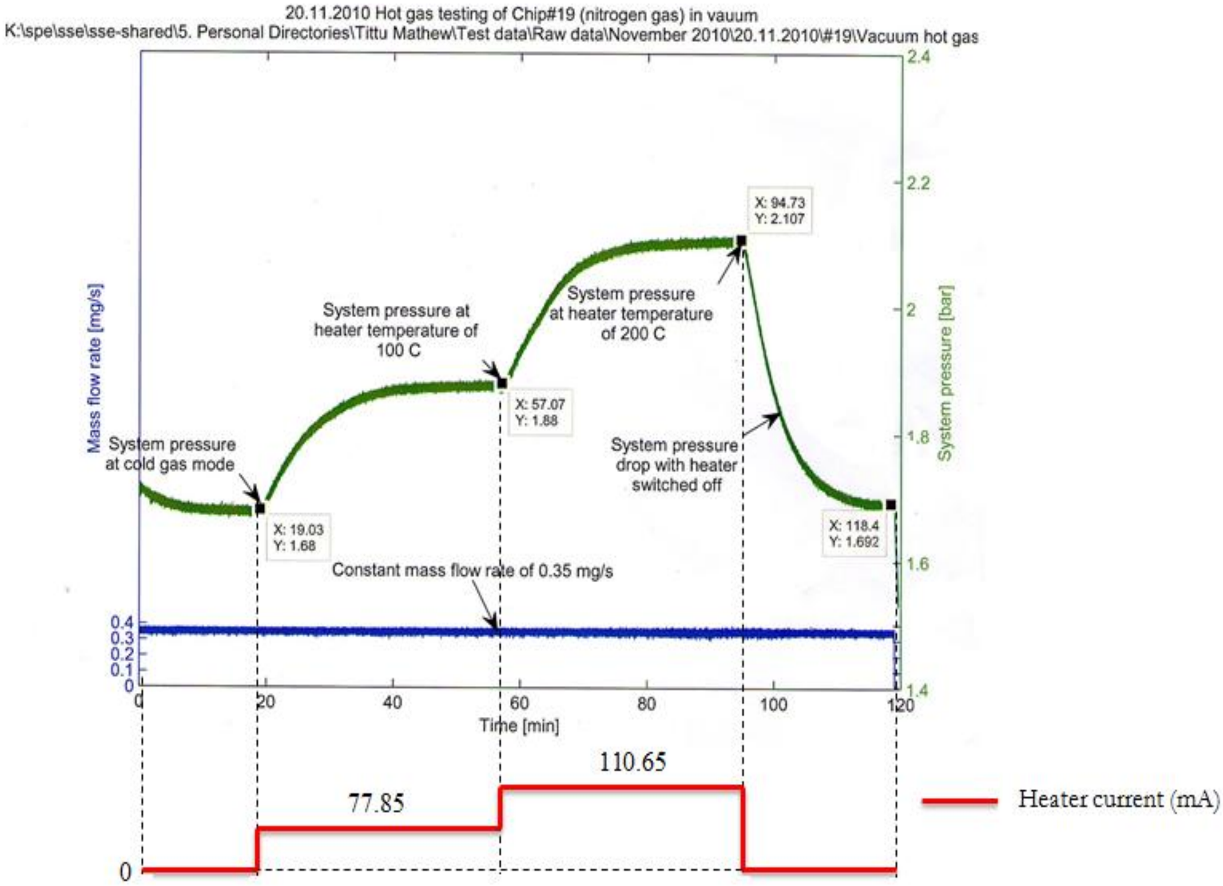

Figure 6.16: Test plot from the hot gas test campagn performed on chip #19 at vacuum conditions.

Figure 6.16 shows the test plot from the hot gas test campaign performed on chip #19 at vacuum conditions. The plot ID is AV_NV_15 in appendix 7. It shows a plot of measured system pressure and mass flow rate over time for a period of 2 hours. Also included in the plot is the history of heater current (highlighted in red). During the test campaign, the mass flow rate through the chip is kept constant at a randomly selected value of 0.35 mg/s while the micro-thruster chip is heated to two different heater temperatures - 100 and 200 ^{o}C. During the initial part of the test campaign, the current supply from the sourcemeter is turned off and the system pressure is allowed to stabilize for the set mass flow rate.

Then the sourcemeter output is switched on and the current input is manually increased in order to achieve a heater resistance value of 73.39 Ω that corresponds to a heater temperature of 100 ^{o}C, while still keeping the mass flow rate unchanged. From table 6.9, we see that to achieve a heater temperature of 100 ^{o}C with no propellant flow through the chip, the input current should be around 75 mA. With propellant flow through the chip, we require an input electric power larger than 0.41 W to achieve a heater temperature of 100^{o}C. This translates to a value of input current larger than 75 mA. Based on the studies performed in section 3.2 in chapter 3, we see that to heat a nitrogen gas propellant flow rate of 0.35 mg/s from an initial temperature of 25^{o}C to 100^{o}C, a heating power of 27.27 mW is required. This heating power is the same as the difference in input electric power to achieve a heater temperature of 100^{o}C with and without propellant heating, as shown below:

$$27.27E\text{-}3\ \text{W} = P_{el,\,with\ mass\ flow}(T_h=100^oC) - P_{el,\,without\ mass\ flow}(T_h=100^oC)\quad \text{W} \tag{6.10}$$
$$\leftrightarrow 27.27E\text{-}3\ \text{W} = I^2.(73.39\ \Omega) - 0.41\ \text{W}$$
$$\leftrightarrow I = 0.077\ \text{A} = 77.19\ \text{mA}$$

From the calculations, we see that a new input current level of 77.19 mA is required to achieve a heater temperature of 100°C with nitrogen gas flow rate of 0.35 mg/s. Keep in mind that no dedicated controller software was developed to keep the temperature of the device at a constant value; instead this parameter was controlled manually by constantly adjusting the heater resistance value at 73.39 Ω as the systems pressure stabilizes. In figure 6.16, the input current history is shown as a straight line which is not the real case, and also the recorded input current level is 77.85 mA which is slightly larger than the predicted value.

Once a stable system pressure reading is achieved at a heater temperature of 100°C, the input current setting is again changed, this time to achieve a higher heater temperature of 200°C. The predicted new input heater current to achieve a heater temperature of 200°C with a nitrogen gas flow rate of 0.35 mg/s is 110.91 mA which is slightly larger than the recorded input current of 110.65 mA from figure 6.16. Once a stable pressure reading is reached for a heater temperature of 200°C, the sourcemeter output is switched off and the system pressure is allowed to stabilize with no current input to the heater and keeping the mass flow unchanged. Towards the end of the test campaign, a command of zero mass flow is fed to the MFC to stop the gas flow through the system.

From figure 6.16, following points can be noted:

1) The time history starts at zero. One can see that the system pressure is already greater than 1 bar at the beginning of the test campaign and that the mass flow rate through the system is already set at 0.35 mg/s. This is because the system was already pressurized by setting a mass flow rate of 0.35 mg/s and then the LabView program that controls the test was abruptly stopped from running due to a human error.
2) The stabilized system pressure recorded for a mass flow rate of 0.35 mg/s at cold gas mode is 1.68 bars. Comparing this value with the system pressure recorded during the cold gas test campaign of chip #19 with the corresponding mass flow rate from table 6.4, we see a difference of 0.17 bar (or 10%).
3) With each step change in heater input current, we find that the system pressure changes. From the system pressure curve, we find that it takes some time for it to adjust with the new heater setting before it reaches a stable value. Once a stable pressure was obtained, the heater input settings were changed.
4) Based on the recorded heater current of 77.85 mA, we calculate an input heating power of 34.49 mW as follows:

$$P_{heat}=(77.85E\text{-}3)^2\,\text{x}\ 73.39 - 0.41$$
$$\leftrightarrow P_{heat} = 0.034\ \text{W} = 34.49\ \text{mW}$$

This heating power corresponds to the power required to heat the nitrogen gas at a mass flow rate of 0.35 mg/s from an initial temperature of 298.15 K to 392 K. Comparing this final fluid temperature with that of the heater temperature (100°C), we see that the fluid flow is getting heated to a temperature larger than that of the heater, which cannot be possible. On the other hand, based on the recorded heater current of 110.65 mA, we calculate an input heating power of 58.46 mW, which translates to a final fluid temperature of 185°C which is lower than that of the heater temperature (200°C).

6.2.4 Hot gas test data elaboration

Once we have studied how a sample test plot from a hot gas test campaign looks like, in this section we present the test results obtained during the hot gas testing of some of the MEMS micro-thrusters followed by data elaboration. But before we step into the test result discussion, first the challenges faced during the hot gas test campaign are highlighted, especially with regard to the proper functioning of the heater and keeping the thin aluminium bond wires between the contact pads on the chip and the gold pads on the PCB intact during handling. In some other chips, the aluminium heater was found to be not working and was found to be showing an open circuit when an external power was applied across it. On closer inspection of MEMS micro-thruster chips from wafer #1 under a microscope, we were able to assess the damage to the heater layer and they are reported in table 6.10.

Table 6.10: Heater conditions of thruster chips.

Chip #	Heater conditions
6	I+ bond wire damaged. Heater surface not clean due to the presence of leakage spray. Small aluminium heater layer missing near the corner at one spot along the heater.
7	V^+ bond pad on the device was damaged.
8	Heater looks intact except but was found to show open circuit when connected to an external power supply.
9	This was taken out of the lot as the channel was found to be blocked.
10	V^+ needs preparation with wire bonding; scratch in the heater.

From the table above, we see that most of the thruster chips had a damage either with their bond pads on the chip/PCB or with the heater layer. The cause for the damage to the bond pad's was due to the repeated wire bonding which was done everytime when the thin bond wires gets damaged. The cause for the cracks and for small portion of the heater missing can be either due to the difference in thermal expansion of aluminium and silicon or can be a manufacturing defect. Usage of spray to detect the spot of leakage in the feed system close to the thruster vicinity was found to be not advisable. As a result, testing of those damaged chips at high temperatures was never done.

Table 6.11 lists all the thruster chips for which the hot gas testing was performed, along with their design value of geometric features.

Table 6.11: Geometrical features of the thruster chips used in hot gas test campaign.

ID	Channel depth H_{ch} [μm]	Number of channels N	Nozzle throat width W_t [μm]	Silicon islands (Yes/No)
Chips from wafer #1				
11	50	3	10	No
Chips from wafer #3				
14	150	1	10	No
17	150	1	5	Yes
19	150	3	10	Yes

From the table above, we see that only chip #11 from wafer #2 was used for the hot gas test campaign. Chip #12 was not used for testing as it had the same geometrical features as that of chip #11, except for its silicon islands. On the other hand, three thruster chips from wafer #3 were tested with hot gas (chip #14, 17 and 19).

Figure 6.17 plots the system pressure as a function of heater temperature at a given mass flow rate for the four selected micro-thrusters. The test data is presented in tabular form in table 6.12.

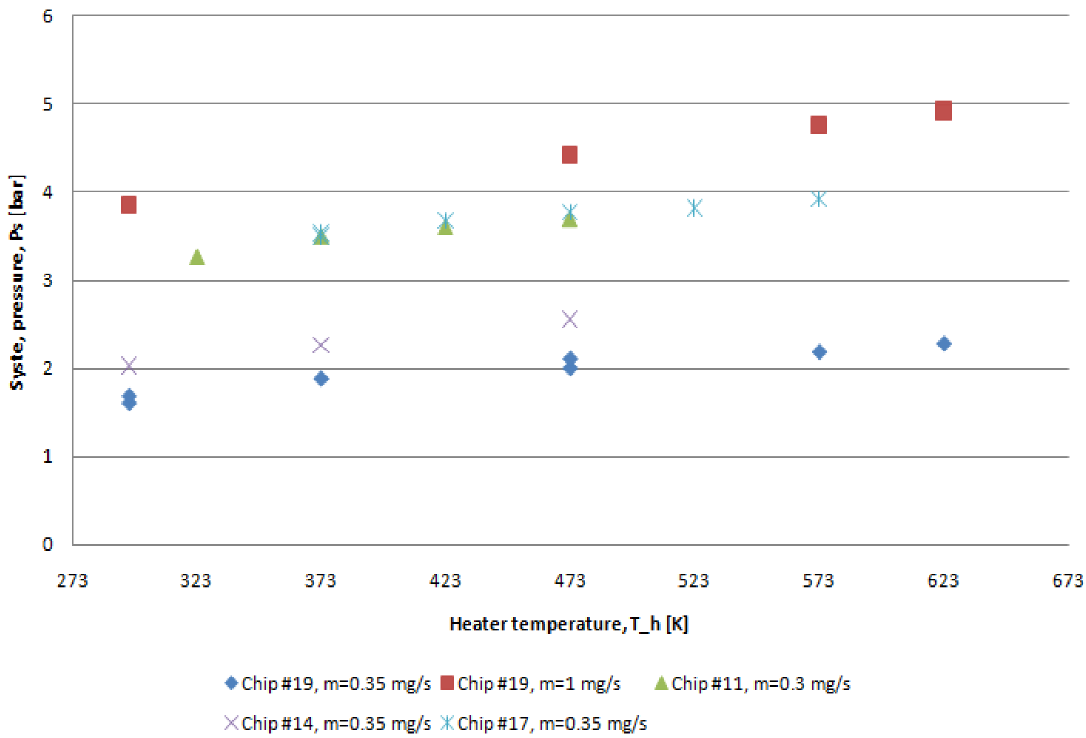

Figure 6.17: System pressure vs. heater temperature at different mass flow rates for thruster chips #19, 11, 14 and 17.

Table 6.12: Test data from the hot gas testing of thruster chips #19, 11, 14 and 17.

Heater temperature T_h [^oC]	**System pressure,** p_{sys} [bar]				
	Chip #19 (m=0.35 mg/s)	**Chip #19** (m=1 mg/s)	**Chip #11** (m=0.3 mg/s)	**Chip #14** (m=0.35 mg/s)	**Chip #17** (m=0.35 mg/s)
23	1.64	3.86		2.03	
50			3.26		
100	1.88		3.50	2.27	3.50
150			3.61		3.68
200	2.05*	4.42	3.70	2.56	3.77
250					3.82
300	2.19	4.76			3.92
350	2.29	4.92			

**- The reported value is the average of two system pressures recorded at the same mass flow rate and heater temperature during two different hot gas test campaign performed in different dates.*

From figure 6.17, we see that the system pressure is increasing in a linear fashion with the heater temperature for a given propellant mass flow rate for all the micro-thrusters. From the calculated heater temperature values plotted along the x-axis, we see that that the highest temperature to which MEMS thruster chips were heated was roughly 4% higher than the requirement. On a close look, we see that:

1) Chip #17 shows a higher system pressure compared to chip #14 and 19, for the same mass flow rate and heater temperature. This is due to the larger chamber pressure at smaller throat area for chip #17 (A_t=750 μm^2, design value) compared to that of chip #14 and 19 (A_t=1500 μm^2), as per the ideal rocket motor theory. When comparing the system pressure values for chip #14 and 19, we see that the system pressure is consistently higher in the former by a percentage of 20 to 25 %. This highlights the advantage of going for a multi-channel design over a single channel with same cross-sectional area.
2) Table 6.12 contains the values of system pressure at cold gas mode for chip #19 and 14 at 0.35 mg/s and chip #19 at 1 mg/s. Now, comparing this value with their respective system pressures recorded during the cold gas test campaign for the same mass flow rate from table 6.4, we see that the current set of values is consistently lower by a percentage within a range of 2 to 13%.

Once the system pressure trend with heater temperature is presented and elaborated, the next step is to study the heater performance in terms of total electric input power to heat the propellant flow to the heater temperature. In figure 6.18, the electric input power is plotted against the heater temperature for a given mass flow rate for four selected thruster chips. The test data is presented in a tabular form in table 6.13.

From figure 6.18, we find that the total input electric power increases with the heater temperature for all the test cases. The trend can be fitted with a second order polynomial with good fit. One major point that is evident from the figure is that a maximum heater temperature of 623 K (= 350 ^oC) could be achieved with a total electric input power of less than 3 W. Though this is value is three times higher than what was required, such power levels falls within the power budget of micro-spacecrafts belonging to class-II (refer back to table 1.1 in chapter 1). Keep in mind that the highest recorded heater temperature of 623 K is only 2/3rd of the maximum achievable heater temperature limited by the melting point of aluminium (melting point of aluminium is 933.47 K [6.4]). Neglecting the differences between the total electric input power at the same heater temperature and propellant mass flow rate for different thruster chips, the data can be fitted with a second order polynomial, $y=1E\text{-}5x^2-0.0016x-0.4536$ (R^2=0.9937). By playing around with this trend equation, a heater temperature of 933 K can be achieved with an input power of less than 7 W. On a closer inspection, we find that for the same propellant mass flow rate and heater temperature, chip #14 requires a consistently higher input electric power, followed by chip #19 and then #17.

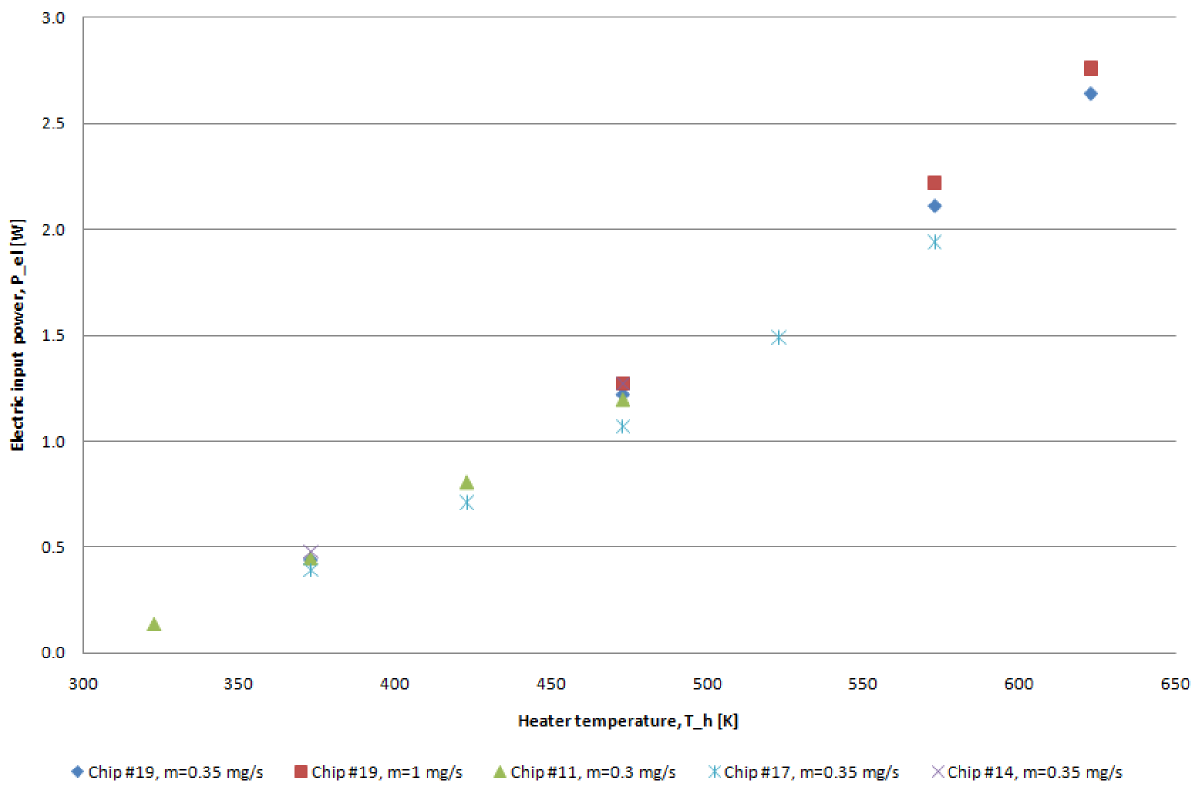

Figure 6.18: Total electric input power vs heater temperature.

Table 6.13: Test data for the total electric input power vs. heater temperature.

Heater temperature T_h [K]	**Total input electric power**, P_{el} [W]				
	Chip #19 (m=0.35 mg/s)	**Chip #19** (m=1 mg/s)	**Chip #11** (m=0.3 mg/s)	**Chip #14** (m=0.35 mg/s)	**Chip #17** (m=0.35 mg/s)
323			0.14		
373	0.44		0.45	0.48	0.39
423			0.81		0.71
473	1.22	1.27	1.20	1.27	1.07
523					1.49
573	2.11	2.22			1.94
623	2.64	2.76			

During the sample test data plot discussion in section 6.2.3, we had highlighted two main points: 1) the effective mass flow through the micro-thruster is 20-30 % less compared to the commanded mass flow due to leakage and 2) the external power supply was manually controlled resulting in error in calculating the chamber temperature from the power that goes into propellant heating. In figure 6.19, the ratio of chamber pressure-to-square root of chamber temperature is plotted as a function of effective mass flow rate for chip #19. For the chamber temperature, we take it to be the same as that of the heater temperature. The chamber pressure is then derived from the measured system pressure by subtracting the pressure drop in the feed system and that across the micro-channels by taking the fluid properties at the bulk temperature (Bulk temperature is defined as the average of the inlet fluid temperature which is the room temperature and the heater temperature). According to the ideal rocket motor theory, this should show a linear trend for a given throat area and propellant. Also, we compare the derived values with that of the ideal case.

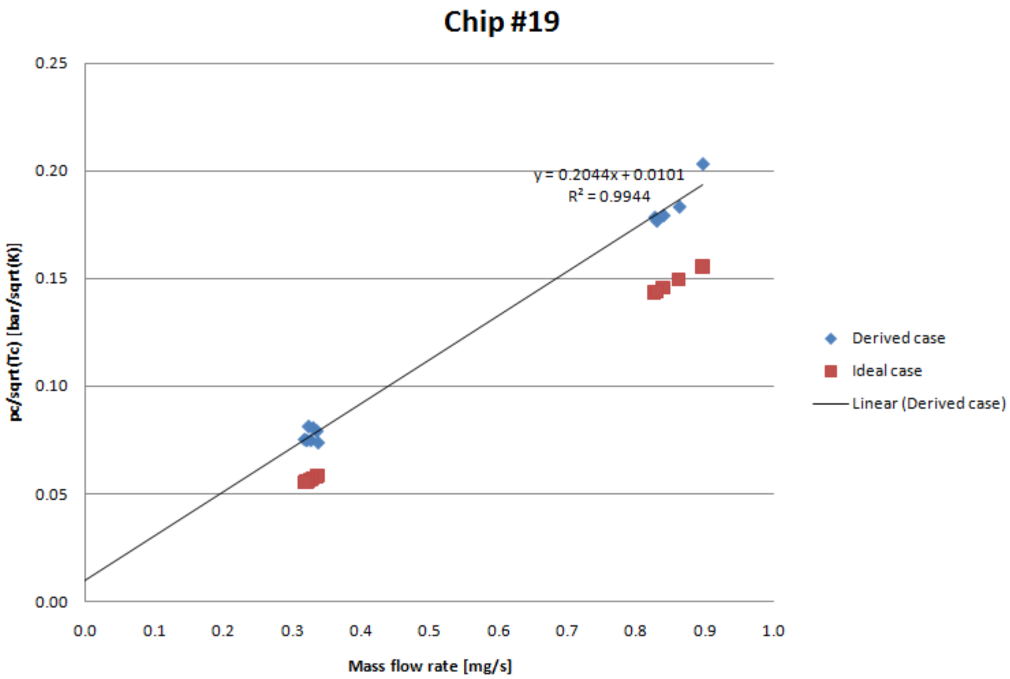

Figure 6.19: Ratio of chamber pressure to the square root of chamber temperature vs. propellant mass flow rate for chip #19.

From the figure above, we see that the trend shown by the derived case can be fitted with a linear equation. Comparing with the ideal case, we see that the derived values are consistently higher for all mass flow rates. Table 6.14 lists the calculated values of the discharge coefficient for different mass flow rates and heater temperature for chip #19.

Table 6.14: Discharge coefficient for chip #19 at different mass flow rates and heater temperature.

Heater temperature, T_h [K]	**m_dot = 0.35 mg/s**	**m_dot= 1 mg/s**
473	0.76	0.82
573	0.74	0.81
623	0.73	0.80

From the table, we can see the following:

1) The discharge coefficient is consistently higher for larger mass flow rate at all heater temperatures. This is because the throat Reynolds number is directly proportional to the mass flow rate, hence resulting in lesser displacement of the flow streamlines at the throat due to boundary layer formation at higher mass flow rates.
2) The discharge coefficient is decreasing with increasing heater temperature for both mass flow rates of 1 and 0.35 mg/s. This is because as the gas flow gets heated to a high temperature, its viscosity increases as we had already studied in chapter 3. This increase in flow viscosity results in a decrease of flow Reynolds number at the throat, resulting in lesser effective throat area for flow expanion due to boundary layer growth.

The propellant heating efficiency is defined as the ratio of the power that goes into the propellant heating to the total electric input power. In figure 6.20, this propellent heating efficiency is plotted against the heater temperature for a given mass flow rate for chip #19.

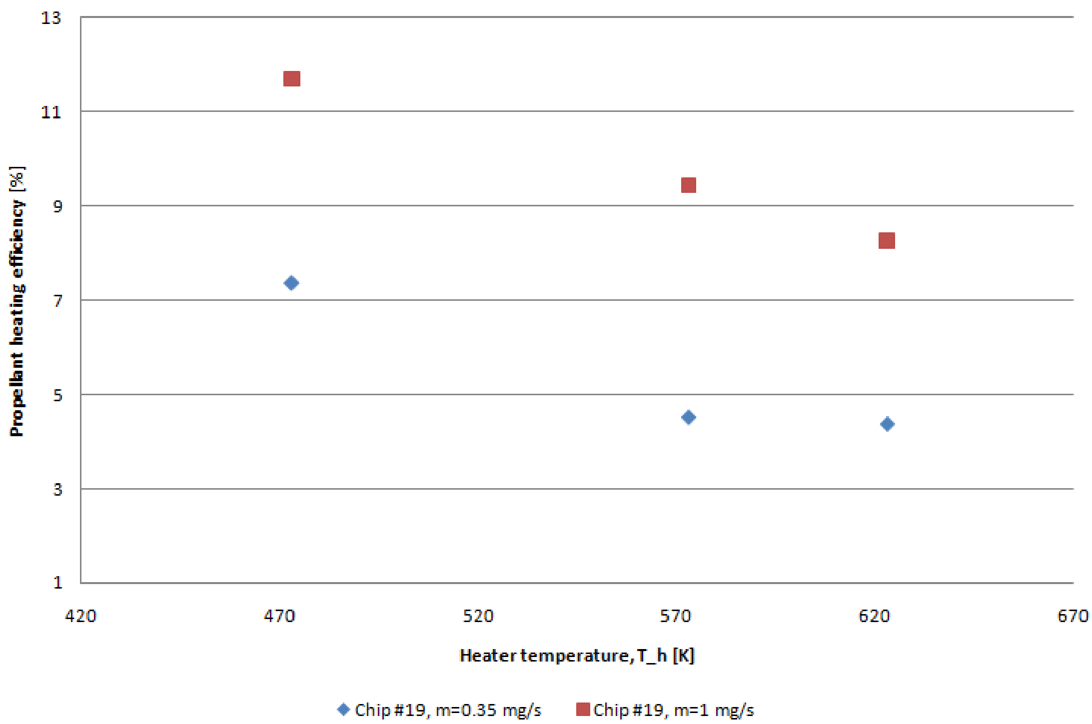

Figure 6.20: Propellant heating efficiency vs. heater temperature for chip #19.

From the figure above, we see that the heater efficiency is decreasing with the heater temperature for a given mass flow rate. This is due to the increasing parasitic heat losses in the form of natural convection and radiation at higher temperatures. We also see that for a given heater temperature, the maximum heat transfer efficiency is seen for larger mass flow rate. This is because at high mass flow rate, larger will be the flow velocity through the channels resulting in better forced convective heat transfer between the channels and the gas flow.

6.3 Conclusion

The test results at both hot and cold gas mode was presented, elaborated and compared with the theory in this chapter. From the sample test plots, the system pressure was found to respond quickly with any change in input mass flow rate or with input electric current during the cold and hot gas mode respectively. The propellant flow could be heated to a chamber temperature of 350^{o}C with a total input electric power of less than 3 W. On the other hand, the leakage from the feed system was found to be significant in the order of 20 to 30%. The derived chamber pressure was found to be higher than the ideal for all the cases, even after taking into account the leakage effects. Taking into account a 10% deviation in the throat geometry and the accuracy limits of the sensors was found to be not enough to explain the difference betweent the ideal and the derived chamber pressure values. This points to the inadequacy of the adopted relations used for frictional pressure drop calculations in the micro-channels. For the time being, the ratio of ideal to the derived chamber pressure was defined as the discharge coefficient of the nozzle, according to the ideal rocket motor theory. This performance parameter was found to decrease rapidly at lower throat Reynolds number due to growth in boundary layer thickness at the throat resulting in reduced nozzle throat cross-sectional area for flow expansion. The maximum propellant heating efficiency was found to be less than 13%, which opens a window to research upon further reducing the heat losses in future MEMS thruster designs.

6.4 Reference

[6.1] B.T.C. Zandbergen, Thermal rocket propulsion (Lecture notes).

[6.2] Robert L. Bayt; Analysis, Fabrication and Testing of MEMS-based micropropulsion system; MIT thesis (June 1999).

[6.3] G. A. Kuluva, N. M. Hosack; Supersonic nozzle discharge coefficient at Low Reynolds number; AIAA Journal, 9(9):1876-1877, 1971.

[6.4] http://webbook.nist.gov/chemistry/

Page intentionally left blank

Chapter 7

CONCLUSIONS & RECOMMENDATIONS

7.1 Conclusions

The design, fabrication and testing of the first prototype of a novel MEMS micro-resistojet has been investigated in this research work. In the following, the main results of the work are summarized, followed by a set of recommendation for future study in section 7.2.

1) In chapter 2, the design and analysis of a two-dimensional planar micronozzle was performed. Six different nozzle designs were proposed with an expansion ratio of 25:1 and nozzle throat widths of 10 and 5 μm and channel depths of 50 and 150 μm. First, the nozzle performance in terms of thrust and specific impulse were studied under ideal conditions. Second, the effect of low Reynolds flow on the thruster performance was studied using a simple modeling tool developed by the author. Third, the improvement made in specific impulse with propellant heating was presented. A drop in nozzle efficiency was observed with decreasing flow Reynolds number at the throat, thereby highlighting the prominence of viscous losses in microfluidic flows.

2) Chapter 3 dealt with the design and analysis of the heater section for MEMS resistojet, inspired from a MEMS heat sink concept. Four different chamber geometries were considered, single and multi-channel designs, with all having the same length of 2 cm inorder to provide a thermally fully developed flow. The sharp increase in pressure drop with propellant mass flow rate at micro-scales was highlighted. The three different modes of heat losses were studied, which were free convection and radiation to the test surroundings and conduction through the structure. The later was found to be the most predominant heat loss mechanism.

3) In chapter 4, focus was given on the fabrication of micro-thrusters using MEMS technology. The main steps in the fabrication of the device using a 4 mask process and the wire bonding and glueing of the thruster chips to the PCB and the thin needles with the metal tip into the inlet manifold of the chip were presented. Second, some of the fabricated geometries were measured with special instruments and there was found to be a maximum deviation of 10% in the fabricated geometry from the actual design value.

4) In chapter 5, we discussed the test setup for the characterization of a MEMS thruster chips. Due to micro-scale geometries, certain parameters like the chamber pressure and temperature required for the proper thruster characterization could not be directly measured. Hence special steps were taken to calculate from other measured parameters. For the cold gas testing, the propellant mass flow was kept as the controlled parameter and the pressure just outside the inlet of thruster chip was measured. For the hot gas testing, the input electric current was the controlled parameter, along with the measurements of the propellant mass flow and system pressure. Second, pressure drop in the feed system in between the pressure sensor and the inlet of MEMS heater section was analytically studied and was found to be less when compared to that across the micro-channels in the heater section for the same propellant mass flow.

5) Chapter 6 gave the measurements of the mico-thrusters, divided into two sections –cold gas and hot gas test results. In all the test plots, the system pressure was found to respond quickly with any change in input mass flow or heater current. As was expected, the multi-channel device was showing the same system pressure compared to the single channel device, but exhibiting a lower pressure drop. Theoretically derived chamber pressure values in the range of 1-5 bars were obtained for propellant flow rate of 0.15-1.5 mg/s at cold gas mode. The hot gas test result discussion was further divided into two parts: characterization of the heater and the measurements with fluid flow. Input electric power of 1.03 W at a supply voltage of less than 10 V was required to achieve a heater temperature of 191.56^{o}C with no mass flow. The propellant flow could be heated to a heater temperature of 350^{o}C with a total electric power of less than 3 W, in the order of 1mW/K at mass flow rates of 1 mg/s. Ratio of the ideal to theoretically calculated chamber pressure, defined as the discharge coefficient of the micro-nozzle, was found to be 80% at higher end of the mass flow range and found to decrease by a favtor of 1.6 at lower end of mass flow range. Heat transfer and pressure drop modeling presented in chapter 3 were found to be currently not sufficiently developed and the theory was found to predict more than the ideal/experimental values. This suggests that the current prototype of MEMS thruster device requires adequate research in the future.

7.2 Recommendations

1) With slight modifications made in the production settings, both the nozzle (throat width, channel depth and nozzle expansion ratio) and the chamber geometry (number of channels, length and depth of channels) can be easily adapted.

2) The bond wires acting as an electrical interface between the gold pads on the PCB and the aluminium contact pads on the chip was found to be extremely delicate while handling. Therefore, in future designs, it is advised to avoid such delicate thin bond wires and try to achieve electrical interface by using spring loaded pins.

3) The chamber pressure was derived from the measured system pressure by using relations that are widely used in macro-fluidic systems. For future designs, it is recommended to include a pressure tap at the micro-nozzle entry so that this parameter can be directly measured and based on the experimental results, new relations for pressure drop estimations in micro-scale can be developed. The pressure sensor used to measure the system pressure was quite bulky. In future, to achieve the goal of an integrated propulsion system miniaturised pressure sensors from Lucas NOVA or Honeywell which is far less bulky and light weight with less power consumption tha can be soldered on a PCB, should be used.

4) There existed a large volume of feed system in between the mass flow controller and the thruster chip. Hence, it took minutes for the system pressure to stabilize for a given mass flow or heater temperature. In future, it can be thought of storing the propellant gas in pressurized metal canisters and close to the thruster chip. By measuring the rate of drop in tank pressure during the thruster actuation time can tell us the propellant consumption rate. By integrating a miniaturized mass flow sensor from Honeywell in the system just before the inlet of the thruster chip, any leakage in the feed system can be taken into account by comparing the mass flow measured by the sensor with the calculated propellant consumption from the tank pressure history.

5) The discharge coefficient of the micro-nozzle for the present study was calculated by taking the ratio of the ideal to derived chamber pressure values. In theory, this performance parameter is defined as the ratio of actual mass flow from the thruster outlet to the input mass flow rate. The actual mass flow rate from the thruster outlet can be studied by measuring the rise in vacuum chamber pressure over time during the thruster actuation, after taking into account any leakage from the chamber.

6) We reported a maximum heater temperature of 350°C using aluminium as the heater material. For the current design, the maximum achievable temperature was limited by the melting temperature of the aluminium and also due to the limitations from the safe operating temperature range for the epoxy glue. With silicon having a melting temperature of more than 1600 K, definitely the propellant flow can be heated to a much higher temperatures by making use of new heater materials having much higher melting temperatures like for e.g. molybdenum or titanium. Calculated propellant heating efficiency was found to be very low, in the range of 13%. This is mainly due to large conduction losses within the silicon structure; silicon being a very good thermal conductor. To prevent the conduction losses back to the feed system through the metallic needles, it is advised to use less conductive materials like Pyrex capillary tubes as the fluidic interface between the feed system and thruster chip. In future, it can be even thought of integrating the heater within the channels which has proven to show a higher heat transfer efficiency from MEMS heat sink design studies.

7) A maximum heater temperature of 350°C was demonstrated with the present concept. This is much higher than the boiling point of water. Hence, it is recommended to try the the same micro-resistojet thruster concept with water as the propellant. Using water as propellant can take it to the next step of achieving a higher propellant density and hence reduced system mass.

8) To better understand the flow at micro-scale through visualization technique, the color schlieren technique can be used. Such imaging technique is in practice by the microfluidics department of TUDelft.

9) During the hot gas testing of MEMS thruster chips, the input current from the external power supply was manually contolled to achieve certain heater temperature. In future, it is advised to develop a PID control algorithm that can automatically control the input heater current and thereby help to calculate the effective power that goes into propellant heating.

10) Finally, we see a huge potential of integrating our MEMS micro-thruster with other micro-propulsion components like the micro-valves and miniaturized sensors, which never has been done before at such scales. In future, it is advised to collaborate with the University of Twente who has prior experience in developing micro-valves intended to produce precise impulse bits for attitude control of cubesats.

Page intentionally left blank

Appendix

Appendix 1 – sample calculations in chapter 1

SAMPLE CALCULATION #1

===

Verification of the values presented in table 1.2 by taking the case of impulse bit requirement for an angular pointing accuracy of 17 milliradians in 20 seconds for a 1-Unit cubesat.

According to Wertz and Larson [1.21], the impulse bit requirement for a given attitude pointing accuracy is given by:

$$I\_bit = F \times t = \frac{MoI \times \omega}{d}$$

where F is the thrust, t the time over which the thrust acts, MoI the mass moment of inertia of the satellite, d the thruster moment arm and ω the angular velocity of the satellite. Substituting the values in the above table, we get:

$$I\_bit = F \times t = \frac{MoI \times \omega}{d} = \frac{0.017\, {}^{kg}\!/\!_{m^2} \times \dfrac{17E-3rad}{20s}}{0.1m}$$

$$\Leftrightarrow I\_bit = 1.4E-4Ns$$

The same calculation procedure was used to verify the remaining values of impulse bit given in table for different impulse satellite classes and different pointing accuracy and the results were validated. Equation 1.2 shows the thrust required for a slew maneuver. The minimum thrust values presented in table 1.2 are for a slew maneuver of 180 degrees in 1 minute with a dead band of 40 seconds. Therefore, the time required for acceleration and coasting of satellite will be 10 seconds each$\left(\frac{60-40}{2}\right)$. Then the angular rate will be then:

$$\dot{\theta} = \frac{180\deg}{60s} = 3\, {}^{\deg}\!/\!_{s}$$

To reach 3 deg/s in 10 seconds requires an acceleration of:

$$\ddot{\theta} = \frac{\dot{\theta}}{t} = \frac{3\, {}^{\deg}\!/\!_{s}}{10s} = 0.3\, {}^{\deg}\!/\!_{s^2} = 5.24E-3\, {}^{rad}\!/\!_{s^2}$$

Then the thrust required for the slew will be:

$$F = \frac{I\ddot{\theta}}{d'} = \frac{0.017\, {}^{kg}\!/\!_{m^2}\; 5.24E-3\, {}^{rad}\!/\!_{s^2}}{\sqrt{2} \times 0.1m} \times 1000 = 0.6mN$$

The moment arm for the slew maneuver is taken as the diagonal length of a square face of cubesat. Comparing this with the corresponding value in table 1.2, we see that the value which we calculated is one order of magnitude larger than the value quoted in the table. Similar calculation procedure was carried out for other two satellite classes and we could reproduce the values with an accuracy of 5 %.

===

SAMPLE CALCULATION #2

==

Design input values:

Target thrust, F	:	1 mN
Propellant	:	Nitrogen
Propellant temperature, Tc	:	800 K
Chamber pressure, p_c	:	2 bar
Ambient pressure, p_a	:	10 millibar

According to ideal rocket motor theory, the thrust is given by:

$$F = \dot{m} C_F c^*$$

Characteristic velocity, c^* , which reflects on the energy level of the propellant available for propulsion purposes, is given by:

$$c^* = \frac{1}{\Gamma}\sqrt{RT_c} = \frac{1}{0.682}\sqrt{296.83 \, {}^{J}\!/_{kg-K} \times 800K} = 714.52 \, {}^{m}\!/_{s}$$

The thrust coefficient, C_F on the other hand, reflects on the amplification of thrust due to gas expansion in the nozzle and is given by:

$$C_F = \Gamma\sqrt{\frac{2\gamma}{\gamma-1}\left(1-\left(\frac{p_e}{p_c}\right)^{\frac{\gamma-1}{\gamma}}\right)} + \left(\frac{p_e - p_a}{p_c}\right)\frac{A_e}{A_t}$$

The exit pressure of the nozzle is taken as 5 millibar, which is slightly higher than the summerfield criterion for flow separation in the expansion section of nozzle ($\frac{p_e}{p_a} > 0.45$).This then gives the nozzle exit to chamber pressure a value of $\frac{p_e}{p_c} = \frac{5E-3bar}{2bar} =$ 2.5E-3. Substituting this value in the following relation, we get for the area ratio of the nozzle as:

$$\frac{A_e}{A_t} = \frac{\Gamma}{\sqrt{\frac{2\gamma}{\gamma-1}\left(\frac{p_e}{p_c}\right)^{\frac{2}{\gamma}}\left(1-\left(\frac{p_e}{p_c}\right)^{\frac{\gamma-1}{\gamma}}\right)}} = \frac{0.682}{\sqrt{\frac{2\times1.384}{1.384-1}\left(2.5E-3\right)^{\frac{2}{1.384}}\left(1-\left(2.5E-3\right)^{\frac{1.384-1}{1.384}}\right)}} = 21.41$$

Then, the thrust coefficient will be:

$$C_F = 0.682\sqrt{\frac{2\times1.384}{1.384-1}\left(1-\left(2.5E-3\right)^{\frac{1.384-1}{1.384}}\right)} + \left(\frac{5-10}{2}\right)\times 1E-3\times 21.41 = 1.59 \text{ [-]}$$

Substituting the values for the characteristic velocity and the thrust coefficient in the thrust formula, we get:

$$\dot{m} = \frac{F}{C_F c^*} = \frac{1E-3N}{1.59\times 714.52 \, {}^{m}\!/_{s}} = 0.88 \, {}^{mg}\!/_{s}$$

The throat area for the nozzle can e determined by using the relation:

$$A_t = \frac{mc^*}{p_c} = \frac{0.88E-6\,{}^{kg}/_{s} \times 714.52\,{}^{m}/_{s}}{2E5Pa} = 3.14E-9\,\mathrm{m}^2$$

Specific impulse follows using:

$$I_{SP} = \frac{F}{\dot{m}\,g} = \frac{1E-3N}{0.88E-6\,{}^{kg}/_{s}\;9.81\,{}^{m}/_{s^2}} = 115.83\,\mathrm{s}$$

The propellant mass for the required ΔV for the QB50 mission is:

$$m_p = m_o\left(1-e^{-\frac{\Delta V}{I_{SP}g}}\right) = 2kg\left(1-e^{-\frac{20\,{}^{m}/_{s}}{9.81\,{}^{m}/_{s^2}\,115.83s}}\right) = 0.03\,\mathrm{kg}$$

Heat input is then calculated as:

$$P_{heat} = \dot{m}\,\Delta H = 0.88E-6\,{}^{kg}/_{s} \times \frac{15.14\,{}^{kJ}/_{mole}}{28.01\,{}^{gm}/_{mole}} = 0.48\,\mathrm{W}$$

Assuming a power plant efficiency of 80%, the power required from the power system will be:

$$P_{ele} = \frac{P_{heat}}{\eta} = \frac{0.48W}{0.8} = 0.6\,\mathrm{W}$$

Volume for propellant storage will be:

$$V_{stor} = \frac{m_p R T_{stor}}{p_{stor}} = \frac{0.03kg \times 296.83\,{}^{J}/_{kg-K}\,298K}{5E5Pa} = 5.31E-3\,\mathrm{m}^3.$$

Assuming a spherical tank, then the diameter of the tank will be 0.22 m.

===

Page intentionally left blank

Appendix 2 – Optimum nozzle expansion angle

DETERMINATION OF OPTIMUM EXPANION ANGLE FOR A GIVEN EXPANSION RATIO OF A NOZZLE

From table 2.1 in chapter 2, we have seen how a nozzle half-divergence angle α contributes to the effective thrust of nozzle in the form of flow divergence factor. When the divergence angle is reduced, the nozzle length should increase for a given expansion ratio. But longer the nozzle length, larger will be the distance for the development of boundary layer thereby leading to greater blockage of the nozzle exit area. Therefore, a trade-off should be performed between the flow blockage due to boundary layer formation in longer nozzles and the divergence loss due to larger divergence angles so as to find the best expansion angle for a nozzle with a given expansion ratio. To perform a qualitative trade-off, thrust calculations were carried out using design case #4 with $10^o, 20^o, 30^o, 40^o$ and 50^o as the half-divergent angle for a given stagnation conditions of p_c = 5 bar and T_c=298 K and the results are shown in figure A2.1.

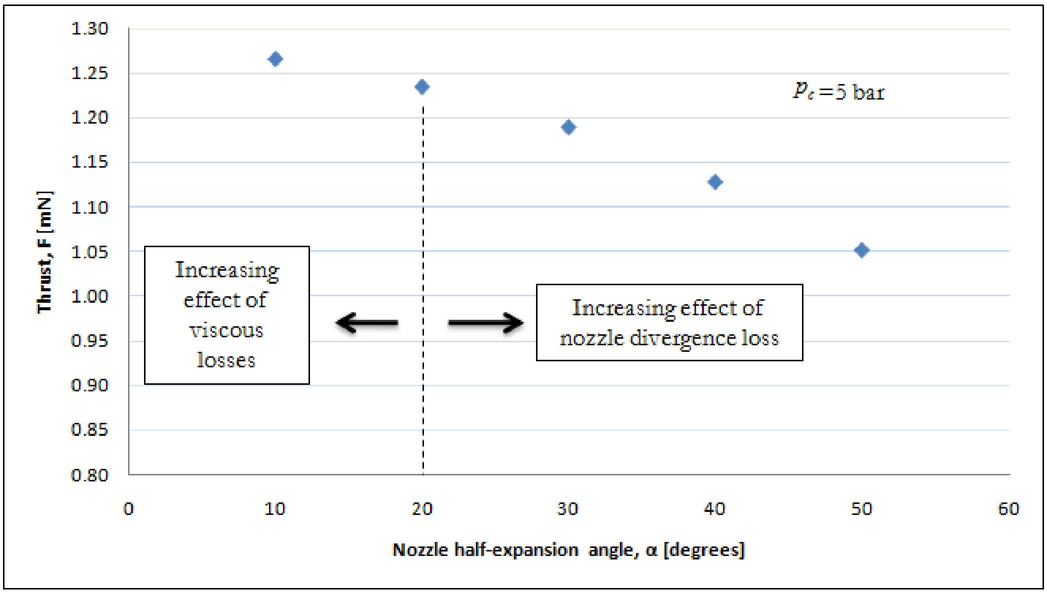

Figure A2.1: Effective thrust produced as a function of half-divergence angle for a nozzle with a given expansion ratio of 25:1.

Nozzle with the shortest expansion angle (10^o) is found to give the highest thrust. The rapid reduction in thrust for nozzle half-expansion angle in excess of 20^o is a direct result of divergence loss.

Page intentionally left blank

Appendix 3 – sample calculation in chapter 3

SAMPLE CALCULATION

==

Sample calculations for design case #2 at an input mass flow rate of 2 mg/s and heater chamber temperature T_c of 600 K.

Step 1: Mass flow per channel:

In case of a multiple channel design, the input mass flow is assumed to be evenly distributed. In that case, mass flow per channel will be:

$$\dot{m}_{/ch} = \frac{\dot{m}}{N} = \frac{2\,{}^{mg}\!/_{s}}{3} = 0.67\,{}^{mg}\!/_{s}$$

Step 2: a) Total width of heat sink (this determines the size of MEMS thruster lateral to the fluid flow direction)

$$W = N.W_{ch} + (N-1).W_f + 75\mu m \times 2$$
$$\Leftrightarrow 3\times 50\mu m + (3-1)\times 100\mu m + 75\mu m \times 2$$
$$\Leftrightarrow 500\mu m$$

b) Hydraulic diameter of the channel

$$D_h = \frac{2H_{ch}W_{ch}}{H_{ch}+W_{ch}}$$
$$\Leftrightarrow \frac{2.150.50}{150+50} \Leftrightarrow 75\mu m$$

c) Cross-sectional area of the channel

$$A_{ch} = 50\mu m.150\mu m = 7500\mu m^2$$

d) Aspect ratio of the channel

$$\alpha = \frac{H_{ch}}{W_{ch}} = \frac{150}{50} = 3$$

e) Fin cross-sectional area and perimeter

$$A_f = L_{ch}W_f = 2cm \times 100\mu m = 2E-6m^2$$
$$P_f = 2L_{ch} = 2\times 2cm = 0.04m$$

Note: The fin cross-sectional area is the area perpendicular to the heat flow and the perimeter is taken as 2 times the channel length, considering that the fin width is negligible compared to its longitudinal length.

Step 3: Flow Reynolds number

$$\mathrm{Re} = \frac{4\dot{m}_{/ch}}{\pi D_h \mu_{g,@T_{mean}}} = \frac{4\times 0.67E-6\,{}^{kg}\!/_{s}}{\pi \times 75E-6m \times 2.215-5\,{}^{Ns}\!/_{m^2}} = 527$$

Step 4: Hydro-dynamic and thermal development length

$$L_{hy,d} = z^{+}\,\mathrm{Re}\,D_h = 0.055 \times 527 \times 75E-6m = 0.22cm$$

$$L_{th,d} = z^{*}_{th}\,\mathrm{Re}\,D_h\,\mathrm{Pr} = 0.061 \times 527 \times 75E-6m \times 0.64 = 0.15cm$$

Comparing the two values with the total channel length, we see that the gas flow is both thermally and hydraulically fully developed during its flow through the channel.

Step 5: Heat transfer calculations

For a fully developed flow, we take the nusselt number for an aspect ratio α' defined as channel width-to-channel height ratio (=1/3=0.333) as 5.22. Now, the convective heat transfer coefficient, h is calculated as:

$$h = \frac{Nu.k_{g,@T_{mean}}}{D_h} = \frac{5.22 \times 0.03534\,{}^{W}\!/_{mK}}{75E-6m} = 2461.39\,{}^{W}\!/_{m^2K}$$

Fin parameter, m is defined as:

$$m = \sqrt{\frac{h.P_f}{A_f.k_{Si}}} = \sqrt{\frac{2461.39\,{}^{W}\!/_{m^2K} \times 0.04m}{2E-6m^2 \times 63.25\,{}^{W}\!/_{mK}}} = 882.19\,{}^{1}\!/_{m}$$

Fin efficiency is defined as:

$$\eta_f = \frac{\tanh(mH_{ch})}{mH_{ch}} = \frac{\tanh(882.19\,{}^{1}\!/_{m} \times 150E-6m)}{882.19\,{}^{1}\!/_{m}\,150E-6m} = 99.42\%$$

Heat flux at the channel walls:

$$q'' = \frac{q}{NL_{ch}(2H_{ch}\eta_f + W_{ch})} = \frac{0.64W}{3 \times 2E-2m \times (2 \times 150E-6m \times 0.9942 + 50E-6m)}$$

$$\Leftrightarrow 3.04E4\,{}^{W}\!/_{m^2}$$

$$T_{s,\max} - T_c = \frac{q''}{h} = \frac{3.04E4\,{}^{W}\!/_{m^2}}{2461.39\,{}^{W}\!/_{m^2K}} = 12.35K$$

Therefore, the maximum surface temperature will be observed at the channel exit, which is:

$$T_{s,\max} = 12.35 + 600 = 612.35K$$

Step 6: Calculation of thermal resistance

a) Conduction thermal resistance

$$R_{sub} = \frac{t}{k_{Si}L_{ch}W} = \frac{410E-6m}{63.25\,{}^{W}\!/_{mK} \times 2cm \times 500\mu m} = 0.648\,{}^{k}\!/_{W}$$

b) Constriction thermal resistance

$$R_{constr} = \frac{(W_{ch}+W_f)}{\pi k_{Si}} \ln\left(\frac{1}{\sin\left[\frac{\pi W_f}{2(W_{ch}+W_f)}\right]}\right) = \frac{(50+100)E-6m}{\pi \times 63.25 \, {}^{W}\!/\!_{mK}} \ln\left(\frac{1}{\sin\left[\frac{\pi\times 100E-6m}{2\times(50+100)E-6m}\right]}\right)$$

$$\Leftrightarrow 0.011 \, {}^{k}\!/\!_{W}$$

c) Convection thermal resistance

$$R_{conv} = \left[{}^{1}\!/\!_{R_{fin}} + {}^{1}\!/\!_{R_{base}}\right]^{-1}$$

$$\Leftrightarrow \left[\eta h 2 L_{ch} H_{ch}(N-1) + h W_{ch} L_{ch} N\right]^{-1}$$

$$\Leftrightarrow \left[0.9942\times 2461.39 \, {}^{W}\!/\!_{m^2K} \times 2\times 2E-2m\times 150E-6m\times(3-1) + 2461.39 \, {}^{W}\!/\!_{m^2K} \, 50E-6m\times 2E-2m\times 3\right]^{-1}$$

$$\Leftrightarrow 27.21 \, {}^{k}\!/\!_{W}$$

d) Bulk thermal resistance

$$R_{heat} = \frac{1}{\dot{m}_g \, c_{p,g}} = \frac{1}{2E-6 \, {}^{kg}\!/\!_{s} \; 1051.62 \, {}^{J}\!/\!_{kgK}} = 475.46 \, {}^{k}\!/\!_{W}$$

It can be seen that the constriction thermal resistance is the lowest among the four types, with an order of magnitude lower than the conduction thermal resistance. The convective thermal resistance is larger by two orders of magnitude compared to conduction thermal resistance. The bulk thermal resistance is the largest contributor to the thermal resistance of the overall heat sink.

$$R_{total} = R_{constriction} + R_{conduction} + R_{convection} + R_{bulk}$$

$$\Leftrightarrow 503.33 \, {}^{k}\!/\!_{W}$$

Using relation (3.55), we can calculate the maximum surface temperature of the heat sink as:

$$T_{surf,\max} = T_{g,in} + qR_{total}$$

$$\Leftrightarrow 298K + 0.64W \times 503.33 \, {}^{k}\!/\!_{W}$$

$$\Leftrightarrow 617.7K$$

This value is slightly higher than the value calculated for $T_{s,max}$ in step 5 by 5 K.

==

Page intentionally left blank

Appendix 4 - Test control interface

CONTROL PANEL OF LABVIEW PROGRAM

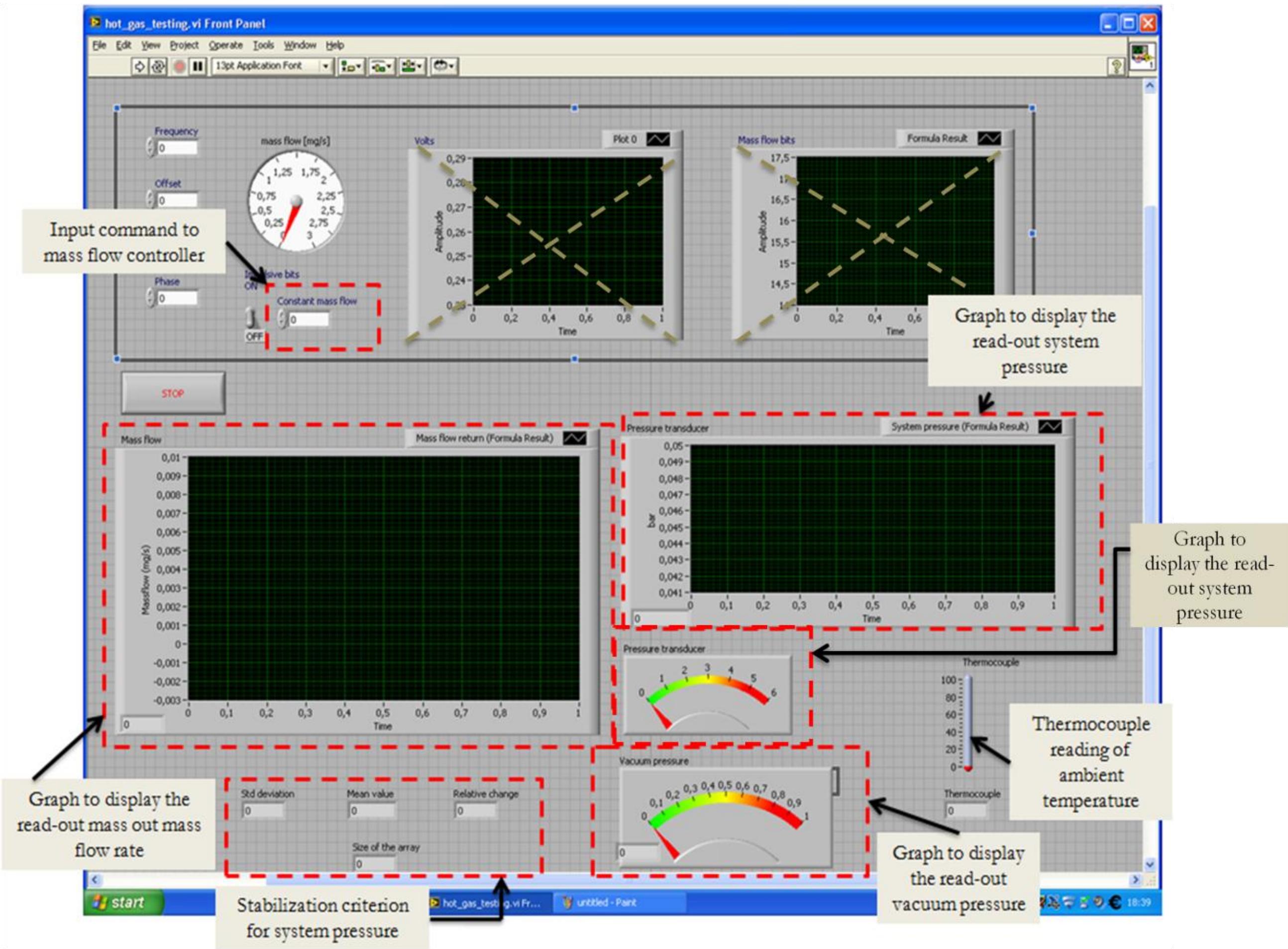

Figure A4.1: Control panel of the Labview program.

BLOCK DIAGRAM OF LABVIEW PROGRAM

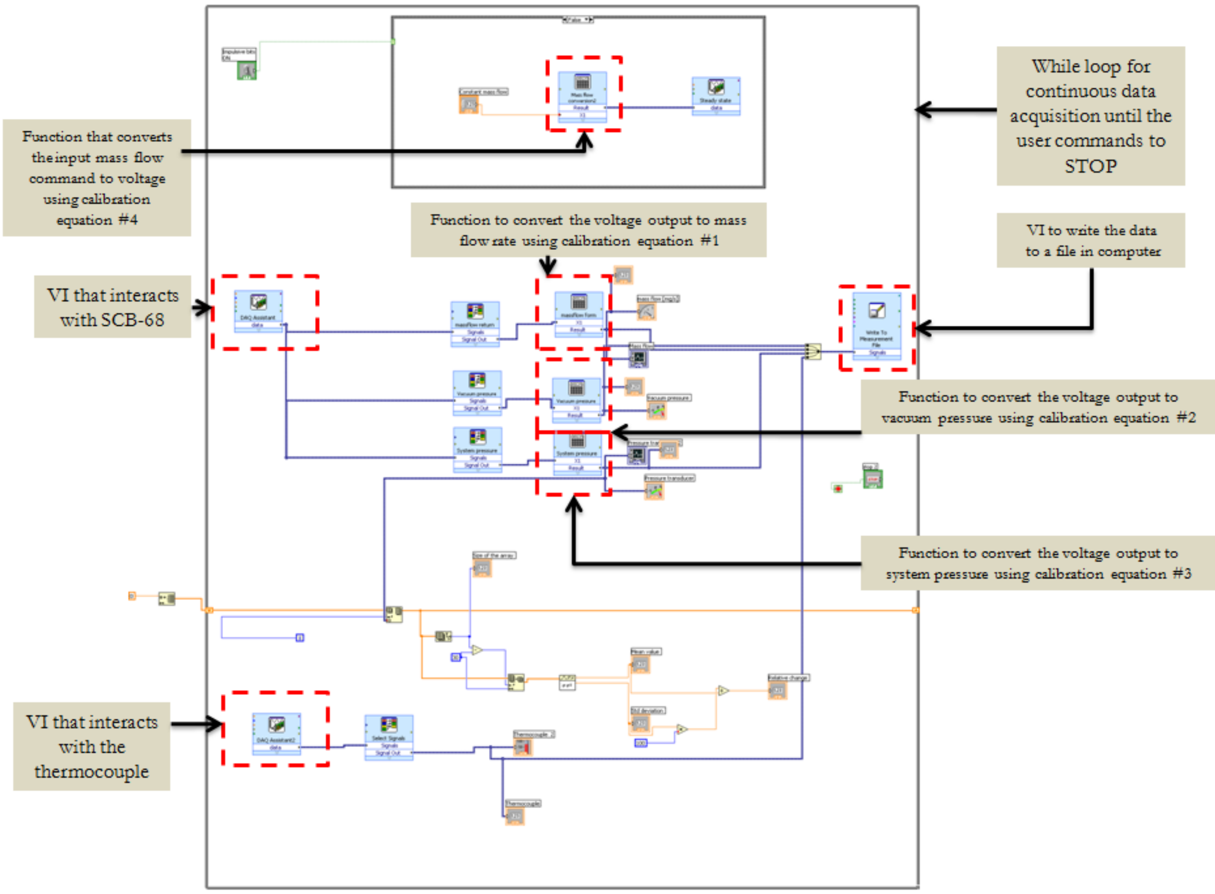

Figure A4.2: Block diagram of the Labview program.

Appendix 5 – Operation of Keithley Sourcemeter

OPERATION OF KEITHLY SOURCEMETER

Step 1:	Switch on the power.
Step 2:	Go to the CONFIG -> MEAS -> V-MEAS -> SENSE-MODE and select the "4-wire" option. Then press "EXIT" a few times back. "4W" indicator should Appear on the panel.
Step 3:	Go to MODE and select the OHM-METER.
Step 4:	Push the rotating knob to edit the source value. Set the range from 000.000 mA. To measure the heater resistance at room temperature, set the current input level at 0.1 mA. Set the current to higher values inorder to heat up the chip starting with 0.01 A, 0.05 A and so on.
Step 5:	Press the "OUTPUT ON/OFF" button (the blue LED should be lit) to input the Set current rhrough the system.
Step 6:	Wait for some time until the readings are more stable under visual inspection and then record the measured data.

Page intentionally left blank

Appendix 6 – Anomaly report

ANOMALY REPORT

Modification #1

Action: The cable that was connects the PXI-8331 to the PCI was replaced with the one provided by NI.

Observation: As soon as the LABVIEW program was run, the system hangs; there was no change in color of the LED of PXI's after the LABVIEW program was run (fig A6.1). There was no signal acquisition from the load sensor.

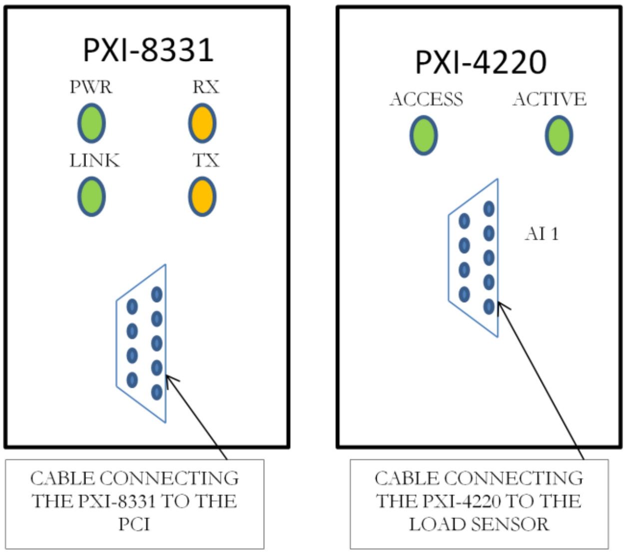

Fig A6.1: Schematic of the load sensor PXI during modification #1.

Modification #2

Action: This time the PXI-8331 was replaced with the one provided by NI, and not changing the cable from modification #1.

Observation: LABVIEW program was run. Signal acquisition was shown on the LABVIEW front panel. Fig A6.2 shows the LED colors during the signal acquisition.

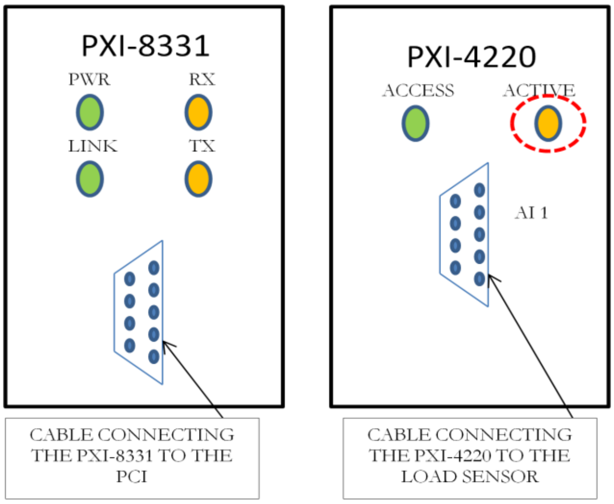

Fig A6.2: Schematic of the load sensor PXI during modification #2.

After a few minutes of signal acquisition, the following change in LED color was observed (fig A6.3) and the system hangs.

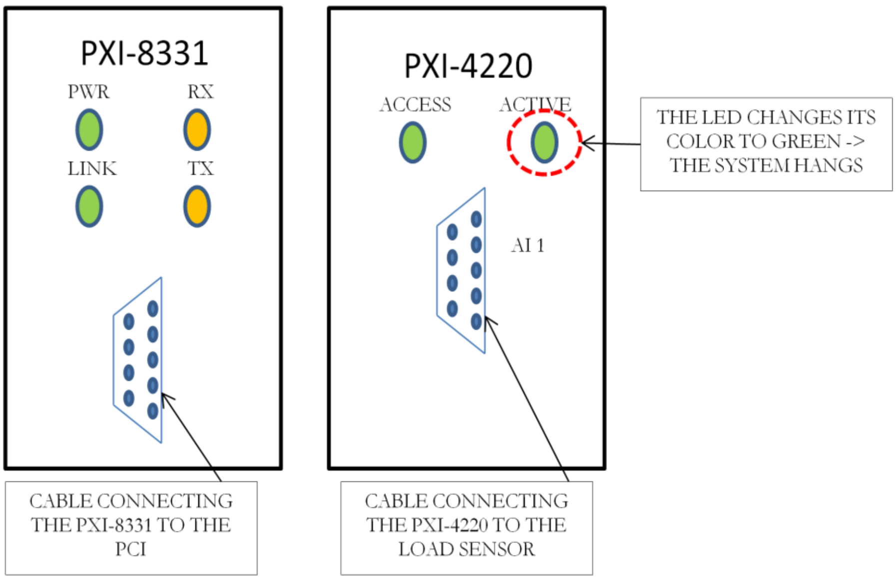

Fig A6.3: Schematic of the load sensor PXI during modification #3.

Appendix 7 – Test plots

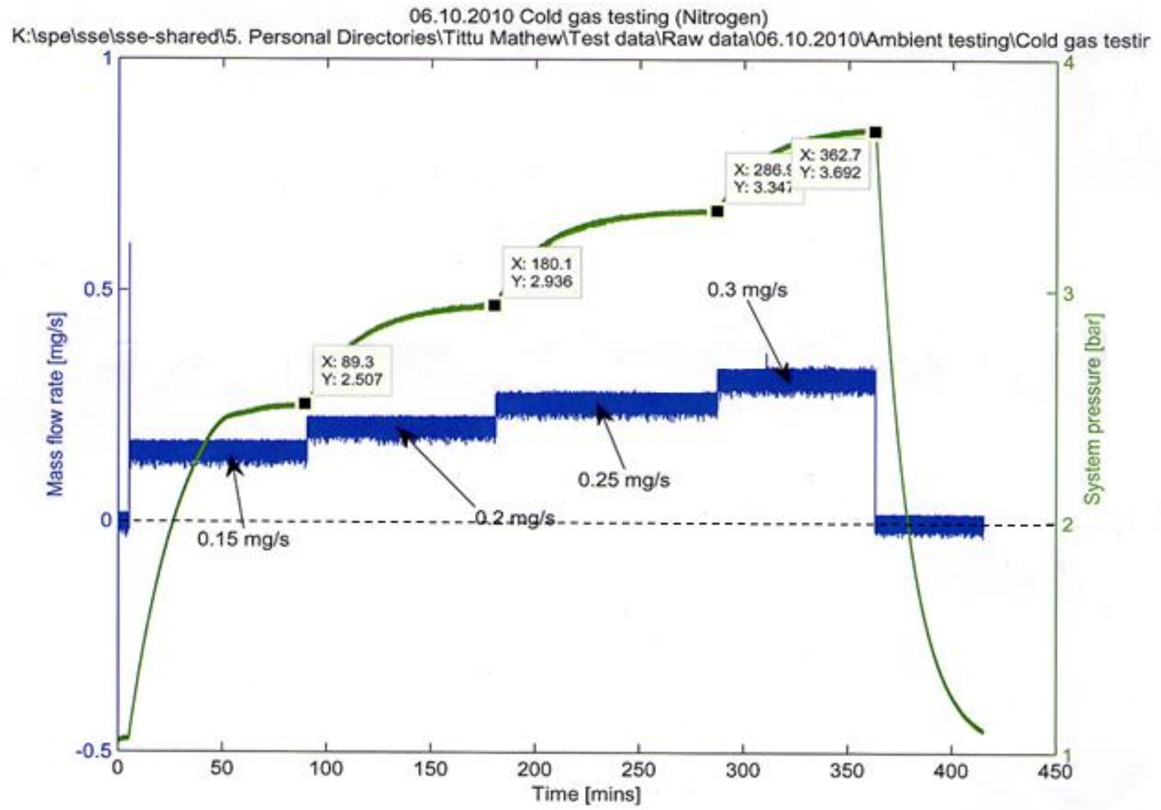

AP_OCT_1

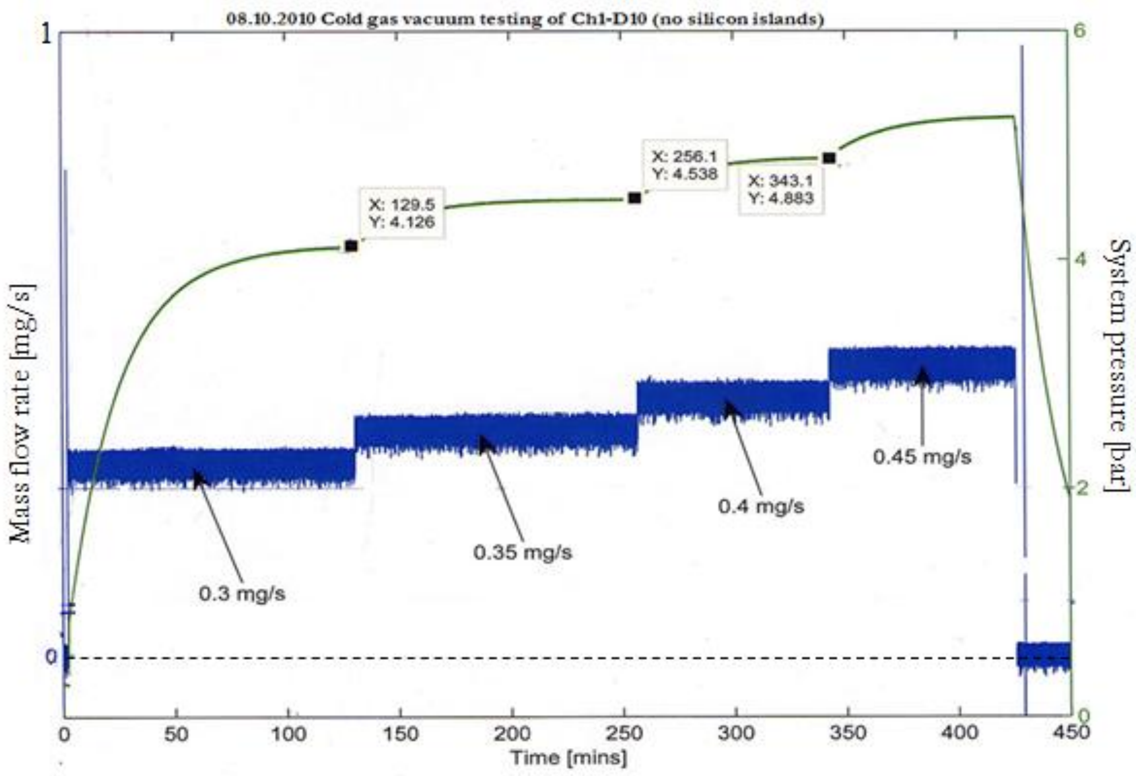

AP_OCT_2

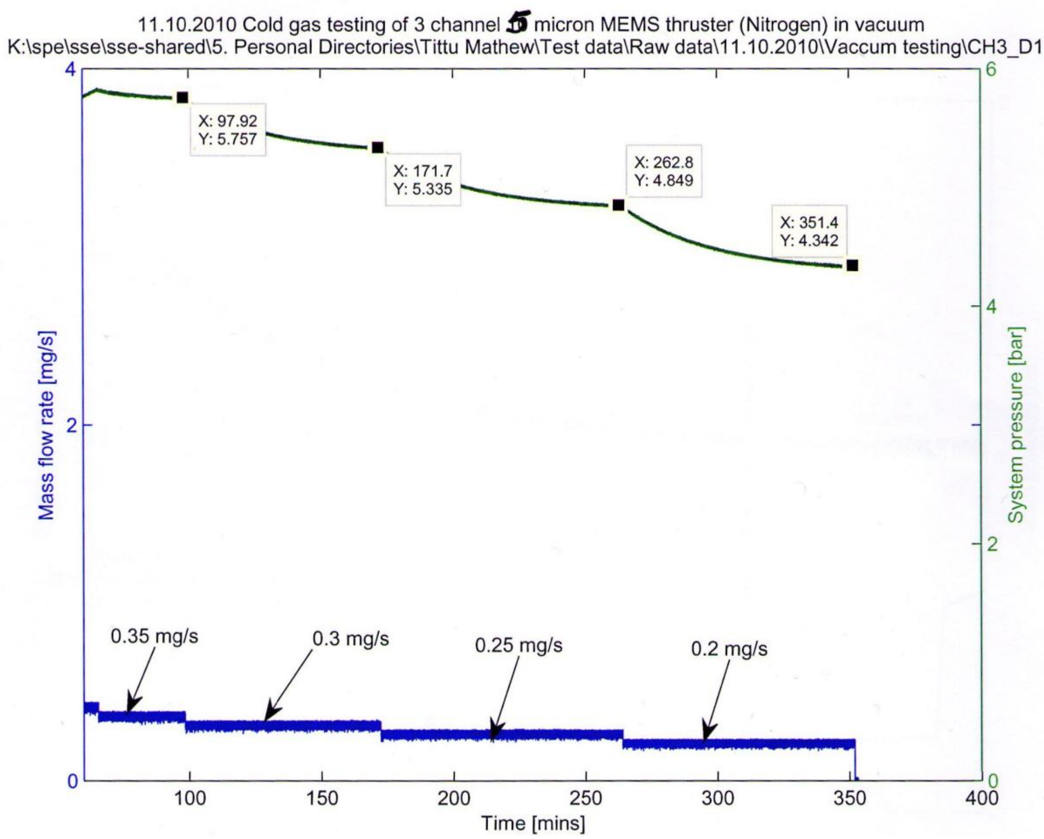

AP_OCT_3

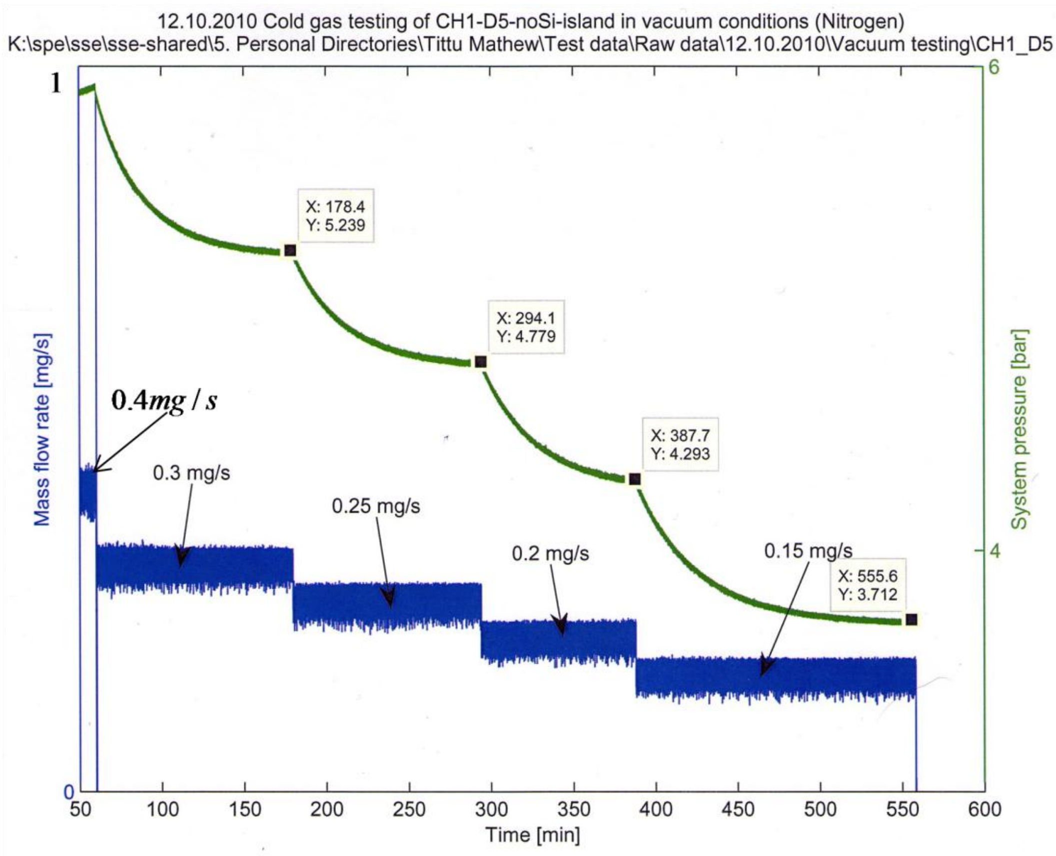

AP_OCT_4

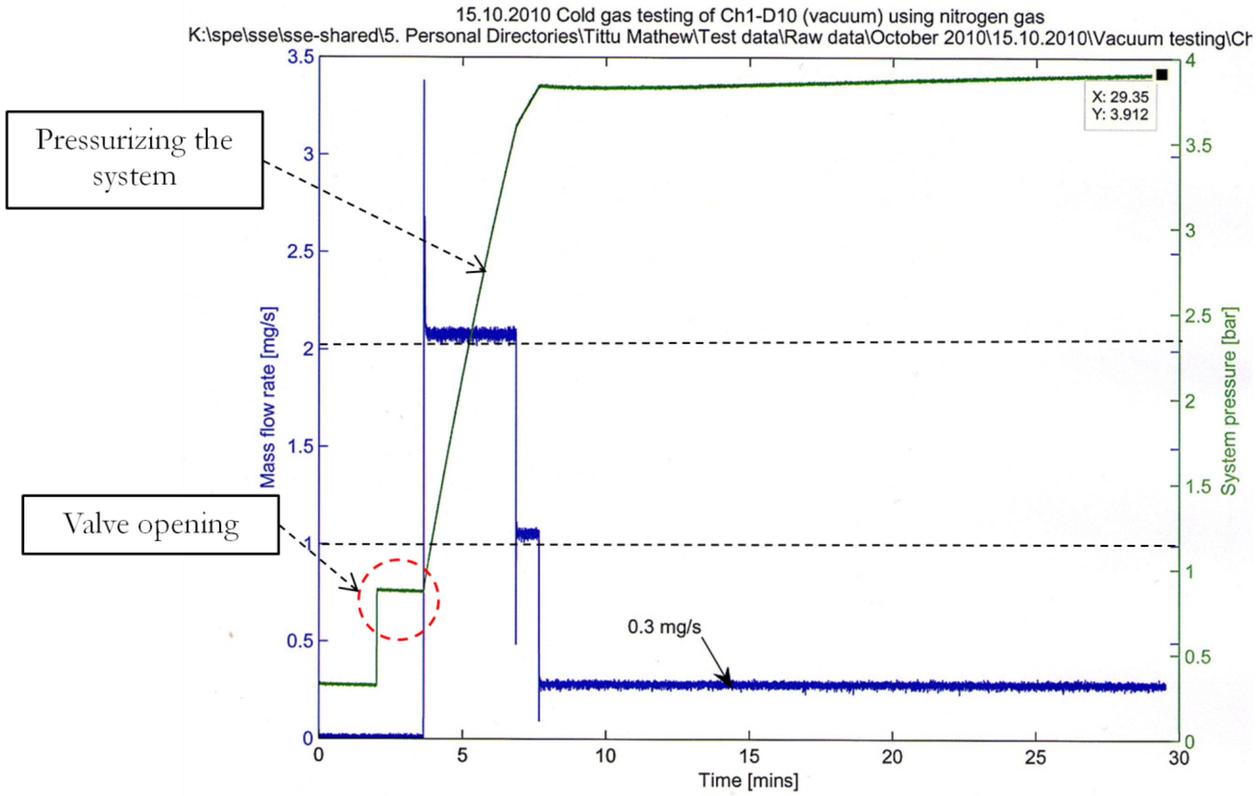

AP_OCT_5

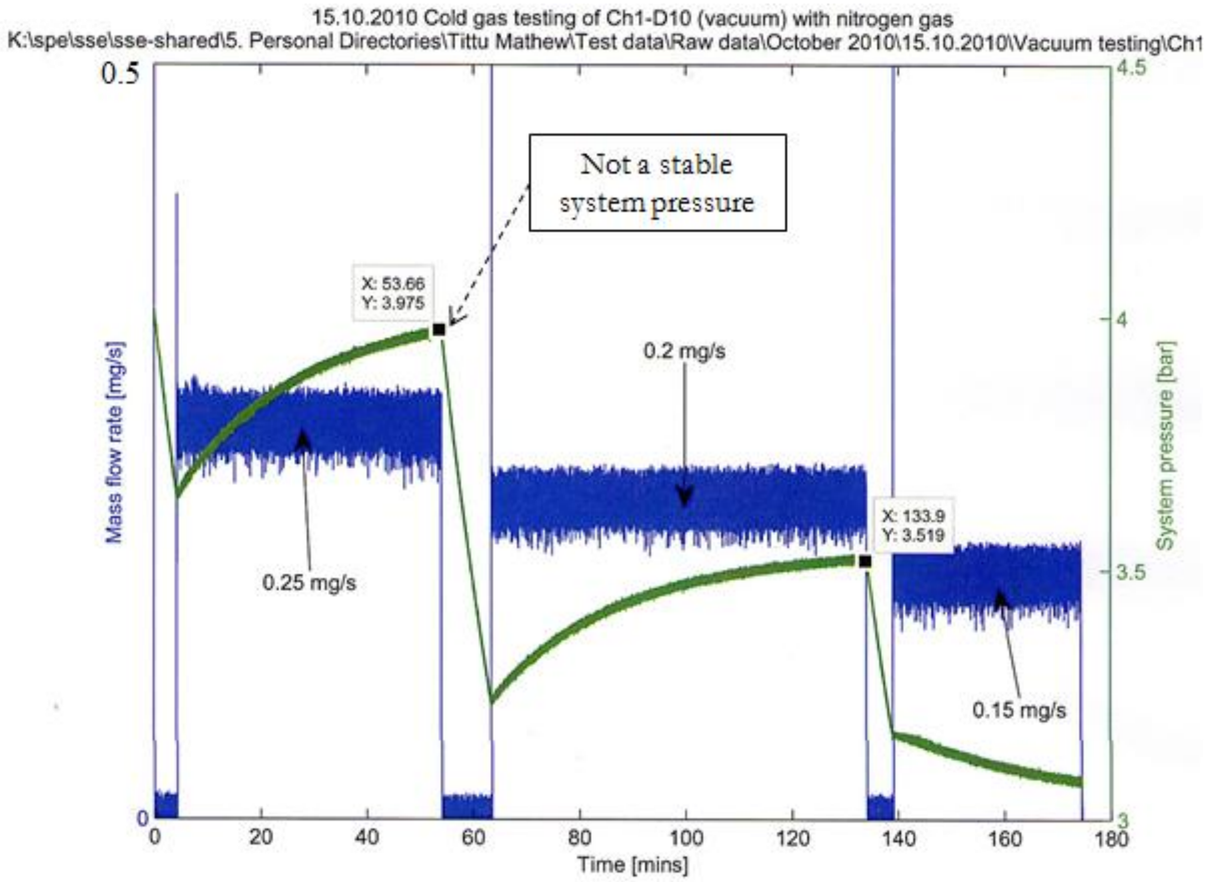

AP_OCT_6

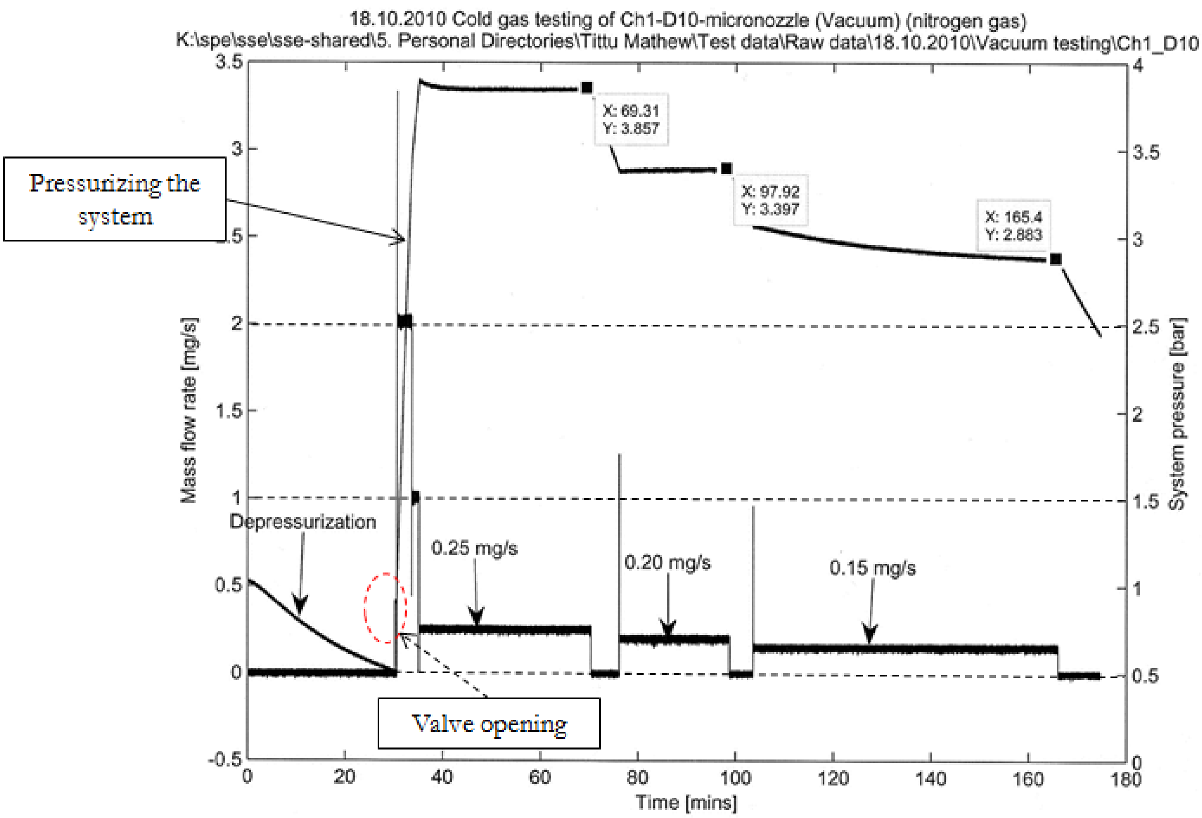

AP_OCT_7

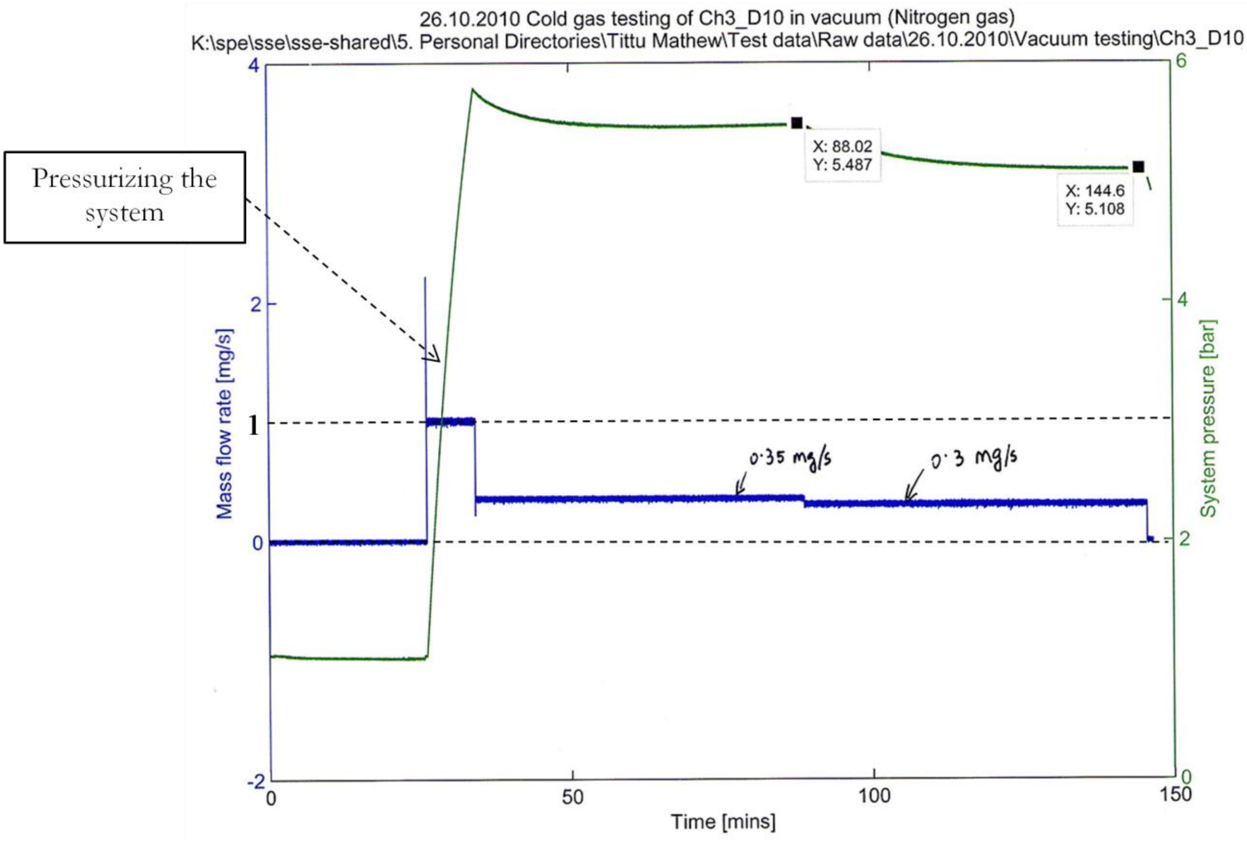

AP_OCT_8

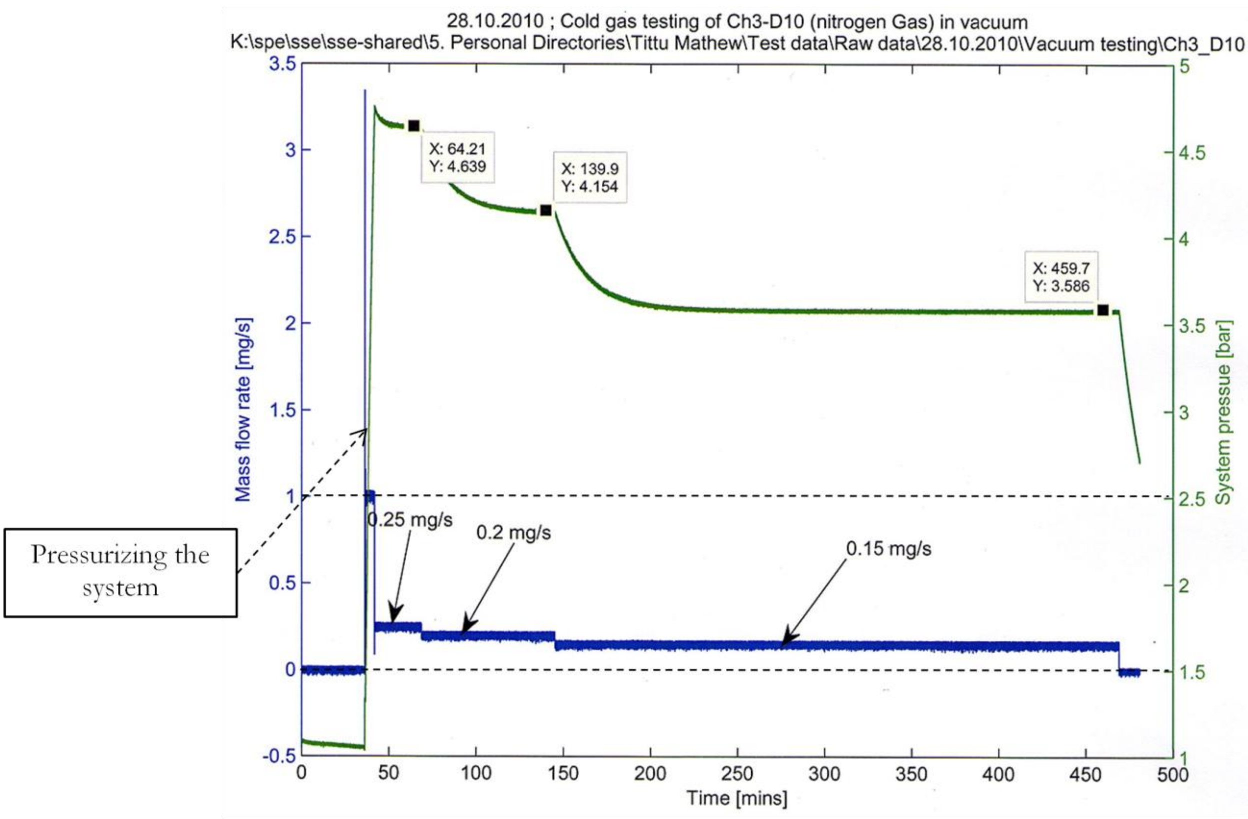

AP_OCT_9

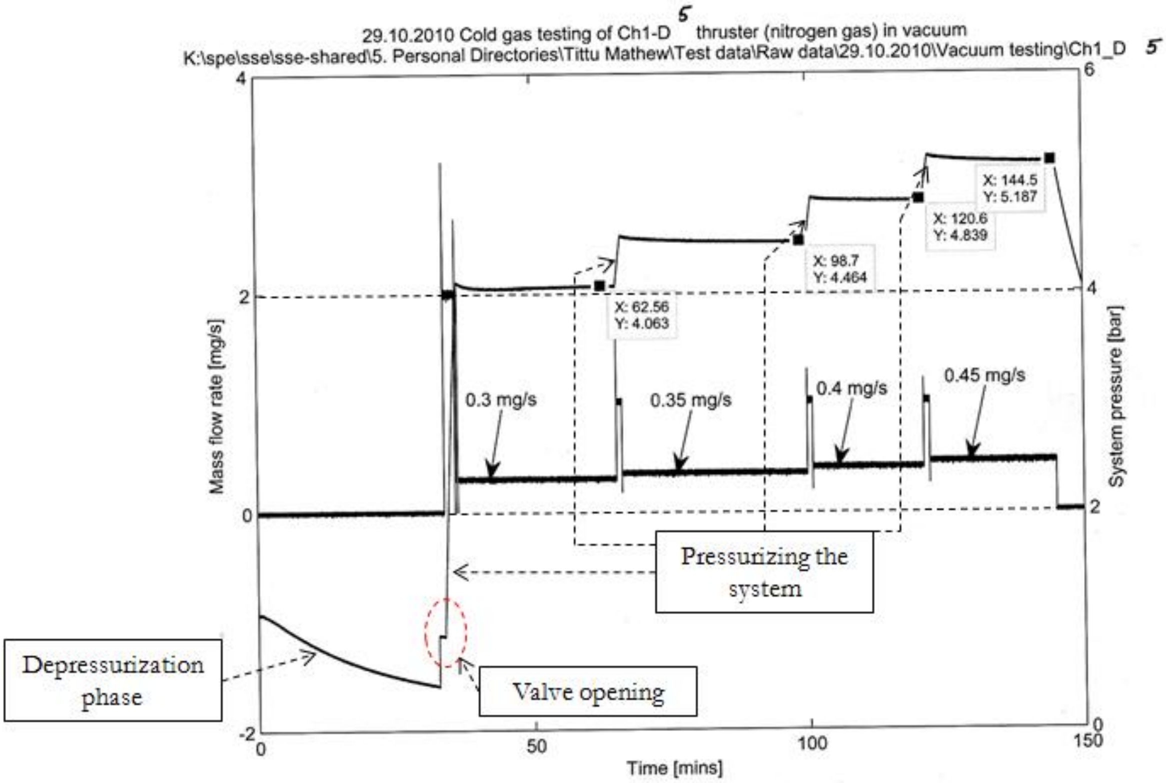

AP_OCT_10

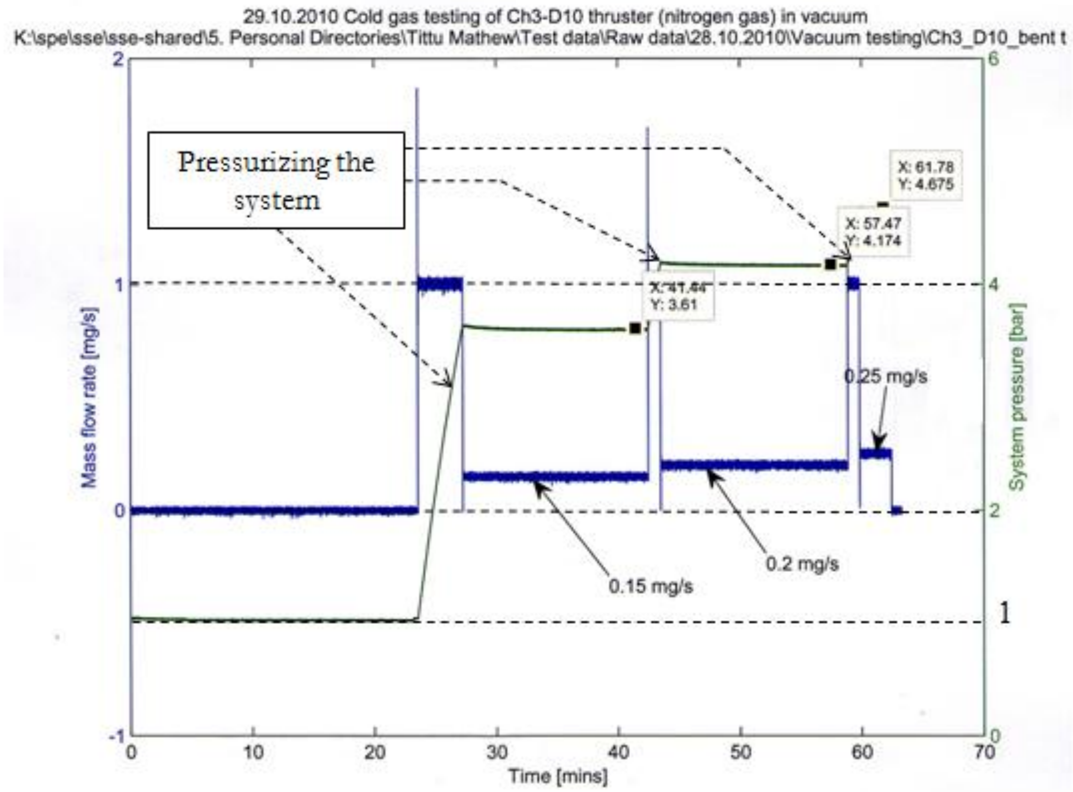

AP_OCT_11

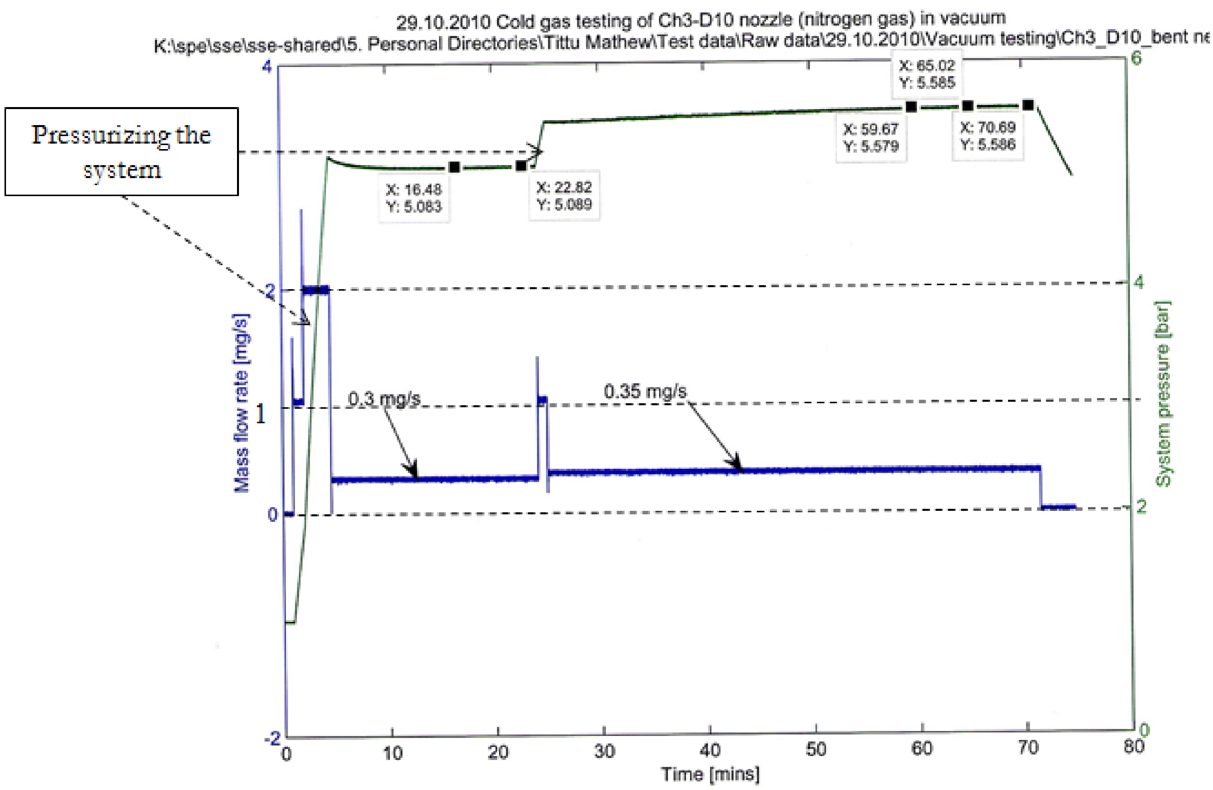

AP_OCT_12

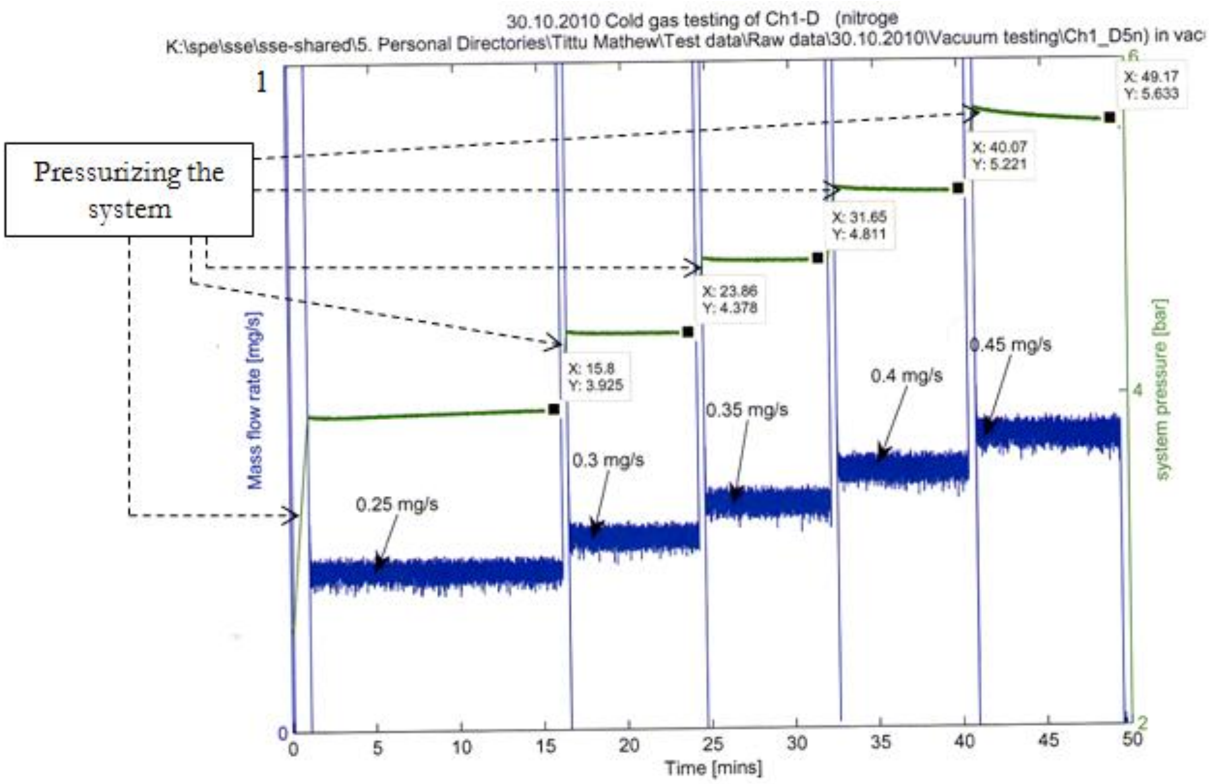

AP_OCT_13

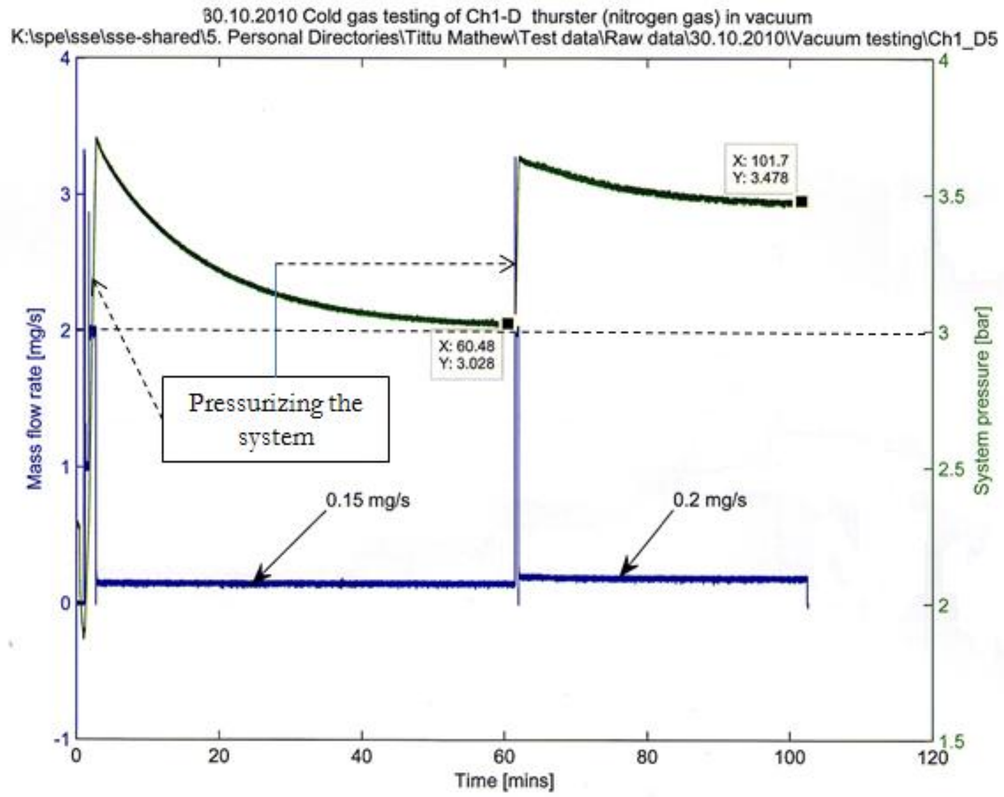

AP_OCT_14

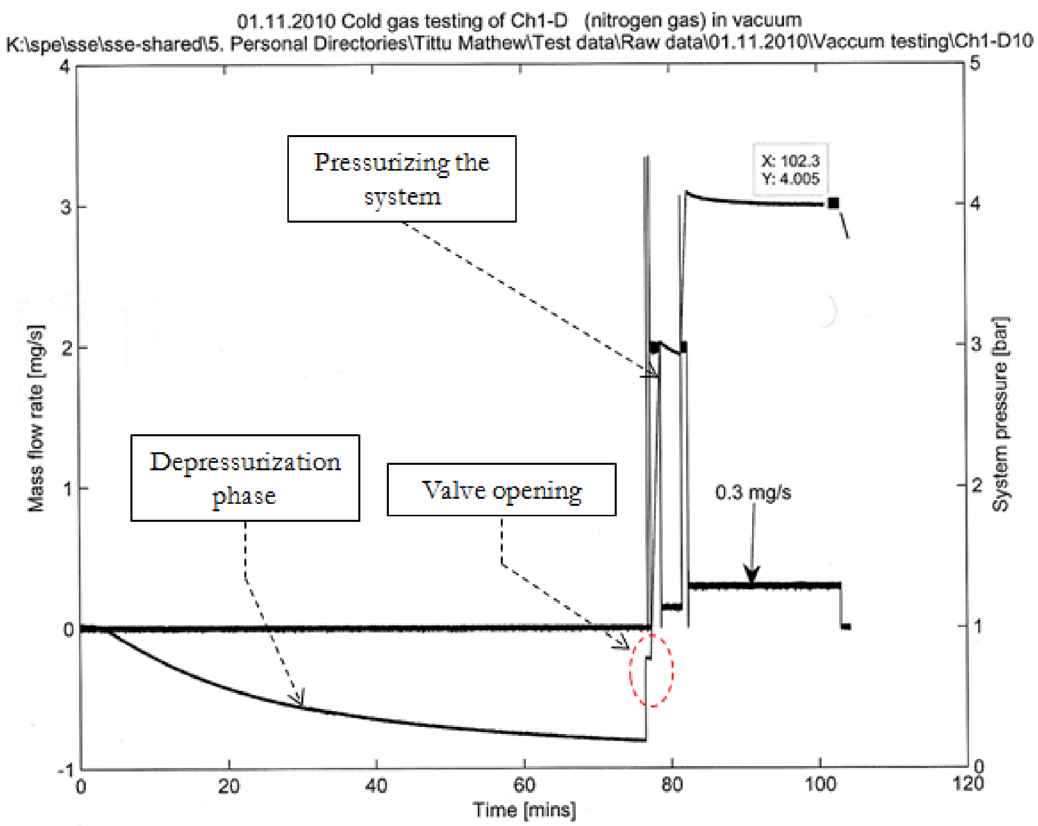

AP_NV_1

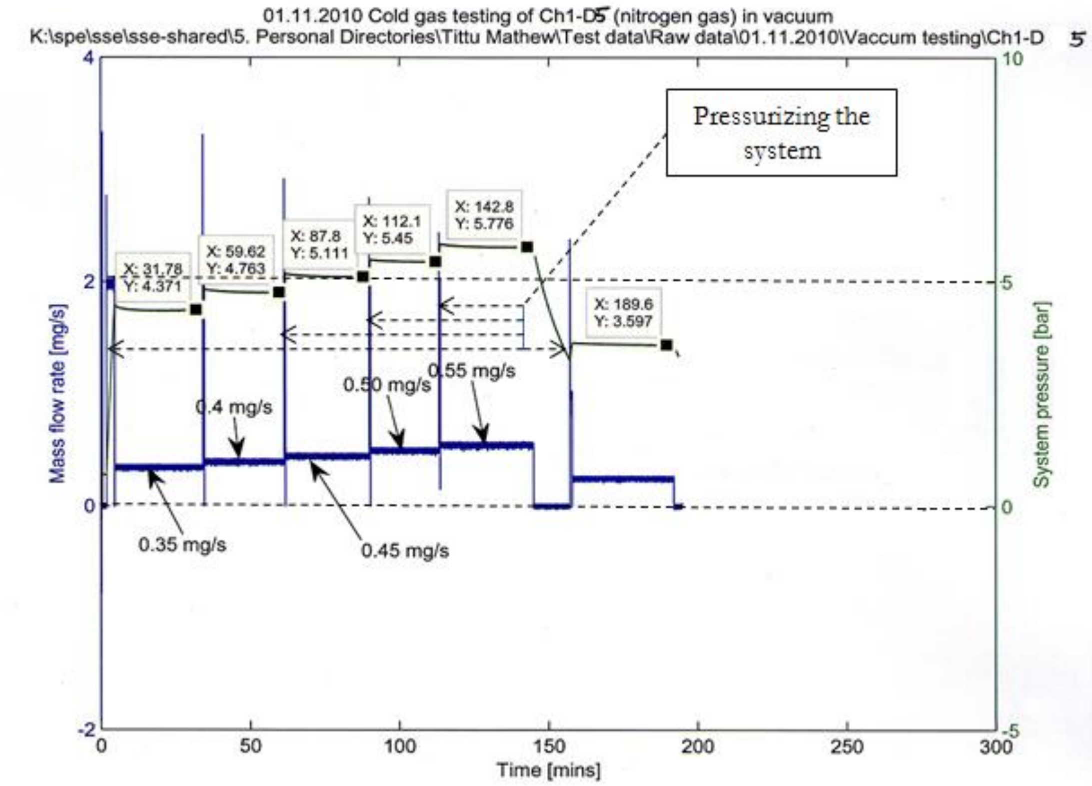
01.11.2010 Cold gas testing of Ch1-D5 (nitrogen gas) in vacuum
K:\spe\sse\sse-shared\5. Personal Directories\Tittu Mathew\Test data\Raw data\01.11.2010\Vaccum testing\Ch1-D 5
Pressurizing the system
X: 31.78
Y: 4.371
X: 59.62
Y: 4.763
X: 87.8
Y: 5.111
X: 112.1
Y: 5.45
X: 142.8
Y: 5.776
X: 189.6
Y: 3.597
0.35 mg/s
0.4 mg/s
0.45 mg/s
0.50 mg/s
0.55 mg/s
Mass flow rate [mg/s]
System pressure [bar]
Time [mins]

AP_NV_2

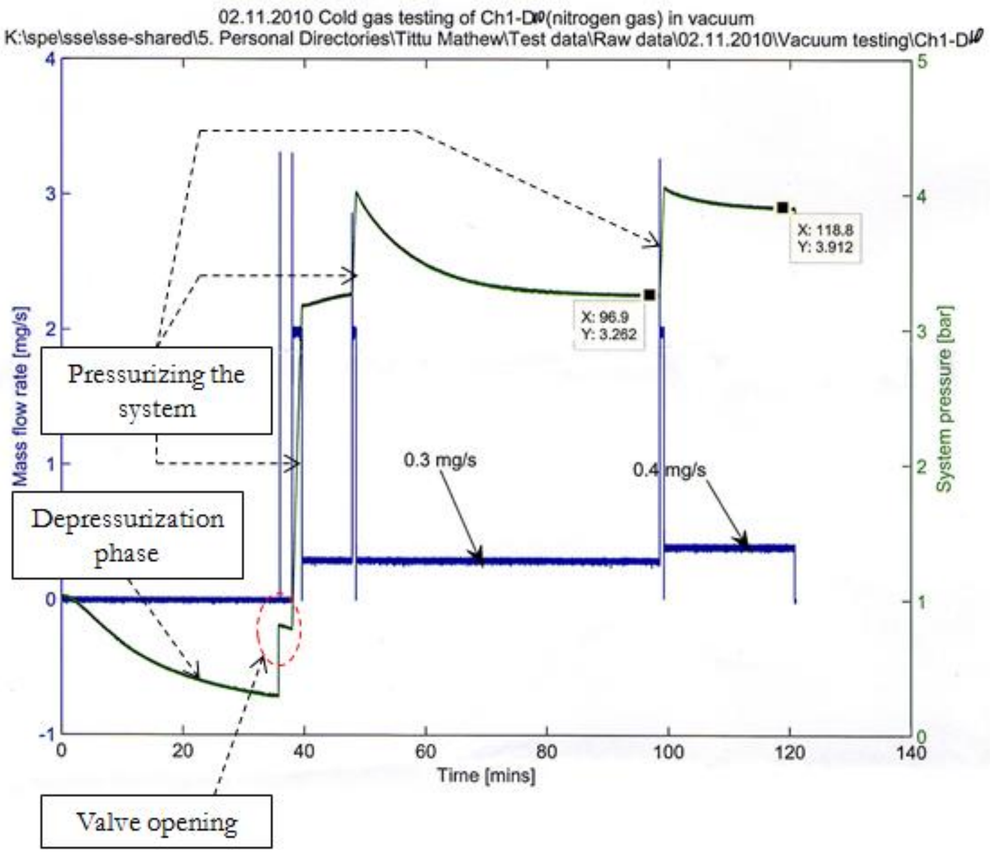
02.11.2010 Cold gas testing of Ch1-D10 (nitrogen gas) in vacuum
K:\spe\sse\sse-shared\5. Personal Directories\Tittu Mathew\Test data\Raw data\02.11.2010\Vacuum testing\Ch1-D10
Pressurizing the system
Depressurization phase
Valve opening
X: 96.9
Y: 3.262
X: 118.8
Y: 3.912
0.3 mg/s
0.4 mg/s
Mass flow rate [mg/s]
System pressure [bar]
Time [mins]

AP_NV_3

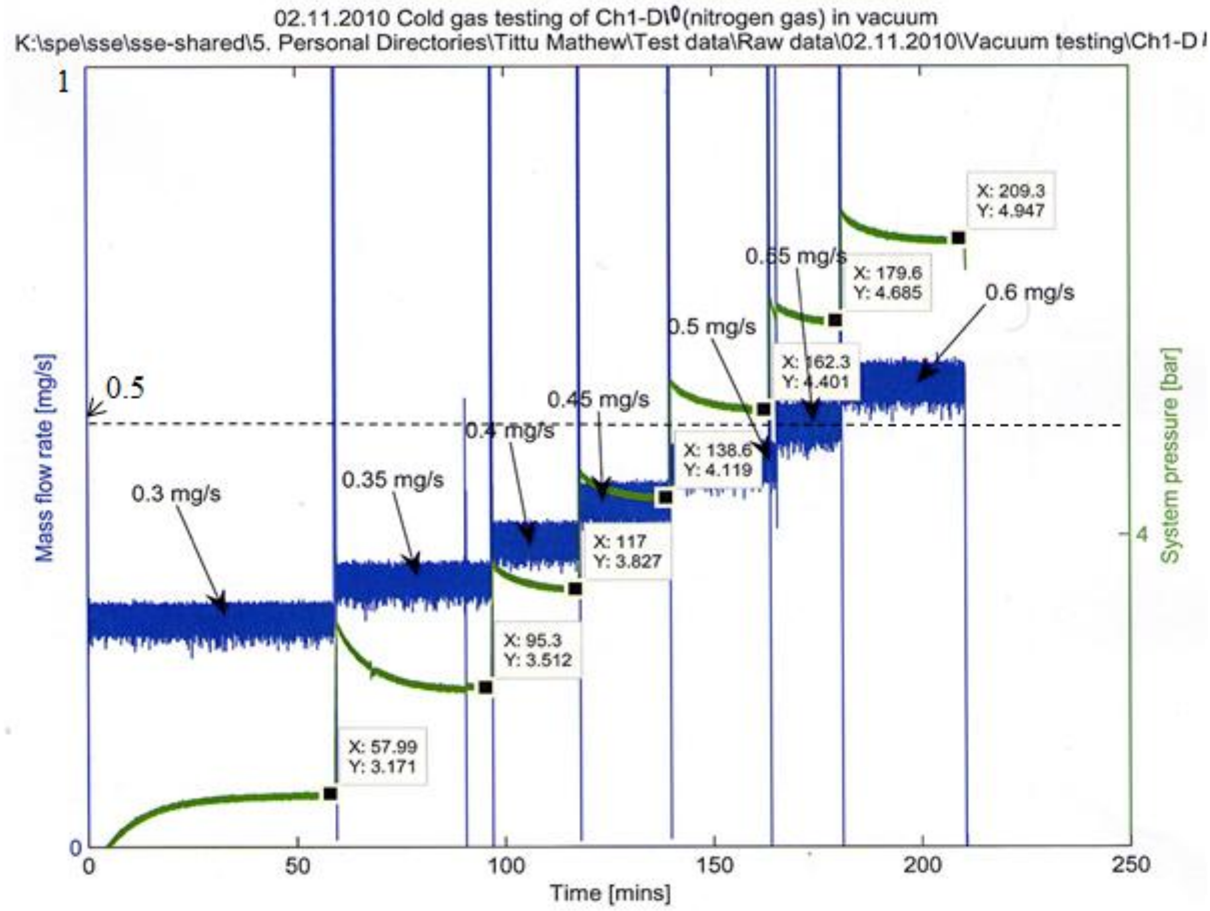

AP_NV_4

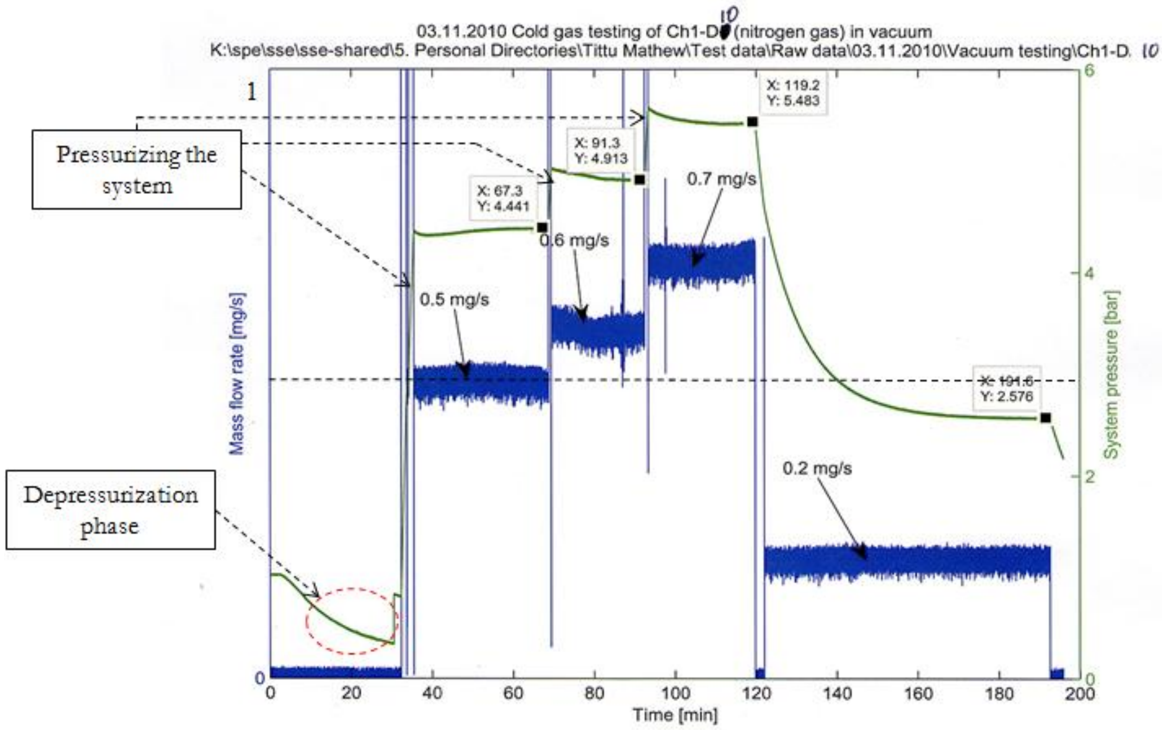

AP_NV_5

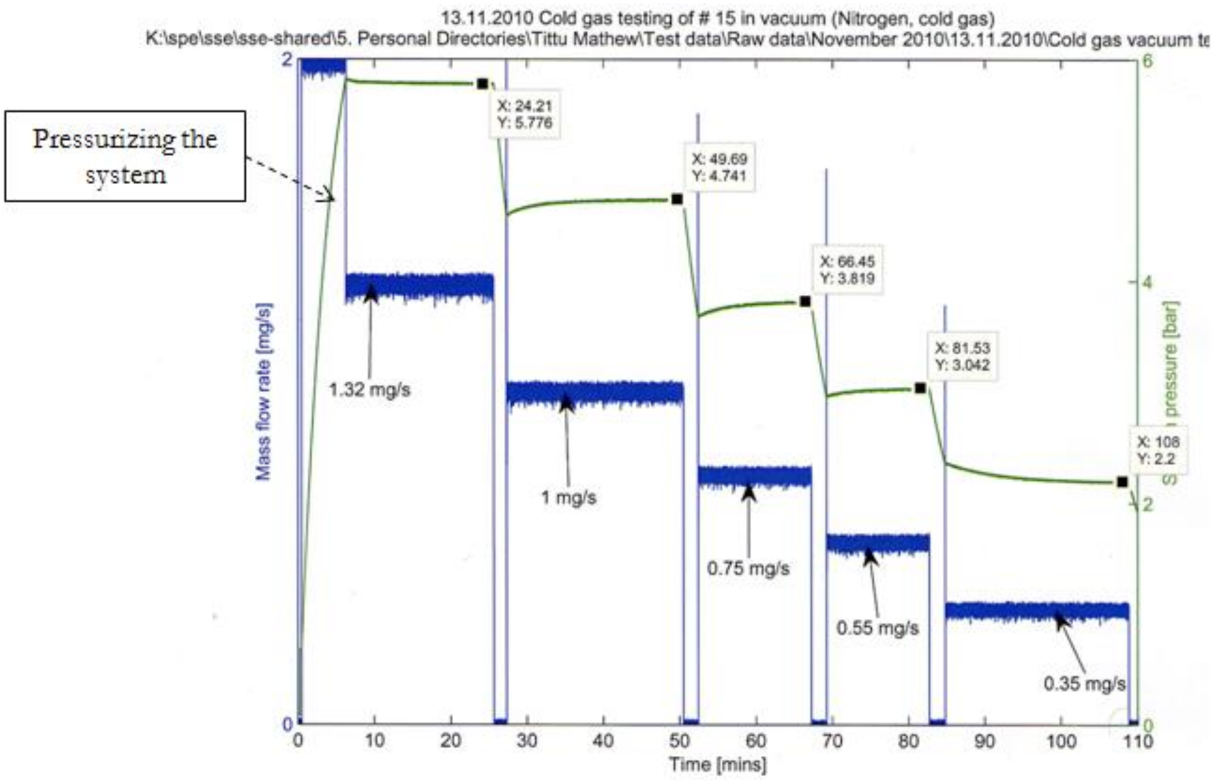
13.11.2010 Cold gas testing of # 15 in vacuum (Nitrogen, cold gas)
K:\spe\sse\sse-shared\5. Personal Directories\Tittu Mathew\Test data\Raw data\November 2010\13.11.2010\Cold gas vacuum te
Pressurizing the system
X: 24.21
Y: 5.776
X: 49.69
Y: 4.741
X: 66.45
Y: 3.819
X: 81.53
Y: 3.042
X: 108
Y: 2.2
1.32 mg/s
1 mg/s
0.75 mg/s
0.55 mg/s
0.35 mg/s
Mass flow rate [mg/s]
Time [mins]

AP_NV_6

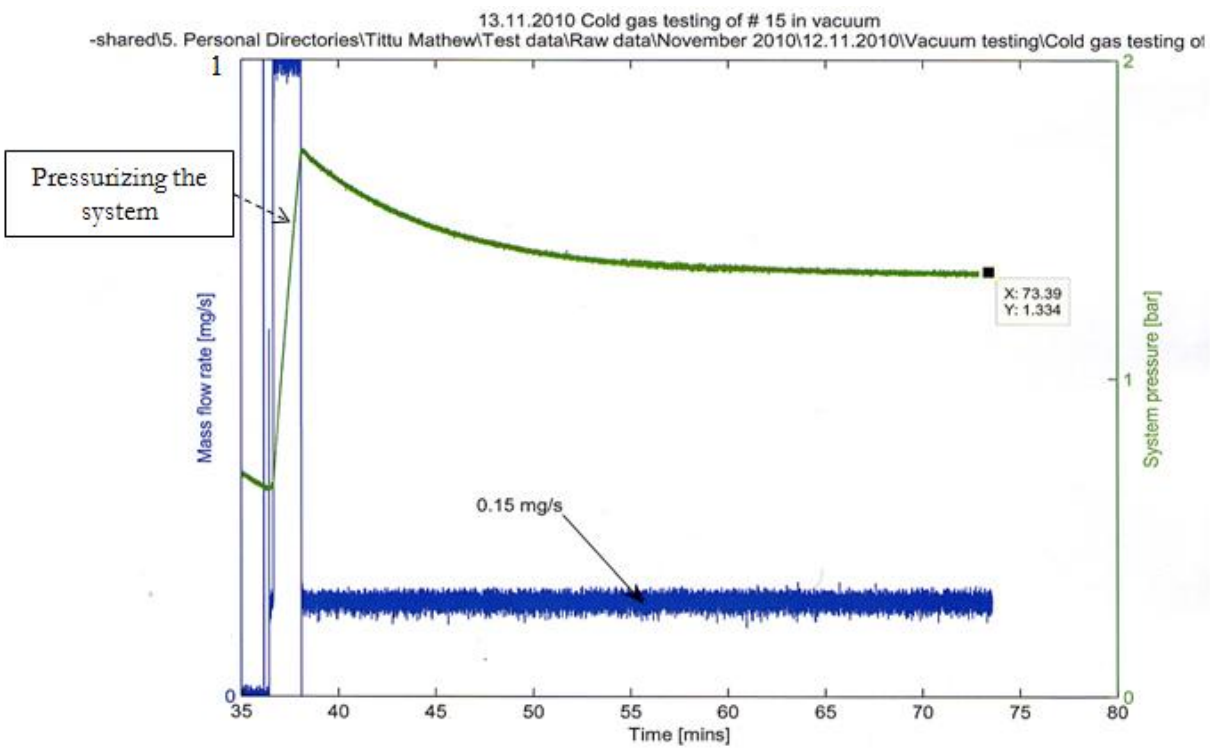
13.11.2010 Cold gas testing of # 15 in vacuum
-shared\5. Personal Directories\Tittu Mathew\Test data\Raw data\November 2010\12.11.2010\Vacuum testing\Cold gas testing of
Pressurizing the system
X: 73.39
Y: 1.334
0.15 mg/s
Mass flow rate [mg/s]
System pressure [bar]
Time [mins]

AP_NV_7

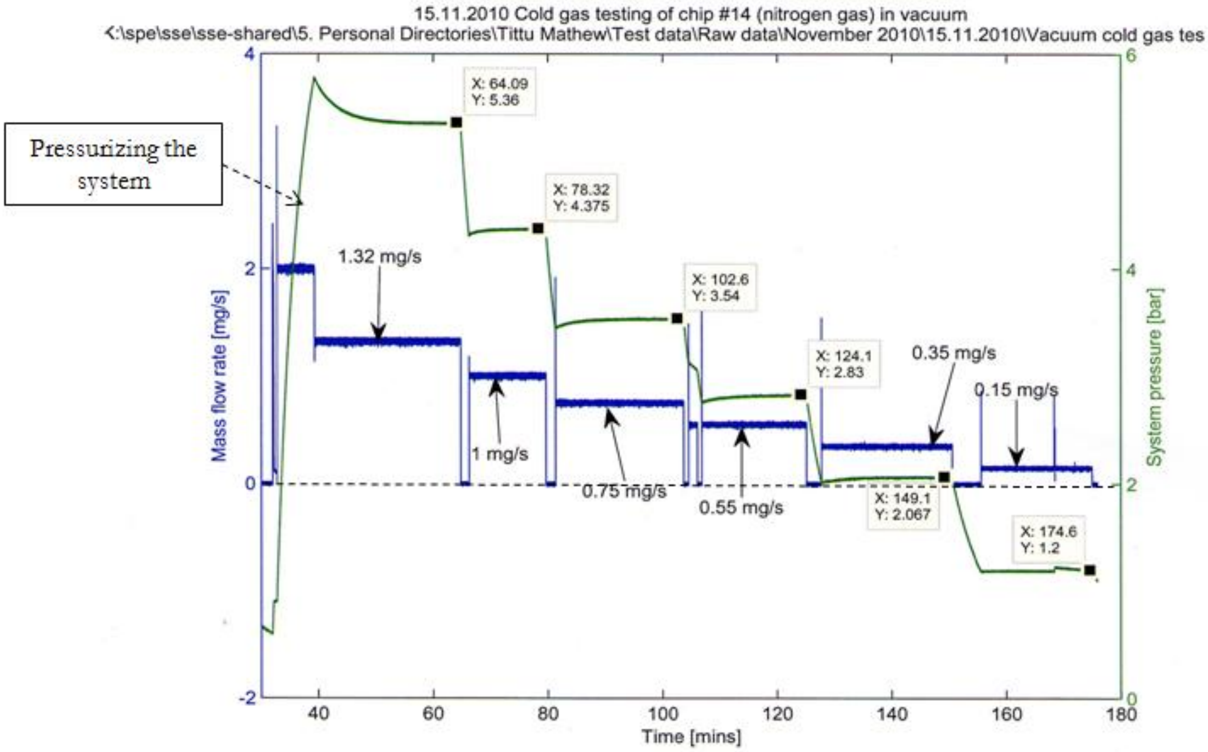
15.11.2010 Cold gas testing of chip #14 (nitrogen gas) in vacuum
K:\spe\sse\sse-shared\5. Personal Directories\Tittu Mathew\Test data\Raw data\November 2010\15.11.2010\Vacuum cold gas tes
Pressurizing the system
X: 64.09
Y: 5.36
X: 78.32
Y: 4.375
X: 102.6
Y: 3.54
X: 124.1
Y: 2.83
X: 149.1
Y: 2.067
X: 174.6
Y: 1.2
1.32 mg/s
1 mg/s
0.75 mg/s
0.55 mg/s
0.35 mg/s
0.15 mg/s
Mass flow rate [mg/s]
System pressure [bar]
Time [mins]

AP_NV_8

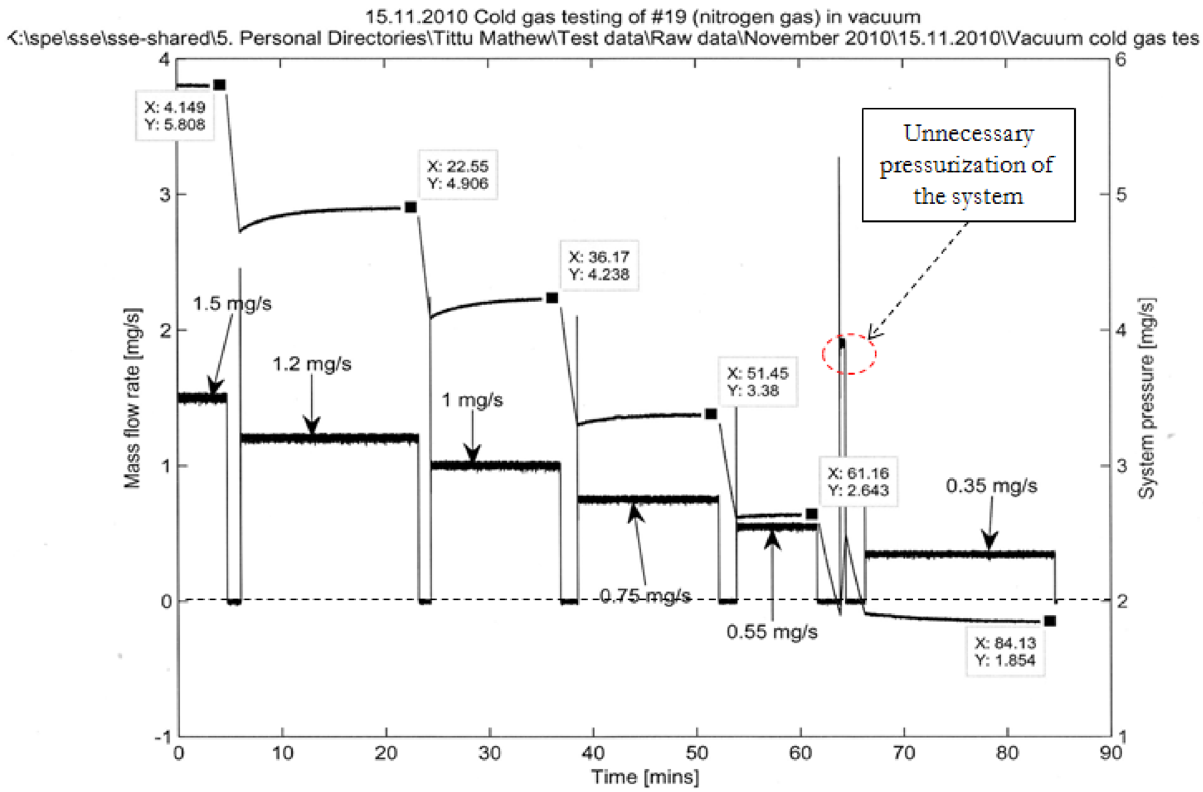
15.11.2010 Cold gas testing of #19 (nitrogen gas) in vacuum
K:\spe\sse\sse-shared\5. Personal Directories\Tittu Mathew\Test data\Raw data\November 2010\15.11.2010\Vacuum cold gas tes
X: 4.149
Y: 5.808
X: 22.55
Y: 4.906
X: 36.17
Y: 4.238
X: 51.45
Y: 3.38
X: 61.16
Y: 2.643
X: 84.13
Y: 1.854
Unnecessary pressurization of the system
1.5 mg/s
1.2 mg/s
1 mg/s
0.75 mg/s
0.55 mg/s
0.35 mg/s
Mass flow rate [mg/s]
System pressure [mg/s]
Time [mins]

AP_NV_9

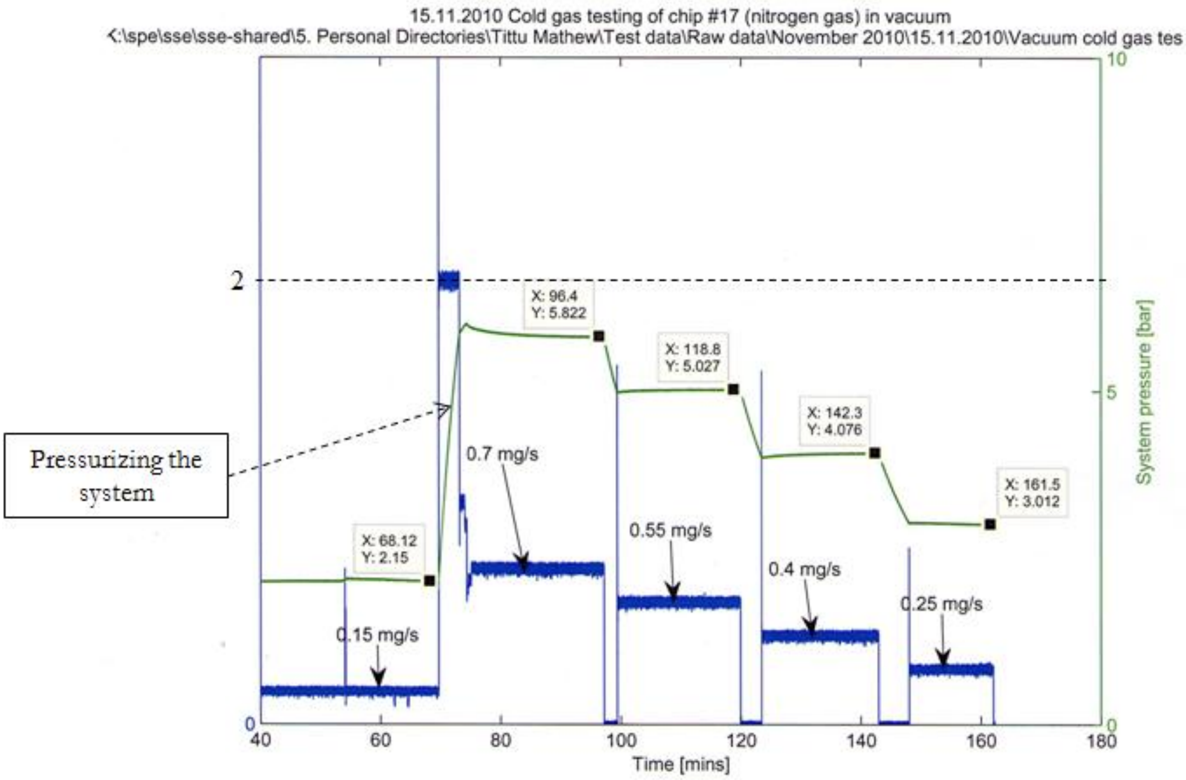

AP_NV_10

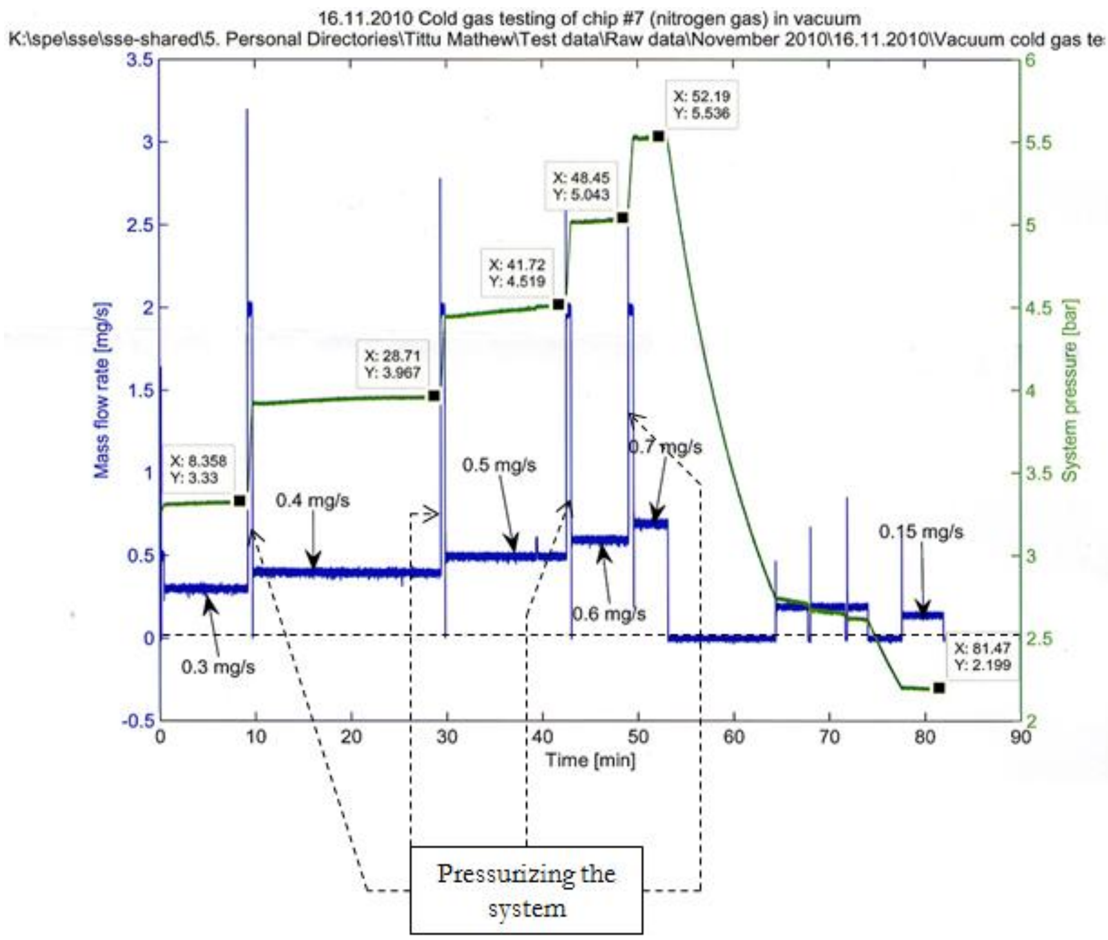

AP_NV_11

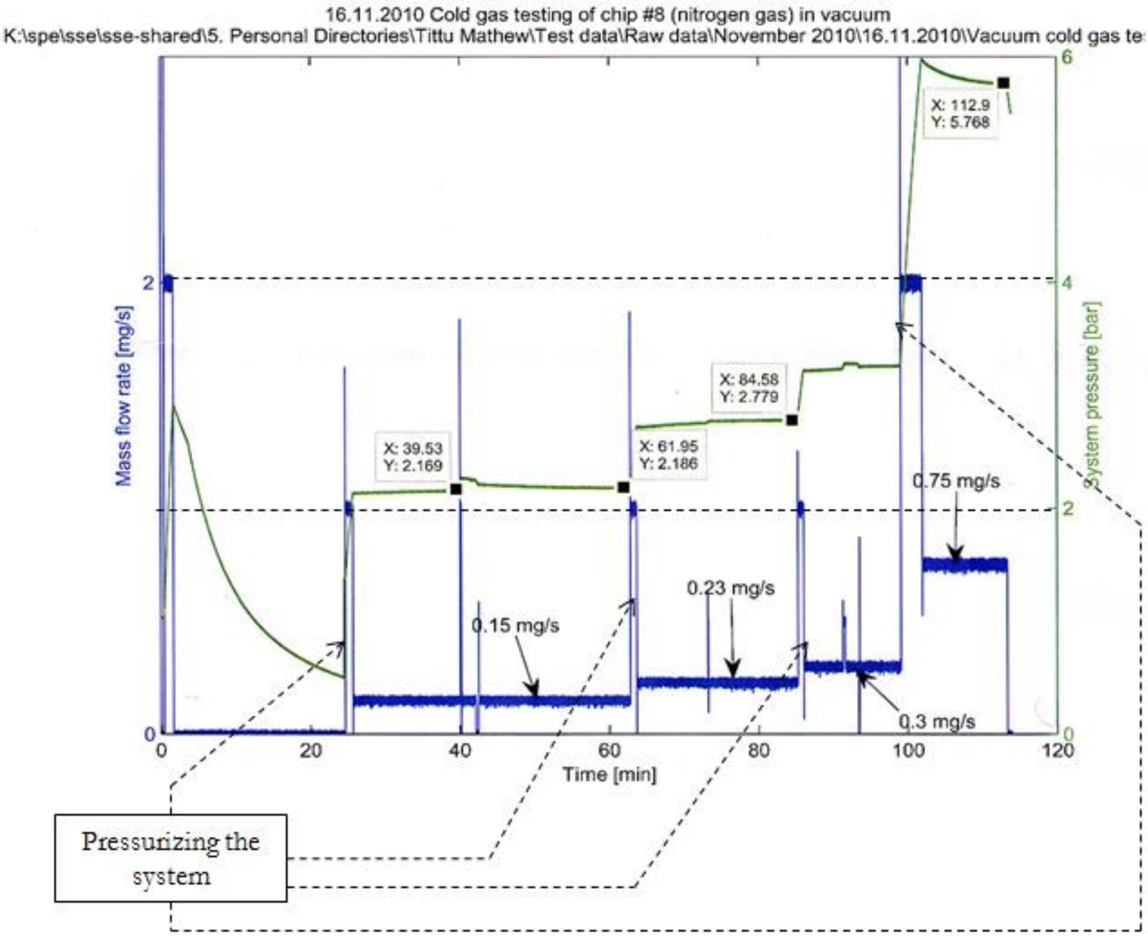

AP_NV_12

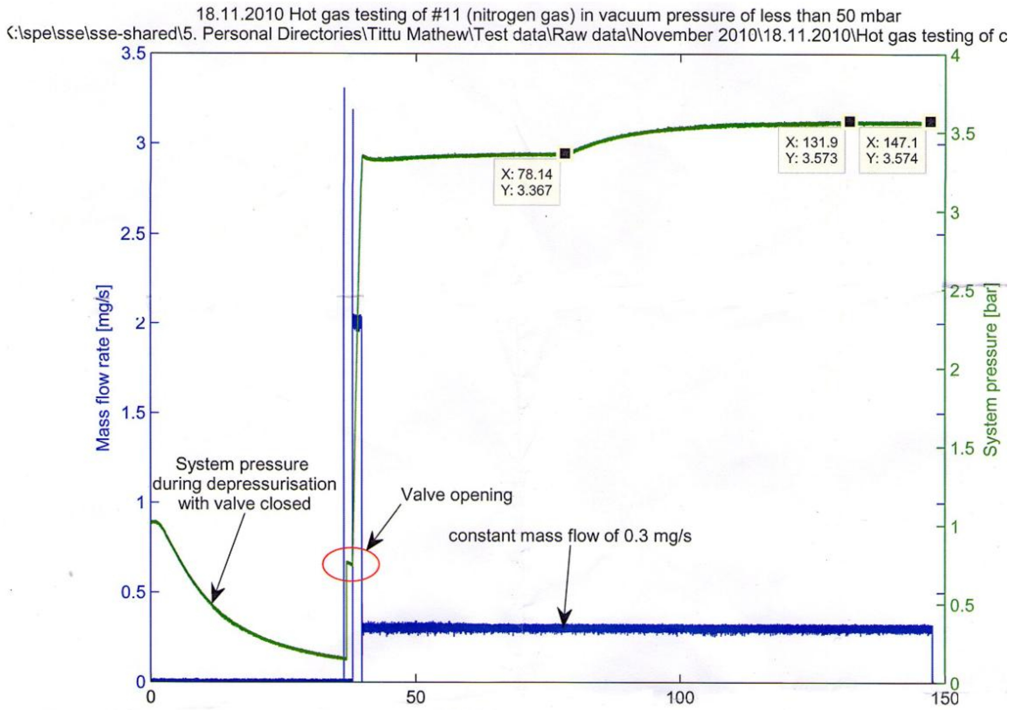

AP_NV_13

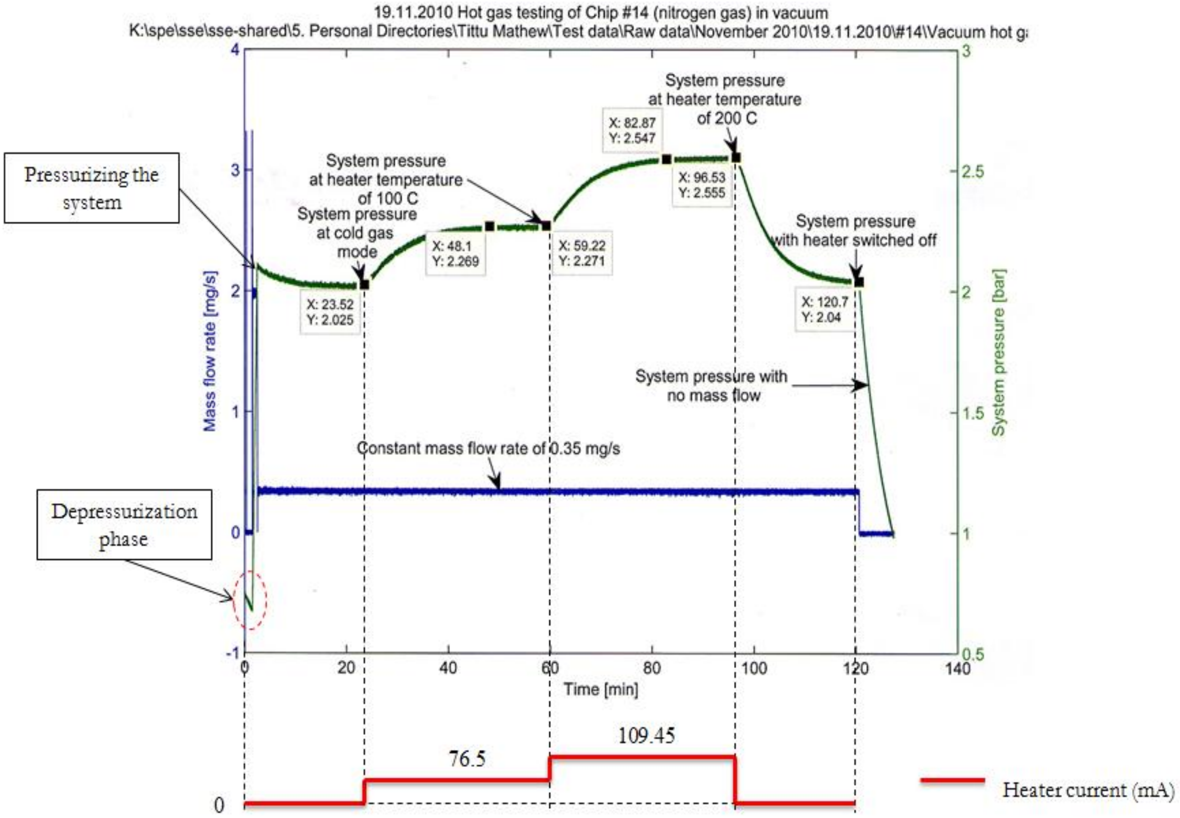
19.11.2010 Hot gas testing of Chip #14 (nitrogen gas) in vacuum
K:\spe\sse\sse-shared\5. Personal Directories\Tittu Mathew\Test data\Raw data\November 2010\19.11.2010\#14\Vacuum hot g
Pressurizing the system
Depressurization phase
System pressure at heater temperature of 100 C
System pressure at cold gas mode
System pressure at heater temperature of 200 C
System pressure with heater switched off
System pressure with no mass flow
Constant mass flow rate of 0.35 mg/s
X: 23.52 Y: 2.025
X: 48.1 Y: 2.269
X: 59.22 Y: 2.271
X: 82.87 Y: 2.547
X: 96.53 Y: 2.555
X: 120.7 Y: 2.04
Mass flow rate [mg/s]
System pressure [bar]
Time [min]
76.5
109.45
Heater current (mA)

AP_NV_14

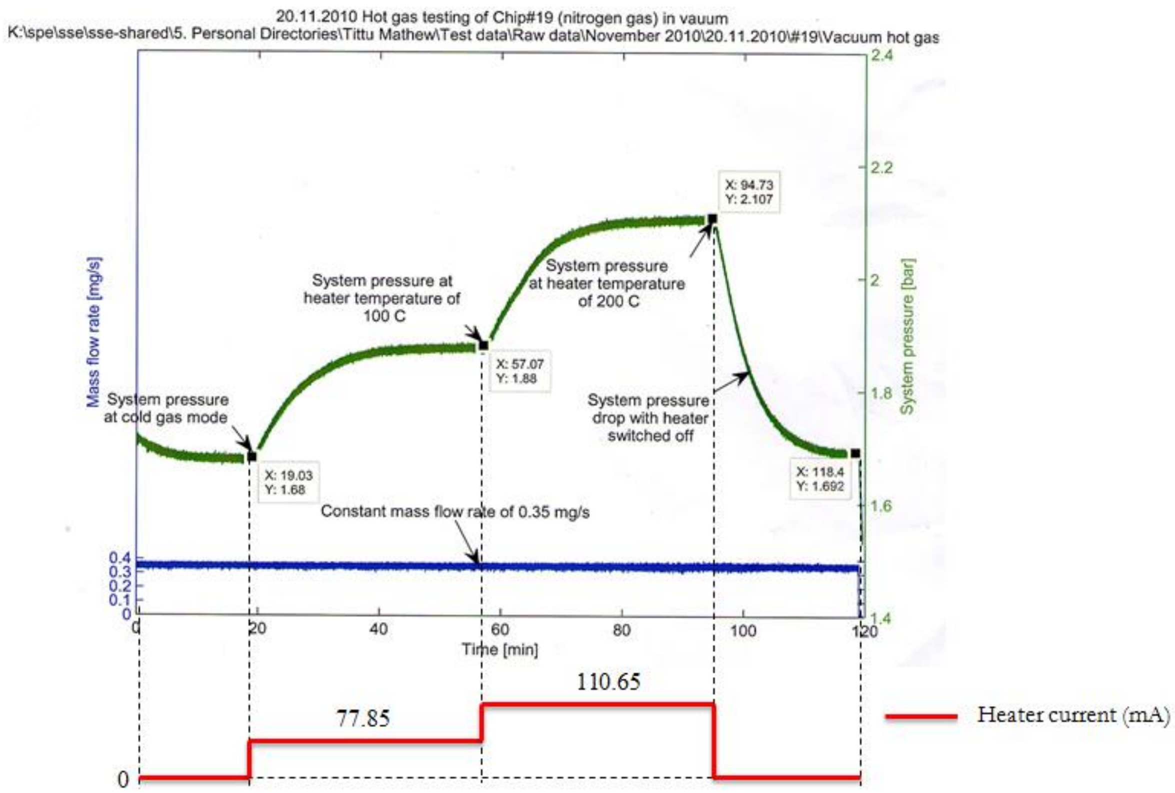
20.11.2010 Hot gas testing of Chip#19 (nitrogen gas) in vauum
K:\spe\sse\sse-shared\5. Personal Directories\Tittu Mathew\Test data\Raw data\November 2010\20.11.2010\#19\Vacuum hot gas
Mass flow rate [mg/s]
System pressure [bar]
System pressure at cold gas mode
System pressure at heater temperature of 100 C
System pressure at heater temperature of 200 C
System pressure drop with heater switched off
Constant mass flow rate of 0.35 mg/s
X: 19.03 Y: 1.68
X: 57.07 Y: 1.88
X: 94.73 Y: 2.107
X: 118.4 Y: 1.692
Time [min]
77.85
110.65
Heater current (mA)

AP_NV_15

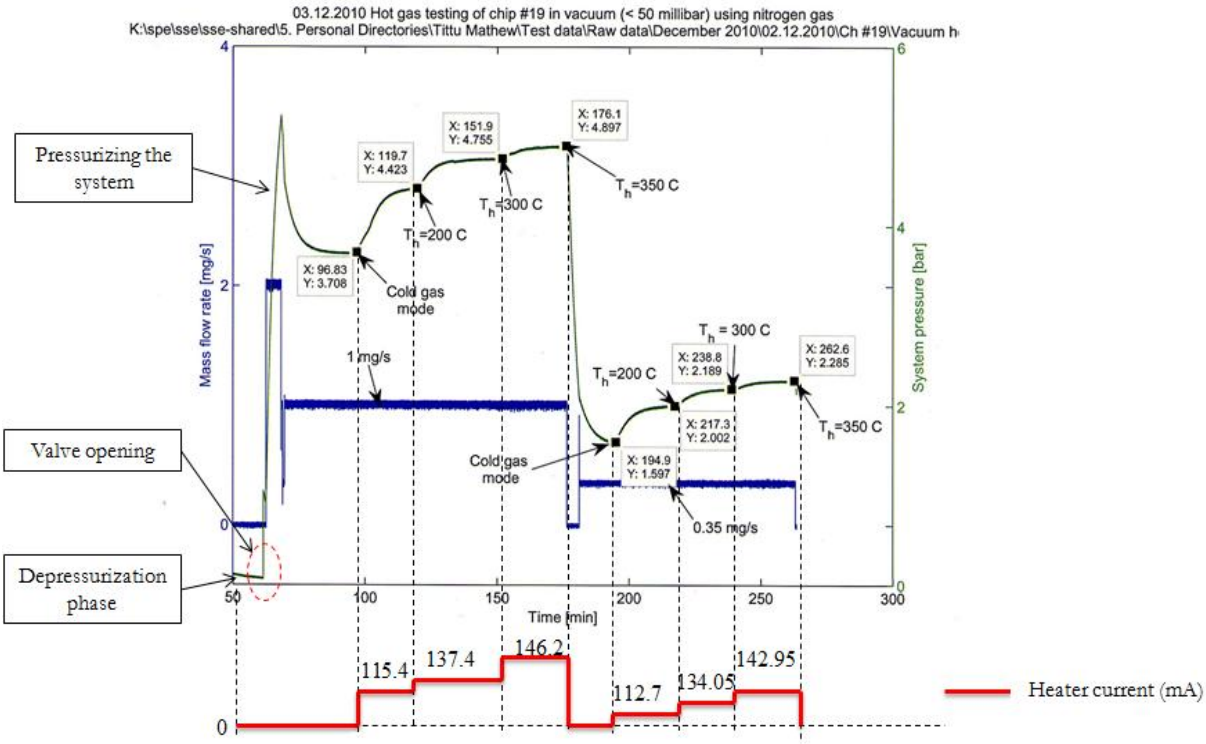
03.12.2010 Hot gas testing of chip #19 in vacuum (< 50 millibar) using nitrogen gas
K:\spe\sse\sse-shared\5. Personal Directories\Tittu Mathew\Test data\Raw data\December 2010\02.12.2010\Ch #19\Vacuum h
Pressurizing the system
Valve opening
Depressurization phase
Mass flow rate [mg/s]
System pressure [bar]
Time [min]
X: 96.83 Y: 3.708
X: 119.7 Y: 4.423
X: 151.9 Y: 4.755
X: 176.1 Y: 4.897
Th=200 C
Th=300 C
Th=350 C
Cold gas mode
1 mg/s
Th=200 C
Th = 300 C
X: 238.8 Y: 2.189
X: 262.6 Y: 2.285
X: 217.3 Y: 2.002
X: 194.9 Y: 1.597
Th=350 C
Cold gas mode
0.35 mg/s
115.4
137.4
146.2
112.7
134.05
142.95
Heater current (mA)

AP_DC_1